Simulation and Design for a Multiphase Microreactor for the Direct Fluorination of Toluene

Andreas Schuster

Thesis for the Degree of Doctor of Philosophy

University of Edinburgh

2005

THE U.K.V. EDINBURGH

Acknowledgements

I would like to thank the following colleagues and foundations for helping me during the preparation of my thesis:

My PhD supervisors, Professor Jack Ponton, Dr. Rama Lakshmanan and Dr. Khellil Sefiane for giving me the opportunity to do this work and for their support.

The Birse foundation for the funding for this project.

The University of Edinburgh, the Society of Chemistry and Industry, and the Royal Academy of Engineers for providing additional financial support.

My parents and brother for their love and encouragement helping me during the good and bad times of my project.

Ross and Christophe, my office mates during the last 4 years, for providing Unix support and an inspirational work environment.

My friends, fellow PhD students in the Department and many others in Edinburgh and in Germany for their encouragement and company during activity outside University.

Declaration

The work described in this thesis is original work of the author and was carried out without the assistance of others, except where explicitly stated in the text. It has not been submitted, in the whole part, for any other degree at the University.

Publications

Parts of this thesis have been published in scientific journals:

Schuster A., Lakshmanan R., Ponton J., Sefiane K., "Modelling a novel miniaturised reactor / separator system", J. Chem. Technol. Biot., Vol. 78, 342-346 (2003)

Pear reviewed publications:

Schuster A., Lakshmanan R., Ponton J., Sefiane K., „Simulation and design of a non-adiabatic multiphase microreactor", International Journal of Chemical Reactor Engineering, Vol. 1, A45, http://www.bepress.com/ijcre/vol1/A45 (2003)

Abstract

Small-scale production represents a paradigm change in the chemical industry, which is traditionally based on economies of scale. In such an environment microreactors (channel <1mm) may be competitive through organisational benefits, technological superiority, and inherent safety and quality. A lot of research has been done in the field of microreactor technology and it has been shown that the inherent properties of microreactors facilitate efficient conversion of reactant combinations that are generally considered unfavourable due to low yields or safety considerations.

The reaction of elemental fluorine with organic toluene is investigated, with regard to the yield of desired product and process safety. A microreactor configuration is proposed to address the problems of this direct fluorination reaction, which is extremely exothermic and prone to explosions. In addition to the favourable inherent features of miniaturised reactors there is a multifunctional catalytic membrane separating the reactants. A mathematical model of this process is developed, based on heat, mass and momentum conservation equations, and equations describing the reaction chemistry. The finite element method was found to be suitable to solve this specific equation set, because its intrinsic structure facilitates efficient handling of the present boundary value problem and simultaneous solution of coupled differential equations.

In a simulation study the process model is used to analyse heat and mass transfer processes and to determine the achievable performance of the catalytic membrane microreactor with regard to the selectivity, the production rate, the conversion of toluene and process safety. As a benchmark for the effectiveness of the membrane, we use experimental data (Jähnisch et al, 2000), and simulation results obtained with a falling film microreactor. It is shown that the reactor size has a strong influence on the outcome of the reaction. Small size reaction channels facilitate reactant contacting and heat management, which in turn results in higher product yield and process safety. The catalytic function of the membrane is the key to strongly improve the yield of desired product with the direct fluorination of toluene. Additionally the membrane adds to process safety and flexibility through decoupling of the momentum of the gas and the liquid flow and high heat conductivity. In this connection the reaction channel may be enlarged without compromising process safety, resulting in higher overall reactor output and economic competitiveness.

Contents

1 Introduction 1

1.1 Plant miniaturisation 1

1.1.1 Scale of chemical plants 1

1.1.2 Envisioning microreactors 1

1.1.3 First principle properties of microreactors 2

1.1.4 Process design with microreactors 3

1.2 Micro-reaction processes 3

1.2.1 Applications of microreactors 3

1.2.2 Direct fluorination processes 4

1.3 Outline of the thesis 5

2 Micro-reaction processes 7

2.1 Introduction 7

2.2 Overview: Applications of microreactor systems 7

2.3 Direct fluorination of toluene 9

2.3.1 Gas/liquid phase process description 9

2.3.2 Catalysed direct fluorination 10

2.4 Process Intensification with microreactors 11

2.4.1 Definition and motivation 11

2.4.2 Multifunctional reactors 12

2.4.3 Intra-reactor multifunctionality 13

2.5 Micro-scale multiphase membrane reactors 15

2.5.1 Inert membrane contactors 15

2.5.2 Catalytic membrane reactors 16

2.6 Summary 18

3 Development of microreactor models 19

3.1 Introduction 19

3.2 Falling film reactor model 19

3.2.1 Microreactor configuration 19

3.2.2 Conservation equations 21

3.2.3 Physical property parameters from the literature 22

3.3 Membrane reactor model 24

3.3.1 Microreactor configuration 24

3.3.2 Conservation equations 24

3.3.3 Transport processes within the membrane 26

3.3.4 Non-dimensional numbers 28

3.4 Discretisation and numerical solution 29

3.4.1 Modelling micro-systems 29

3.4.2 Numerical solvers 30

3.5 Finite element solution scheme 31

3.5.1 Basics 31

3.5.2 Specifying the geometry 31

3.5.3 Discretisation of the modelling domain 32

3.5.4 Element equations 33

3.5.5 Geometry scaling 34
3.5.6 Equation implementation 36
3.5.7 Discussion 37
3.6 Stability and accuracy of numerical schemes 38
3.6.1 FEM error analysis 38
3.6.2 Stability and accuracy of stepper routines 39
3.7 Summary 40

4 Empirical determination of model parameters 42
4.1 Introduction 42
4.2 Reaction chemistry of the direct fluorination of toluene 43
4.2.1 Reaction mechanism 43
4.2.2 Reaction kinetics 46
4.2.3 Heat of reaction 47
4.2.4 Reaction mechanism involving heterogeneous catalysis 47
4.3 Gas absorption 49
4.3.1 Estimation of gas solubilities 49
4.4 Matching simulations and experiments 51
4.4.1 Unknown model parameters 51
4.4.2 Fitting parameters using experimental data 51
4.4.3 Results 53
4.4.4 Discussion 57
4.5 Summary 58

5 Simulation preliminaries **59**

5.1 Introduction 59

5.2 Performance parameters 59

5.3 Reaction conditions and reaction kinetic analysis 60

5.3.1 Reactor configuration and reactant feed 60

5.3.2 Reaction kinetics and temperature 62

5.3.3 Membrane layout (CMMR only) 64

5.3.4 Summary: Reaction conditions 64

5.4 Process hydrodynamics 65

5.4.1 Flow profiles and pressure drop 66

5.4.2 Gas/liquid interface 68

5.4.3 Liquid phase flow 75

5.4.4 Surface forces and hydrodynamic instabilities 79

5.4.5 Summary: Process hydrodynamics 82

5.5 Chapter summary 83

6 Isothermal reactor analysis **80**

6.1 Introduction 80

6.2 Operating conditions with the FFMR 80

6.2.1 Modelling domain and procedure 80

6.2.2 Results 81

6.2.3 Discussion 84

6.3 CMMR operation 84

6.3.1 Modelling domain and procedure 84

6.3.2 Results: Membrane parameters 85

6.3.3 Results: High conversion of toluene 87

6.3.4 Results: Multiphase contacting 88

6.4 Summary 89

7 Non-adiabatic reactor analysis 98

7.1 Introduction 98

7.2 Heat generation and heat removal 98

7.2.1 Model and procedure 98

7.2.2 Results 101

7.2.3 Discussion 112

7.3 Non-isothermal process simulations 112

7.3.1 Model and procedure 112

7.3.2 Results 113

7.3.3 Discussion 119

7.4 Entrance effects 120

7.4.1 Model and procedure 120

7.4.2 Results 121

7.5 Summary 123

8 Heat Sink Design 125

8.1 Introduction 125

8.2 Single channel CMMR configuration 125

8.2.1 Model domain 125

8.2.2 Procedure 126

8.2.3 Result 128

8.3 Multiple channel reactor configuration 133

8.3.1 Model and procedure 133

8.3.2 Results 135

8.3.3 Discussion 138

8.4 Summary 139

9 Conclusions 140

Appendix A : Fluorination of Organic Compounds **149**

A.1 Fluorine bonding with hydrogen and carbon 149

A.2 Methods of fluorination 150

Appendix B: Reaction Chemistry – Direct Fluorination of Toluene **151**

B.1 Literature review 151

B.2 Reaction mechanism 153

B.3 Reaction kinetics 157

B.4 Heat of reaction 159

B.5 Reaction kinetic data collection 161

Appendix C : Physical Property Data **167**

C.1 Parameter values 167

C.2 Parameter calculations 169

C.3 References 172

Appendix D : Reactor Stability and Heat Back-mixing **173**

D.1 Problem statement 173

D.2 Procedure 173

D.3 Results 174

Appendix E : Gas-phase Mass Transfer Coefficient **177**

E.1 Introduction 177

E.2 Smooth film absorption 178

E.3 Liquid-phase and over-all mass transfer coefficients 179

E.4 Sherwood number with smooth and wavy film 181

Appendix F : Finite Difference Method **169**

F.1 Model implementation 169

F.2 Liquid channel PDE-solver 171

F.3 Results and Discussion 172

Appendix G : Miscellaneous **173**

G.1 Surface effects 186

G.1.1 Influence of gravity on the shape of the fluid 186

G.1.2 Fluid instabilities 187

G.2 Residence time 189

G.3 FEM method: Derivation of element equations 190

G.4 Pressure drop 192

G.5 Gas flow entrance length 192

Nomenclature **195**

Acronym List **198**

References **199**

List of figures

Figure 3 1. Sketch of the falling film microreactor configuration 19

Figure 3 2. Scaled geometry of the 2D FFMR domain including boundary and sub-domain labels. 20

Figure 3 3. Scaled geometry of the 3D FFMR domain 21

Figure 3 4. Sketch of the catalytic membrane microreactor configuration 24

Figure 3 5. Scaled geometry of the 2D CMMR domain including boundary and sub-domain labels. 25

Figure 3 6. Scaled geometry of the 3D CMMR domain including boundary and sub-domain labels 25

Figure 3 7. Membrane model: In-line touching cubes, Hsu et al. (1995) 27

Figure 4 1. Falling film reactor by Jähnisch et al. (2000) 52

Figure 4 2. Comparison of the yield Y of desired product between the experimental data and simulations 55

Figure 4 3. Comparison of the conversion X of toluene between the experimental data and simulations 56

Figure 4 4. Comparison of the yield Y of desired product between the experimental data and simulations 56

Figure 4 5. Comparison of the conversion X of toluene between the experimental data and simulations 57

Figure 5 1. Temperature dependency of the reaction kinetic constants of the non-catalysed reaction system 63

Figure 5 2. Selectivity as a function of the temperature and the catalyst activity □ 63

Figure 5 3. Velocity profile in the gas channel with the CMMR. The arrows and the colour code quantify the velocity vector, 67

Figure 5 4. Velocity profile in the gas channel with the FFMR: Negative relative velocity 71

Figure 5 5. Velocity profile in the gas channel with the FFMR: Zero relative velocity 71

Figure 5 6. Velocity profile in the gas channel with the FFMR: High relative velocity 71

Figure 5 7. Sherwood number Sh versus relative Reynolds number $Re_{rel} < 0$ 71

Figure 5 8. Sherwood number Sh versus relative Reynolds number $Re_{rel} > 0$ 72

Figure 5 9. Mean mass transfer coefficient k_g 73

Figure 5 10. Overall mass transfer coefficient k_{total} vs k_g 75

Figure 5 11. Scaled geometry of the 2D dimensional domain including boundary and sub-domain labels. 76

Figure 5 12. Selectivity and conversion with plug and semi-parabolic liquid phase flow profile. 78

Figure 5 13. Selectivity and conversion with plug and parabolic liquid phase flow profile. 78

Figure 5 14. Concentration of toluene cTol in the liquid phase near the reactor entrance; [cTol]=kmol/m3 81

Figure 5 15. Temperature Tl in the liquid phase near the reactor entrance; [Tl]=K 82

Figure 6 1. Influence of temperature on the reactor performance 86

Figure 6 2. Influence of the toluene concentration on the selectivity 87

Figure 6 3. Influence of the toluene concentration on the differential selectivity towards by-products of the series reactions 87

Figure 6 4. Influence of the toluene concentration on the output of FTol 88

Figure 6 5. Influence of the fluorine concentration on the reactor performance 88

Figure 6 6. Influence of the fluorine concentration on the differential selectivity towards products of the series reactions 89

Figure 6 7. Influence of the reactant feed ratio on the selectivity 89

Figure 6 8. Selectivity and conversion of toluene near the reactor entrance versus the membrane thickness 92

Figure 6 9. Reaction of fluorine and ratio between series reaction and toluene near the reactor entrance versus the membrane thickness 93

Figure 6 10. Yield and selectivity obtained with the membrane reactor as function of the catalyst activity compared to the uncatalysed process in the falling film reactor 93

Figure 6 11. Reaction kinetic constant and activation energy versus the catalytic activity 94

Figure 6 12. Performance parameters *X, Y, S* vs normalised x-coordinate 95

Figure 6 13. Concentration profile of fluorine in the liquid phase in a cross-section of the membrane reactor. 96

Figure 6 14. Selectivity *S* and yield *Y* vs liquid layer between solid and gas-phase 96

Figure 7 1: Division of the entire reactor length into *n* sections 100

Figure 7 2. Thermal conductivity enhancement over pure liquid through solid membrane material 102

Figure 7 3. Thermal conductivity enhancement over pure liquid as a function of the porosity 103

Figure 7 4. Heat generation lines for *n* reactor sections and heat removal lines at different coolant temperatures (height ch_f=0.0001m, width *cw*=0.0003m) 105

Figure 7 5. Heat generation lines for *n* reactor sections and heat removal lines at different coolant temperatures (height ch_f=0.0002m, width *cw*=0.0006m) 105

Figure 7 6. Heat generation lines for *n* reactor sections and heat removal lines at different coolant temperatures (height ch_f=0.0004m, width *cw*=0.0012m) 106

Figure 7 7. Mass transfer coefficients k_g and k_l versus temperature 107

Figure 7 8. Absorption enhancement factor and modified Thiele Modulus versus temperature 107

Figure 7 9. Heat generation lines and heat removal lines with varying membrane thickness (height ch_f=0.0001m, width *cw*=0.0003m) 109

Figure 7 10. Heat generation lines and heat removal lines with varying membrane thickness (height ch_f=0.0002m, width *cw*=0.0006m) 109

Figure 7 11. Heat generation lines and heat removal lines with varying membrane thickness (height ch_f=0.0004m, width *cw*=0.0012m) 110

Figure 7 12. Heat generation and heat removal with varying membrane thickness (height ch_f=0.0001m, width *cw*=0.0003m) 111

Figure 7 13. Heat generation with standard reactor geometry and varying membrane thickness (ch_f=0.0001m, *cl*=0.065m) 114

Figure 7 14. Temperature with standard reactor geometry and varying membrane thickness (ch_f=0.0001m, *cl*=0.065m) 115

Figure 7 15. Hot spot temperature as a function of the channel height. Comparison between the FFMR and the CMMR; constant heat flux boundary condition q = 8.0 kJ/m2 116

Figure 7 16. Maximum temperature as a function of the channel height. Comparison between the FFMR and the CMMR; heat load created locally by chemical reaction 118

Figure 7 17. Comparison of conversion *X* and selectivity *S* with the FFMR and the CMMR as function of the reactor size. 118

Figure 7 18. Comparison of the product output and selectivity *S* with the FFMR and the CMMR as function of reactor size. 119

Figure 7 20. Heat transfer coefficient between liquid channel and reactor wall 122

Figure 7 21. Heat flux through the membrane, across the side wall and across the channel bottom; ch=0.2mm, mh=0.05mm 123

Figure 8-1. Uneven and even heat load used as boundary condition 126

Figure 8-2. Temperature distribution at the top of the membrane at uneven heat distribution under varying conditions 131

Figure 8-3. Temperature profile in the cooling channel (co-flow arrangement) 132

Figure 8-4. Temperature distribution at the top of the membrane at even heat distribution 132

Figure 8-5. Scaled geometry of the two dimensional domain including boundary and sub-domain labels 134

Figure 8-6. Temperature distribution at the top of the membrane at uneven heat distribution 137

Figure 8-7. Temperature profile in the cooling channel (cross-flow arrangement), the liquid channel and the membrane domain 138

List of tables

Table 3 1. Boundary conditions with the FFMR 23

Table 3 2. Comparison of boundary conditions with the CMMR and FFMR 26

Table 3 3. Thermal conductivity data 27

Table 3 4. Membrane structure data 28

Table 3 5. Most important mesh generation parameters with FEMLAB 33

Table 3 6. Most important element characterisation parameters 34

Table 4 1. Estimation of the kinetic data of the lumped reactions in Scheme 4 3 at a temperature of T=257K 47

Table 4 2. Estimation of the heat of reaction 47

Table 4 3. Hildebrand coefficients 50

Table 4 4. Specification of unknown physical parameters 51

Table 4 5. Unknown parameters in isothermal system 53

Table 4 6. Experimental data: direct fluorination in a falling film reactor 53

Table 4 7. Hildebrand correlation parameters at T=257K 54

Table 4 8. Reaction kinetic constants at T=257 K 54

Table 4 9. Reaction kinetic constants at T=257 K 55

Table 5 1. Operational parameters 62

Table 5 2. Standard operational parameters 65

Table 5 3. Reynolds numbers in the gas and liquid channel 67

Table 5 4. Operational parameters in addition to the standard parameters 69

Table 5 5. Boundary conditions of the mass conservation equations 69

Table 5 6. Nusselt number at constant temperature boundary condition and rectangular channels with one active wall 70

Table 5 7. Calculation of the gas phase mass transfer coefficient 70

Table 5 8. Flow profiles implemented into the mass conservation equations 76

Table 5 9. Reactor geometry parameters 76

Table 5 10. Calculation of the thermal and solutal Marangoni numbers 81

Table 6-1. Range of operational parameters 85

Table 6-2. Operational parameter settings for high performance 90

Table 7-1. Cases for sensitivity studies 101

Table 7-2. Range of the conductivity ratio I and porosity 101

Table 7-3. Absorption parameter setting sensitivity studies 111

Table 7-4. Range of operational parameters 113

Table 8-1. Boundary conditions with the CMMR 127

Table 8-2. Property data of the liquid coolant (water) at T=273 K 127

Table 8-3. Operating conditions 127

Table 8-4. Temperature distribution at the top of the membrane at uneven heat distribution and co-current flow 130

Table 8-5. Temperature distribution at the top of the membrane at uneven heat distribution with counter-current flow and constant temperature heat sink 130

Table 8-6. Temperature distribution at the top of the membrane at constant heat load 130

Table 8-7. Boundary conditions with the reactor domain 134

Table 8-8. Operating conditions 134

Table 8-9. Temperature distribution at the top of the membrane at uneven heat distribution 136

Table 8-10. Temperature distribution at the top of the membrane at even heat load distribution 137

Chapter 1

Introduction

1.1 Plant miniaturisation

1.1.1 Scale of chemical plants

The most significant trend of the last thirty to fifty years in the manufacturing industries has been miniaturisation. This has reduced the costs of products, while dramatically increasing the size and diversity of the market. Furthermore, these products can be considerably more efficient, easier to use and maintain, safer, cheaper and smaller, especially in the case of electronic equipment (Benson and Ponton, 1993). Following the principle of economy of scale the chemical industry was driven into the opposite direction and at the same time efforts were undertaken to improve these large-scale chemical plants in terms of safety, environmental impact and thermal efficiency. There are limitations to these endeavours and to the efficiency of the entire process, determined by unfavourable inherent features of large-scale equipment: high overall capital investments, complicated and time-consuming scale-up process, high fluid hold-up, heat management and reaction temperature difficult to control, and mixing between different phases is difficult to achieve. These deficiencies become more significant with increasing reactor size.

1.1.2 Envisioning microreactors

Benson and Ponton (1993) suggested the miniaturisation of chemical reaction channels to a sub-millimeter level in which chemical plants might follow the development of consumer products.

The following list gives an overview of the advantages expected from the use of microreactors:

- Inherent safety and reliability
- Improved process control and automation
- Distributed 'Just in time' production
- Fast progression from lab scale to production (Ehrfeld, 2000a)
- Replacing a batch by a continuous process
- Change of product properties
- Intensification of processing

Microfabricated reactors were introduced at the first DECHEMA conference in 1995 as a means for point of use manufacture of chemicals that are required in small quantity (Srinivasan, Jensen et al., 1997).

1.1.3 First principle properties of microreactors

Basically chemical processes in microsystems follow the same principles as in large-scale devices because their dimensions are too large to enable interaction on the molecular level. However, phenomena may be exploited that are negligible or non-existent on the macro-scale. Small reaction channels automatically involve very short diffusion, conduction and mixing path length. Thus, the gradients for temperature, concentration, density, or pressure are relatively high, so that mass, heat and momentum transfer rates are extremely high (increase by factors of 10 to 100 or more compared to conventional devices) (Burns, 1998; Wegeng, 2000). The increase in surface to volume ratio yields advantages in heat transfer and active catalyst surface, e.g. for gas phase reactions on catalyst coated reactor walls. In this manner the amount of catalyst needed may be decreased by a factor of 1000 and the reactor size could decrease by a factor of 10 (Ehrfeld, 2000a).

Laminar flow conditions in micro-channels facilitate theoretical descriptions of the flow process as well as an increase in reliability of simulations and theoretical predictions. Advantages like narrow residence time distributions and uniform mass transport kinetics are unique to microreaction systems. Furthermore, the pressure drop of laminar flow is lower then in the turbulent flow regime (Ehrfeld, 2000b).

1.1.4 Process design with microreactors

Process intensification is a plant design paradigm developed to reduce the capital cost of the production system by designing plants that match precise requirements of the process and meets the business needs. In this manner safety challenges and environmental concerns could be matched as well as closer control of product attributes in order to deliver greater customisation.

Focussing on the design of a chemical reactor unit, process intensification is achieved through multi-functionality of reactors. Here, several "functions" or processes are designed to occur simultaneously inside the reactor. The aim is optimum integration of mass, heat and momentum transfer within a reactor vessel. Microreators help to achieve process intensification on the catalyst and intra-reactor level, e.g. through thin film catalysts with low diffusion barrier or reproducible mixing of multi-phase fluidic systems (Ehrfeld, 2000a; Franz, 2000). Through high fluid property gradients and high surface to volume ratios microreactors facilitate process intensification on inter-reactor level, i.e. synthesis of unit operations. In this manner integration of reaction, heat exchange and separation operations (Quiram, 2000a) can be achieved. In this connection membrane processes become very interesting because some problems traditionally associated with membranes can be overcome on the microscale, e.g. membrane stability, cost of the material and uniformity of the membrane matrix.

1.2 Micro-reaction processes

1.2.1 Applications of microreactors

The technologically unique characteristics of microreactors make them efficient tools for chemical reaction data acquisition and catalyst testing. Combined with the envisioned operational advantages of microreactors outlined above these devices show great potential for chemical production (see Ehrfeld, 1996; Lerou, 1995; Quiram, 2000a). In microchannels more extreme processes may be conducted safely, i.e. very exothermic and potentially explosive reactions and a whole range of currently not considered processes become accessible. Great advantages occur if such alternative processes allow a simpler plant design using fewer unit operation steps at improved yield or selectivity compared to traditional plants.

Clearly, 'economy of scale' is a strong argument for large-scale production and seems to render production in microreactors unprofitable, since the product output is limited and the ratio of construction material to reaction volume is inevitable high for microreactors. However, if a process exploits the advantages of small channels it may be conducted economically in a microreactor. In this work the direct fluorination of toluene is chosen as a sample process in a case study.

1.2.2 Direct fluorination processes

Fluorinated aromatic compounds are of high commercial interest, e.g. as pharmaceuticals, reactive dyestuff, isotope labels and liquid crystals. Two routes are favoured for their synthesis in industry: the Schiemann (Balz and Schiemann, 1927) and the Halex process both of which use fluorinating agents. The yield of both processes is limited due to consecutive multi-step synthesis (Schiemann) and side-reactions due to long reaction times (Halex). A one-step process, like the direct fluorination using elemental fluorine potentially yields a number of advantages: higher yield, process variability for different reactants, less energy consumption, and less waste production, simpler apparatus and cheaper raw materials (Lagow, 1991).

The direct fluorination reaction of organic compounds in the gas/liquid phase follows a very exothermic radical reaction mechanism. This radical mechanism is a complex system of parallel and series reaction steps. Even though it was shown that this reaction can be performed safely at extremely low temperatures and very low concentrations of fluorine for industrial production the apparently unselective attack of atomic fluorine results in a wide product range including significant amounts of tar (Grakauskas, 1970).

With the discovery of the electrophilic fluorination of organic compounds it was shown that fluorine can be a highly selective reactant even though the competing free-radical process negatively affects the overall performance. Earlier work indicated that relatively high yields can be achieved with direct fluorination of aromatic compounds in electrophilic fluorinating agents, e.g. with acetonitrile or trifluoroacetic acid, which also increase the solubility of fluorine in the liquid phase (Conte, 1995). Acidic catalysts were used to turn fluorine into an electrophile limiting the radical reaction, thus increasing the selectivity of the process. (Chambers, 1996).

Microreaction technology was used to produce mono-fluorinated toluene directly from fluorine in a continuous cooled falling film reactor (Jaehnisch et al., 2000). The most important features of this reactor with regard to the specific chemical reaction were controlled reacting conditions, including controlled contacting of the reactants, and efficient heat management. The process was easy to operate but the results indicated that key problems

associated with the process could not be solved, as yet, which were relatively low selectivity and space time yield.

1.3 Outline of the thesis

Up to now there is no reported example of a successfully operating micro-plant for industrial production. Probably, a break-through and a paradigm change in the chemical industry can only be achieved when an example of an effective miniaturised chemical process can be presented.

This thesis begins with a literature review about research by other authors on process design techniques and chemical processes that show great potential for the application with micro-scale reactors (Chapter 2). Chemical reactions are illustrated which take real advantage from miniaturised reaction channels and therewith show the potential of these devices for commercial production of the specific compounds. Furthermore design techniques are considered, which are especially applicable to the micro-scale, i.e. process intensification, simplification and synthesis. An interesting reaction to be conducted on the micro-scale is the direct fluorination of toluene, which is chosen as a sample process. The difficult characteristics of this reaction are illustrated and potential solutions are discussed.

In Chapter 3, a multiphase microreactor (CMMR) is designed addressing the problems inherent to the direct fluorination of toluene. To assess the performance of this device a miniaturised falling film reactor (FFMR) is introduced as benchmark, which had been experimentally used to conduct this chemical reaction. Both microreactor configurations are explained and the development of a mathematical model for the individual process is illustrated:

- The model domain of the FFMR consists of a gas and liquid channel transporting fluorine, and toluene and the reaction products, respectively. The flow hydrodynamics, and heat and mass transfer are described by means of differential equations.
- The CMMR model is an extension of the FFMR model where a porous solid membrane layer sub-domain is introduced between the gas and liquid channel. The set of differential equations is completed through the description of mass and heat transport within the membrane.

The partial differential equations, which make up the process model, cannot be solved analytically. The choice of a numerical method, and the implementation of the mathematical model are explained.

Next, values are assigned to the coefficients occurring in the equation set. This is predominantly material property data, i.e. physical, thermodynamic and chemical property data of the compounds involved. Most of the required information is available from the literature. However, the description of the reaction mechanism and the absorption mass transfer in the literature is not sufficiently detailed. Therefore, in Chapter 4, these two sub-processes are described by approximate algorithms composed of simplified equations with only few unknown parameters. These parameters are determined through fitting the FFMR model to experimental data (Jaehnisch et al., 2000). Furthermore, these experimental results are used to verify the model and an estimate for its accuracy is stated. These steps finalise the development of the CMMR and the FFMR mathematical model and it is ready to be used for process simulations.

First, in Chapter 5, the model describing the CMMR is used to analyse the direct fluorination of toluene and develop an understanding of the process. Key performance parameters are derived from the mass conservation equations and the chemical reaction mechanism. In a simulation study flow hydrodynamics are investigated in the gas and liquid channel of the CMMR and FFMR. The objective is to visualise the flow characteristics and their influence on the performance of the process. Special attention is paid to the operational characteristics that go along with the transition from the falling film reactor to the membrane reactor.

Next, in Chapter 6, isothermal process analysis is accomplished. The influence of important operating conditions, i.e. temperature, reactant concentrations and residence time, on the performance of the FFMR and the CMMR is investigated with focus on the selectivity, the production rate and the conversion of toluene. Furthermore, we aim to study to what extent the catalytic membrane inside the CMMR can improve the chemical reaction compared to the FFMR.

The objective in Chapter 7 is to investigate heat generation and heat removal with the direct fluorination in micro-channels using a non-isothermal reactor model. Here, the influence of the channel size is illustrated with regard to the temperature in the reaction plane, the yield and selectivity and the production rate. In this connection we consider to what extent the catalytic membrane can support heat removal from the reaction plane.

Finally, in Chapter 8, the assumption of a constant temperature heat sink at the bottom of the reactor housing is dropped and single-phase cooling is implemented. The design of this integrated heat exchanger is investigated with the goal of minimising temperature variations in reactor cross-sections and along the reactor to avoid local hot spots.

Chapter 2

Micro-reaction processes

2.1 Introduction

This chapter reviews research by other authors on processes that were conducted successfully in microreactors and process design techniques that show potential for the development of microreactors. First, chemical reaction processes are illustrated, which are known as difficult processes but successful conduction in microreactors is reported in the literature. A particularly interesting group of reactions are fluorinations of organic substances. Special focus is on the gas/liquid phase direct fluorination of toluene.

Next, the paradigm underlying the design of miniaturised process plants, i.e. process intensification, is investigated with special focus on the concept of multifunctional reactors. Membrane reactors are introduced because they facilitate multiple functions and the use of membrane contactors with multiphase reactions is illustrated.

2.2 Overview: Applications of microreactor systems

In this section applications of micro-technology with chemical reaction processes are illustrated leading to novel process routes or significant improvement and simplification compared to traditional processes. These processes are difficult to run in large scale apparatuses because of the following characteristic features: h*azardous chemicals, highly exothermic series – parallel reactions, limited mass transfer rate, equilibrium limited and product inhibited* processes.

Hazardous chemicals require special care and processing conditions in industrial production. Floyd et al. (2000) developed a micro-reactor for the production of hazardous speciality chemicals. They focussed on organic peroxides, which are synthesised in simple processes but raise problems due to their hazardous appearance. As results from their experiments they found that microreactors yield improvements to conventional equipment in the key issues of temperature sensing, thermal management, fast mixing and reduction in fluid hold-up.

Highly exothermic behaviour and *series – parallel reactions:* In such cases the yield may be improved significantly with an appropriate reactor design. Typical representatives of this type are heterogeneous partial oxidation reactions which are extensively studied by the microreactor community (Hsing et al., 2000). Schmidt et al. (1994) studied the partial oxidation of methane on a Pt-catalyst in a microreactor. This reactor performed at high conversions without compromising the yield. This was possible through efficient mass and heat transfer, reduction of the homogeneous reaction in small channels with large catalyst surface area, narrow residence time distribution, and very short contact times. Additionally the difficulties in scaling up partial oxidation processes from lab-scale to industrial production level may be overcome by microreactors.

The overall conversion of multiphase reactions in industrial reactors is often *limited by the rate of mass transfer.* Further obstacles to high conversions are *equilibrium limited and product inhibited* processes (Harold et al., 1993). Franz et al. (2000) studied dehydrogenation reactions in catalytic membrane microreactors. The highly H_2-selective palladium membrane is used to drive the conversion beyond equilibrium. Micro-fabricated reactors enable a broader use of expensive materials because of their small size, fast thermal response time, and higher efficiencies. The same reactor allows the use of impure hydrogen feed for hydrogenation reactions. The conversion of immobilised nitrile hydratase to nicotamide is *limited by product inhibition.* The coupling of reaction and in-situ product separation can significantly increase the product throughput per unit reactor volume, compared with a unifunctional reactor. Hessel et al. (2000) studied the direct fluorination of toluene in a microreactor. Besides the high exothermic character the biggest concerns were the low selectivity to mono-fluorinated compounds and low solubility of the fluorine in toluene causing *mass transfer limiting mixing problems*. The two-phase contacting was accomplished by means of a micro bubble column and a falling film microreactor. The selectivity improved only slightly at higher conversions compared to the industrial process. However, the microreactor system is simpler and potential process improvements were identified.

More recently microreactors have been used for the preparation of solid particles. In this manner highly uniform micro polymer beads and microcapsules were obtained. (Nisisako T., 2003). The production of fine inorganic particles was accomplished in a microreactor

exploiting fast mixing, rapid heat transfer and fast diffusion. With this process tight control of the particle size, the size distribution and crystal characteristics was facilitated, which qualifies these nuclei for crystallization of photofunctional fine particles (Nagasawa H, 2003). Microreaction technology was also used successfully with biochemical processes. Here the concentration gradient driven mixing and the large surface area are exploited to contact reactant species. Miyazaki M. (2003) immobilized enzymes on the microreactor surface in a biochemical process. They demonstrate high efficiency, which enables hydrolysis of substrate within seconds and report suitability of this miniaturised process for small quantity industrial production.

The processes illustrated here exploit the inherent features of micro-channels such as large catalyst surface area, efficient mass transfer between two phases, tight residence time distribution, and very short contact times. Some of them also rely on heat exchanger integration which provides excellent thermal management, and heat transfer facilitating nearly isothermal conduction of highly exothermic processes. In the upcoming section, details about the direct fluorination of toluene are illustrated to show the potential for improvement through effectively designed microreactors and the use of porous catalytic membranes.

2.3 Direct fluorination of toluene

2.3.1 Gas/liquid phase process description

The most common industrial process for the preparation of fluoro-toluenes is the Schiemann reaction. Industrial production using this process is complex due to the need for two separate, consecutive reactions. The direct fluorination of toluene is a simple one-stage process but the characteristics of the process are problematic, as the following list summarises:

1) Dangerous reactants
2) Multiphase system (gas-liquid reaction)
3) Exothermic reactions (fast radical reactions)
4) Multiple products (series-parallel reaction mechanism)
5) Low conversion, mass transfer inhibited reactions (Clark and Bastock., 1996).

The key issues to assure safe conditions and high yield and conversion are integrated heat removal and efficient and controlled gas-liquid contacting.

The direct fluorination of toluene has been conducted on a research level using different designs of laboratory batch reactors and continuous flow microreactors (Jähnisch et al., 2000; DeMas et al., 2003; Grakauskas, 1970; Chambers, 1999). The microreactors were operated under conditions that would be suitable for industrial production. It was shown that

microreactors facilitate very efficient heat management and contacting (Jähnisch et al., 2000, Ehrfeld et al., 2000) owing to their small dimensions and high surface area to volume ratio. The total yield of mono-fluorinated product was of the same order of magnitude compared to the traditional Schiemann reaction (Balz and Schiemann, 1927). However, the electrophilic fluorination yields three mono-fluorinated isomers, whereas the Schiemann process produces only one isomer. Therefore, the fluorination in the microreactor has to be improved with respect to the obtainable selectivity and product output, e.g. through the use of catalysts (illustrated in the next section) or concerted reactor design (see Section 2.4).

2.3.2 Catalysed direct fluorination

Homogenous catalysis

Direct fluorination of organic substrates, aiming on a low level of fluorination, is best conducted in the solvent phase (Bigelow, 1947). Polar aprotic solvents, one of which is acetonitrile, favour ionic reaction, like electrophilic fluorinations of organic compounds and repress unwanted radical reactions Masel (2001).

Further improvements in terms of selectivity towards mono-fluorinated compounds can be obtained using protic acids (formic or sulphuric acids) with direct fluorination of aromatic substrates (Chambers, 1996). The Acid turns fluorine into an electrophile and the reaction may be carried out at room temperature and relatively high yields. By using 98%-sulphuric acid as homogeneous catalyst with the direct fluorination of an organic compound the selectivity towards the desired fluorinated compound increased towards 84%, from 53% with the solvent acetonitrile only. Furthermore, the addition of a Lewis acid, such as aluminium-trichloride often improves the yield and regio-selectivity with aromatic fluorinations. (Clark et al., 1996).

However, homogeneously catalysed liquid phase systems demand a complex process design in terms of additional catalyst recycle, complete separation of traces of catalyst form the product after its deactivation and high class construction materials due to corrosiveness of acids (Mitsutani, 2001). Solid catalysts in both liquid and vapour phase reactions can eliminate these problems.

Heterogeneous catalysis

Metal oxides are widely used in heterogeneous catalysis because they are chemically resistant up to very high temperatures and a wide variety of structures is available. These characteristics originate from the properties of oxygen, which exhibits the second strongest

electronegativity of all elements and a wide range of acidity / basicity properties is observed which depend on the involved metal. The use of silica based molecular sieves with fluorination reactions was investigated by Sams (1978). Here, the focus of the study was on the shape selectivity of the catalytic pores. These pores clog up during a reaction and get deactivated quickly. This is due to the fact that metal oxides used as heterogeneous fluorination catalysts, undergo a fundamental change of their surface composition and become at least partially fluorinated when exposed to HF (L. Kolditz et al., 1981).
Taking into account that fluorine is even more electronegative than oxygen and that it is able to form a large variety of different compounds which are often as chemically and thermally stable as oxides, one should expect an even higher acidity in some metal fluorides than in corresponding metal oxides (Kemnitz, 1998). One of the most prominent heterogeneous Lewis acid catalysts for these reactions is the Swarts catalyst (SbF_5, SbF_3Cl_2). These catalysts are used for the syntheses of chlorofluorocarbons (CFCs) and hydrofluorocarbons (HFCs) in halogen exchange reactions (Cl / F exchange):

$$R\text{-}C\text{-}Cl + HF \xrightarrow{SbF_5} R\text{-}C\text{-}F + HCl$$

No deactivation of the catalysts is reported which suggests that neither HF nor HCl react with the catalyst. More details about metal fluorides used with fluorination reaction can be found in the literature: Rodriguez et al. (1999), Alonso et al. (2003), Kemnitz et al. (1998). In the next section reactor design techniques are introduced which are particularly suitable on the micro-scale and also allow heterogeneous catalysis.

2.4 Process intensification with microreactors

2.4.1 Definition and motivation

"Process intensification (PI) can be considered to be a design philosophy where the fundamental requirements of a chemical process are analysed, and a process plant is designed which matches the precise requirements of the process and meets the business needs" (Green et al., 1997). The original motivation was to reduce the capital cost of the production system. Recently, more potential benefits have been identified: enhanced intrinsic safety, reduced environmental impact and energy consumption, rapid plant response, and greater possibilities for distributed manufacturing. In this manner possible key-drivers for the process industries of the future (Perkins, 1997) can be addressed, i.e. the challenges of safety and

environmental concerns as well as closer control of product attributes in order to deliver greater customisation.

Process intensification can affect the design and the processing technology of the entire chemical plant. In this work, the focus is on process intensification on the reactor level achievable through innovations in reactor design (fields like novel catalysts, efficient process control and automation were not within the scope of this work). Reactor units can be intensified using the concept of multifunctional reactor systems (Dautzenberg and Mukherjee, 2001).

2.4.2 Multifunctional reactors

By definition, several "functions" or processes are designed to occur simultaneously in multifunctional reactors. One aims for optimum integration of mass, heat and momentum transfer within a reactor vessel. To achieve optimal performance with multifunctional reactors, it is important to understand where the integration of functionality occurs. Dautzenberg and Mukherjee (2001) made the following classification:

Type A: Multifunctionality operating at the catalyst level. This may be achieved by combining catalytic properties with an engineered catalyst structure, e.g. thin film catalysts with low diffusion barrier for reactants and intermediate products.

Type B: Multifunctionality at the reaction interface. The chemical reaction is integrated with enhanced inter-phase transport properties. As an example we consider the 'Monolith Reactor': Its advantages include high external surface area, which may be plated with catalyst, high interfacial mass transfer rates and low pressure drops (Stankiewisz, 2001).

Type C: Multifunctionality at the inter-reactor level. The integration of the chemical reaction with unit operation steps within the same apparatus may yield advantages in process operability that are impossible to achieve otherwise (Rinard, 1998). There are two main phenomena to be considered:

C1) Chemical reaction with inter-reactor energy transfer.

C2) Chemical reaction with inter-reactor mass transfer.

Research in recent years prove micro-scale reactors capable of process intensification in the first two fields, e.g. through thin film catalysts with low diffusion barrier or reproducible mixing of multi-phase fluidic systems (Ehrfeld, 2000a; Franz, 2000). The realisation of inter-reactor multifunctionality in micro-systems is further investigated in the following paragraph.

2.4.3 Intra-reactor multifunctionality

Nishida et al. (1981) have defined process synthesis as "the act of determining the optimal interconnection of process units as well as the optimal type and design of the units within the processing system". Here, process synthesis is considered with the goal of integrating unit operations in one housing together with the reaction channel. In this connection examples for well-known techniques with large-scale processes are:

- Integration of a heat exchanger unit into a chemical reactor to control the reaction temperature to prevent runaway with highly exothermic reactions and to achieve better catalyst utilisation.
- Coupling of a chemical reaction with mass transfer aiming at in-situ separation of products from the reaction zone.

However, there are limitations to the use of these concepts with traditional reactors, which applies to mass transfer integration in particular, which rely on random turbulent transport phenomena.

Microfabrication supports the combination of components and functions (Wegeng, 2000). The miniaturisation of the reaction channels effectuates significant enlargement in surface area, which results in increased transport of heat and matter. The gradient of all physical properties of the fluid is relatively high in small channels. High transfer rates and short diffusion paths permit rapid changes in temperature, efficient heat management or fast mixing and separation processes (Ehrfeld, 2000b; Quiram, 2000a).

Heat exchange integration

It is often desired to control the temperature of the process tightly. All chemical reactions are in principle accompanied by evolution or absorption of heat. In practice, therefore, a reaction hardly ever proceeds entirely under isothermal conditions. Ways of keeping the steady states of an exothermic reaction mixture between the appropriate temperature limits are

- Withdrawal of heat during the reaction
- Dilution of the solid catalyst with inert particles, e.g. with a good heat conductivity, to reduce local conversion rate in a catalyst in a cooled reactor and remove heat effectively.

The first point involves heat exchanger synthesis, which is the topic of this section and the latter statement is discussed above (Section 2.3.1).

With microreactors fluid hold-up in the reaction channels is low and heat conduction paths are short in thin sheets of fluid. The fluid is in the laminar flow regime and heat removal is achieved by transversal conduction. In this manner integrated heat exchangers facilitate

efficient heat transfer and tight control of the temperature in the reaction plane can be achieved. Microreactors have been shown to remove heat effectively even with very exothermic reactions, e.g partial oxidations (Hsing, 2000). Furthermore the high heat exchange capacity and low fluid hold-up can be very useful if fast heating or cooling of the reacting fluid is required (Ehrfeld, 2000a).

Integration of heat exchange and reaction can be accompanied by operational difficulties which can result in reactor instabilities and thermal runaway. In general a PFR will not show dynamic unstable characteristics because by definition it does not exhibit back-mixing of heat. However, instabilities may occur in a PFR if by means of a heat exchanger the reaction heat is mixed back to the reactor feed stream. Thus the integrated heat exchanger has to be designed properly to avoid such effects. With microreactors the channel walls take up a relatively big percentage of the reactor volume. Conduction of heat within the walls may contribute to reactor instability.

Mass transfer integration

It is often desired to control the concentration of compounds inside a chemical reactor. This allows operation of the reaction at the desired conditions avoiding spatial variations. Turbulent mixing is the most common way of mixing fluids, i.e. turbulent mixing in stirred tanks and bubble columns or trickle bed packed reactors for liquid/liquid and gas/liquid process respectively. These reactors are obstructed with flow mal-distribution and locally varying conditions, among others.

With microreactors contacting is accomplished by bringing thin sheets of fluid in close proximity. The fluid is in the laminar flow regime and mixing is achieved by transversal diffusion. In this manner micro-mixers bring together reactants in a predictable, controlled and efficient way. The separation of components works in a similar way. Štěpánek et al. (1999) showed that adsorption can be effectively used for product removal in connection with a chemical reaction in a multifunctional microreactor.

Furthermore, unit operations can be effectively used on a micro-scale, which are not commonly used in large-scale equipment, due to strong deficiencies. In this connection, the use of membranes or porous hollow fibres holds great potential for the separation and the contacting of fluids, e.g in a multiphase system.

2.5 Micro-scale multiphase membrane reactors

In industrial practice membrane processes are not widely spread due to several problems, e.g. stability, uniformity and price of the membrane materials (Ilinitch et al., 2000). It is believed that these deficiencies can be overcome through miniaturisation of the reaction vessel.

On the micro-scale the capital costs of the membrane material are not the key problem because only very few material is needed and process are more efficient, i.e. facilitate a high space-time yield (Ehrfeld, 2000a). Furthermore, it is easier to achieve equal pore structure with a very small membrane for the use in a microreactor. This is due to more effective quality assessment and novel membrane production techniques, which would not work on a large scale, i.e. production of single crystal zeolites (Wang and Jacobson, 2001).

Special manufacturing techniques for microreactor applications have been developed. Zeolite coatings and films (5- 20 μm) were successfully grown onto flat and micro-scale silicon substrates. Furthermore, micro-tunnels were created by combining bent zeolite structures on silicon substrates. The mechanical strength of freestanding zeolite can be improved by introducing a porous support layer. In this manner the zeolite layer can be thin facilitating high mass flux across the membrane. The most common materials are alumina and stainless steel (Chiang, 2001).

New membrane reactors applications have been developed which do not require perm-selectivity and therefore appear to be closer to industrial success. These processes do not rely on product separation but rather separated reactant feeding and residence time control. In the following sections the potential use of inert and catalytic macro-porous membranes is illustrated and explained using real process examples.

2.5.1 Inert membrane contactors

With the membrane reactor in distributor mode the reactants are separated by a membrane or a mesh, which imposes a diffusion barrier on the system. In this manner controlled contacting of reactants is ensured, which is useful if the reaction is highly exothermic and temperature management is important, series reactions negatively affect the selectivity or mass transfer limitation in multiphase systems occur. The direct fluorination of organic substances shows these characteristics and in the following several advantages are listed, which may be achieved with distributed feed mode:

- Wider range of operating conditions: It is possible to operate at overall reactant ratios in the feed that would be within the explosive region if the same composition was fed at the entrance of a tubular reactor.
- Momentum of the gas and liquid phases are decoupled, allowing gas/liquid flow without risk of flooding and occurrence of waves even with counter-current flow.
- Reactant segregation to either side of the membrane. Under certain conditions (fast reaction conditions compared to mass transport) it is useful to confine the reaction in a finite reaction zone inside the porous structure, avoiding the slip of reactants to the opposite side.
- Safer operation with reduced formation of hot spots and a lower probability of runaway due to locally limited concentration of reactants in the reaction zone. The avoidance of hot spots can give additional increments of selectivity by suppressing undesired reactions that take place at high temperatures, and may help to extend catalyst life, where a heterogeneous catalyst is used.
- Increasing the specific membrane area through novel membranes. In recent years, ceramic hollow fibre modules have become available with potential surface to volume ratios in modules larger than $1000m^2/m^3$ (Saracco et al., 1999). These devices could have great impact on operations where effective contacting of fluids is required, e.g. in separation processes or multiphase reactions. It is envisioned to use a bunch of hollow fibres to obtain very high surface areas (Cussler, 2002).

The distributor mode strategy has been employed successfully with series-parallel reaction networks where the creation of the desired product benefits from low partial pressure of the distributed reactant. For example with partial oxidations or hydrogenations low O_2 or H_2 concentrations in the reacting mixture yield higher selectivity towards intermediate products. This effect has been demonstrated with various processes, e.g. methane oxidation (Coronsa and Santamaria, 1999). With the advances in production of inorganic tubes of small diameters and thin membranes and the possibility of heat exchange in the liquid phase or membrane support this type of reactor is a possible alternative to trickle flow worthwhile considering (Vitulli et al. 1997; Tilgner et al., 1997).

2.5.2 Catalytic membrane reactors

Much industrial research effort has been invested to develop alternative heterogeneous catalyst technologies because homogeneously catalysed liquid phase systems are accompanied by more complex process design in terms of additional catalyst recycle,

complete separation of traces of catalyst from the product after its deactivation. In some cases high class construction materials have to be used due to corrosiveness of the catalyst (e.g. in case of acids). (Akio Mitsutani, 2001). In the following paragraph active contactors are considered where the catalytic is plated on a membrane, which separates the reactants.

Active contactors

A porous membrane plated with a catalytic layer can be considered an active contactor where the controlled diffusion of reactants to the catalyst can lead to an engineered catalytic reaction zone (opposing reactant mode). We distinguish between tri-phase (gas/liquid/solid) and bi-phase (mostly gas/solid) systems. Tri-phase membrane reactors operate with liquid reactants introduced at one side of the reactor and gaseous reactants at the other side. Bi-phase systems are simpler and involve gas-feed from both sides of the membrane. Some interesting bi-phase process arrangements exist, which can be found in the literature (Sloot et al., 1990, Saracco et al., 1999, Golman et al., 1997, and Julbe, 2001). In the upcoming section only tri-phase processes are further discussed. An example for such a process would be the direct fluorination of organic compounds like toluene on a solid catalyst surface. The features of the inert membrane in distributor mode listed above, apply here too.

Tri-phase processes

Tri-phase reactions (equilibrium and irreversible reactions) are often mass transfer limited by the absorption of the volatile component and access of this reactant to the catalyst. These systems can be improved by feeding reactants from separate sides of a membrane, if the reaction is sufficiently fast compared to transport resistance. Here, the aim is to create a defined interface between gas and liquid with a high specific area and catalytic activity. Indeed, the volatile reactant does not have to diffuse through a liquid film, since a gas/liquid interface is created inside the pores in direct contact with the catalyst. (Julbe, 2001). Thus, the gaseous reactant cannot be limiting anymore, contrary to conventional reactors (Peureux, 1995). A practical example is the reaction between aqueous H_2O_2 and n-hexane vapour. Both reactants reach the catalyst surface by diffusion through the membrane which is placed at the gas/liquid interface. In a conventional reactor, where the catalyst particles are suspended, the reaction rates are quite low because of the immiscibility of the organic and aqueous phases, which leads to a very low concentration of organic reactant in the aqueous phase where the reactions take place.

With tri-phase processes the chemical reaction takes place within a catalytic membrane. Certain catalytic layers, e.g. zeolites, have a highly uniform pore-structure and pore sizes round about the size of many molecules. In the pores of these membranes shape-selectivity and electrostatic effects occur through the highly polar interior of the material influencing the recombination of atoms. The chlorination of toluene with elemental chlorine is traditionally

catalysed by liquid Lewis Acids. This catalyst was replaced by a variety of zeolites, which improved the selectivity towards para-chlorination towards 74.5% (ZSM-5). In addition to the solid catalyst the presence of chloroacetic acid led to further significant improvement in the para: ortho ratio. (Clark, 1997).

Usually a co-solvent must be added to the reaction system to increase the mutual solubilities of these two immiscible phases, thus increasing the reaction rates. Using such a membrane interphase contactor, potentially the use of co-solvent can be avoided at industrial scale which would be a great advantage considering downstream separation effort (Wu, 2000).

2.6 Summary

In this chapter the possibilities offered by micro-reaction technology are illustrated. The processes described in the first section are generally perceived as difficult due to their characteristics but were conducted successfully on the micro-scale. The paradigm underlying these examples is process intensification through multifunctional reactors and process synthesis. The unique characteristics of microreactors support the synthesis of unit operations and in particular the use of membrane processes. Membrane technology has potential with multiphase processes on the micro-scale. Here, the focus is on macro-porous membranes because currently permselective membranes are available only for few fluid systems. Porous membranes can be used as inert contactor or catalytic contactor separating the feed of the reactants, which flow on either side of the membrane. In this manner significant advantages for the process can be obtained.

The direct fluorination of toluene was chosen as a sample process because it is a demanding reaction and gives rise to safety issues. It has been demonstrated that microreactors can be used for the safe conduction of this reaction but the selectivity and production rate are not satisfactory. Reports about catalysed direct fluorination show that the selectivity can be greatly improved. Catalyst materials were suggested in the literature and some heterogeneous catalysts are already in use with similar reactions. Following from these incentives, an active contactor membrane microreactor is designed in the next chapter to conduct the direct fluorination of toluene.

Chapter 3

Development of microreactor models

3.1 Introduction

Two microreactor configurations intended for the direct fluorination of toluene and the appertaining model representation will now be presented. First, a falling film type reactor configuration (FFMR) is built in accordance with an experimental apparatus created by Jähnisch et al. (2000). A detailed process model is developed based on mass, heat and momentum conservation equations.

The second device is a novel catalytic membrane microreactor (CMMR) designed in this work. The structure of the model domain is similar to the FFMR but extended through a catalytic membrane. Here, most of the equations and boundary conditions introduced with the FFMR can be adopted and additionally, a model is implemented that describes heat and mass transport within the membrane. Finally, methods for the discretisation of the modelling domain and numerical solution of the partial differential equations are investigated.

3.2 Falling film reactor model

3.2.1 Microreactor configuration

The characteristics of the direct fluorination of toluene process demand an individual reactor design, to assure safe conditions and high yield and conversion. Jähnisch et al (2000) designed a falling film microreactor to conduct this reaction. The liquid phase reaction channels of this device have sub-millimetre size. This reactor contained many

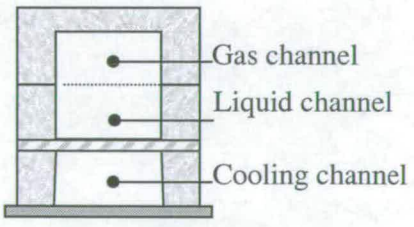

Figure 3-1. Sketch of the falling film microreactor configuration

channels in parallel to increase the overall throughput.

To create a model of this process for a simulation study it is sufficient to understand the occurrences in a single reaction channel. Therefore, an abstract representation of the falling film reactor was created as shown in Figure 3-1. This sketch shows the gas and liquid reactant channels open to one another, and the cooling channel, all united in one reactor housing. A schematic of the appertaining model domain representation is illustrated in Figure 3-2. The cross-section of the gas, liquid and cooling channel are shown with important boundaries. Here, the reactor cross section is split vertically where conditions in both halves are equal due to symmetry and thus, merely one halve has to be considered. Figure 3-3 introduces the compounds involved and the measures of the reactor. In the model formulation, molecular fluorine is represented by F_2, toluene (C_7H_8) by *Tol* and the desired monofluorinated product (C_7H_7F) is *FTol* whereas by-products are symbolised by F_2R ($C_{14}H_{16}F_2$), F_5R ($C_7H_7F_5$) and $F_{10}R$ ($C_{14}H_{16}F_{10}$). The gaseous feed to the reactor consists of fluorine diluted in nitrogen (N_2) and in the liquid phase toluene is dissolved in acetonitrile (*AcN*). The reaction system is illustrated in detail in scheme B-1 (Appendix B).

The gas and the liquid streams are arranged in cocurrent flow. At the gas/liquid interface the gaseous component absorbs into the liquid phase (in Figure 3-3 the location of the gas liquid interface is indicated by a red line) and reacts immediately with the liquid reactant. The arrangement of the coolant flow is flexible, so that co-current, counter-current and cross-flow setting is possible.

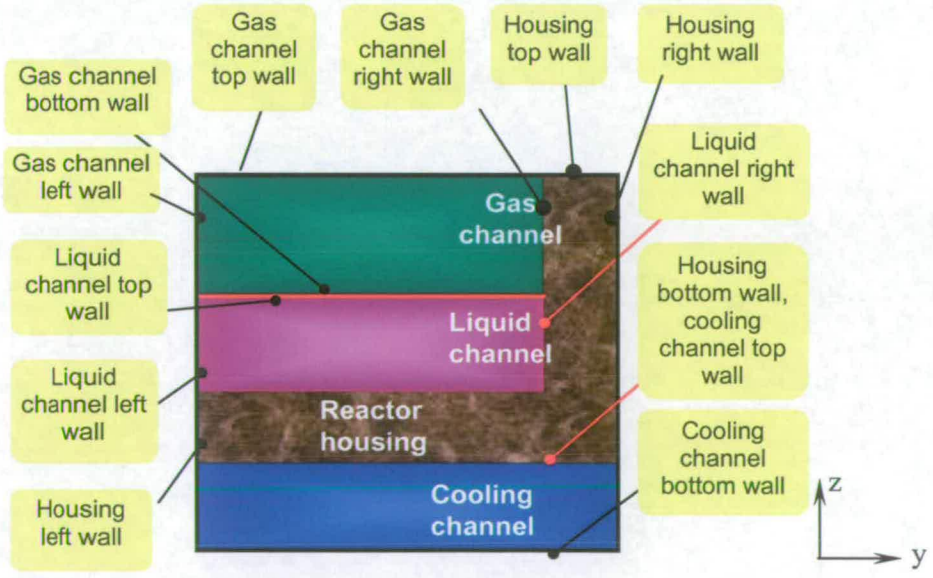

Figure 3-2. Scaled geometry of the 2D FFMR domain including boundary and sub-domain labels.

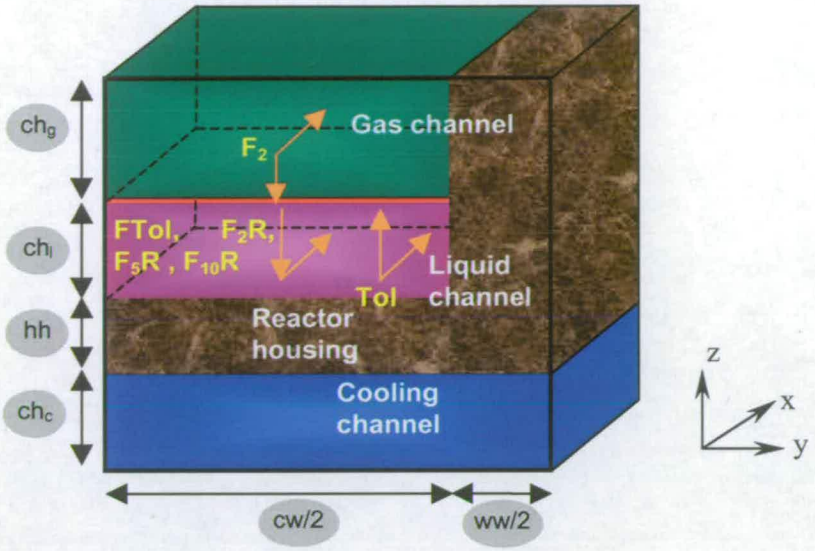

Figure 3-3. Scaled geometry of the 3D FFMR domain. Orange arrows indicate mass transport by diffusion and convection

3.2.2 Conservation equations

Chemical processes in micro-systems follow the same principles as in large-scale devices because their dimensions are too large to enable interaction on the molecular level. Therefore, the equations traditionally used to describe processes can also be used with microreactors. However, transport phenomena gain importance on the micro-scale, which are often neglected when modelling larger equipment. Heat and mass transfer is accomplished through diffusion normal to the direction of the flow. In the absence of turbulence, transfer phenomena are fully describable by diffusion and convection equations and it is possible to develop a rigorous and deterministic process model. The mathematical process model was developed on the basis of the following assumptions:

- Navier-Stokes equations are suitable to predict the laminar flow characteristics in the micro-channels investigated in this study. This assumption is based on the fact that the smallest channel for the gaseous components has a hydraulic diameter of 150 µm. The mean free path of nitrogen at standard conditions is approximately 60 nm which results in a Knudsen number in the order of $Kn = 6 \cdot 10^{-4}$. This number indicates that the gas can be considered to be a continuum, rarefaction or non-continuum effects do not occur and the Navier-Stokes equations apply (Xu et al., 2000). The mean free path of liquids is much smaller compared to gases and thus

rarefaction is not occurring in the micro-channels of the size considered in this work (d_h>150 μm).

- The diffusion is assumed to be describable by Fick's law for an ideally diluted system. This implies that the system is considered as thermodynamically ideal (within Henry's law region).
- The thermo-physical properties are temperature dependent.

Under the assumptions stated above the conservation of mass, momentum, and energy for the fluid and solid housing can be written as follows (Welty et al., 2000):

Conservation of momentum: $\vec{v}_\Omega \cdot \nabla\left(\overline{\rho}_\Omega \vec{v}_\Omega\right) = -\nabla p + \nabla \cdot \left(\overline{\eta}_\Omega \nabla \vec{v}_\Omega\right)$ (3-1)

Conservation of mass: $-\nabla\left(D_{\varphi,\Omega} \cdot \nabla c_{\varphi,\Omega}\right) + \vec{v}_\Omega \cdot \nabla c_{\varphi,\Omega} = -\sum \nu_{\varphi,i} \cdot r_i$ (3-2)

Conservation of energy: $\nabla\left(-\overline{k}_\Omega \cdot \nabla T_\Omega\right) + \vec{v}_\Omega \cdot \overline{c}_{p,\Omega} \frac{\partial\left(\overline{\rho}_\Omega T_\Omega\right)}{\partial x} = -\sum \nu_{\varphi,i} \cdot r_i \cdot \Delta H_{r,i}$ (3-3)

where Ω denotes a sub-domain: gas- *(g)*, liquid *(l)* channel, membrane *(mem)* or reactor housing *(s)*; φ stands for compounds: F_2, *Tol*, *FTol*, F_2R, F_5-R and $F_{10}R$; $D_{\varphi,l}$ is the binary diffusion coefficient of compound φ in acetonitrile in the liquid phase; $D_{F2,g}$ is the binary diffusion coefficient of fluorine in nitrogen in the gas phase.

The equations describing the conservation of momentum apply to the fluid channels only. Therefore, considering the reactor housing equation Eq. (3-1) is not applicable and furthermore $\vec{v}_\Omega$ is zero, which implies that the convective terms in Eq. (3-2) and Eq. (3-3) are zero. A simplified model is used for the gas flow where no reaction and no heat transfer take place; thus Eq. (3-3) does not apply here. The most important boundary conditions are illustrated in Table 3-1.

3.2.3 Physical property parameters from the literature

The equations displayed above describe a real process, and therefore, physical property and reaction kinetic data associated with the components involved is of great significance, i.e. physical property values, mass and heat transfer parameters and reaction kinetic values. The physical property data and most of the transport parameters are either available from the literature or estimation techniques are reported; see Table C-1 and Table C-2 in Appendix C.

So far, the development of the FFMR model was straightforward and only few assumptions had to be taken. However, two very important parts of the model, i.e. reaction kinetics and gas absorption, cannot be determined theoretically. In Chapter 4 values for parameters involved in these two phenomena are determined based on theoretical knowledge and empirical data from the literature.

Table 3-1. Boundary conditions with the FFMR

Boundary	Conservation equation	FFMR - Boundary condition
Liquid channel top wall	Energy	$-\overline{k}_l \cdot \left(\frac{\partial T_l}{\partial z}\right)^* = 0$
Housing bottom wall	Energy	$T_s = T_c$
Liquid channel bottom wall, Liquid channel right wall	Energy	Stiff spring boundary approximating a Dirichlet boundary condition insuring continuity in flux: $-\overline{k}_l \cdot \left(\frac{\partial T_l}{\partial z}\right) = M\left(T_h - T_l\right)$ where M is a large enough number to let the temperature difference in the brackets approach zero (Constantinides and Mostoufi, 1999).
Gas channel - , Liquid channel - , Housing left wall	Energy	Symmetry $-\overline{k}_\Omega \cdot \left(\frac{\partial T_\Omega}{\partial y}\right) = 0$
Liquid channel top wall	Mass	$-D_{F_2,l} \cdot \left(\frac{\partial c_{F_2}}{\partial z}\right)^* = k_g \cdot \left(\overline{x}_{F_2,g} - c^*_{F_2,S}/(H_c \cdot p)\right)\frac{\overline{\rho}_g}{\overline{u}_{m,g}}$
Gas channel bottom wall	Mass	$\dot{N}^*_{F_2} = k_g \cdot \left(c^*_{F_2,S}/(H_c \cdot p) - \overline{x}_{F_2,g}\right)\frac{\overline{\rho}_g}{\overline{u}_{m,g}}$
Gas channel - , Liquid channel - , Housing left wall	Mass	Symmetry $-D_{\varphi,\Omega} \cdot \left(\frac{\partial c_{\varphi,\Omega}}{\partial y}\right) = 0$
Liquid channel top wall	Momentum	No boundary specified
Liquid channel bottom wall	Momentum	No-slip flow $u_l = 0$, $v_l = 0$, $w_l = 0$
Gas channel top wall	Momentum	No-slip flow $u_g = 0$, $v_g = 0$, $w_g = 0$
Liquid and gas channel right and left wall	Momentum	Slip flow: $-n_x \cdot u_\Omega - n_y \cdot v_\Omega - n_z \cdot w_\Omega = 0$
Gas channel bottom wall	Momentum	No boundary specified (effectively: $u_g^* = u_l^*$; $v^* = 0$; $w^* = 0$)
Reactor exit	Momentum	$p = p_{atmosphere}$

3.3 Membrane reactor model

3.3.1 Microreactor configuration

In this work a novel reactor configuration is proposed, i.e. a catalytic membrane microreactor (CMMR), to improve the direct fluorination of toluene. This device can be considered an extension to the FFMR, presented above. A porous membrane was implemented between the gas and liquid streams effectively creating two separate channels, see Figure 3-4. The membrane is composed of an inert support layer and a catalytic layer, i.e. solid acid, both of which are porous layers with no permselectivity. A cooling channel was integrated in the reactor to absorb the heat generated by the reaction. Reactor multi-functionality and process synthesis, as illustrated in Section 2.4, were the key design paradigms underlying the CMMR configuration.

In Figure 3-5 a two-dimensional schematic of the membrane reactor cross-section is displayed, showing the CMMR modelling domain and important boundaries. The modelling domain represents half of the physical reaction channel, because of symmetry the second half is simply the mirror image. The gas and the liquid streams are in co-flow mode separated by the membrane. It is assumed that liquid fills the pores of the membrane due to the capillary effect at uniform pressure in the whole reactor. The gaseous component absorbs into the liquid phase (in Figure 3-6 the location of the gas liquid interface is indicated by a red line) and reacts immediately with the liquid reactant.

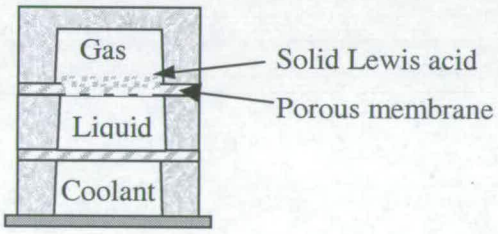

Figure 3-4. Sketch of the catalytic membrane microreactor configuration

3.3.2 Conservation equations

The fluid channels of the CMMR configuration resemble the ones of the FFMR. Thus, the mathematical process model developed for the latter can be adopted for the used with the CMMR. The governing equations describing mass, heat and momentum conservation in the fluid channels are identical. However, the boundary conditions at the interfaces between the fluid channels and the membrane with the CMMR are different from the once with the FFMR, see Table 3-2. Additionally, a model for the heat and mass transfer within the

membrane was developed, see Section 3.3.3. Finally, the electrophilic reaction is catalysed by the solid acid catalyst plated on the membrane. Considerations concerning heterogeneous catalysis of the direct fluorination reaction are introduced in Chapter 4.

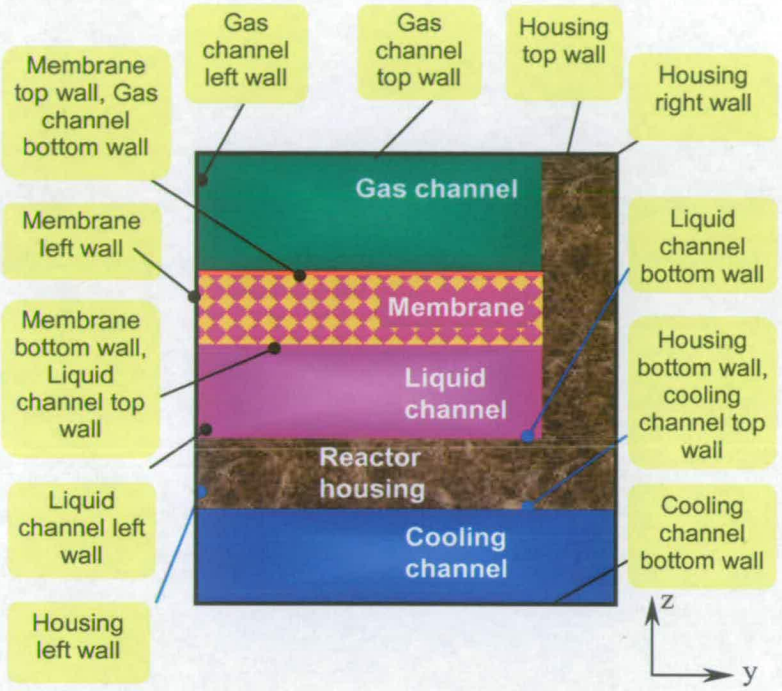

Figure 3-5. Scaled geometry of the 2D CMMR domain including boundary and sub-domain labels.

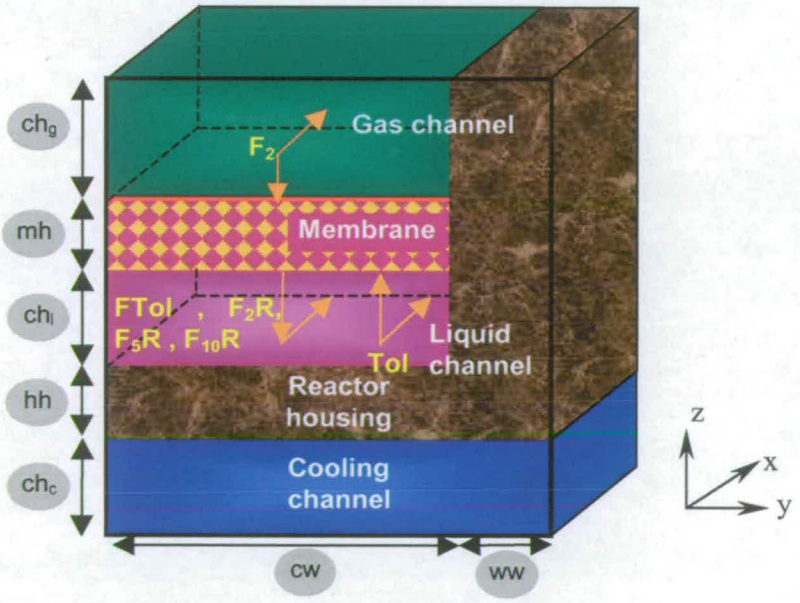

Figure 3-6. Scaled geometry of the 3D CMMR domain including boundary and sub-domain labels. Orange arrows indicate mass transport by diffusion and convection

Table 3-2. Comparison of boundary conditions with the CMMR and FFMR

Boundary	Conservation equation	Falling Film Reactor - Boundary condition	Membrane Reactor - Boundary condition
Liquid channel top wall	Energy	$-\overline{k}_l \cdot \left(\frac{\partial T_l}{\partial z}\right)^* = 0$	No boundary specified
Membrane top wall	Energy	/	$-\overline{k}_{mem} \cdot \left(\frac{\partial T_l}{\partial z}\right)^* = 0$
Housing bottom wall	Energy	$T_s = T_c$	$T_s = T_c$
Liquid channel top wall	Mass	$-D_{F_2,l} \cdot \left(\frac{\partial c_{F_2}}{\partial z}\right)^* = k_g \cdot \left(\overline{x}_{F_2,g} - c^*_{F_2,S}/(H_c \cdot p)\right)\frac{\overline{\rho}_g}{\overline{u}_{m,g}}$	No boundary specified
Membrane top wall	Mass	/	$-D_{F_2,mem} \cdot \left(\frac{\partial c_{F_2}}{\partial z}\right)^* = k_g \cdot \left(\overline{x}_{F_2,g} - c^*_{F_2,S}/(H_c \cdot p)\right)\frac{\overline{\rho}_g}{\overline{u}_{m,g}}$
Gas channel bottom wall	Mass	$\dot{N}^*_{F_2} = k_g \cdot \left(c^*_{F_2,S}/(H_c \cdot p) - \overline{x}_{F_2,g}\right)\frac{\overline{\rho}_g}{\overline{u}_{m,g}}$	$\dot{N}^*_{F_2} = k_g \cdot \left(c^*_{F_2,S}/(H_c \cdot p) - \overline{x}_{F_2,g}\right)\frac{\overline{\rho}_g}{\overline{u}_{m,g}}$
Liquid channel top wall	Momentum	No boundary specified	No-slip flow $u^*_l = 0$, $v^*_l = 0$, $w^*_l = 0$
Gas channel bottom wall	Momentum	No boundary specified	No-slip flow $u^*_g = 0$, $v^*_g = 0$, $w^*_g = 0$

3.3.3 Transport processes within the membrane

A practical membrane would probably be composed of a support layer and a catalytic layer with their characteristic properties (see Section 2.5). In this work, the membrane is modelled as one homogeneous layer. It is assumed that the catalytic layer is very thin and therefore negligible, concerning mass and heat transfer, yet, the membrane is catalytically active.

Considering the mass transfer model, the macro-porous membrane is characterised by two parameters, i.e. the porosity ε and the tortuosity τ, while the exact shape of the pores is not specified. There is no pressure difference across the membrane thus in the membrane mass transfer is driven by diffusion only. In a macro-porous liquid system the influence of the pore wall is minor and diffusion occurs by the same mechanism as in the bulk fluid (Kaerger

and Ruthven, 1992). The diffusion coefficient for each species in the porous membrane is the effective coefficient $D_{eff,\varphi}$ calculated by the following equation (Froment and Bischoff, 1990):

$$D_{eff,\varphi} = D_{\varphi,l}\frac{\varepsilon}{\tau} \tag{3-4}$$

Heat transfer through the membrane is based on a membrane model whose porous structure is displayed in Figure 3-7. Here it is assumed that the membrane is composed of regular square units. Hsu et al. (1995) found an accurate description of the conductivity of porous media $\bar{k}_{mem}$, i.e. the mixed phase of liquid and solid, see Eq. (3-5). It is assumed that there is no convective flow in the membrane. Thus, heat transfer is accomplished by conduction only.

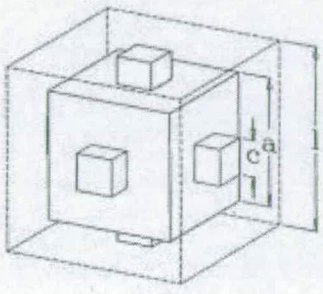

Figure 3-7. Membrane model: In-line touching cubes, Hsu et al. (1995)

$$\frac{\bar{k}_{mem}}{\bar{k}_l} = 1-\gamma_a^2-2\gamma_a\gamma_c+2\gamma_c\gamma_a^2+\frac{\gamma_c^2\gamma_a^2}{\lambda}+\frac{\gamma_a^2(1-\gamma_c^2)}{1+\gamma_a(\lambda-1)}+\frac{2\gamma_c\gamma_a(1-\gamma_a)}{1+\gamma_c\gamma_a(\lambda-1)} \tag{3-5}$$

where $\gamma_a = a/l$; $\gamma_c = c/a$ are geometric factors (c, a, l are defined in Figure 3-7) and $\lambda = \bar{k}_l/\bar{k}_s$ is the ratio of the thermal conductivities of the liquid ($\bar{k}_l$) and the solid phase ($\bar{k}_s$) within the porous membrane. Important data used to describe heat transfer within the membrane is illustrated in Table 3-3 and Table 3-4.

Table 3-3. Thermal conductivity data

Compound	Symbol	Value	Unit
Acetonitrile	k_{AcN}	0.000188	kJ m^{-1} s^{-1} K^{-1}
Toluene	k_{Tol}	0.000131	kJ m^{-1} s^{-1} K^{-1}
Liquid (here, 10% Toluene in Acetononitrile)	$\bar{k}_l$	0.000182	kJ m^{-1} s^{-1} K^{-1}
Membrane support layer (made of stainless steel)	$\bar{k}_s$	0.044	kJ m^{-1} s^{-1} K^{-1}
Ratio of liquid and solid thermal conductivities	$\lambda = \frac{\bar{k}_l}{\bar{k}_s}$	0.004143 (with $\bar{k}_l$ based on 10% toluene in acetonitrile)	/

Table 3-4. Membrane structure data

Parameter	Symbol	Value	Unit
Structure parameter	$\gamma_a = \frac{a}{l}$	0.1945	/
Structure parameter	$\gamma_c = \frac{c}{a}$	0.8	/
Porosity	$\varepsilon = 1 - \left(\gamma_a^2 + 4 \cdot \gamma_a \cdot \gamma_c \cdot \frac{(1 - \gamma_c \cdot \gamma_a)}{2} \right)$	0.7	/
Tortuosity	τ	4	/

3.3.4 Non-dimensional numbers

The direct fluorination of toluene considered in this work is a multiphase process where the reaction is limited by mass transfer. In general, the limiting step is the absorption of fluorine into the liquid phase. Two dimensionless numbers are introduced which can be used to characterise the process with emphasises on the absorption of fluorine.

The dimensionless contact time Λ is introduced to give an indication of the achievable conversion. It is defined as the ratio of the absorption flux of the volatile reactant into the liquid phase and the feed flux of the liquid reactant, see Eq. 3-6. Thus, it represents the ratio of mass flux of both reactants to the reaction zone. For the liquid phase reactant the overall feed flow rate is considered assuming that diffusion in z-direction is not limiting.

$$\Lambda = \frac{\text{intial rate of absorption}}{\text{liquid feed flow rate}} = \frac{k_g \cdot H_c \cdot p \cdot x_{F_2,F} \cdot cl}{\overline{v}_l \cdot c_{Tol,F} \cdot ch_l} \tag{3-6}$$

While the dimensionless contact time is a measure for the achievable conversion in the reactor, the Thiele Modulus is introduced to quantify the extent of the mass transfer limitation with respect to fluorine absorption considering a differential reactor. The Thiele modulus Φ is the ratio between the initial rate of reaction and the initial diffusive flux:

$$\Phi_{F_2} = \delta \cdot \left(\frac{r_{F_2,0} / c_{F_2,S,0}}{D_{F_2,l}} \right)^{1/2} \tag{3-7}$$

where Φ_{F2} is the Thiele modulus with respect to fluorine, $r_{F2,0}$ is the overall initial rate of disappearance of F_2, and δ is the characteristic length of the reactive diffusion mass transfer.

Here, the initial diffusion flux of the dissolved reactant can be replaced by the initial mass absorption rate, which results in the following equation for the modified Thiele modulus:

$$\Phi_{F_2,\mathrm{mod}} = \left(\delta \frac{r_{F_2,0} / c_{F_2,S,0}}{k_g \frac{\overline{\rho}_g}{\overline{u}_{m,g}} \cdot \frac{\overline{x}_{F_2,g} - x^*_{F_2,g}}{x^*_{F_2,g} \cdot H_c}} \right)^{1/2} \tag{3-8}$$

The modified Thiele modulus is much larger than unity for strongly mass transfer limited reactions, like the direct fluorination of toluene.

3.4 Discretisation and numerical solution

3.4.1 Modelling micro-systems

Unlike traditional plant design which focuses on flowsheets and unit operations, micro-chemical plant design emphasises detailed understanding of individual components. In this connection multiple length scales and complex geometries have to be handled (Jensen, 1998). Therefore, standard simulation tools are not universally applicable (Quiram, 2000a), as physical phenomena are different from conventional systems. Heat, mass and momentum conservation are described in detail by means of differential equations. These equations are strongly coupled within a homogenous phase. Thus, the governing equations must be solved simultaneously with appropriate boundary conditions.

Furthermore, inter-phase coupling may occur, e.g between two fluid channels or between the fluid channel and the reactor housing. As example we consider heat transfer between a fluid channel and the reactor housing in a non-adiabatic microreactor. Here, the fluid cooling flux across the reactor walls may be non-uniform, e.g. due to non-uniform wall thickness. This circumstance is referred to as conjugated heat transfer problem (Shah, 1978). As a result, heat transport cannot be described using simplified equations based on heat transfer coefficients. The heat conservation equation of the channel wall has to be analysed simultaneously with the one of the liquid phase in order to establish the wall-fluid interface heat transfer flux distribution. This conclusion can be generalised for any kind of inter-phase coupling.

3.4.2 Numerical solvers

Analytical solutions for the governing equations contained in the process model (Eq. 3-1 to 3-3) are not available and therefore approximation methods are sought. Among these the finite difference method and variational methods such as Rayleigh-Ritz and Garlekin methods are most popular and were considered in this work (see Section 3.5 for a detailed description). Note, that a numerical scheme that is suitable for the use with the CMMR model can be used with the FFMR, too, since the latter is a special case of the CMMR model with a membrane thickness mh=0.

The finite difference approximation is based on replacing the derivatives by difference quotients (or the function is expanded in a Taylor series) on a discrete numerical grid. In this manner sets of algebraic equation are obtained which are solved after implementing the boundary conditions, for the solutions at the mesh points. A simplified finite difference scheme was developed as a short-cut process model, which was a simplified version of the model presented above. This algorithm is illustrated in Appendix G. The results obtained showed that this method was inefficient (with regard to the solution of boundary value problems) and limited to isothermal and 2D modelling.

The finite element technique is based on a powerful mathematical concept, i.e. the variational methods of approximation. In these, the solution over the reactor model domain is assumed to be a linear combination of appropriately chosen approximation functions and undetermined coefficients. These functions together with weight functions are the building blocks of the weighted-residual statement of the differential equation, which yields values for the coefficients. The main disadvantage of variational methods is the difficulty in selecting approximate functions for arbitrary geometries. The finite element method handles this problem through dividing the modelling domain into geometrically simple sub-domains and providing a systematic procedure for the derivation of the approximation functions. Thus, the finite element method can be viewed as an element-wise application of the Rayleigh-Ritz or weighted residual methods (Reddy, 1993). The finite element method naturally handles complex geometries and boundary value problems. Easy handling of the finite element method is achieved through the use of the commercial software package FEMLAB, which allows accurate specification of the model geometry and equations. Furthermore, this software is specialised on coupled differential equations. In the next section, the use of the finite element method and FEMLAB in particular is explained for the process model introduced above.

3.5 Finite element solution scheme

3.5.1 Basics

Using the finite element method a complex modelling domain is represented as a collection of geometrically simple sub-domains. The solution over each sub-domain is approximated by a linear combination of shape functions and undetermined coefficients. These functions together with weight functions are the building blocks of the weighted-residual statement of the differential equation, which yields values for the coefficients. According to Reddy (1993) the three basic features of the finite element method are the following:

- Division of the whole reactor model domain into parts
- Derivation of approximation functions over each element
- Assembly of elements, which is based on continuity of the solution and the balance of internal fluxes.

In this section it is explained how the finite element method is implemented in the software package FEMLAB, which is the software package that is employed for the finite element modelling. Furthermore, the most important user defined parameters are introduced and the implementation of the model equations is explained. For further reading there are many publications about the finite element technique available, e.g. Reddy (1993) and Buchanan (1995).

3.5.2 Specifying the geometry

Femlab's graphical user interface was used to specify the reactor geometry. A graphics toolbox may be used to compose the reactor model domain using basic shapes. Conceptually, a geometry is a collection of bounded geometric objects called domains. The terms used for these domains in 3D space in FEMLAB are: sub-domain (3D domain), boundary (2D), edge (1D), and vertex (0D). Every domain is bounded by domains of smaller dimension, e.g. a sub-domain in 3D is bounded by boundaries, edges and vertices and a boundary is bounded by edges and vertices etc. The domain constitutes the bounded space in which computation takes place. The space surrounding the domain is not taken into consideration.

3.5.3 Discretisation of the modelling domain

The starting point for the finite element method is the partition of the geometry, i.e. the entire reactor model domain, into small units of a simple shape. The reactor geometry and the scope of this work necessitate three-dimensional modelling. However, the full model is too complex to be modelled in a 3D finite element mesh. Therefore, we use two different ways to discretise a 3D domain:

A) 3D finite element (x,y,z - coordinates) grid

B) 2D finite element (y,z- coordinates) grid plus a Runge Khutta type stepper routine (x-coordinate)

where method B) is computationally less intensive. In this work, the mass and heat conservation equations were solved using a 2D finite element grid (method B) for the investigation of mass and heat transport and the chemical reaction. The momentum and heat equations were solved in a 3D finite element mesh to analyse heat conduction and heat sink design. The consequences from separating momentum and mass transport are analysed in Chapter 5.

With 2D finite element mesh, FEMLAB partitions the sub-domains into triangles or mesh elements approximating the arbitrarily shaped domain boundaries. The sides of the triangles are called mesh edges, and their corners are mesh vertices. Similarly, with a 3D finite element mesh the sub-domains are partitioned into tetrahedrons (mesh elements), whose faces, edges and corners are called mesh faces, mesh edges, and mesh vertices, respectively. The boundaries in the geometry are partitioned into triangular boundary elements (mesh faces).

Using the 2D finite element mesh the third spatial coordinate had to be transformed into a time coordinate (see Section 0), which is then discretised by means of a forward differences scheme of the intial value problem type. FEMLAB has several built in solvers, e.g. Runge Khutta type algorithms, which can be employed to obtain a numerical solution. In this work the MATLAB based solver ODEs15 was used because it is a good all-round solver which can handle stiff problems. Using this approach initial value problems can be solved effectively, however, no second order differential equations are allowed in this direction, which is achieved by neglecting the diffusion in the direction of the flow. Also the Navier-Stokes equations cannot be solved in this direction. These assumptions are discussed in the result section (Chapter 5).

The finite element grid is created automatically by FEMLAB based on user specified parameters the (see Table 3-5). The step size and accuracy required for the forward

difference scheme have to be defined by the user. The grid size and accuracy of the solver are very important parameters with respect to the numerical convergence the accuracy of the solution and the time-efficiency of the solver.

Table 3-5. Most important mesh generation parameters with FEMLAB

Parameter	Remark
Finite element grid:	
Maximum element size for sub-domains	/
Mesh growth rate	The rate at which the triangle edge length grows away from a small part of the geometry.
Mesh curvature factor	This factor controls the triangle edge length in comparison to the curvature of the geometry
Stepper routine:	
Output times	A MATLAB vector of times at which a solution to a time-dependent model should be generated. The relevant time span depends on the dynamics of the model.
Time-stepping algorithm	The ODE/DAE solver that performs the time stepping. The default is the variable-order stiff solver ode15s
Initial step size Maximum step size	/

3.5.4 Element equations

Using the finite element method, the solution of the differential model equations Eq. (3-1) – Eq. (3-3) over the entire domain is represented through a linear combination of appropriately chosen approximation functions and undetermined coefficients. The reasons for choosing algebraic polynomial approximation functions are: a) the integrals of these functions can easily be evaluated numerically and b) interpolation theory of numerical analysis can be used to develop the approximation functions systematically, which is exploited by FEMLAB. In this work Lagrange family interpolation functions with order k are used. The order of an element is an important parameter, similarly to the grid resolution, regarding accuracy and computational intensity of the numerical solver. This approximation is then inserted into the weak form of the equation to determine the unknown parameters. Weight functions are implemented into the weak formulation to obtain the necessary amount of equations.

FEMLAB is using weight functions, which are equal to the approximation function (Garlekin finite element model).

The integrals occurring in the weak form are computed using a quadrature formula. Such a formula computes the integral over a mesh element by taking a weighted sum of the integrand evaluated in a finite number of points in the mesh element. The order of a quadrature n is chosen such that it integrates all polynomials of degree k exactly. The accuracy of the quadrature increases with its order. On the other hand, with rising order the number of evaluation points increases, too, and so does the computational effort. As a rule of thumb one can take the order n of the quadrature to be twice the order of the finite element k. In FEMLAB's data structures the order of the quadrature formula is denoted by '*gporder*'. (*gp* stands for Gauss points). The order of pointwise constraints of the Lagrange element is denoted by '*cporder*' and by default equals the order k of the highest polynomial in the element. The setting of these parameters can influence the accuracy of the numerical solution. Within the scope of this work particularly careful adjustment was required to solve the Navier-Stokes equation set. The most important parameters are summarised in Table 3-6. More details about the derivation of approximation functions are illustrated in the Appendix F.3.

Table 3-6. Most important element characterisation parameters

Remark	Parameter	Default value
Order of a Lagrange element	shlag	k, depending on the variable u under consideration
Order of the quadrature formula	gporder	n=2·k
Order of Lagrange points	cporder	k

3.5.5 Geometry scaling

The differential equations were implemented in the solver routine in the way they are displayed in Section 3.2.2. A rigorous non-dimensionalisation would not yield any benefits, however, the geometry was scaled which effectively results in the non-dimensionalisation of the Cartesian coordinates. This step was necessary to allow optimum discretisation of the ill-conditioned modelling domain geometry, where the dimension in the direction of the x-coordinate was two orders of magnitude larger as compared to the y- and z-coordinates. The

following procedure was adopted to accomplish this task, which is exemplified using the temperature derivative with respect to the z-coordinate:

$e.g.\frac{\partial T_l}{\partial z}$:

where $[z]=m;$ $z\in[0,ch_l]$

with dimensionless variable $[z^+]=/;$ $z^+\in[0,z_l]$

and transformation factor $z_{fac}=\frac{z}{z^+}:=\frac{ch_l}{z_l}$

we get $\frac{\partial T_l}{\partial z}=\frac{\partial T_l}{\partial z^+\cdot z_{fac}}$

If z_l equals unity we get $z_{fac}=ch_l$ which often results in well conditioned meshes with multidimensional problems. Applying geometry scaling to the 3D heat conservation equation (Eq. 3-3)

$$\nabla\left(-\overline{k}_{\Omega}\cdot\nabla T_{\Omega}\right)+\vec{v}_{\Omega}\cdot\overline{c}_{p,\Omega}\frac{\partial\left(\overline{\rho}_{\Omega}T_{\Omega}\right)}{\partial x}=-\sum\nu_{\varphi,i}\cdot r_i\cdot\Delta H_{r,i} \tag{3-3}$$

we do the following substitutions:

$$\begin{aligned} x&=x^+\cdot x_{fac}\,; & dx&=dx^+\cdot x_{fac}\\ y&=y^+\cdot y_{fac}\,; & dy&=dy^+\cdot y_{fac}\\ z&=z^+\cdot z_{fac}\,; & dz&=dz^+\cdot z_{fac} \end{aligned}\quad, \tag{3-9}$$

which results in the following equation:

$$\nabla\left(-\frac{\overline{k}_{\Omega}}{x_{fac}^2}\cdot\frac{\partial T_{\Omega}}{\partial x^+},-\frac{\overline{k}_{\Omega}}{y_{fac}^2}\cdot\frac{\partial T_{\Omega}}{\partial y^+},-\frac{\overline{k}_{\Omega}}{z_{fac}^2}\cdot\frac{\partial T_{\Omega}}{\partial z^+}\right)+\frac{\vec{v}_{\Omega}\cdot\overline{c}_{p,\Omega}}{x_{fac}}\frac{\partial\left(\overline{\rho}_{\Omega}T_{\Omega}\right)}{\partial x^+}=-\sum\nu_{\varphi,i}\cdot r_i\cdot\Delta H_{r,i} \tag{3-10}$$

Note: that anisotropic scaling in x,y and z directions (FEMLAB, 2004) is used with Eq. (3-10).

Using the 2D finite element mesh combined with a stepper routine, the third spatial coordinate had to be transformed into a time coordinate to be able to use the time stepping facility built into FEMLAB. The following approach was used, which is exemplified using a spatial derivative of the liquid phase temperature:

$e.g. \frac{\partial T_l}{\partial x}$

where $[x]=m; \qquad x_{dim} \in [0, cl]$

with transformation factor $\overline{v}_l = \frac{x}{t}; \; [\overline{v}_l] = \frac{m}{s}$

and time variable $[t]=s; \; t \in \left[0, \frac{cl}{\overline{v}_l}\right]$

we get $\frac{\partial T_l}{\partial x} = \frac{\partial T_l}{\partial t \cdot \overline{v}_l}$

further, with the dimensionless time variable $t^+ = t \cdot \frac{\overline{v}_l}{cl}; \; t^+ \in [0,1]$

we get $\frac{\partial T_l}{\partial x} = \frac{\partial T_l}{\partial t^+ \cdot cl}$

where $\overline{v}_l$ denotes the mean velocity in x-direction. The time coordinate t has been non-dimensionalised resulting in t^+. Transforming the x-coordinate of Eq. (3-12) into a time coordinate, we obtain the following heat conservation equation:

$$\nabla\left(-\frac{\overline{k}_\Omega}{y_{fac}^2} \cdot \frac{\partial T_\Omega}{\partial y^+}, -\frac{\overline{k}_\Omega}{z_{fac}^2} \cdot \frac{\partial T_\Omega}{\partial z^+}\right) + \frac{\overline{v}_\Omega \cdot \overline{c}_{p,\Omega} \cdot \overline{\rho}_\Omega}{cl} \cdot \frac{\partial T_\Omega}{\partial t^+} = -\sum \nu_{\varphi,i} \cdot \Delta H_{r,i} \qquad (3\text{-}11)$$

In this representation the 1st spatial derivative with respect to x is transformed into a time derivative. With this transformation all 2nd derivatives over x had to be neglected.

3.5.6 Equation implementation

In this work, a general and basic modelling environment was used to allow maximum user control of the modelling. In this environment partial differential equations are implemented into FEMLAB by customising the coefficients of generalised PDEs:

$$\begin{cases} d_a \frac{\partial u}{\partial t^+} + \nabla \cdot \Gamma = F & in\,\Omega \\ -n \cdot \Gamma = G & on\,\partial\Omega \\ 0 = R & on\,\partial\Omega \end{cases} \qquad (3\text{-}12)$$

where Ω is a bounded region (domain), $\partial\Omega$ is the boundary of the region, and n is the outward unit normal vector. The first equation is the PDE. The second and third equations are the Neumann and Dirichlet boundary conditions, respectively.

The coefficient d_a is called *mass coefficient*. For a system of equations, u is a vector of dependent variables. In this case coefficient d_a can be a matrix. The terms Γ, F, G, and R are often called coefficients. They can be functions of the space coordinates, the solution u, and the derivatives of u ; F, G, and R are scalar, while Γ is a vector (Γ is often called the flux vector). Of course, the coefficients can vary with time.

As example the implementation of the mass conservation Eq. (3-2) is shown for component φ in the liquid phase with 2D finite element discretisation combined with a stepper routine:

$$u = c_{\varphi,\Omega}$$

$$\Gamma = \begin{bmatrix} -D_{\varphi,l}\dfrac{\partial c_{\varphi,l}}{\partial x^{+}\cdot x_{fac}^{2}} \\ -D_{\varphi,l}\dfrac{\partial c_{\varphi,l}}{\partial y^{+}\cdot y_{fac}^{2}} \end{bmatrix} \tag{3-13}$$

$$F = -(r_1 + r_2 + 4\cdot r_3 + 2\cdot r_4)$$

$$d_a = \frac{\overline{v}_{\Omega}}{cl}$$

The boundary between the liquid and the gas phase can be described as follows, using mass transport of fluorine as an example:

$$G = k_g\left(\overline{x}_{F_2,g} - \frac{c^{*}_{F_2,S}}{H_c\cdot p}\right)\frac{\overline{\rho}_g}{\overline{u}_{m,g}}\frac{1}{y_{fac}} \tag{3-14}$$

R=0

3.5.7 Discussion

The finite element method naturally handles boundary value problems and therefore is particularly suitable for the use with the model description of the direct fluorination in microreactors. The commercial software used in this study, i.e. FEMLAB, provides an environment that leaves a high level of control to the user. We chose to self-define all equations and various solver settings were controlled to improve the solution process.

The order of the element refers to the degree of polynomial used to represent the solution over the element. The amount of elements used in a problem depends mainly on the element type and accuracy desired. To obtain high accuracy solutions it is required to investigate the convergence characteristics of the finite element approximation and increase the number of elements or the order of the element. Thus, these parameters vary between experiments depending on the accuracy of the solution required. Stability and accuracy of the numerical solver routine are discussed in the next section.

3.6 Stability and accuracy of numerical schemes

Important issues about the numerical integration of differential equations are the accuracy, error propagation, stability, and convergence of the solution. Here, two types of stability considerations are distinguished: inherent stability and numerical stability. Inherent stability is determined by the mathematical formulation of the problem. Numerical stability depends on the error propagation in the numerical integration algorithm (Constantinides, A. and Mostoufi N., 1999).

3.6.1 FEM error analysis

The errors introduced to the finite element solution of a given differential equation can be associated with the following main sources (Reddy, 1993):

- Domain approximation error; due to the approximation of the domain
- Quadrature and finite arithmetic errors; due to the numerical evaluation of integrals and the numerical computation on a computer
- Approximation error; due to the approximation of the solution by means of an approximation function

In this work the reactor model domain geometry has a regular shape and can be approximated accurately using a triangular finite element discretisation scheme. The latter two error contributions lead to inaccuracy of the solution, which can be minimised by optimising key parameters of the numerical solver (illustrated in Table 3-6).

Convergence of finite element solvers

"The finite element solution U_h^e is said to converge"... "to the true solution U^e if

$$\left\| U^e - U_h^e \right\|_m \leq c \cdot h^p \qquad for\ p > 0$$

where c is a constant independent of U^e and U_h^e, h is the characteristic length of an element, and $2m$ is the order of the differential equation to be solved. The constant p is called the rate of convergence which, in the weak form of the differential equation, depends on the order of the derivative and the degree of the polynomials used to approximate u" (Reddy, 1993). Thus, the error in the approximation can be reduced either by reducing the size of the elements (h-convergence) or increasing the degree of approximation (p-convergence), i.e. order of polynomial k with regard to the nomenclature introduced in Section 3.5.4.

The decision, when to stop refining the mesh and increasing the degree of the approximations stays with the analyst, who can decide which accuracy is required. In practice numerical simulations are conducted with increasing mesh resolution and as soon as the variation in the results is sufficiently small the process is stopped. In a similar manner the degree of a polynomial is determined.

3.6.2 Stability and accuracy of stepper routines

In this work the finite element method is combined with a stepper routine where appropriate. The stepper routine employed is a Runge-Kutta type algorithm implemented in Matlab as ODE 15s.

Problem definition

Three types of errors corrupt the solution of numerical stepper routines: truncation error, round off error, and the propagation error. The latter occurs because the solution at a certain step depends on the previous step and the error can grow with time. If it grows unboundedly with increasing amount of steps along a coordinate, the solution is unstable. The solution scheme is said to be stable if the error is bounded, i.e. does not exceed a certain limit.

The numerical scheme is consistent with the continuous problem if round-off and truncation errors go to zero as the step size h takes the limit $\lim(h \rightarrow 0)$. Accuracy is a measure of the closeness between a numerical scheme and the exact solution. Stability instead, is a measure of the boundedness of the approximate solution with the independent variable. A numerical scheme is convergent if it is stable and consistent (see Isaacson and Keller, 1966).

Step size α-family algorithms

In this section we look at the convergence and stability behaviour of α-family approximation methods (one of which is the ODE15s solver), which can be described by

$$(1-\alpha)\cdot \dot{u}_i + \alpha \cdot \dot{u}_{i+1} = \frac{u_{i+1}-u_i}{h_{i+1}} \qquad for\ 0 \le \alpha \le 1 \tag{3-15}$$

where u is the dependent variable. This type of algorithm is commonly used with parabolic equations like Eq. (3-13).

Algorithms of the α-family for which $\alpha \ge 1/2$ are inherently stable. This was exploited with the finite difference scheme illustrated in (Appendix G), where a Cranck-Nicolson method with $\alpha = 1/2$ was employed, which converges with second order accuracy.

Using FEMLAB a Runge Khutta (RK) type stepper algorithm with variable accuracy (ODE 15s, see Matlab manual) is used in combination with a 2D finite element grid. Standard RK algorithms $(\alpha < 1/2)$ are conditionally stable algorithms, which are stable only when certain restrictions on the step size h are satisfied. The stability condition depends on the largest eigenvalue λ of the differential equations and α:

$$h < h_{cr} \equiv \frac{2}{(1-2\alpha)\lambda}. \tag{3-16}$$

where h_{cr} denotes the critical sep size. In this work, the eigenvalues of the equations are not available and therefore the step size is determined in an iterative process of varying the step size h and checking the simulated values of the key variables.

3.7 Summary

Two reactor configurations are illustrated in this chapter with the appertaining model representations, i.e. the FFMR and CMMR. In this work, both reactors are used to conduct the fluorination of toluene reaction. The FFMR reactor model consists of the mathematical description of heat, mass and momentum conservation in a defined 3D modelling domain. The CMMR can be considered an extension of the FFMR where a membrane separates the gas and liquid phase. Thus, the most part of the mathematical models is identical merely certain boundary conditions are different and the CMMR model features equations to

describe mass and heat transfer processes within the membrane. This description of the membrane is not an image of a real mesh but rather a theoretical model characterised by several relevant parameters.

The mathematical equations are too complex to be solved analytically and a commercial finite element solver was found suitable to handle the problem. All the simulations conducted within this work are based on this method. This result is in line with Quiram et al. (2000a) who recommend the FEM-simulation for evaluation and scale-up.

Most of the physical property parameters contained in the process models can be determined from data published in the literature. The underlying reaction mechanism and the Henry constant, which are important components of both, the FFMR and the CMMR model, are not available and have to be determined in the course of this work. In the upcoming chapter the FFMR model is used to quantify the missing parameters by matching model predictions with experimental data.

Chapter 4

Empirical determination of model parameters

4.1 Introduction

The structure of the FFMR and CMMR models is illustrated in Chapter 3. In this chapter the core process model applying to both reactors is completed and validated by means of experimental data. Physical and chemical information in two fields is implemented that is not available in the literature: 1) The reaction mechanism and kinetic parameters, and 2) the absorption of fluorine into the liquid phase. Additionally, the catalytic function of the membrane is considered with regard to its influence on reaction kinetic.

First, a simplified reaction mechanism for the direct fluorination of toluene is developed, based on information from the literature. Several parameters are involved in the mathematical description of the reaction system for which estimated values are determined. The reaction mechanism is assumed to be the same with the FFMR and the CMMR model. However, with the membrane reactor heterogeneous catalysis supports the electrophilic reaction as explained in Section 4.2.4. Thereafter, a scheme is introduced which is describing fluorine mass transfer between the gas and the liquid phase. Again, values for the parameters involved in the description of this process are estimated.

Finally, a procedure is illustrated where the estimated model parameters are tuned so that the FFMR model results match experimental data published by Jähnisch et al. (2000). The complete model is then tested and verified with experimental data.

4.2 Reaction chemistry of the direct fluorination of toluene

4.2.1 Reaction mechanism

Various researchers have worked on the direct fluorination of organic compounds. Yet, the complete reaction mechanism of the direct fluorination of toluene is not well documented. Thus, in this work a reaction mechanism is developed for this process based on information about fluorination of organic compounds reported in the literature (see Appendix B.1). The direct fluorination reaction involving the reactants fluorine F_2 and toluene C_7H_8 consists of a radical chain reaction system competing with an electrophilic mechanism, which yields the desired mono-fluorinated product C_7H_7F.

The radical reaction follows a very complex reaction mechanism. Radicals formed during the reaction potentially react with any species in the mixture to some extent, even solvent acetonitrile (see Appendix B). The reaction kinetics of the termination steps depend to some extent on interaction with the reactor wall or other inert, energy removing parts inside the reactor. Free surfaces tend to bind radical species, which are crucial as chain carriers for (particularly explosive) gas-phase reactions (Veser, 2001). Termination steps play a very important role as they determine the reaction order of the radical reaction system and the extent of the chain propagation and therewith the selectivity of the overall process. Despite the high level of complexity a reaction mechanism was assembled which is illustrated in Scheme 4-1 (see Appendix B for details).

The reaction rate constants of the main elementary reaction steps and their temperature dependence are not well explored. Even for the simpler electrophilic reaction no explicit data is available. As a consequence from this lack of data vast simplifications were introduced in two steps to obtain a realistic but compact reaction mechanism (see Appendix B for details). Scheme 4-2 shows the predominant reactions and finally Scheme 4-3 represents the simplified mechanism which is implemented in the FFMR process model. This series-parallel reaction system is illustrated in Scheme 4-4 with the key component toluene.

The most important assumptions going along with the derivation of this mechanism are:

- Rupture of C-C bonds is not taken into account since it is associated with gas-phase rather then liquid phase fluorination of organic compounds (Bigelow, 1947).
- Experimental results reported by Jähnisch et al. (2000) suggest that the reaction mechanism has reaction order 1 with respect to both reactants therefore only the termination step is included that leads to these conditions.
- A fixed number of fluorine atoms is added to the ring of one toluene molecule, thus only few partially fluorinated compounds are considered while intermediate products

are neglected. Here, the aromatic structure of the ring is destroyed and all free electron sites are paired with fluorine radicals.

- The temperature dependence of the reaction kinetic constant is implemented in form of the Arrhenius equation for each reaction i.(i ∈ [1,4]):

$$k_i = k_{i,0} \cdot EXP\left(\frac{E_{A,i}}{\Re \cdot T}\right) \tag{4-1}$$

$$F_2 + C_7H_8 \xrightarrow[\text{electrophilic reaction}]{k_e} C_7H_7F + HF$$

Initiation

$$F_2 + C_7H_8 \xrightarrow[\text{radical addition}]{k_{i1}} F^\bullet + C_7H_8F^\bullet$$

$$F_2 + C_7H_7F \xrightarrow[\text{radical addition}]{k_{i2}} F^\bullet + C_7H_7F_2^\bullet$$

radical chain propagation:

$$F^\bullet + C_7H_8 \xrightarrow[\text{radical addition}]{k_{q1}} C_7H_8F^\bullet \qquad F_2 + C_7H_8F^\bullet \xrightarrow[\text{radical addition}]{k_{p1}} F^\bullet + C_7H_8F_2$$

$$F^\bullet + C_7H_7F \xrightarrow[\text{radical addition}]{k_{q2}} C_7H_7F_2^\bullet \qquad F_2 + C_7H_7F_2^\bullet \xrightarrow[\text{radical addition}]{k_{p2}} F^\bullet + C_7H_7F_3$$

$$F^\bullet + C_7H_8F_2 \xrightarrow[\text{radical addition}]{k_{q3}} C_7H_8F_3^\bullet \qquad F_2 + C_7H_8F_3^\bullet \xrightarrow[\text{radical addition}]{k_{p3}} F^\bullet + C_7H_8F_4$$

$$F^\bullet + C_7H_7F_3 \xrightarrow[\text{radical addition}]{k_{q4}} C_7H_7F_4^\bullet \qquad F_2 + C_7H_7F_4^\bullet \xrightarrow[\text{radical addition}]{k_{p4}} F^\bullet + C_7H_7F_5$$

$$F^\bullet + C_7H_8F_4 \xrightarrow[\text{radical addition}]{k_{q5}} C_7H_8F_5^\bullet \qquad F_2 + C_7H_8F_5^\bullet \xrightarrow[\text{radical addition}]{k_{p5}} F^\bullet + C_7H_8F_6$$

$$F^\bullet + C_7H_8F_6 \xrightarrow[\text{radical substitution}]{k_{q7}} C_7H_7F_6^\bullet + HF \qquad F_2 + C_7H_7F_6^\bullet \xrightarrow[\text{radical addition}]{k_{p6}} F^\bullet + C_7H_7F_7$$

$$F^\bullet + C_7H_7F_7 \xrightarrow[\text{radical substitution}]{k_{q8}} C_7H_6F_7^\bullet + HF \qquad F_2 + C_7H_6F_7^\bullet \xrightarrow[\text{radical addition}]{k_{p7}} F^\bullet + C_7H_6F_8$$

$$F^\bullet + C_7H_6F_8 \xrightarrow[\text{radical substitution}]{k_{q9}} C_7H_5F_8 + HF \qquad F_2 + C_7H_5F_8^\bullet \xrightarrow[\text{radical addition}]{k_{p8}} F^\bullet + C_7H_5F_9$$

$$F^\bullet + C_7H_5F_9 \xrightarrow[\text{radical substitution}]{k_{q10}} C_7H_4F_9^\bullet + HF \qquad 2C_7H_4F_9^\bullet \xrightarrow[\text{radical addition}]{k_x} C_{14}H_8F_{18}$$

$$\phi^\bullet + \phi \xrightarrow[\text{radical polymerisation}]{k_{r1}} product \qquad etc.$$

termination

$$2 \cdot \phi^\bullet + X \xrightarrow[\text{radical polymerisation}]{k_{t1}} product$$

$$2 \cdot F^\bullet + X \xrightarrow[\text{recombination}]{k_{t2}} F_2$$

$$F^\bullet + \phi^\bullet \xrightarrow[\text{recombination}]{k_{t3}} product$$

where φ can be any hydrocarbon (C_7H_7F to $C_7H_6F_8$)

X symbolises unspecified reaction partners, i.e. reactor walls

Scheme 4-1. Reaction mechanism for the direct fluorination of toluene

$$F_2 + C_7H_8 \xrightarrow[\text{electrophilic reaction}]{k_e} C_7H_7F + HF$$

Initiation

$$F_2 + C_7H_8 \xrightarrow[\text{radical addition}]{k_i} F^\bullet + C_7H_8F^\bullet$$

polymerisation

$$C_7H_8F^\bullet + C_7H_8 \xrightarrow[\text{radical polymerisation}]{k_{r1}} C_{14}H_{16}F^\bullet$$

radical chain propagation :

$$F^\bullet + C_7H_8 \xrightarrow[\text{radical addition}]{k_{q1}} C_7H_8F^\bullet \qquad F_2 + C_{14}H_{16}F^\bullet \xrightarrow[\text{radical addition}]{k_{p1}} F^\bullet + C_{14}H_{16}F_2$$

$$F^\bullet + C_7H_7F \xrightarrow[\text{radical addition}]{k_{q2}} C_7H_7F_2^\bullet \qquad F_2 + C_7H_7F_2^\bullet \xrightarrow[\text{radical addition}]{k_{p2}} F^\bullet + C_7H_7F_3$$

$$F^\bullet + C_{14}H_{16}F_2 \xrightarrow[\text{radical addition}]{k_{q3}} C_{14}H_{16}F_3^\bullet \qquad F_2 + C_{14}H_{16}F_3^\bullet \xrightarrow[\text{radical addition}]{k_{p3}} F^\bullet + C_{14}H_{16}F_4$$

$$F^\bullet + C_7H_7F_3 \xrightarrow[\text{radical addition}]{k_{q4}} C_7H_7F_4^\bullet \qquad F_2 + C_7H_7F_4^\bullet \xrightarrow[\text{radical addition}]{k_{p2}} F^\bullet + C_7H_7F_5$$

$$F^\bullet + C_{14}H_{16}F_4 \xrightarrow[\text{radical addition}]{k_{q5}} C_{14}H_{16}F_5^\bullet \qquad F_2 + C_{14}H_{16}F_5^\bullet \xrightarrow[\text{radical addition}]{k_{p5}} F^\bullet + C_{14}H_{16}F_6$$

$$F^\bullet + C_{14}H_{16}F_6 \xrightarrow[\text{radical addition}]{k_{q7}} C_{14}H_{16}F_7^\bullet \qquad F_2 + C_{14}H_{16}F_7^\bullet \xrightarrow[\text{radical addition}]{k_{p7}} F^\bullet + C_{14}H_{16}F_8$$

$$F^\bullet + C_{14}H_{16}F_8 \xrightarrow[\text{radical addition}]{k_{q9}} C_{14}H_{16}F_9^\bullet \qquad F_2 + C_{14}H_{16}F_9^\bullet \xrightarrow[\text{radical addition}]{k_{p9}} F^\bullet + C_{14}H_{16}F_{10}$$

termination

$$F^\bullet + C_{14}H_{16}F^\bullet \xrightarrow[\text{radical addition}]{k_t} C_{14}H_{16}F_2$$

Scheme 4-2. Predominant elementary reactions with the direct fluorination of toluene

$$F_2 + C_7H_8 \xrightarrow[\text{electrophilic reaction}]{k_1} C_7H_7F + HF \qquad r_1 = k_1 \cdot c_{F_2} \cdot c_{C_7H_8}$$

$$F_2 + 2Tol \xrightarrow[\text{radical addition}]{k_2} C_{14}H_{16}F_2 \qquad r_2 = k_2 \cdot c_{F_2} \cdot c_{C_7H_8}$$

$$4 \cdot F_2 + C_{14}H_{16}F_2 \xrightarrow[\text{radical addition}]{k_3} C_{14}H_{16}F_{10} \qquad r_3 = k_3 \cdot c_{F_2} \cdot c_{C_{14}H_{16}F_2}$$

$$2 \cdot F_2 + C_7H_7F \xrightarrow[\text{radical addition}]{k_4} C_7H_7F_5 \qquad r_4 = k_4 \cdot c_{F_2} \cdot c_{C_7H_7F}$$

Scheme 4-3. Simplified reaction mechanism and associated power law reaction kinetics

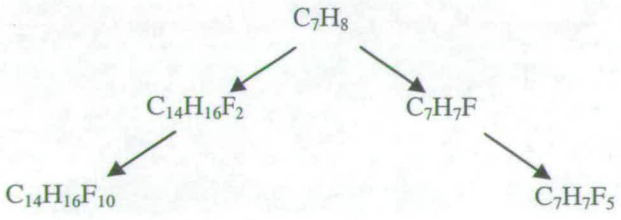

Scheme 4-4. Series-parallel reaction with regard to reactant toluene

4.2.2 Reaction kinetics

Reaction Scheme 4-3 was created in this work and therefore no reaction kinetic data is available in the literature for these lumped reactions. To get an approximate estimate of the kinetics of these lumped reactions their derivation from the elemental reactions was accomplished using pseudo steady state approximation (see also Appendix B). However, even for the elementary reactions (Scheme 4-2) there are no values explicitly given in the literature. Some kinetic data is available for related elemental reactions involved in the gas-phase fluorination of methane, ethane, and toluene as well as solvent phase chlorination of some organic compounds. Based on this data an attempt for an order of magnitude estimation was undertaken here, see Table 4-1. No estimate was produced for the electrophilic reaction because there was no data available in the literature covering the fluorination of toluene in acetonitrile solvent.

Reaction kinetic parameter estimation

The estimation of liquid phase reaction constants was partially accomplished using data for gas phase reactions. Here, one of the major assumptions implies that the kinetics of the elementary fluorination steps of the radical mechanism are similar in liquid and gas-phase. This can be justified considering that in general solvents have a much larger effect on ionic reactions than on radical reactions and also solvents have only little effect on neutral species (Masel, 2001).

Next, the occurrence of the electrophilic reaction in the solvent phase is discussed. In general, the same elementary reactions occur in solution that one sees in the gas phase. However, ionic reactions show much higher overall rates in polar solvents than in the gas phase. The electrophilic fluorination of toluene is an aromatic substitution reaction with ionic character. Polar aprotic solvents, one of which is acetonitrile, favour reactions of ions while non-polar solvents (like toluene) favour radical reactions. No kinetic data is available for the electrophilic fluorination reaction but it can be deduced, that polar acetonitrile solvent supports this ionic reaction over the radical reaction (Masel, 2001).

At this point is should be mentioned that kinetic parameters acquired from the literature may be inappropriate for the description of reactions in micro-channels. For example termination reactions of a radical reaction system can be strongly catalysed by the reactor walls. Thus data describing chemical kinetics in macro-scale devices may not be very accurate. Therefore, there is a need to validate estimated values with experimental results, see Section 4.4. In this manner the determination of the pre-exponential factor and the activation energy are accomplished later in this chapter using the FFMR model.

Table 4-1. Estimation of the kinetic data of the lumped reactions in Scheme 4-3 at a temperature of T=257K

Reaction	Rate constant / $l \cdot mol^{-1} \cdot s^{-1}$	Determined from
k1	supported by aprotic polar solvent	/
k2	1.4E+04 ± 100%	calculation, see Appendix B
k3	7.0E+04 ± 100%	calculation, see Appendix B
k4	7.0E+04 ± 100%	calculation, see Appendix B

4.2.3 Heat of reaction

The reaction mechanism proposed in this work, Scheme 4-3, involves four exothermic lumped reactions. The heat exerted by any of these lumped reactions is calculated from the heats of formation of the individual compounds involved and the bond strength between atoms and compounds. Here, only a summary of the heat of reaction data is given, but a more comprehensive derivation of that data is shown in Appendix B. The lumped reactions in Scheme 4-3 are all exothermic reactions with the following individual heat production at standard conditions (298 K), see Table 4-2. The temperature dependence of this heat of reaction was not considered as it varies very little in the considered temperature range.

Table 4-2. Estimation of the heat of reaction of the lumped reactions in Scheme 4-3

No.	Reactants			Products			$\Delta H_{r,298}$ [kJ mol^{-1}]
1	F_2	+	C_7H_8	→	$F\text{-}C_7H_7$	+ HF	-478
2	F_2	+	$2 \cdot C_7H_8$	→	$F_2\text{-}(C_7H_8)_2$		-1296
3	$F_2\text{-}(C_7H_8)_2$	+	$4 \cdot F_2$	→	$F_{10}\text{-}(C_7H_8)_2$		-3680
4	$F\text{-}C_7H_7$	+	$2 \cdot F_2$	→	$F_5\text{-}C_7H_7$		-1840

4.2.4 Reaction mechanism involving heterogeneous catalysis

Using the CMMR the fluorination of toluene is catalysed through a catalytic solid membrane featuring Lewis acid sites. The focus is on the effect of the acidic groups on fluorine turning it into an electrophile. This effect was demonstrated by Chambers et al. (1996) who investigated the influence of homogeneous Lewis acid catalysts on direct fluorination of organic compounds. By using 98%-sulphuric acid as homogeneous catalyst the selectivity towards the

desired fluorinated compound increased towards 84%, from 53% with the solvent acetonitrile, only.

Heterogeneous reactions occur between one or more constituents that can be identified with specific sites and involve some additional steps to be taken into account. These are primarily mass transfer steps of the reactant and the product between the fluid bulk and the catalyst pores, including adsorption and desorption at interior sites of the catalyst (Fogler, 2001; Zaspalis 1990). Modeling active sites and dual site absorption on the membrane, e.g. Langmuir-Hinschelwood kinetics, are beyond the scope of this work.

Clark and Macquarrie (1997) showed that solid acid catalysts, e.g. zeolite ZSM-5, may improve the selectivity of reactions through shape-selectivity and electrostatic effects occuring within the highly polar interior of the material. They showed this effect with the chlorination of toluene. Shape selectivity is an interesting feature of some heterogeneous catalysts. However, firstly this kind of molecular interaction goes beyond the scope of this simulation study and Clark (1997) reported deactivation of their silica catalyst due to deformation of the pores on interaction with HF.

In this study it is assumed that all the effects listed above are incorporated into the catalyst activity coefficient κ, see Eq. (4-1). The solid catalyst is assumed to uniquely influence the electrophilic reaction. The catalytic activity is expressed in terms of the dimensionless number

$$\kappa = \frac{\text{kinetic constant of reaction 1 with catalyst - } k_{1,Cat}}{\text{kinetic constant of reaction 1 without catalyst - } k_1} \qquad (4\text{-}2)$$

The actual activity of the membrane is not known and κ is introduced into the model as a variable for a sensitivity study.

The most part of the reaction mechanism introduced as part of the FFMR model (see Scheme 4-3) is reused with the CMMR reactor model, merely, reaction 1 changed:

$$F_2 + C_7H_8 \xrightarrow[\text{electrophilic reaction}]{k_{1,Cat.}} C_7H_7F + HF \qquad r_1 = k_{1,Cat} \cdot c_{F_2} \cdot c_{C_7H_8}$$

4.3 Gas absorption

The absorption of a gas into a liquid can be divided into three steps:

- Transport from the bulk gas flow to the interface
- Phase change at the interface itself where there is no resistance so that Henry's law Eq. (4-3) is satisfied. This assumption is justified even though in real applications there is a resistance at the interface otherwise the initial absorption mass flow would be infinite. The mass flow can only be as high as the impingement of the gas on the liquid surface, which is not the limiting process, here.

$$c^*_{F2,l} = H_c \cdot p^*_{F2,g} \tag{4-3}$$

  where $[H_c]$ = kmol·m^{-3}bar^{-1} and $p_{F2,g}{}^*$ and $c_{F2,l}{}^*$ are the partial pressures and the concentration of fluorine at the gas/liquid interface.
- Transport from the interface to the bulk liquid flow.

The first and the third step are described by means of the mass conservation equation for fluorine in the gas and the liquid phase, see Appendix E. The actual phase change is calculated using the Henry constant H_c, which is a physical property parameter of the gas/liquid system.

4.3.1 Estimation of gas solubilities

Gaseous fluorine absorbs into a liquid mixture consisting of acetonitrile and toluene. Experimental results showed, that the solubility of fluorine in this liquid mixture is low, which may therefore be described by Henry's law. In doing so it is assumed that the fugacity of the liquid phase is proportional to the mole fraction with Henry's empirical constant being the proportionality factor. The Henry constant depends strongly on the temperature and its temperature gradient varies significantly with the solute-solvent system. No simple generalisation about the effect of temperature on solubility can be made.

A generally accepted method for the estimation of gas solubilities in non-polar solvents and their temperature dependence was developed by Hildebrand (1964). His correlations use a compound specific solubility parameter, which is derived from the cohesive energy density of the solvent, which in turn is derived from the heat of vaporisation. More detailed three component systems are based on correlations by Hansen (1999), who split the Hildebrand solubility coefficient into sub-parameters and thus take disparities in polar contributions to the total van der Waals force into account. Due to a lack of physical property data available for

fluorine we reverted to the one parameter correlation introduced by Hildebrand and Scott (1964) for the use with the FFMR and CMMR models:

$$\frac{1}{H_c} = f_{pure} \cdot \mathrm{e}^{\frac{25.3\cdot\left(-\delta_{F2-Tol}-x_{Vol,AcN}\cdot(-\delta_{AcN-Tol})\right)^2}{8.314*T}} \cdot \frac{\rho_{AcN}}{u_{m,AcN}} \tag{4-4}$$

where f_{pure} = the fugacity of pure gas, $x_{vol,AcN}$ = volume fraction of acetonitrile in liquid phase and solubility parameters $\delta_{\varphi\text{-}Tol} = \delta_{\varphi}\text{-}\delta_{Tol}$. The solubility parameter can be calculated using the following equation:

$$\delta_{\varphi} = \left[\frac{\Delta H_{V,\varphi} - RT}{V_{m,\varphi,l}}\right]^{1/2} \tag{4-5}$$

where $\Delta H_{V,\varphi}$ is the heat of vaporisation and $V_{m,\varphi,l}$ is the molal volume of component φ in the liquid phase. In Table 4-3 the Hildebrand solubility parameters for fluorine, toluene and acetonitrile are illustrated as they appear in the literature (Hildebrand and Scott, 1964).

Table 4-3. Hildebrand coefficients δ_{φ} for the reactants and the solvent acetonitrile published in Hildebrand and Scott (1964)

Compound	Acetonitrile	Toluene	Fluorine
Hildebrand Solubility parameter $[(J/cm^3)^{0.5}]$	23.9	18.2	15.2

According to the table above toluene is the better solvent for fluorine compared to acetontrile, indicated by the relative proximity of the solubility parameter. However, experimental evidence showed the opposite effect, i.e. fluorine solubility was greatly improved when solvent acetonitrile was added to toluene (Chamber's et al, 1999). This phenomenon is probably due to the fact that acetonitrile is a compound with significant polarity and Hildebrandt's correlation was developed for non-polar solvents. In proximity to polar compounds fluorine molecules can embrace induction of polarity.

Since the data available from literature is not coherent, Hildebrand solubility parameters displayed in the table above are merely used for estimation purposes of the fluorine solubility in pure acetonitile. This estimation is based on the solubility parameters for acetonitrile and fluorine displayed in the table above, which yields an estimate for the Henry constant $H_{c,AcN}$=0.03 kmol·m^{-3}·bar^{-1} at a temperature of 257K in pure acetonitrile. The solubility parameter for toluene is less important since we consider low substrate concentrations in this

work; its value is adjusted such that adding toluene to acetonitrile results in a poorer solubility (see Section 4.4).

4.4 Matching simulations and experiments

4.4.1 Unknown model parameters

In previous sections mathematical descriptions of the reaction mechanism and gas absorption are introduced. The physical parameters involved are displayed in Table 4-4. Assuming that the temperature dependence of the reaction kinetics can be described by the Arrhenius equation two parameters have to be determined for each reaction, i.e. the activation energy $E_{A,1}$ and the pre-exponential factor $k_{0,i}$. The Henry-coefficient for a pure component in a mixture of constant composition can be estimated using the Hildebrand equation and merely one parameter has to be determined, i.e. the difference of the solubility coefficients between the liquid phase and the absorbed gas. These parameters will now be quantified to complete the process model using experimental results published in the literature.

Table 4-4. Specification of unknown physical parameters

Intro	Variable	Unit
Hildebrand coefficient for F_2 in a solution of 90% Acetonitrile and 10% toluene	$\delta_{F2\text{-}Solvent}$	$(J/cm^3)^{0.5}$
Kinetic rate: pre-exponential factors	$k_{0,1}$, $k_{0,2}$, $k_{0,3}$, $k_{0,4}$	$m^3/kmol{\cdot}s$
Kinetic rate: activation energy	$E_{A,1}$, $E_{A,2}$, $E_{A,3}$, $E_{A,4}$	$m^3/kmol{\cdot}s$

4.4.2 Fitting parameters using experimental data

Experimental apparatus and model domain

Jähnisch et al.(2000) present results obtained with the direct fluorination of toluene in a falling film microreactor. A schematic of the falling film microreactor used by Jähnisch et al. (2000) is displayed in the Figure 4-1. The liquid feed flow is distributed over a parallel array of 64 microchannels while one large channel carries the gas flow. In contrast to this experimental apparatus the model for the FFMR introduced in Chapter 3 consists of only a single channel for each phase. To coordinate the data obtained with the model and the experiments it is assumed that all channels perform the same and operating parameters, like

volume flow rate of the gas and the liquid phase, were converted accordingly. The geometry parameters of the 3D FFMR model were adjusted to match the real device.

The model used in this section is simplified with regard to the heat sink and the flow hydrodynamics. The modelling domain does not comprise a cooling channel and the bottom of the reactor housing is assumed to be at constant temperature. The momentum conservation equations are not solved and plug flow is assumed with liquid and gas flow. The numerical solver is based on a 2D finite element discretisation combined with a stepper routine in direction of the flow.

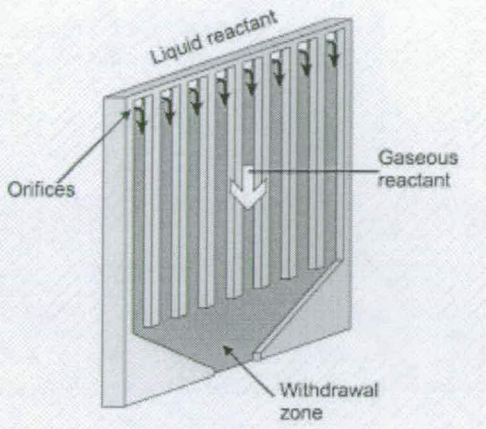

Figure 4-1. Falling film reactor by Jähnisch et al. (2000)

Procedure

The reported experimental data does not allow the derivation of reaction kinetic parameters, directly. The determination of values for the unknown parameters listed in Table 4-4 is based on adjusting the FFMR mathematical model so that the computer simulations yield the same results as experiments under certain operation conditions. This approach can be broken down into the following steps:

- We concentrate on the mass conservation of toluene and the mono-fluorinated compound *FTol*. First, an isothermal process is considered and we obtain a system of two differential equations (mass conservation of the compounds *Tol* and *FTol*) and seven unknown parameters, see Table 4-5.
- From the experimental results published by Jähnisch (2000) we know the change of the concentration of toluene and the mono-fluorinated compound for a reaction at certain operation conditions and thus two of the seven parameters from the table can be eliminated, leaving five to be determined by means of two equations.
- We obtain six independent equations by using three independent sets of experimental data, i.e. experiments no. 1, 3 and 10 in Table 4-6, reporting the conversion of toluene and the yield of mono-fluorinated product plus the operation conditions. This is sufficient to determine the five unknown parameters.
- An iterative procedure had to be applied to fit the parameters to the experimental results: The FFMR process model was employed, estimated values for the unknown parameters were implemented (see Table 4-1 and Section 4.3.1) and the solution of the simulation

was compared to the experimental results. The parameters were changed in an appropriate manner and another simulation was conducted, etc.

- Switching towards a non-isothermal system further four unknowns were introduced, i.e. the activation energies of each reaction. To determine these additional parameters further two sets of experiments at different temperatures were required, i.e. experiments no. 4 and 5 in Table 4-6, and the previous step had to be repeated.

Table 4-5. Unknown parameters in isothermal system

Introduction	Unknown Variable	Unit
Henry constant H_c	H_c	$(J/cm^3)^{0.5}$
Kinetic rate constant	k_1, k_2, k_3, k_4	$m^3/kmol \cdot s$
Concentrations	c_{Tol}, c_{FTol}	$m^3/kmol \cdot s$

Table 4-6. Experimental data available about direct fluorination in a falling film reactor (Jähnisch et al., 2000)

ID	Temp.	Molar ratio θ	Liquid flow	Mol fraction $x_{F2,F}$	Mol fraction $x_{Tol,F}$	Conversion X	Yield Y	Selectivity S
	C	%	ml/h			%	%	%
1	-16	40	11.6	0.1	0.0524	30	11	37
2	-16	54	11.6	0.1	0.0524	38	14	37
3	-16	92.5	11.6	0.1	0.0524	50	20	40
4	-21	40	11.6	0.1	0.0524	23	12	52
5	-42	40	11.6	0.1	0.0524	15	5	33
6	-15	40	19.6	0.1	0.0524	29	13	45
7	-15	20	19.6	0.1	0.0524	15	8	53
8	-15	20	19.6	0.1	0.0524	14	8	57
9	-16	40	19.6	0.1	0.0909	37	15	40
10	-16	100	19.6	0.25	0.0909	62	19	31
11	-16	200	19.6	0.5	0.0909	76	28	37

4.4.3 Results

First, the quality of the experimental data used in this chapter is investigated. It is not possible to accomplish a statistic error analysis for the experimental data. Here, the inaccuracy is determined from experiment 7 and 8 with reference to Table 4-6, which were conducted at the same conditions, but the reported selectivity varies (Sel_7=53 % and Sel_8=57 %). According to this error the error bounds for all performance parameters, conversion, yield and selectivity was set to $err = \pm 2$ %.

Next, the quality of the process model is validated including the absorption and reaction kinetic parameters. The experimental results plus the error band and the model predictions of

the five experiments (1,3,4,5,10) used for the determination of the model parameters are illustrated in Figure 4-2 and Figure 4-3. Here, the definitions for the selectivity, yield and conversion are the same as used in Jähnisch et al. (2000). This comparison shows that it was possible to accurately match the experimental results with model predictions. The simulated conversion is very close to the experimental conversion (Figure 4-3), and the simulated yield matches experimental results within the error bounds (Figure 4-2). A technical reason for deviations between simulation and experiment is the over-determined nature of the equation system (under isothermal conditions six equations were used to determine five parameters). Also, the model has intrinsic errors due to parameter estimations and assumptions taken.

The value for the Henry-constant between fluorine in the form it is used here (see Eq. 4-3 and Table 4-4) at 257 K was found to be H_c=0.0123 kmol/bar. The Henry constant for pure toluene and acetonitrile solvent was set to: $H_{c,Tol}$=0.0026 kmol/bar and $H_{c,AcN}$=0.0123 kmol/bar, respectively. The estimate for the latter ($H_{c,AcN}$ =0.03 kmol/bar) based on solubility coefficients is significantly higher than the actual value that was empirically determined. Considering that a small error in the solubility coefficient can have great influence on the Henry constant this result is acceptable. Values for the solubility coefficients are illustrated in Table 4-7. Values for the reaction kinetic constants determined at T=257 K are illustrated in Table 4-8. The fitted values are within or nearly within the error band of the estimates of the reaction kinetic constants. To take the temperature variations of the chemical kinetics into account the pre-exponential factor and the activation energy were determined for each reaction, see Table 4-9

Table 4-7. Hildebrand correlation parameters at T=257K

Parameter	Fitted value	Estimate	Unit
H_c	0.012	0.03	$kmol \cdot m^{-3} \cdot bar^{-1}$
$\delta_{F2\text{-}Tol}$	-16.8	/	$(J/cm^3)^{0.5}$
$\delta_{F2\text{-}AcN}$	-11.8	8.7	$(J/cm^3)^{0.5}$

Table 4-8. Reaction kinetic constants at T=257 K

Parameter	Fitted value	Estimate	Unit
k_1	$10.85 \cdot 10^3$	/	$m^3 \cdot kmol^{-1} \cdot s^{-1}$
k_2	$4.20 \cdot 10^3$	$14 \cdot 10^3 \pm 7 \cdot 10^3$	$m^3 \cdot kmol^{-1} \cdot s^{-1}$
k_3	$38.6 \cdot 10^3$	$70 \cdot 10^3 \pm 35 \cdot 10^3$	$m^3 \cdot kmol^{-1} \cdot s^{-1}$
k_4	$20.6 \cdot 10^3$	$70 \cdot 10^3 \pm 35 \cdot 10^3$	$m^3 \cdot kmol^{-1} \cdot s^{-1}$

Table 4-9. Reaction kinetic constants at T=257 K

Parameter	Value	Unit
$k_{0,1}$	$3.69 \cdot 10^{12}$	$m^3 \cdot kmol^{-1} \cdot s^{-1}$
$k_{0,2}$	$1.84 \cdot 10^{19}$	$m^3 \cdot kmol^{-1} \cdot s^{-1}$
$k_{0,3}$	$1.54 \cdot 10^{5}$	$m^3 \cdot kmol^{-1} \cdot s^{-1}$
$k_{0,4}$	$2.88 \cdot 10^{5}$	$m^3 \cdot kmol^{-1} \cdot s^{-1}$
$E_{A,1}$	42.0	kJ/mol
$E_{A,2}$	77.0	kJ/mol
$E_{A,3}$	4.3	kJ/mol
$E_{A,4}$	4.3	kJ/mol

Having determined these parameters the model is fully functioning. The quality of the process model was validated by comparing simulation results obtained with the FFMR model to experimental data, which have not been used for the determination of the model parameters, see Figure 4-4 and Figure 4-5. In general the predictions are in good agreement with the experimental data, with one major exception, which is experiment 11.

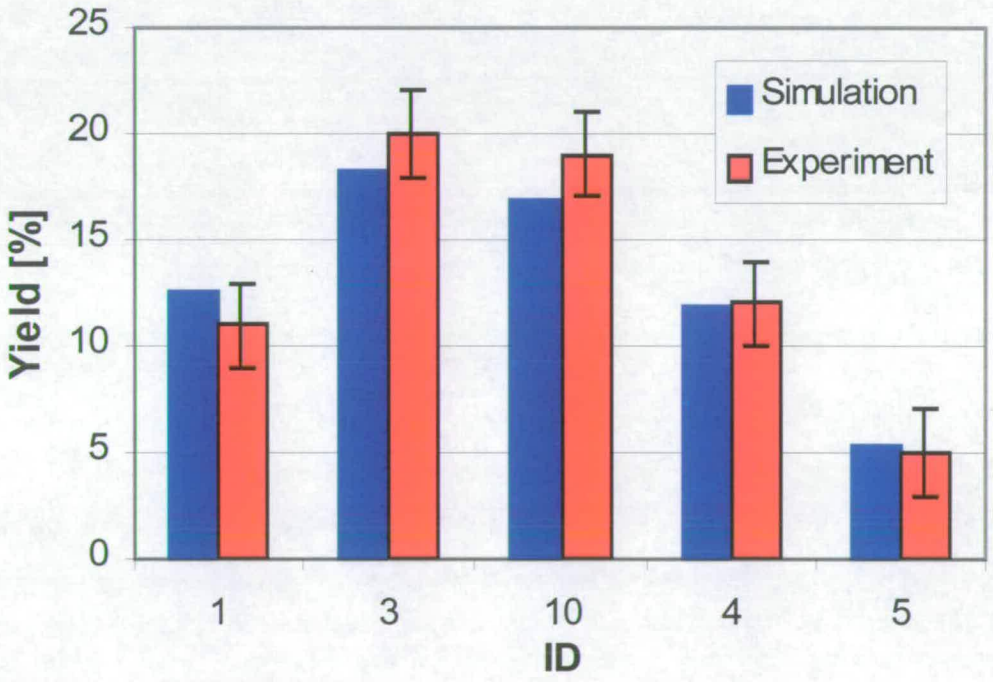

Figure 4-2. Comparison of the yield Y of desired product between the experimental data and simulations

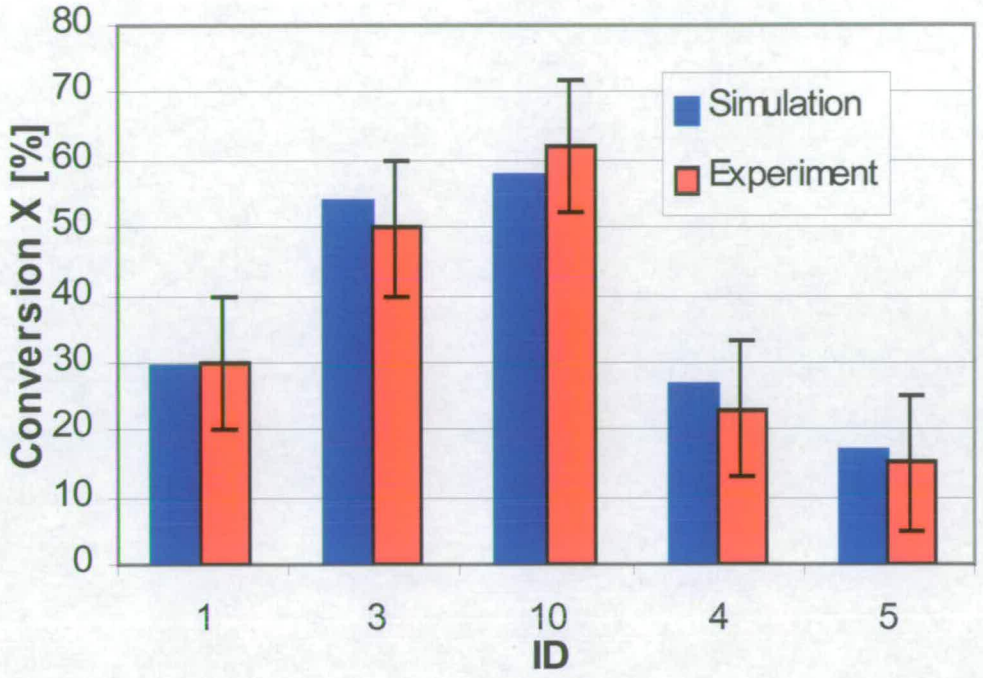

Figure 4-3. Comparison of the conversion X of toluene between the experimental data and simulations

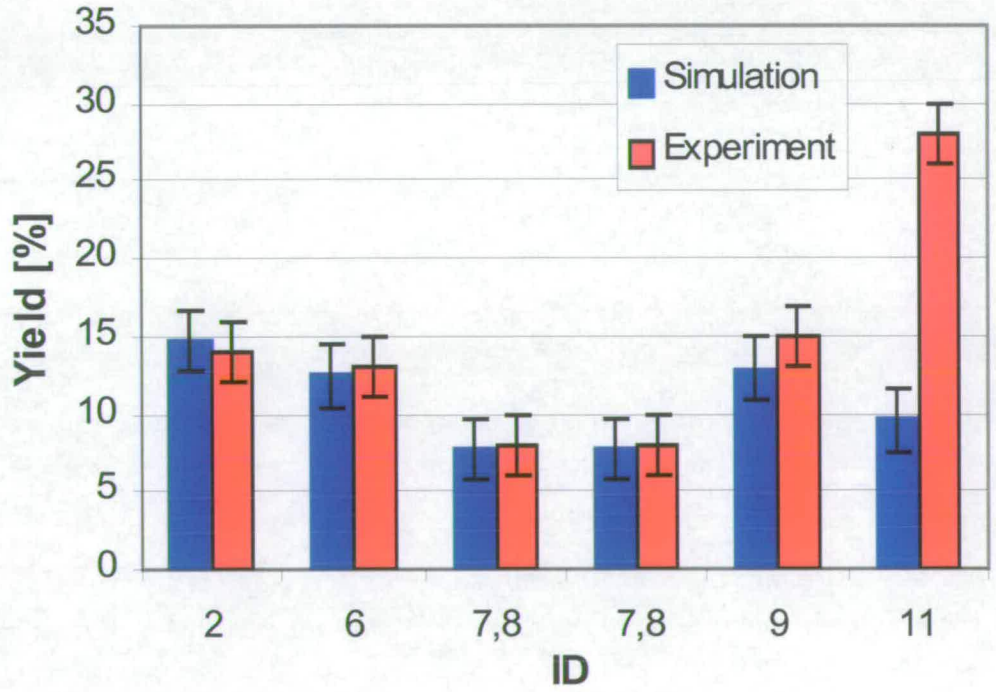

Figure 4-4. Comparison of the yield Y of desired product between the experimental data and simulations

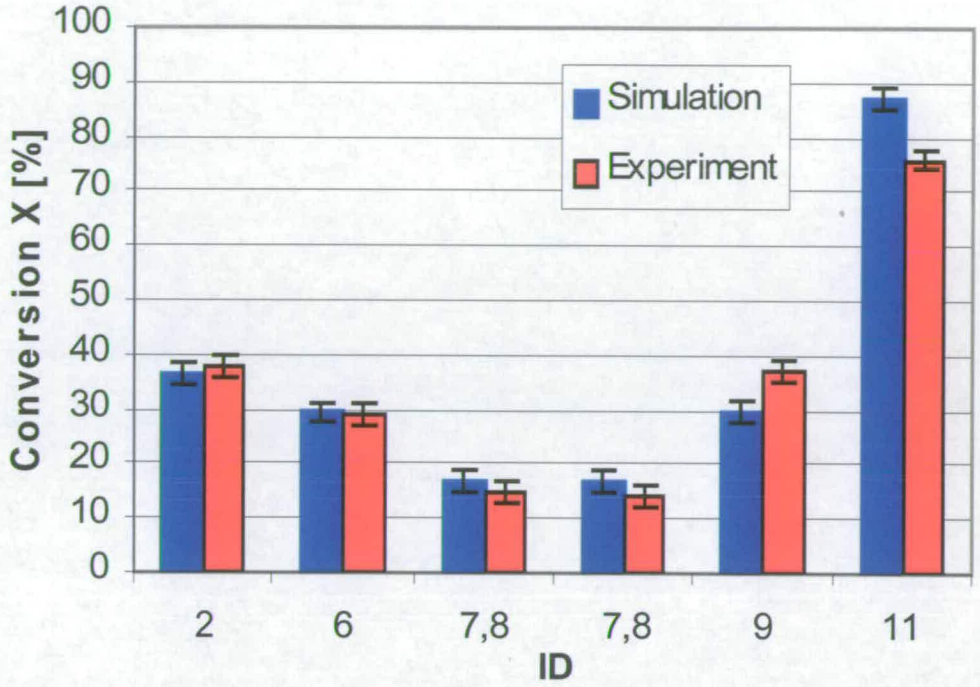

Figure 4-5. Comparison of the conversion X of toluene between the experimental data and simulations

4.4.4 Discussion

The experimental data used for parameter fitting was not intended for this purpose, there are only few data sets available and these results are afflicted by inaccuracy. Also, the model is based on a simplified reaction mechanism (see Appendix), which might have influenced the determination of the reaction kinetic parameters and the Henry constant used in this work. Furthermore, the reactor performance predictions were obtained assuming a plug flow profile, which causes inaccuracy of up to 2.7% with respect to conversion, yield and selectivity (see Section 5.2). All these facts potentially influence the quality of the model predictions.

However, the validation of the model showed that the overall performance of the reactor model fits the experimental results relatively well. Merely, experimental data point 11, at increased concentration of fluorine, cannot be matched by the simulations. Here, the selectivity is very high at high conversions, which could be explained with a change in reaction order through an increased influence of the recombination of fluorine termination reaction (reaction k_{t2} in Scheme B-1, see Appendix B). Another possibility would be a catalytic effect, perhaps stemming from products or intermediates, turning fluorine into an

electrophile thus supporting the electrophilic reaction. Furthermore, surface tension effects are not included in the model, which might have an impact on the mass and heat transfer processes in the FFMR. The surface tension is a function of the composition and the temperature. Process conditions, which result in high temperature and/or concentration gradients in the reaction plane, are most likely to be influenced by surface tension.

4.5 Summary

The process model is completed with regard to the reaction kinetics and the gas absorption. Values for parameters describing the reaction kinetic and the absorption of fluorine within the FFMR process model are estimated. These estimates have a relative error of up to $err_{rel} = \pm 100\%$. Therefore, to improve the accuracy of these values the model for the FFMR is fitted to experimental data. The experimental data is not very plentiful and afflicted with an absolute error of approximately ±2%. With this procedure values are found for the model parameters, which are within or nearly within the error bounds of the estimates. In this manner the accuracy of the model parameters is improved significantly, but some inaccuracy remains, which is hard to quantify. The absolute error of the yield, selectivity and conversion predictions obtained with the model is at least $err = \pm 2\%$ since this is the inaccuracy of the experimental data. For the validation of the completed model experimental data is employed which was not previously used for parameter fitting. The validation proves the applicability and accuracy of the model for the range of operational conditions it is designed with. Extrapolation, for example towards very high reactant concentrations, cannot be recommended because high errors can occur.

The values found with the FFMR model for the reaction kinetic parameters and the Henry constant are adopted for the use with the CMMR model. Furthermore a catalyst activity coefficient κ is introduced taking into account all effects connected to the heterogeneously catalysed reaction. Assumptions going along with this process are shown in Section 4.2.3 (concerning heterogeneous catalysis) and Section 3.4.3 (about transport process within the membrane). Note, that the membrane model does not allow detailed insight in the functionality of the membrane or membrane deactivation.

Chapter 5

Simulation preliminaries

5.1 Introduction

This chapter discusses preparations for the simulation of the direct fluorination of toluene process. Appropriate performance parameters are introduced that are used to evaluate the performance of the reactor configurations during simulations.

Thereafter the model descriptions for the FFMR and CMMR are used to analyse the direct fluorination of toluene and develop an understanding of the process. Using this approach, the most influential operational parameters and reactor design features are sought. Finally, in a simulation study flow hydrodynamics are investigated in the gas and liquid channel of the CMMR and FFMR. The objective is to visualise the flow characteristics and their influence on the performance of the process. This information is used to simplify the model for further simulation studies and to estimate the error that goes along with this procedure.

5.2 Performance parameters

In a chemical process the selectivity with respect to the desired product as well as reactant recovery and recycle determine the economics of the plant operation. In general, if the key reactant can be recovered and recycled to the reactor section, the selectivity, which is based on the converted amount of this reactant, is the key factor. On the other hand if the reactant cannot be recovered and is wasted during the operation, then the yield, which is based on the amount of this compound in the feed, is the economic key factor.

Considering the direct fluorination of toluene in the CMMR configuration fluorine is easily recovered, no costly separation step is necessary, and it can be recycled to the reactor feed. The reaction products accumulate in the liquid phase, also containing reactant toluene. Thus,

the recovery of toluene depends on the separation technology and effectiveness, which makes toluene the key component.

There is no easy way to determine the key performance parameter unless an economic evaluation of the entire process is performed. The separation of toluene from mono-fluorinated toluene may be very expensive which would make the yield with respect to toluene the key economic parameter. Also, fabrication and operation of large micro-channel arrays may be undesired; then a high output per channel would be interesting. The selectivity with respect to the desired product is an important parameter, too.

Selectivity S, yield Y and conversion X are defined as follows:

$$S = \frac{F_{FTol}}{F_{Tol,F} - F_{Tol}}$$
$$Y = \frac{F_{FTol}}{F_{Tol,F}} \qquad (5\text{-}1)$$
$$X = \frac{F_{Tol,F} - F_{Tol}}{F_{Tol,F}}$$

where $F_{Tol,F}$ is the molar flow rate of toluene in the feed, F_{Tol} is the molar flow rate of toluene at the reactor exit; and F_{FTol} is the molar flow rate of mono-fluorinated products (ortho, meta, para) at the reactor exit. All performance parameters are based on the key-compound toluene. The underlying series-parallel reaction system with regards to the key component, toluene, is illustrated in Scheme 5-1.

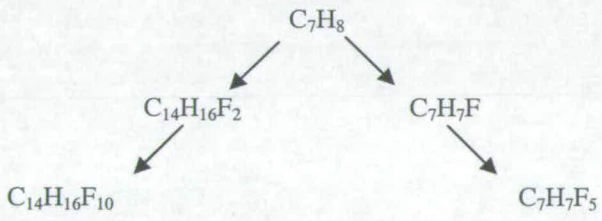

Scheme 5-1. Series-parallel reaction with regard to reactant toluene

5.3 Reaction conditions and reaction kinetic analysis

5.3.1 Reactor configuration and reactant feed

In this section two important non-dimensional numbers are introduced. These dimensionless quantities are used to understand more about the influence of the reactor layout and operating conditions on the achievable conversion X and selectivity S of the process:

- The differential selectivity of mono-fluorinated toluene with respect to the conversion of toluene is defined in Eq. (5-2). The integration of this quantity over the entire reaction plane results in the selectivity S.

$$dS = \frac{\text{net production of } C_7H_7F}{\text{series-parallel reaction to undesired product}}$$

$$= \frac{r_1 - r_3}{r_2 + r_4} = \frac{k_1 c_{F_2} c_{C_7H_8} - k_3 c_{F2} c_{C_7H_7F}}{k_2 c_{F_2} c_{C_7H_8} + k_4 c_{F2} c_{C_{14}H_{16}F_2}} \tag{5-2}$$

$$= \frac{k_1 c_{C_7H_8} - k_3 c_{C_7H_7F}}{k_2 c_{C_7H_8} + k_4 c_{C_{14}H_{16}F_2}}$$

Following Eq. (5-2) the following settings should enhance the differential selectivity:

1) High concentration of toluene
2) Low concentration of mono-fluorinated toluene
3) Concentration of fluorine inconsiderable

- The dimensionless residence time Λ (see also Section 3.3.4) is an indicator for the achievable conversion of toluene:

$$\Lambda = \frac{\textit{initial absorption flux of fluorine}}{\textit{feed flux of toluene}}$$

$$\Lambda = \frac{k_g \cdot H_c \cdot p \cdot x_{F_2,F} \cdot cl}{\overline{v}_l \cdot c_{C_7H_8,F} \cdot ch} \tag{3-6}$$

The achievable conversion increases with rising Λ and therefore the following setting for concentrations are desirable:

4) High concentration of fluorine in the reaction zone
5) Low liquid velocity and concentration of toluene in liquid phase
6) Flat reactor

The results found through the interpretation of the non-dimensional numbers illustrate the influence of key parameters on the process performance. Some of the findings need discussion because these quantities do not reflect the entire process in detail and conclusions may be incomplete. Contrary to what was suggested above the concentration of fluorine may have an influence on the selectivity S. This is, because all chemical reactions take place at the interface between the gas and liquid phase, within a narrow reaction zone. Here, transversal diffusion of the liquid phase components, including toluene and mono-fluorinated toluene, influences the occurrence of series and parallel reactions. In this connection the local

concentration of fluorine in the liquid phase probably does influence the selectivity because the overall local rate of reaction is controlled by fluorine absorption.

A flat reactor, i.e. a reactor at a low aspect ratio ch_l/cw, is beneficial for high conversions because the reaction zone is relatively large per cross-section. However, there is a physical limit to the liquid thickness in an open channel (with the FFMR) and the pressure drop is increasing with decreasing aspect ratio.

5.3.2 Reaction kinetics and temperature

The fluid temperature inside the reactor influences several process parameters, e.g physical property data and diffusivities. Within the temperature range considered, among all model parameters the reaction kinetic constants show strongest variations with temperature. The reaction kinetic constants of the four reactions involved are displayed in Figure 5-1 as a function of the temperature. High ratios r_1/r_2 and r_2/r_3 are beneficial to the differential selectivity dS. At high temperatures (T>270K) the unselective radical fluorination of toluene r_2 dominates due to relatively high dissociation of fluorine. At low temperatures the radical chain propagation reactions towards higher fluorinated compounds (r_3+r_4) is very strong compared to the electrophilic reaction r_1. Thus, we expect the optimum process temperature of operation to be an intermediate temperature.

In Figure 5-2 the selectivity towards mono-fluorinated-toluene is plotted versus the temperature and as a function of the solid catalyst activity κ. The pertaining operational parameters are listed in Table 5-1. The selectivity has a maximum towards mono-fluorinated toluene at an intermediate temperature. The solid acid catalyst supports the electrophilic reaction and in this manner the maximum selectivity is shifted towards higher values that occur at higher temperatures.

Table 5-1. Operational parameters

Description	Variable	Value	Unit
Liquid phase velocity		$\overline{v}_l$=0.00284	m/s
Toluene feed concentration	$x_{Tol,F}$	0.0524	kmol/m^3
Fluorine feed concentration	$x_{F2,g,F}$	0.1	/
Molar ratio f fluorine and toluene feed	θ	1	/
Reactor geometry	ch, cw, x_f	0.0001, 0.0003, 0.065	m

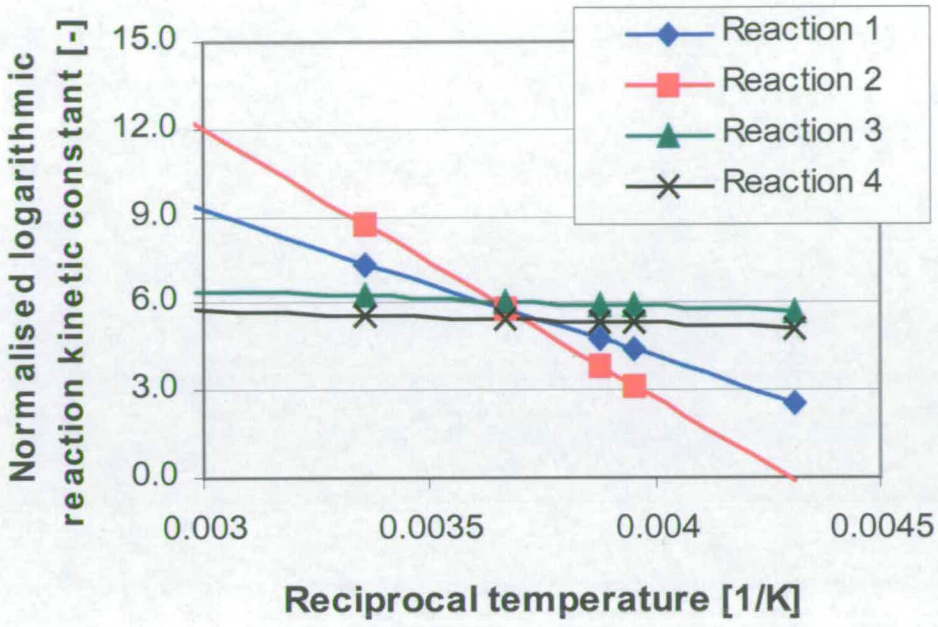

Figure 5-1. Temperature dependency of the reaction kinetic constants of the non-catalysed reaction system (see Scheme 1)

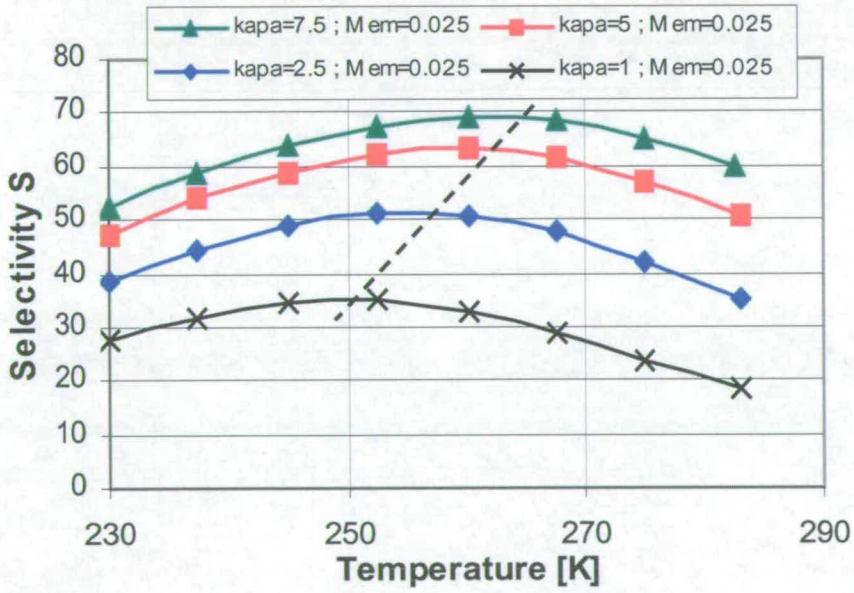

Figure 5-2. Selectivity as a function of the temperature and the catalyst activity κ

5.3.3 Membrane layout (CMMR only)

We found above that high concentrations of toluene and low concentrations of desired product in the reaction plane yield high selectivity. The membrane imposes a resistance on transversal diffusion, which influences the concentration distribution of the liquid phase compounds and thus the reaction system. The two parameters describing this resistance are the membrane porosity ε and the tortuosity τ.

The catalytic function of the membrane supports the electrophilic reaction. The efficiency of the catalyst is particularly important because it is likely to have a bigger impact on the selectivity S than any other parameter as it is influencing the reaction mechanism in a favourable fashion.

5.3.4 Summary: Reaction conditions

Investigating the non-dimensional performance parameters differential selectivity and non-dimensional residence time as well as the operational characteristics of the CMMR significant operational parameters with the direct fluorination of toluene were found to be:

1) Feed concentrations c_{Tol}, c_{F2} and reactant flux ratio ϕ
2) Liquid velocity v_l or residence time (distribution) t
3) Catalytic activity of the membrane κ
4) Membrane thickness, porosity and tortuosity
5) Operational temperature T_l
6) Channel height ch_l,

Furthermore, important operations occurring inside the reactor were identified which cannot be represented by a single parameter:

7) Fluorine absorption
8) Heat management

This list is the base for the upcoming simulation studies where the influence of these parameters and operations on the performance of the CMMR is quantified and compared to the FFMR. Standard values for operational parameters are illustrated in Table 5-2. Hydrodynamic issues, involved in point 2) and 7) are investigated in Section 5.4.

Table 5-2. Standard operational parameters

Description	Parameter	Value	unit
Feed concentration of fluorine	$x_{F2,F}$	0.1	/
Feed concentration of toluene	$x_{Tol,F}$	0.0524	/
Ratio of molar reaction feed	θ	1	/
Liquid phase bulk velocity	$\overline{v}_l$	0.00284	m/s
Liquid phase bulk velocity	$\overline{v}_g$	0.00284	m/s
Coolant temperature, feed temperature	T_c, $T_{l,F}$	257.15	K
Absolute pressure	p	1	bar
Channel height	ch_l	0.1	mm
Channel width	cw_l	0.3	mm
Reactor length	x_f	65	mm
Aspect ratio	a=ch/cw	0.33	/
Gas channel height, with FFMR: with CMMR:	ch_g	5 3.9	mm
Gas phase mass transfer coefficient	k_g	~0.85	m/s
With membrane			
Membrane tortuosity	τ	4	/
Membrane porosity	ε	0.7	/
Membrane height	mh	0.025	mm
Catalytic activity	κ	5	/

5.4 Process hydrodynamics

Rigorous modelling of fluid hydrodynamics is a very involving endeavour. However, on the microscale phenomena may influence the process that are negligible in large scale devices. Therefore, in this section the hydrodynamics of the bulk flow in the gas and liquid phase of the CMMR and the FFMR are investigated in detail. The objective is to understand the flow hydrodynamics inside the FFMR and CCMR and their influence on the performance parameters introduced above. Thereafter, these results are used to simplify the model with regard to the description of flow hydrodynamics for upcoming simulation studies and estimating the error that goes along with this procedure.

With the minimisation of the reaction channels parameters alternate that influence the momentum conservation equations. With increasing surface area per volume ratio the viscous forces build up and the ratio between inertia and viscous forces, i.e. the Reynolds number, decreases. In this manner flow turbulence is suppressed. We look at the hydrodynamic properties of the fluid flow in the microreactor configurations under consideration, namely

- Flow regime and Reynolds number (Section 5.4.1)
- Multiphase flow and mass transfer across the phase boundaries (Section 5.4.2)
- Developing gas flow (Section 5.4.2)
- Liquid phase flow and residence time distribution (Section 5.4.3)
- Hydrodynamic instability at the gas/liquid interface (Section 5.4.4)

5.4.1 Flow profiles and pressure drop

Modelling domain and procedure

In this section the mathematical model for the FFMR and CMMR introduced in Chapter 3 is used for the investigation of the hydrodynamics of the gas and the liquid bulk flow. The reactor is operated isothermally, thus the cooling channel and the heat conservation equation (Eq. 3-3) are removed from the original model. The numerical solver is based on a 3D finite element discretisation, which allows the calculation of second order spatial derivatives of the velocity vector comprised in the Navier-Stokes equations, and three-dimensional fluid flow can be simulated. The fluid flow obeys the no-slip boundary condition at the channel walls because rarefaction effects do not occur.

The momentum conservation equations are solved for the gas and liquid channel with the appropriate boundary conditions. Concerning fluid bulk flow the FFMR and the CMMR are distinguished by the boundary condition at the gas/liquid interface, only. The reactors are operated at standard conditions (see Table 5-3).

Results

With the CMMR we have effectively two separate channels and thus the flow in both compartments develops the typical parabolic velocity profile (where $u_l^* = u_g^* = 0$). The Reynolds number for the fluid flow in the liquid and gas phase is calculated and both flows are in the laminar viscous flow regime (Re<2300), see Table 5-3. The velocity plot (Figure 5-3) shows that the flow development region in the gas channel is very short. A full parabolic profile develops very quickly leaving a very short developing region near the reactor mouth. The liquid flow reaches the developed parabolic flow regime even earlier. The influence of the liquid phase developed flow profile is further investigated in Section 5.4.3.

With the FFMR the major difference compared to the CMMR lies in the fact that the momentum of the gas and liquid channel are coupled and thus the velocity profile in the gas channel cannot be determined without knowing the velocity of the liquid and gas phase. Furthermore, in the liquid channel a semi laminar profile develops with maximum speed at the gas/liquid interface $u_l^* = 1.5 \cdot \overline{u}_l$. Here, the velocity in the gas phase takes on the velocity of the liquid phase, which has consequences for the shape of the velocity profile and gas absorption, see Section 5.4.2. The zone of developing flow is very short in the gas channel of the FFMR, too.

For pressure drop considerations the pressure loss of the gas phase is considered because compression energy has to be provided to drive the gas flow, whereas the liquid may be accelerated by gravity (idea of falling film reactor). The pressure drop in the micro-channels is very low (approx. 0.10 Pa) even with the smallest channels and highest velocities used (see Appendix G.4). Thus, the energy costs for the compression is negligible and the total pressure loss is not a crucial parameter for the design of the reactor. However the pressure drop gains

importance when it comes to the supply of fluid to a parallel array of hundreds of micro-channels, which is not further discussed in this work.

Table 5-3. Reynolds numbers in the gas and liquid channel as a function of the bulk fluid velocity and standard conditions

	Gas channel (Ω=g)	Liquid channel (Ω=l)
Velocity $\bar{v}_\Omega$ [m/s]	Re_g	Re_l
0.002	1.39	0.342
0.004	2.79	0.683
0.008	5.58	1.367
0.016	11.15	2.733

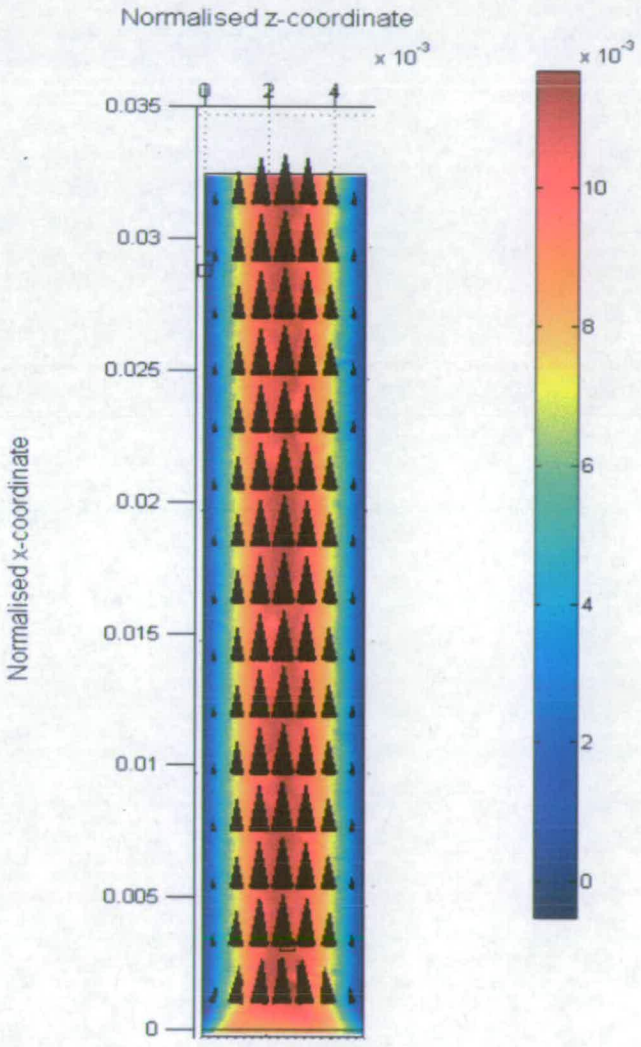

Figure 5-3. Velocity profile in the gas channel with the CMMR. The arrows and the colour code quantify the velocity vector, $[\vec{v}_g] = m/s$

5.4.2 Gas/liquid interface

Modelling domain and procedure

In this section, the mathematical model for the FFMR and CMMR introduced in Chapter 3 is used for the investigation of the hydrodynamics and mass transport in the gas phase. The goal is to develop a Reynolds-number correlation for the gas-phase mass transfer coefficient k_g. The gas channel is analysed separately from the remaining reactor, thus, merely the isothermal gas channel domain is considered with the Navier-Stokes and mass conservation equations. The operating conditions are illustrated in Table 5-4. The boundary conditions for the mass and momentum conservation equations are shown in Table 5-5, and Table 3-1 and 3-2 respectively.

In Appendix E absorption of a gaseous component into a thin film is introduced and the use of mass transfer coefficients is explained. An algorithm is illustrated for the calculation of mass transfer coefficients with gas absorption at smooth or quiescent liquid interfaces. In this connection criterions for the occurrence of smooth film are analysed. The gas phase mass transfer coefficient k_g depends on axial diffusion, the size of the reactor, and the flow pattern in the channel. Thus, mass transfer correlations are commonly developed using the dimensionless Sherwood number

$$Sh = \frac{k_g \cdot d_h}{D_{AB}} \tag{5-3}$$

in combination with Reynolds *Re* and Schmidt *Sc*. The diffusivity, channels size and flow mode are covered by *Sh* and *Re*. The Schmidt *Sc* number is composed of fluid property parameters. Within the scope of this work this effect is neglected and correlations are based on *Sh* and *Re*, only.

Here, the Sherwood number serves the same function as the Nusselt number *Nu* for heat-transfer correlations. Furthermore, the values for *Nu* are analogous to the once for *Sh* and may be used to calculate the mass-transfer coefficient k_g for mass transport at smooth or quiescent liquid interfaces. This is very useful because heat transfer phenomena are much better explored and reported in the literature.

In the previous section we found that there is a small region where the gas flow is developing. In this region the mass transfer coefficient is different from the one in developed flow further downstream. The latter is the most significant mass transfer coefficient applicable with the largest part of the reactor and therefore is the prime target in this investigation. The entrance region is considered in a separate section.

Table 5-4. Operational parameters in addition to the standard parameters (Table 5-2)

Description	Parameter	Value - FF	Value - Mem	Units
Feed fluorine concentration	$x_{F2,g,F}$	0.1	0.1	/
Liquid velocity at liquid channel top wall	u_l^*	0.00284·1.5	0	m/s
Gas channel height	ch_g	5	5	mm
Mean gas velocity	$\overline{v}_g$	0.002-0.04	0.008	m/s

Table 5-5. Boundary conditions of the mass conservation equations with the FFMR and the CMMR in the gas channel domain

Boundary description	Boundary conditions
Top wall	$\frac{dc_{F2}}{dz}=0$
Left wall	$\frac{dc_{F2}}{dz}=0$
Right wall	$\frac{dc_{F2}}{dz}=0$
Bottom wall	$c_{F2}=0$
Reactor entrance	$c_{F2}= c_{F2,F}$

Results: FFMR gas phase mass transport

As reported in Section 5.4.2, developed laminar flow in the liquid phase of the FFMR reactor has a semi laminar velocity profile. In the gas phase we get laminar flow and the velocity profile depends on the relative velocity $\overline{v}_{g,rel} = \overline{v}_g - u_l^*$ between liquid and gas flow:

- at relative velocities below zero we get an S-shaped profile (Figure 5-4)
- at relative velocities near zero we get a semi-parabolic profile (Figure 5-5)
- at high relative velocities we get a parabolic profile (Figure 5-6)

To produce correlations between *Sh* and *Re* we distinguish between relative velocity below and above zero. In Figure 5-7 the Sherwood number *Sh* is plotted versus the relative Reynolds number Re_{rel} at varying temperatures for relative velocities below zero. A correlated curve can be fitted to the data points with good accuracy:

$$Sh = 0.78 \cdot \mathrm{Re}_{rel}^{\,2} + 0.43 \cdot \mathrm{Re}_{rel} + 5.07 \qquad (5\text{-}4)$$

The mass transfer coefficient rises with increasing slope for decreasing gas phase velocities. The corresponding velocity profile takes on a semi-parabolic shape at relative velocities near zero (see Figure 5-4) and with decreasing relative velocity an S-shaped velocity profile

develops with zero velocity at the channel wall and the velocity of the liquid flow at the gas/liquid interface (see Figure 5-5).

In Figure 5-8 the Sherwood number *Sh* is plotted versus the relative Reynolds number Re_{rel} at varying temperatures for relative velocities larger than zero. The correlated curve matches the simulated data reasonably well:

$$Sh = 4.698 \cdot \mathrm{Re}_{rel}^{(-0.0276)} \tag{5-5}$$

Apparently, the influence of the temperature is not completely covered, though, using the two non-dimensionless numbers *Sh* and *Re*. We find that the velocity profile changes from a semi parabolic shape to a parabolic profile with increasing relative velocities starting at zero, as shown in Figure 5-6. We get decreasing Sherwood numbers *Sh* with rising gas phase Reynolds number but its value asymptotically approaches a limit value with increasing development of a parabolic flow profile. This value is the Sherwood number at fully developed laminar flow in a tube. We can use Nusselt number correlations to calculate this value, which were developed to describe heat transfer. The latter is well explored and reported by Shah and London (1978) at various aspect ratios, see Table 5-6. Here, the gas channel has an aspect ratio a=0.1724 and interpolating between the values given in Table 5-6 yields the corresponding Nusselt number and the desired Sherwood number has the same value *Sh*=4.024. At a fluid temperature of T=257 K and a reactor with certain hydraulic diameter d_h the mass transfer coefficient k_g can be calculated from this *Sh* number, see Table 5-7.

Table 5-6. Nusselt number at constant temperature boundary condition and rectangular channels with one active wall reported in Shah, London (1978)

Parameter	Values		
a [-]	0.3	0.2	0.1
Nu [-]	3.626	3.909	4.27

Table 5-7. Calculation of the gas phase mass transfer coefficient with standard conditions (see Table 5-3) and *Sh*=4.024

Parameter	$D_{F2,g}$	ch_g	cw_g	d_h	Sh	k_g
Unit	$m\ s^{-1}$	m	m	m	/	$m\ s^{-1}$
Value	$1.55 \cdot 10^{-5}$	0.005	0.029	0.008529	4.024	~0.0074

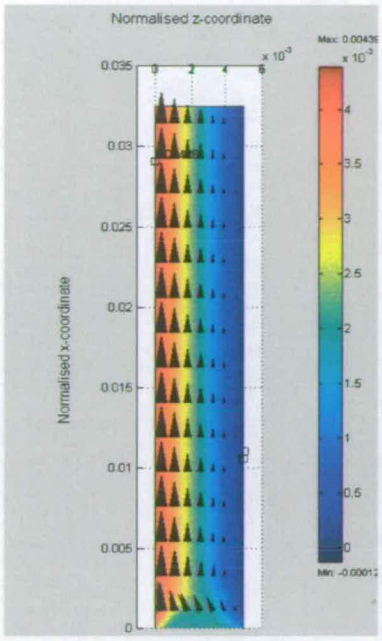

Figure 5-4. Velocity profile in the gas channel with the FFMR, $[\vec{v}_g] = m/s$. Negative relative velocity

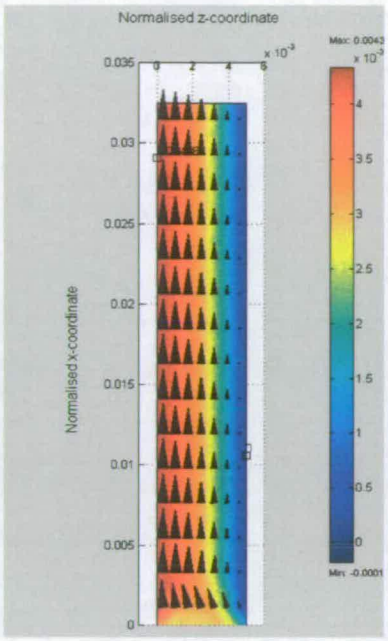

Figure 5-5. Velocity profile in the gas channel with the FFMR, $[\vec{v}_g] = m/s$. Zero relative velocity

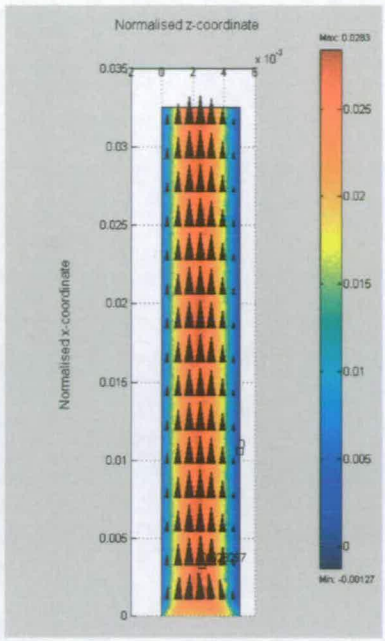

Figure 5-6. Velocity profile in the gas channel with the FFMR, $[\vec{v}_g] = m/s$. High relative velocity

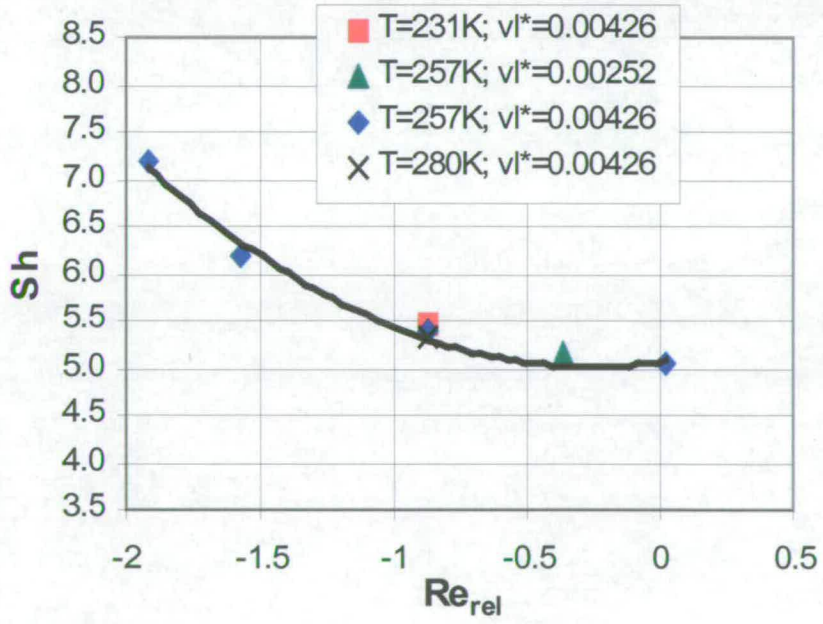

Figure 5-7. Sherwood number *Sh* versus relative Reynolds number $Re_{rel} < 0$

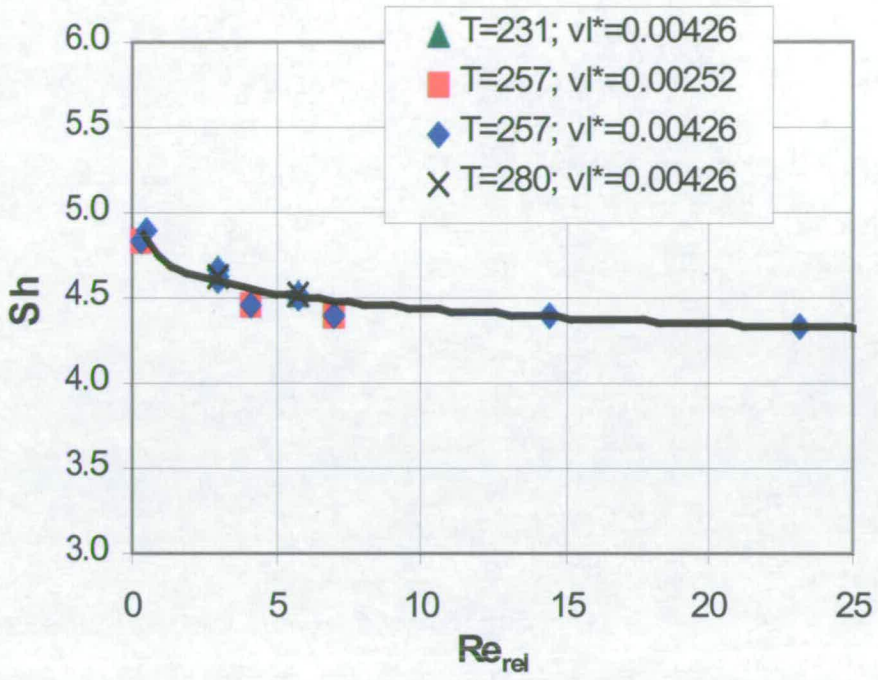

Figure 5-8. Sherwood number *Sh* versus relative Reynolds number $Re_{rel} > 0$

Results: CMMR gas phase mass transport

With the CMMR a membrane separates the gas and liquid channel and thus the momentum equations are decoupled. In this manner a parabolic flow profile develops in both channels with no-slip boundary conditions on the walls. Under these conditions *Sh* is independent of *Re* and the velocity in the gas channel. For rectangular channels Nusselt number correlations have been developed to determine heat transfer coefficients, see results of Shah and London (1978) displayed above. As already mentioned in previous paragraphs values for Nusselt numbers *Nu* are analogous to values for Sherwood numbers *Sh*. The result for a reactor with aspect ratio a=0.1724 is $Sh = Nu = 4.024$. This value for *Sh* and the corresponding k_g is the same as calculated for the FFMR at high relative gas velocities, see Table 5-7. Thus, mass transport from the gas bulk flow to the phase boundary with the CMMR is at the low limit of the range achievable with the FFMR. However, implementing a membrane separating the gas and liquid flow decouples the momentum flows of the gas and the liquid streams. Therewith, the size of the gas channel can be adjusted in a wide range with the CMMR potentially resulting in high velocities without compromising predictability and safety of the process. In this manner the absorption flux of fluorine can be influenced because it is a strong function of the hydraulic diameter of the gas channel. By definition the Sherwood number, Eq. (5-3), and and thus the mass transfer coefficient increases linearly with decreasing channel size and with increasing diffusivity. Note, that the diffusivity is a relatively strong function of the

temperature. High relative velocities between the gas and the liquid phase (Re_{rel} >25) inside the FFMR could result in the development of waves on the liquid surface leading to turbulent motion in the gas phase and temporally varying local conditions.

Results: CMMR gas phase mass transport with developing flow

In Figure 5-9 the local mass transfer coefficient is plotted versus the reactor x-coordinate. Near the reactor mouth k_g is elevated and levels off after about 5% (3mm) of the reactor length. This value can be reproduced using the standard equation for the calculation of the flow entrance length (see Appendix G.5). Even though the entrance length is very short, elevated values of k_g potentially may have a significant influence on the process because it is at the beginning of the reactor where the chemical reaction is strongest. However, an increase in k_g does not necessarily have a strong influence on the overall inter-phase mass transfer, which is shown in the next section.

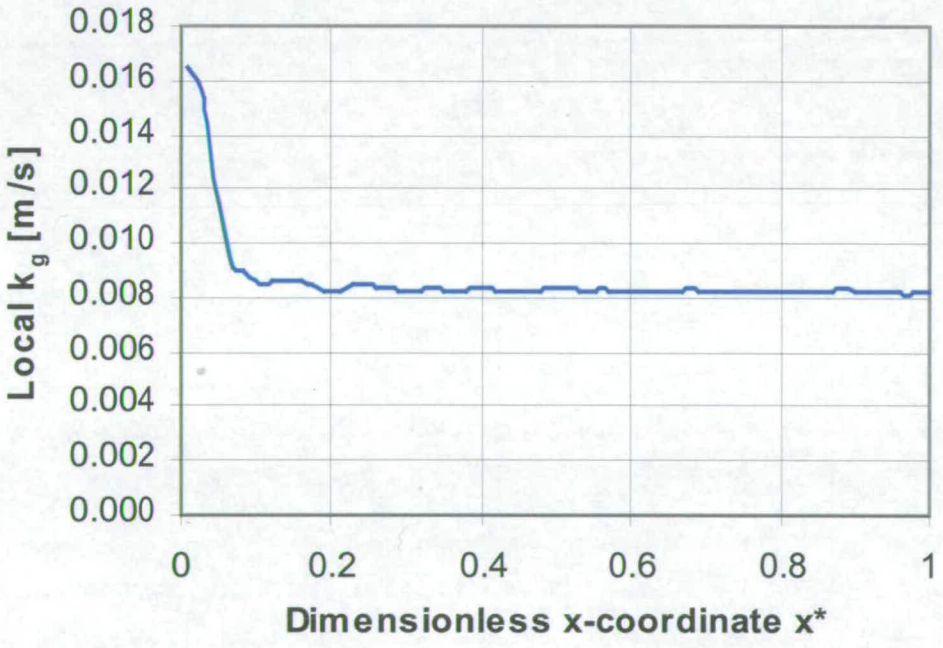

Figure 5-9. Mean mass transfer coefficient k_g in a cross-section along the dimensionless x-coordinate

Results: Multiphase mass transfer

So far we analysed gas phase mass transfer towards the liquid phase. We found that it is possible to improve the gas phase mass transfer coefficient, most notably, by increasing the temperature or decreasing the gas channel size depending on the reactor configuration. Furthermore, in the developing flow regime near the reactor entrance high values for k_g exist. But to what extend does such improvement influence the overall absorption rate of gas into the liquid phase? The overall mass transfer coefficient k_{total} is composed of the gas phase and the liquid phase mass transfer resistance:

$$k_{total} = \frac{1}{\frac{1}{k_g} H_c \frac{\overline{u}_{m,g}}{\overline{\rho}_g} + \frac{1}{k_l}} \tag{5-6}$$

where the mass flux across the boundary is given by:

$$\overline{N}^*_{F2} = k_{total} \left(\overline{x}_{F2,g} H_c - \overline{c}_{F2,l} \right) \tag{5-7}$$

The influence of the gas phase mass transfer coefficient k_g on the overall absorption process depends on its relative magnitude compared to k_l. The latter parameter is calculated from the reaction and diffusion kinetics and thus is a strong function of the temperature, see Eq. (E-9). As mentioned above, k_g can be calculated form the Sherwood Number according to Eq. (5-3). In Figure 5-10 k_{total} is plotted as a function of k_g with the temperature as an additional parameter. At low temperatures (T<=260 K) k_l is very small and rate limiting while k_g has few influence on k_{total}. With increasing temperature k_l rises and the influence of k_g on the overall absorption rate increases. Between T=260K and 290 K for example k_{total} triples when k_g increase from 0.01 to 0.1 m/s, however further increase has nearly no effect.

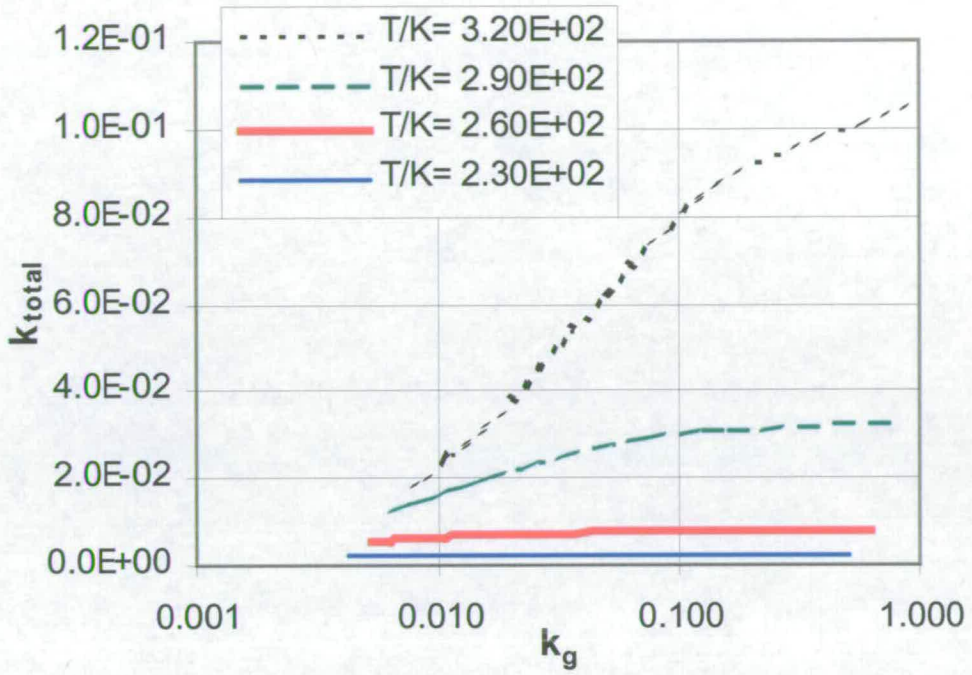

Figure 5-10. Overall mass transfer coefficient k_{total} vs k_g

5.4.3 Liquid phase flow

The liquid flow in the FFMR and CMMR has a characteristic laminar flow profile after a very short developing zone near the reactor mouth. This laminar liquid flow with its characteristic residence time distribution may have detrimental impact on the selectivity of the process under consideration (see also Appendix G.2). It is subject of this section to investigate the extent of this impact.

Modelling domain and procedure

The focus is on the liquid phase flow profile and we employ the 3D model with 2D finite element discretisation for the FFMR, as introduced in Chapter 3. Assuming that the influence of the left and right reactor walls on the flow profile are negligible the boundary conditions at these walls for the momentum equations were changed into slip-flow conditions. Thus, the liquid channel resembles a flat plate wetted with a liquid film, which is in contact with the gas-phase, see Figure 5-11. The Navier-Stokes equations were solved analytically for the flat plate arrangement. The resulting flow profile was implemented into the mass conservation equations and the momentum conservation equation was removed from the model. Three different profiles are investigated, see Table 5-8. These three profiles are the ideal plug flow, the semi-laminar and the laminar flow profile. The semi-laminar profile and the laminar

profile represent the flow profile in the liquid channel of the FFMR and the CMMR, respectively. Fluorine absorption is described by means of a constant mass transfer coefficient k_g facilitating comparable conditions. The reactor geometry is specified in Table 5-9 and the operation conditions are standard values as introduced in Table 5-3.

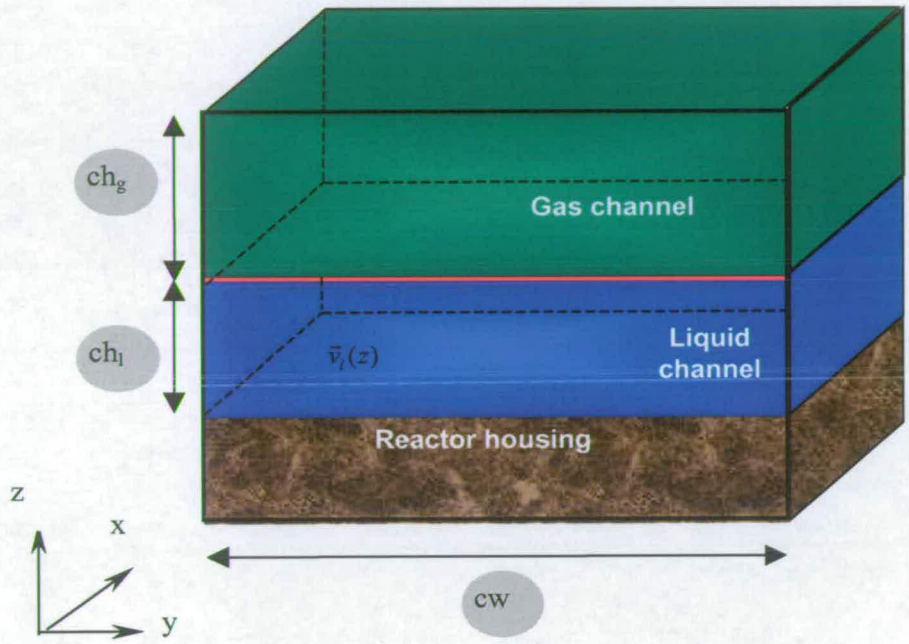

Figure 5-11. Scaled geometry of the 2D domain for discretisation of mass and heat transfer equations including boundary and sub-domain labels.

Table 5-8. Flow profiles implemented into the mass conservation equations

Velocity profile	Description	Remark
Plug flow	$\vec{v}_l = \overline{v}_{l,0}$	Idealised Plug flow
Semi parabolic profile	$\vec{v}_l(z) = 1.5 \cdot \overline{v}_{l,F}\left[1-\left(\frac{z^+}{ch_l}\right)^2\right]$	Flow profile of liquid film with FFMR
Full parabolic profile	$\vec{v}_l(z) = 6 \cdot \overline{v}_{l,F}\left[\left(\frac{z^+}{ch_l}\right)-\left(\frac{z^+}{ch_l}\right)^2\right]$	Flow profile in channel closed by membrane (CMMR)

Table 5-9. Reactor geometry parameters

Parameter	Value	Unit
cl	0.065	m
ch_l	0.0001	m
cw_l	Not specified	
mh	$mh \xrightarrow{\lim} 0$	m

Results: Semi-parabolic flow profile versus plug flow

The laminar flow profile (Poisseuille flow from the beginning) yields higher conversion of toluene X and higher selectivity S than plug flow, see Figure 5-12. With plug flow, initially, all molecules are spread evenly throughout a reactor cross-section. Considering a semi-laminar profile the concentration of liquid-phase reactant is highest near the reaction plane. Therefore, the latter arrangement results in faster diffusion of toluene to the reaction plane. A high concentration of toluene at the reaction plane results in high conversion of toluene and reduces the series reactions to higher fluorinated compounds. This effect is strengthened through steeper gradients of the concentrations of intermediate products pointing away from the reaction plane, initiated by high velocities in the liquid phase at the reaction plane. Therefore, not only does the conversion X benefit from a semi-parabolic profile but also the selectivity S increases.

Results: Parabolic flow profile versus plug flow

The full laminar flow profile (Poisseuille from the beginning) yields lower conversion of toluene X and lower selectivity with respect to the desired compounds S than plug flow, see Figure 5-13. The conversion is lower with laminar profile because liquid material is now concentrated in the middle of the channel removed from the reaction plane. Thus, we get essentially the opposite effect to what is said above in the section comparing the semi-laminar profile and plug flow. The concentration of toluene at the reaction plane is lower compared to plug flow, which has a detrimental influence on the selectivity. Also, the gradient of the intermediate products at the reaction plane is low due to the no-slip boundary condition and low velocity near the membrane.

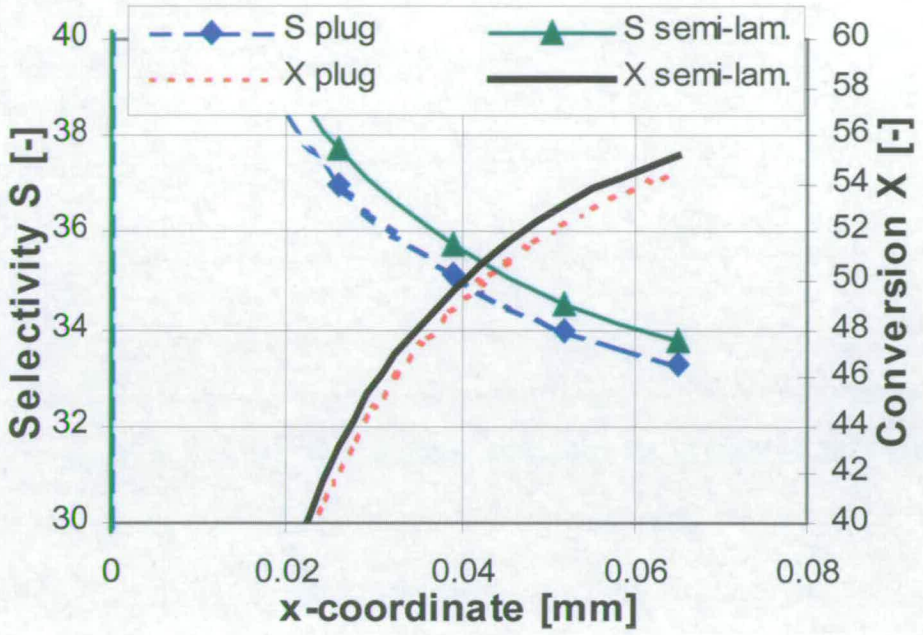

Figure 5-12. Selectivity and conversion with plug and semi-parabolic liquid phase flow profile.

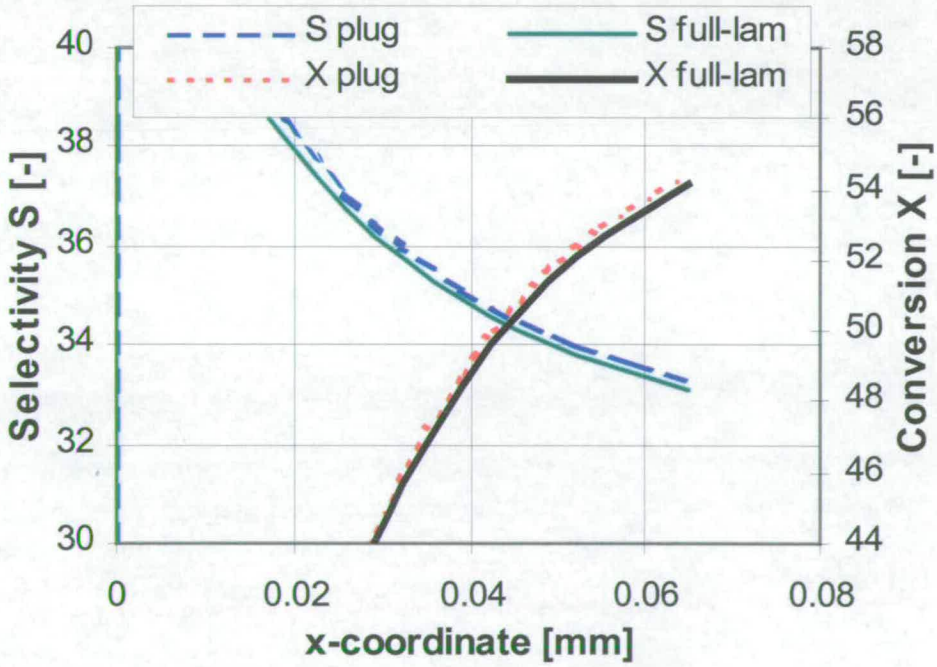

Figure 5-13. Selectivity and conversion with plug and parabolic liquid phase flow profile.

Discussion

In general, a laminar flow profile in the liquid channel influences the selectivity of the process and the conversion of the liquid phase compound. The results presented above show that a semi-parabolic and a full-parabolic profile have opposite effects with regard to ideal plug flow. While the previous results in improved performance compared to idealised plug flow, the latter has detrimental impact. The influence of the residence time distribution caused by the velocity profile cannot be deduced from the results presented above. The outcome of this investigation suggests that the transversal diffusion effects going along with the velocity profile exert stronger influence on the reactor performance than the residence time distribution.

However, the deviation of either laminar profile from the results achieved with plug flow, in terms of the mean relative error, is within a 2.7 % margin. This is the intrinsic error when approximating one of the laminar profiles with idealised plug flow.

5.4.4 Surface forces and hydrodynamic instabilities

The bulk flow in the liquid phase is described by means of the Navier-Stokes equations. However, secondary convective motion may occur due to the Raleigh Bernard effect (natural convection) and surface forces.

Raleigh Bernard convection is strong in situation where a fluid layer is heated from the bottom and cooled from the top. In this work, the reactors are arranged so that cooling is applied from the bottom while the heat of the chemical reaction is exerted at the top of the liquid layer. In general, this setting results in a stabilisation of the fluid.

With the FFMR the liquid surface is in direct contact with the gas phase. Here, surface tension forces occur at the interface, which may cause surface instabilities and convective motion (Marangoni convection) within the liquid phase. Inside the CMMR a membrane is implemented at the gas/liquid interface, which is suppressing secondary convection in the liquid phase. Thus, in the next section Marangoni convection in the FFMR is further investigated.

Marangoni convection with the FFMR

Temperature gradients in the surface of a liquid lead to unbalanced tensile forces, which results in a displacement of fluid into the cooler region (with higher surface tension). A similar effect occurs when concentration gradients exist in a two-component fluid, which have different surface tension. The tendency of a liquid to Marangoni convection can be

expressed through the Marangoni number, which is the balance of viscous drag and heat or mass diffusivities respectively:

$$Ma_{th} = \frac{\partial \bar{\sigma}_l}{\partial T_l} \frac{d_h \cdot \Delta T_l^*}{\bar{\eta}_l \cdot \bar{\alpha}_l} \tag{5-8}$$

$$Ma_{conc} = \frac{\partial \bar{\sigma}_l}{\partial c_{Tol}} \frac{d_h \cdot \Delta c_{Tol}^*}{\bar{\eta}_l \cdot D_{Tol,l}} \tag{5-9}$$

For the calculation of the solutal and thermal Marangoni number the surface tension gradients and thus temperature and concentration variations must be quantified for a physical system. In Figure 5-14 and Figure 5-15 the concentration of toluene and temperature in the reaction plane are shown with a standard FFMR and standard operating condition (illustrated in Table 5-2). The minimum and maximum values occur at the left and right edge of the interface and the differences between these extremes are used to calculate the Maragoni numbers, see Figure 5-10. Both Marangoni numbers are relatively high and the convective time scales are low compared to the diffusive time scale of the system (Eq. 5-10). Also, the convective time scales are much smaller than the residence time of the liquid in the reactor ($\tau > 20s$) and thus Marangoni convection potentially influences the liquid flow system (see Appendix G.1 for details).

$$\tau_{conv,th} = \frac{d_h \cdot \bar{\eta}_l}{\frac{\partial \bar{\sigma}_l}{\partial T_l} \Delta T_l^*} \quad ; \quad \tau_{conv,conc} = \frac{d_h \cdot \bar{\eta}_l}{\frac{\partial \bar{\sigma}_l}{\partial c_{Tol}} \Delta c_{Tol}^*}$$

$$\tau_{diff,th} = \frac{d_h^2}{\bar{\alpha}_l} \quad ; \quad \tau_{diff,conc} = \frac{d_h^2}{D_{Tol,l}} \tag{5-10}$$

The direction of the individual convective motion can be found by considering Figure 5-14 and Figure 5-15 knowing that the surface tension rises with decreasing temperature and concentration of toluene. We find that the solutal (anti-clockwise) and thermal Maragoni convection (clockwise) are opposed to each other and thus weaken the convective motion or lead to oscillations.

Table 5-10. Calculation of the thermal and solutal Marangoni numbers

Thermal Marangoni number			Solutal Marangoni number		
Parameter	Value	Unit	Parameter	Value	Unit
ΔT	3.2	K	Δc_B	0.02	kmol/m^3
$\Delta\bar{\sigma}_l = \frac{\partial\bar{\sigma}_l}{\partial T_l}\Delta T_l^*$	-0.4032	mN/m	$\Delta\bar{\sigma}_l = \frac{\partial\bar{\sigma}_l}{\partial c_{Tol}}\Delta c_{Tol}$	-0.020432	mN/m
Ma_{th}	809.67		Ma_{conc}	2955.41	
τ_{diff}	0.16	s	τ_{diff}	11.36	s
τ_{conv}	0.00020	s	τ_{conv}	0.0038	s

Discussion

The results illustrated above fulfil the necessary conditions for convective motion due to surface effects. Whether Marangoni convection occurs in the reactor can only be determined through an experimental investigation. The possible influence of Marangoni convection on the FFMR may be: 1) toluene is transported towards the reaction plane from the bulk and intermediate products are transported away from the reaction zone, 2) the absorption of fluorine might be influenced due to surface renewal through the convective motion. These are important mass transport processes with high influence on the overall reactor performance. More detail is given in the Appendix G.1.

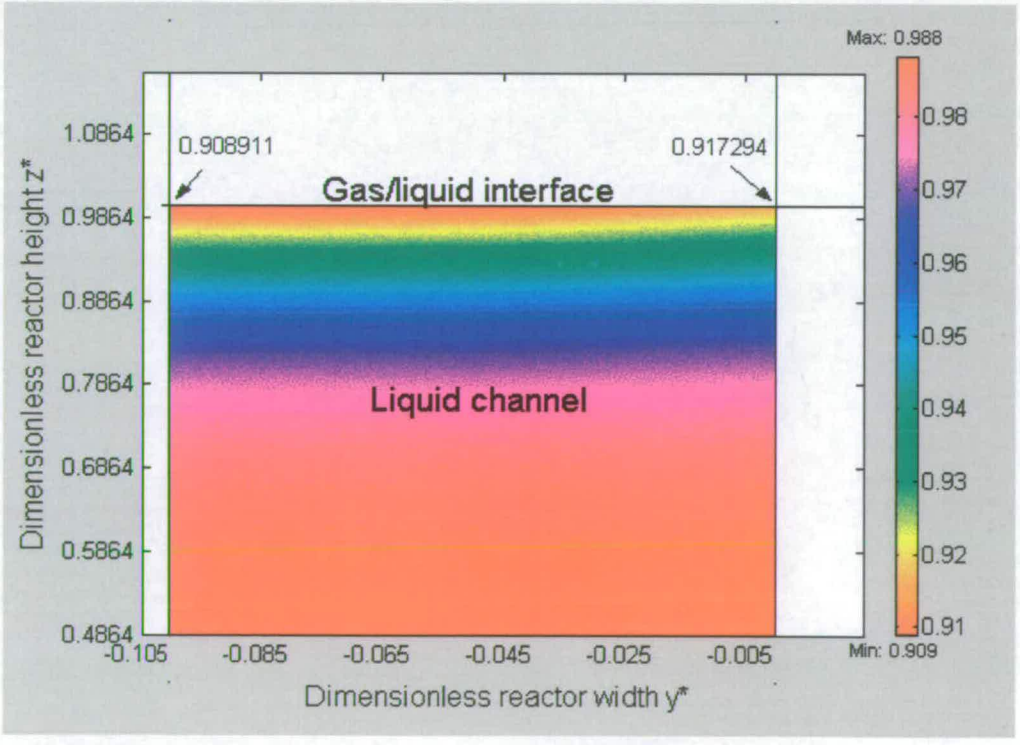

Figure 5-14. Concentration of toluene c_{Tol} in the liquid phase near the reactor entrance; [c_{Tol}]=kmol/m^3

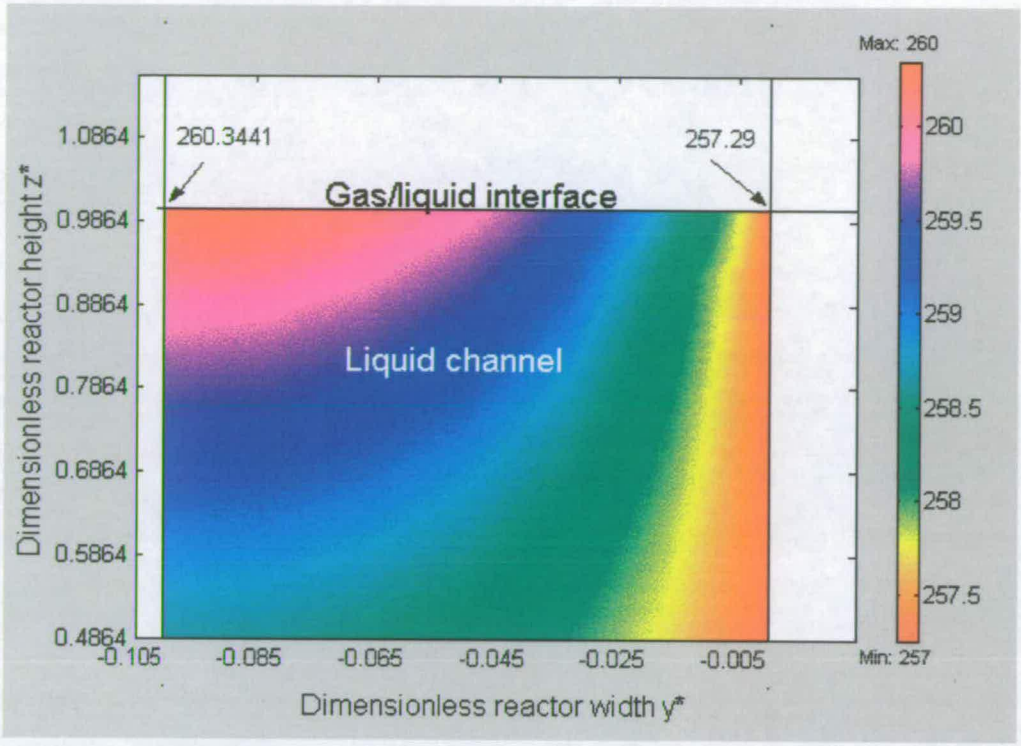

Figure 5-15. Temperature T_l in the liquid phase near the reactor entrance; $[T_l]$=K

5.4.5 Summary: Process hydrodynamics

In this section the hydrodynamics of the fluid flow in the gas and liquid phase were investigated in detail. It is shown that laminar flow exists in the liquid and gas phase. Different flow profiles develop in FFMR and CMMR channels due to the individual boundary conditions. In either case the flow-developing zone in the gas- and liquid phase is very short. The flow profiles in the fluid channels influence the absorption of fluorine. The gas phase mass transfer resistance is quantified using the Sherwood number *Sh*. A mass transfer correlation is created for the FFMR, which calculates *Sh* from the relative Reynolds number Re_{rel}. With the CMMR the Sherwood number is constant and does not depend on the fluid velocity. Implementing the Sherwood number correlation into the reactor models the mass transfer coefficient k_g can be calculated. Thus, the Navier-Stokes equations for the gas phase do not have to be solved anymore and the model introduced in Chapter 3 can be simplified where the gas channel is modelled as plug flow. In the following simulations the gas absorption is described using the mass transfer coefficient for developed flow, ignoring the entrance region. This can be justified because the entrance region is very short and the impact of an elevated k_g on the absorption of fluorine near the reactor entrance is not very strong (at standard operating conditions, T_l=260 K) due to liquid phase limitations.

Liquid phase flow hydrodynamics were considered to analyse the impact of the residence time distribution of the laminar flow regime on the reactor performance. It is found that the residence time distribution does not have a strong influence on the reaction. However, the flow profile influences the transversal diffusion of all liquid phase compounds. In this manner the performance of the CMMR and FFMR are perturbed in opposite orientation. In the remainder of this work the liquid phase flow is modelled as plug flow. Therewith the selectivity S as well as the conversion X are obstructed with relative error of about err_{rel} = -2.7 % with the FFMR and +2.7% with the CMMR. This error occurs when the liquid phase momentum conservation equations are omitted with isothermal process simulations.
Furthermore, surface instabilities could potentially influence the distribution of the liquid phase compounds with the FFMR. Preliminary investigations show that the necessary conditions for the occurrence of Marangoni convection are fulfilled. However, there are two opposing Marangoni related phenomena and the surface tension based driving force has to exceed a certain threshold value to set off a convective motion at all. In this work Marangoni effects are neglected to keep the model as simple as possible. However, the error going along with this assumption is not known exactly.

5.5 Chapter summary

In this chapter the overall production process was investigated to determine the key performance parameter for the CMMR and FFMR. However, this is not possible without knowing details about peripheral unit operations, i.e. separation steps and recycles. Therefore selectivity S and yield Y as well as product output per channel are further considered.
The most influential operational parameters and reactor design features were determined by analysing the process model. Further insight into the importance of feed concentration and concentration distribution in connection with membrane diffusion resistance and distributed feed as well as the influence of the reaction temperature is gained in Chapter 6. Heat management and the size of the reaction channel are discussed in detail in Chapter 7 and Chapter 8.
Flow hydrodynamics potentially influence the performance of the reactor configurations. However, modelling of fluid hydrodynamics in detail is a very involving endeavour. Within the scope of this work this can only be accomplished separately from mass and heat transfer simulation. Therefore, the influence of the following effects was investigated in a preliminary simulation study: laminar flow profile, residence time distribution, gas phase mass transfer resistance, and hydrodynamic instabilities. The resulting information is used to simplify the detail process model for upcoming simulation studies.

Chapter 6

Isothermal reactor analysis

6.1 Introduction

The most important operational parameters with regard to the performance of direct fluorination of toluene process were identified in Chapter 5. In this chapter a simulation study is conducted to analyse the sensitivity of the FFMR process with regard to these operational conditions. With the implementation of a membrane between the gas and the liquid phase additional parameters occur, which influence the operation of the reactor. The influence of these additional parameters on the performance of the CMMR is investigated in Section 6.3.

6.2 Operating conditions with the FFMR

6.2.1 Modelling domain and procedure

In this section mass transport in the liquid phase of the FFMR is investigated using the 3D mathematical model as introduced in Chapter 3. The reactor is operated isothermally, thus the cooling channel and the heat conservation equation (Eq. 3-3) are removed from the original model. The model does not contain momentum conservation equations and for the description of fluorine absorption a Sherwood number correlation is used (see Section 5.4). The numerical solver is based on a 2D finite element discretisation combined with a stepper routine.

In Section 5.3 parameters are discussed which influence the performance of the reactor. Here, feed conditions and reactor design parameters are investigated in terms of a sensitivity study. During this sensitivity study one of the first four parameters illustrated in Table 6-1 is varied while the others are fixed. For the illustration of the results of this investigation the selectivity S is plotted versus the conversion of toluene X, which is a measure of the residence time τ.

Table 6-1. Range of operational parameters

Description	Symbol	Value	Unit
Initial fluorine concentration	$x_{F2,g,F}$	0.06 – 0.25	/
Initial molar reactant ratio	θ	0.2-1	/
Initial toluene concentration	$x_{Tol,F}$	0.05 – 0.15	/
Feed temperature	$T_{l,F}$	232-273 K	K
Residence time	$\tau = \frac{x_f}{\overline{v}_{l,0}}$	τ=0-22.9 where $\overline{v}_l$=0.00163-0.00284 x_f=0-0.065	s m/s m

6.2.2 Results

In Figure 6-1 the influence of the temperature on the reactor performance is shown. The temperature has a very strong influence on the selectivity S. At very low residence time, and thus low conversion X, a very high selectivity S can be achieved at low temperatures. For conversions $X > 10$ % the situation is very different and the optimum selectivity exists at a medium temperature. This is because two phenomena occur simultaneously with increasing temperature:

a) The ratio between series reactions and initiation reactions $(r_3 + r_4) / (r_1 + r_2)$ decreases reducing production of highly fluorinated by-products.
b) The ratio of the parallel reactions r_2/r_1 is shifted towards higher values resulting in higher production of bi-fluorinated by-products.

At the chosen operating conditions the optimum temperature is T_c=252 K. A temperature increase of 20 K leads to a drop of the selectivity S. Interpolating the data points we find that even a 10 K temperature increase would lead to significant decrease of the selectivity.

The conversion increases with the temperature because the reaction kinetics of all reactions increase. This also improves the mass transfer coefficient of the liquid phase, which results in increased absorption of fluorine into the liquid phase and further increases conversion X.

Next, the initial concentration of toluene is the parameter under consideration. With increasing concentration of toluene the selectivity S increases, see Figure 6-2. The selectivity S benefits from high concentrations of toluene because the series reactions r_3 and r_4 are suppressed in favour of reactions r_1 and r_2, which is expressed through the differential selectivity towards products of the series reactions r_3 and r_4 in Figure 6-3. The concentration of toluene in acetonitrile influences the Henry constant, too. A high concentration results in decreasing Henry constant, and thus lower concentration of fluorine in the liquid phase $c_{F2,S}$. In this manner the selectivity is slightly improved because series reactions are limited.

In general, the conversion of toluene decreases with increasing concentration of toluene and a given residence time τ. This leads to higher amounts of unconverted reactant in the outflow.

At the same time the output flow rate of desired product increases significantly with rising concentration $c_{Tol,F}$ and constant molar reactant feed ratio $\theta = 0.4$, see Figure 6-5. This is due to the fact that the reactor volume is used more effectively.

The absorption of fluorine into the liquid phase depends on the concentration of fluorine in the gas phase. A high absorption is detrimental to the selectivity S at otherwise constant conditions, see Figure 6-6. Figure 6-6 illustrates the differential selectivity towards the by-products F_{10}-R and F_5-R versus the conversion of toluene up to $X = 30$ %. The plotted lines indicate the series reactions benefit from higher initial concentrations of fluorine in the gas phase. In this manner slightly higher conversion of toluene can be achieved on the cost of a low selectivity, which drops sharply near the reactor mouth with increasing concentration of fluorine.

The initial molar ratio of the reactants θ is investigated, next. Figure 6-7 shows a plot of the selectivity S versus the conversion X at varying θ. We find that θ has no influence on the trajectory of the plots near the reactor mouth. Further downstream, though, significant differences occur. With high values of θ the concentration of fluorine stays high throughout the reactor and high a conversion of toluene is achieved. However, in this manner series reaction r_4 is supported transforming desired product into waste. Thus, with rising initial ratio the conversion of toluene increases but the selectivity S drops especially with conversion of toluene higher than 40% due to series the reaction of the desired product. The highest selectivity S is achieved at low initial molar reactant ratio θ and highest conversion X at high θ.

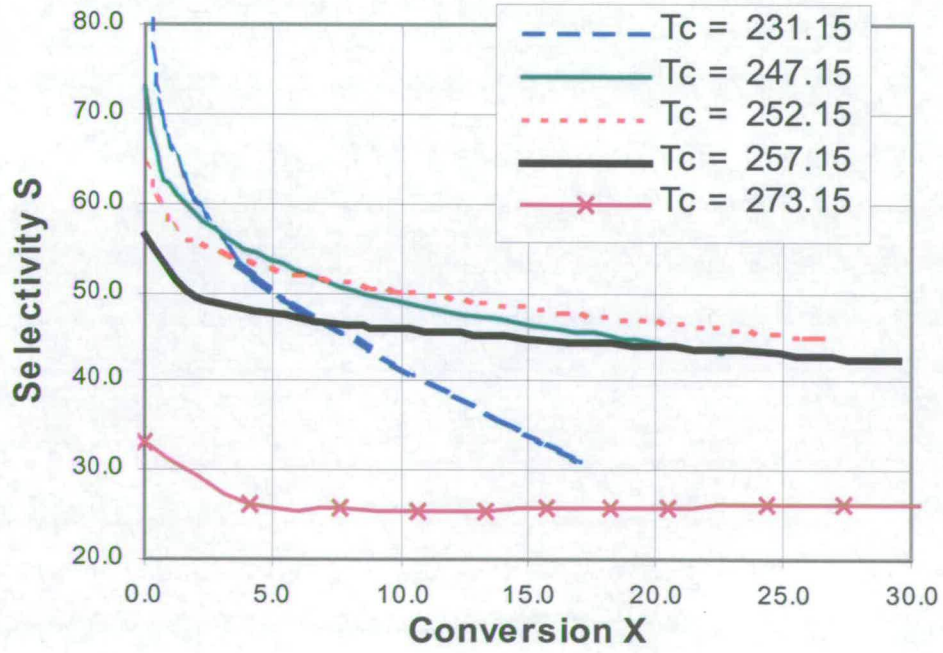

Figure 6-1. Influence of the temperature T_l on the reactor performance; θ=0.4, $x_{F2,F}$=0.1, $c_{Tol,F}$=0.991 kmol/m^3

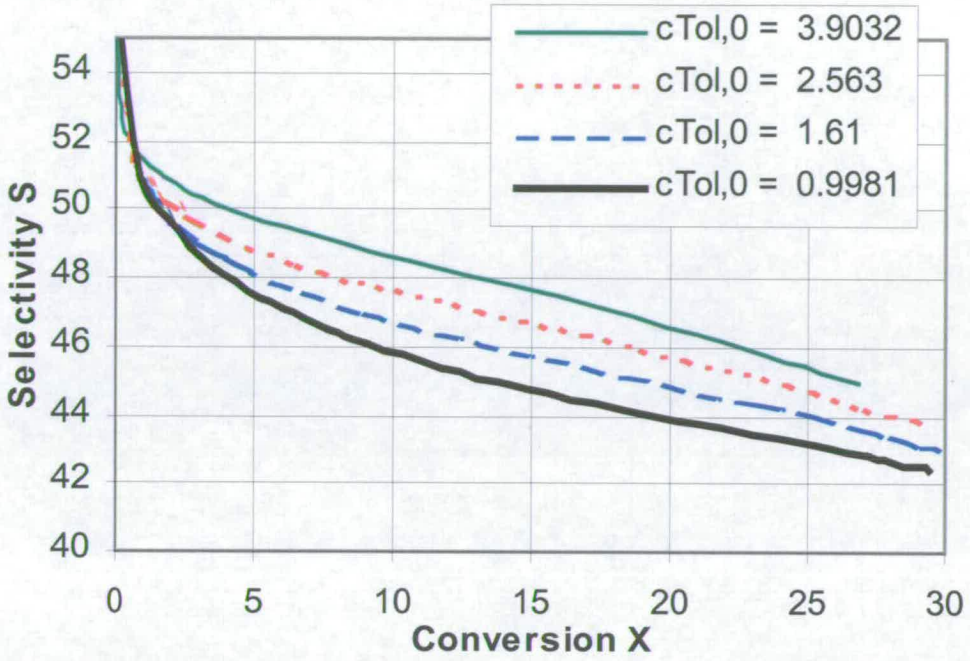

Figure 6-2. Influence of the toluene concentration $c_{Tol,F}$ on the selectivity S; θ=0.4, $x_{F2,F}$=0.1, T_c=257.15 K

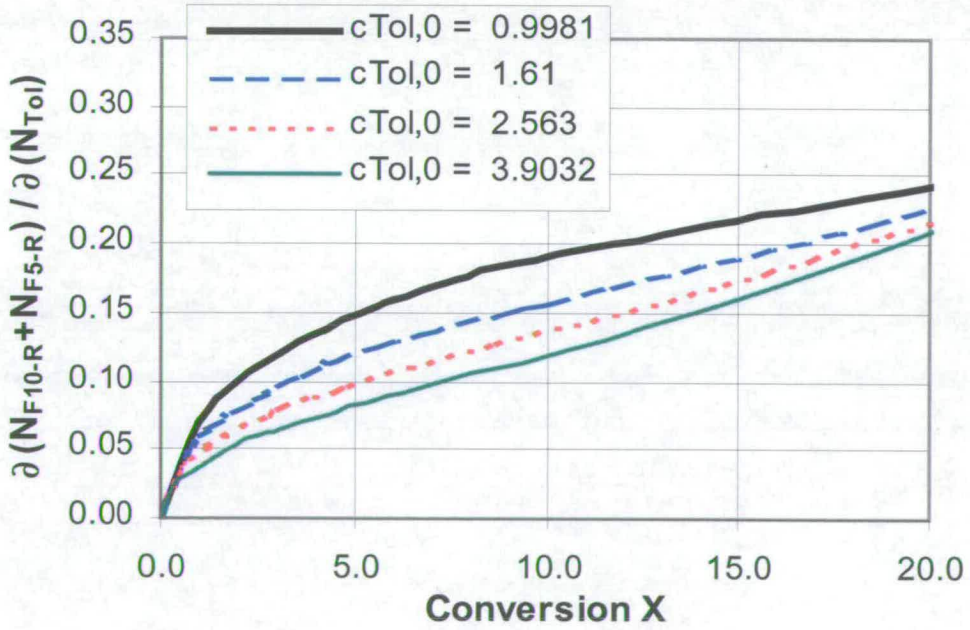

Figure 6-3. Influence of the toluene concentration $c_{Tol,F}$ on the differential selectivity towards by-products of the series reactions $F_{10}R$ and F_5R; θ=0.4, $x_{F2,F}$=0.1, T_c=257.15 K

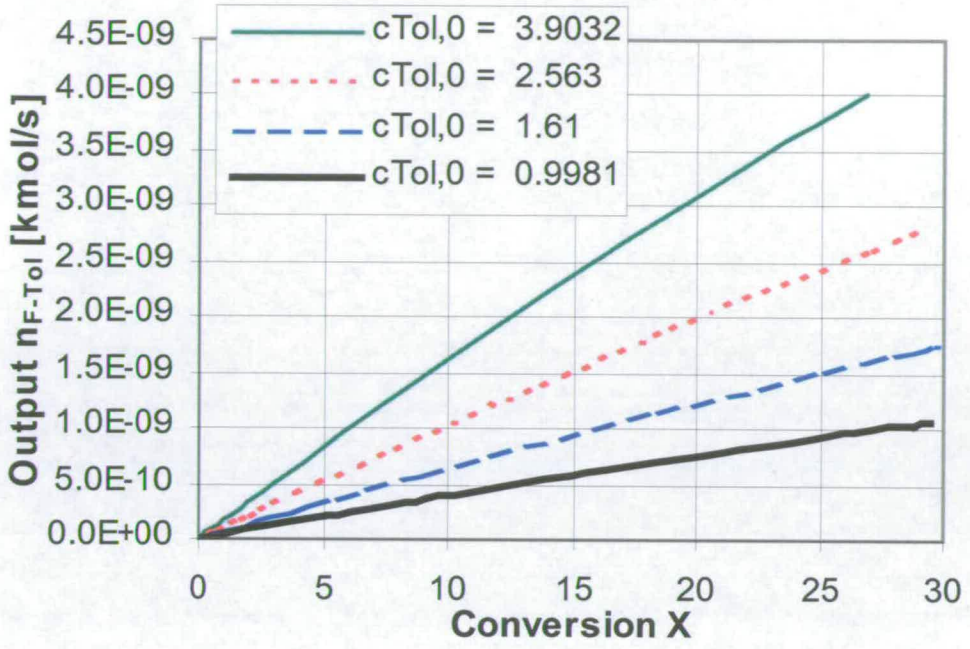

Figure 6-4. Influence of the toluene concentration $c_{Tol,0}$ on the output of *FTol*; θ=0.4, $x_{F2,0}$=0.1, T_c=257.15 K

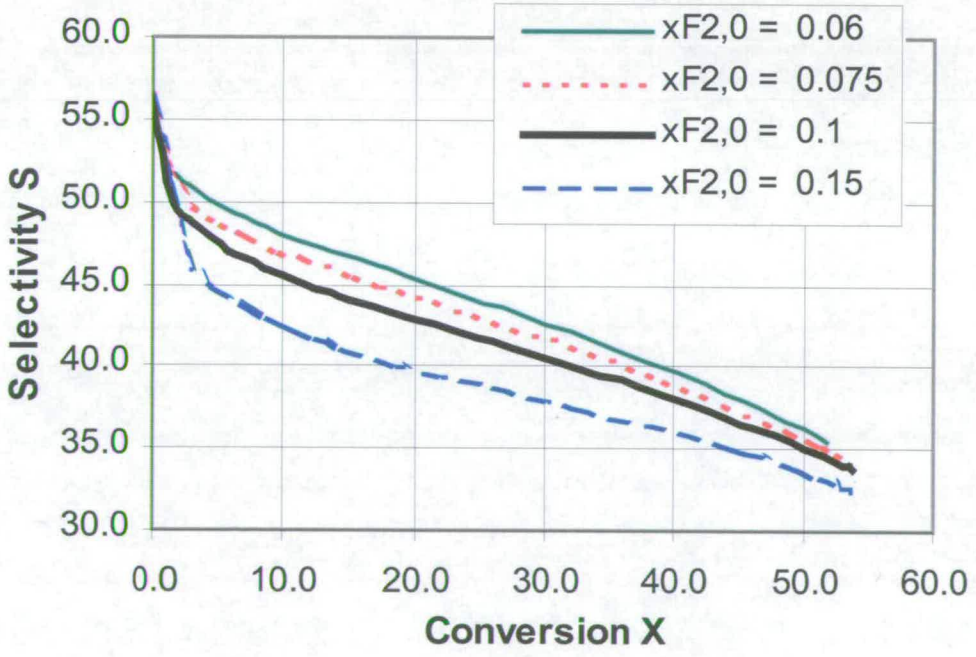

Figure 6-5. Influence of the fluorine concentration $x_{F2,F}$ on the reactor performance; θ=0.925, $c_{Tol,F}$=0.991 kmol/m^3, T_c=257.15 K

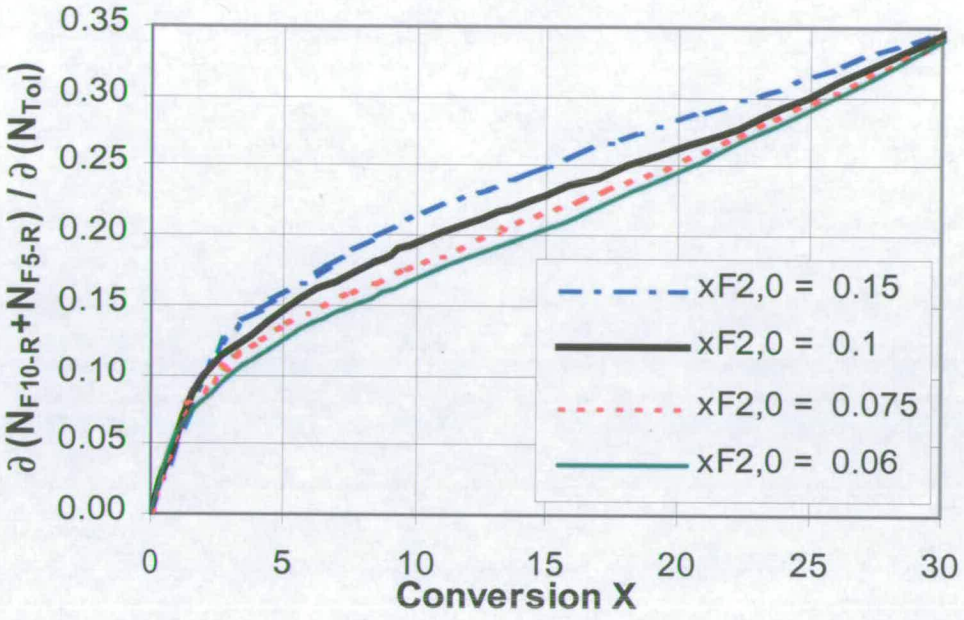

Figure 6-6. Influence of the fluorine concentration $x_{F2,F}$ on the differential selectivity towards products of the series reactions F_{10}-R and F_5-R; θ=0.925, $c_{Tol,F}$=0.991 kmol/m^3, T_c=257.15 K

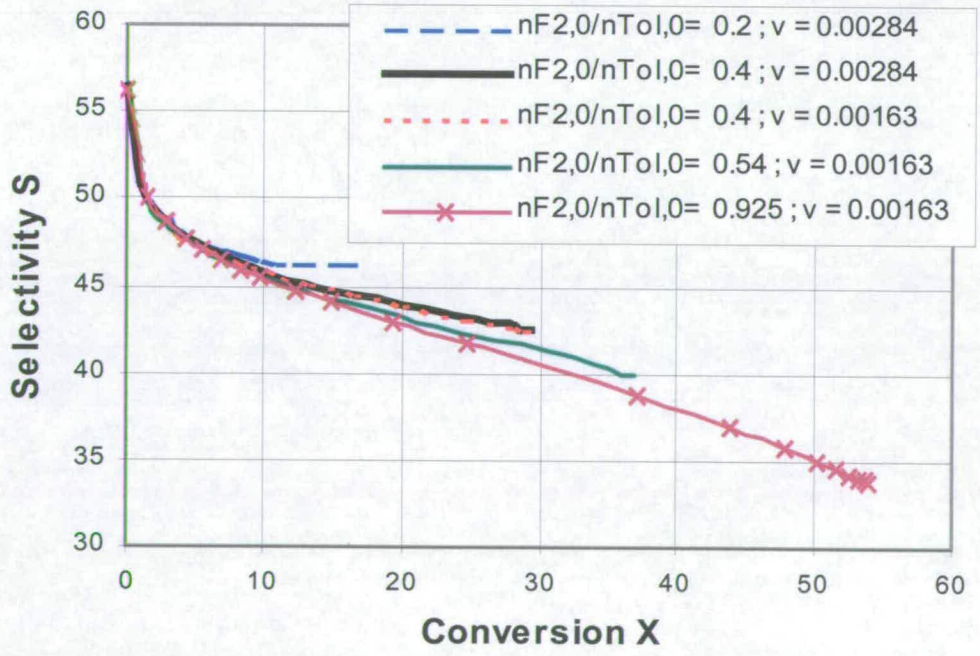

Figure 6-7. Influence of the reactant feed ratio $\theta(n_{F2,F}/n_{Tol,F})$ on the selectivity S; $x_{F2,F}$=0.1, $c_{Tol,F}$=0.991 kmol/m^3, T_c=257.15 K

6.2.3 Discussion

The temperature is the most important variable in this analysis and it has strong influence on the selectivity S of the process. Extreme temperatures to either end of the range yield low selectivity S. Best results are obtained at an intermediate temperature. Therefore tight temperature control and heat removal from the reaction plane are further investigated in Chapter 7.

The setting of initial reactant concentrations influences the reactor performance. These parameters show opposite influence on the selectivity S and the conversion X. Furthermore, the parameters investigated in this section are strongly linked and therefore a comprehensive sensitivity study would involve the solution of a complex multivariable optimisation problem. This approach is not followed in this work, because there are further parameters that are expected to have stronger influence on the reaction process.

Approximated values for high conversion X and high selectivity S respectively are given in Table 6-2 and to obtain high yield intermediate values may be chosen. With a parameter setting tuned to facilitate high yield Y a selectivity of approximately $S = 44\%$ is obtainable at a conversion of $X = 38\ \%$. In an experimental study Jähnisch et al. (2000) obtained a selectivity of S=37-40% at a conversion of S=37-38%. Thus, the performance of the reactor is only little improved by tuning the operational parameters of the FFMR model. In the next section the performance of the CMMR is investigated.

Table 6-2. Operational parameter settings for high performance

High Selectivity	High Conversion of toluene
$x_{F2,g,F}$<0.075	$x_{F2,g,F}$=0.075-0.1
θ<=0.2	θ>>0.8
$c_{Tol,l,F}$>4 kmol/m^3	$c_{Tol,l,F}$<1 kmol/m^3
T_l=252.15 K	T_l=273.15 K

6.3 CMMR operation

6.3.1 Modelling domain and procedure

In this section the 3D mathematical model for the CMMR is used, as introduced in Chapter 3, for the investigation of mass transport in the membrane and liquid phase. The reactor is operated isothermally, thus the cooling channel and the heat conservation equation (Eq. 3-3) are removed from the original model. The model does not contain momentum conservation

equations and the gas and the liquid flow are modelled as plug flow. Fluorine absorption is calculated from a Sherwood number correlation. The numerical solver is based on a 2D finite element discretisation combined with a stepper routine.

The direct fluorination mechanism consists of two competing reaction systems: A) electrophilic fluorination, B) radical fluorination. The former can be strengthened over the latter by means of an acidic catalyst, which improves the selectivity towards mono-fluorinated products (see also Chapter 4). With the catalytic membrane reactor configuration the solid catalyst is installed directly at the gas-liquid interface (Figure 3-5 and Figure 3-6).

In this section the influence of this catalytic membrane on the reactor performance is investigated. Here, it is assumed that the contact area at the gas/liquid interface is the same as with the FFMR. The catalyst activity κ of the catalytic membrane is treated as a variable in this sensitivity study. As operating conditions standard values are used as introduced in Table 5-3.

6.3.2 Results: Membrane parameters

First, the influence of the membrane thickness on the selectivity S is investigated. Figure 6-8 shows the selectivity S and the conversion X near the reactor entrance as a function of the membrane thickness. The implementation of the membrane imposes diffusion limitations on all compounds. This mass transport resistance causes complex consequences including reduced absorption, reduced concentration of toluene and thus lower reaction rate r_1 and r_2 and increasing concentrations of intermediate product and thus series reactions. Figure 6-9 shows the ratio of the sum of series reactions and the rate of reaction of toluene $(r_3 + r_4) / (r_1 + r_3)$. This ratio increases with increasing membrane thickness leading to lower selectivity S. Therefore a membrane imposing few mass transport limitations is desirable, i.e. a highly porous and thin membrane.

The conversion X drops sharply stepping from no membrane to the thinnest membrane under consideration (see Figure 6-8). This effect derives from the absorption of fluorine, which is reduced by the membrane tortuosity and porosity (Table 3-2). The actual thickness of the membrane has no influence on the absorption. Figure 6-9 shows the rate of reaction of fluorine, which halves due to the implementation of the membrane. Furthermore, transport limitations obstructing the diffusion of toluene to the reaction plane reduce the conversion of toluene. This effect becomes stronger with increasing membrane thickness.

It can be seen in Figure 6-10 that both the selectivity S and the yield Y are lower with the inert membrane reactor (κ=1) compared to the FFMR. This phenomenon follows from the

diffusion limitations on the various compounds, see the previous paragraph. However, with increasing catalyst activity κ the performance obtained with the CMMR (at κ=5: S=70% and X=31%) at is superior to the uncatalysed process in the FFMR (S=42% and X=30%). The data referring to the FFMR reactor in Figure 6-10 are experimental results obtained by Jähnisch et al. (2000).

Discussion

The catalytic membrane used with the CMMR has the potential to improve the selectivity S. To put into perspective the values of catalytic activity κ used in this work we use the following consideration: It is assumed that the catalytic activity κ influenced the activation energy $E_{A,1}$ of electrophilic reaction r_1, exclusively. Using Eq. (4-1) and Eq. (4-2) the change in activation energy can be calculated which is necessary to obtain a certain catalytic activity κ. In Figure 6-11 the activation energy $E_{A,1}$ and the reaction kinetic constant k_1 that goes with it are plotted versus the catalytic activity κ. It can be seen that a 650% increase in k_1 is achieved with only 12% decrease of $E_{A,1}$, which corresponds to κ = 7.5.

The values for the porosity and the tortuosity (ε = 0.7, τ = 4) are typical values for macro-porous membranes found in the literature.

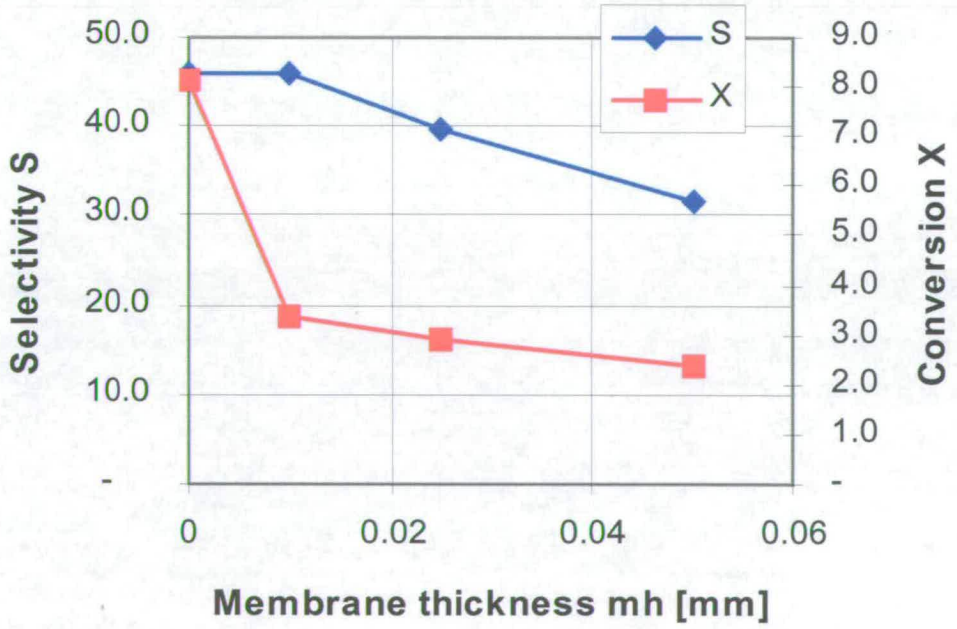

Figure 6-8. Selectivity and conversion of toluene near the reactor entrance versus the membrane thickness; ε=0.7, τ=4; catalyst activity κ=1

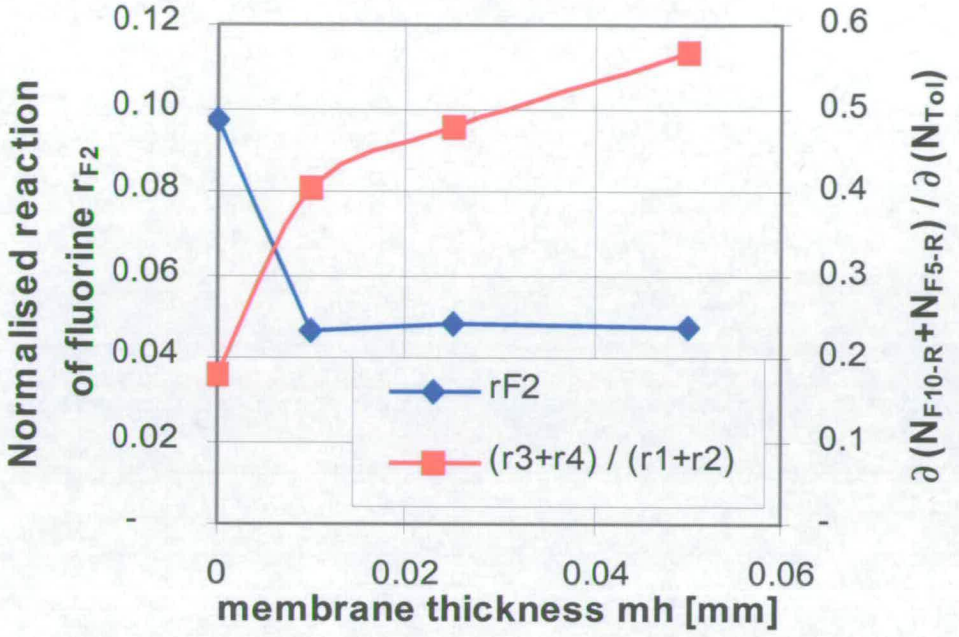

Figure 6-9. Reaction of fluorine and ratio between series reaction and toluene near the reactor entrance versus the membrane thickness; ε=0.7, τ=4; catalyst activity κ=1

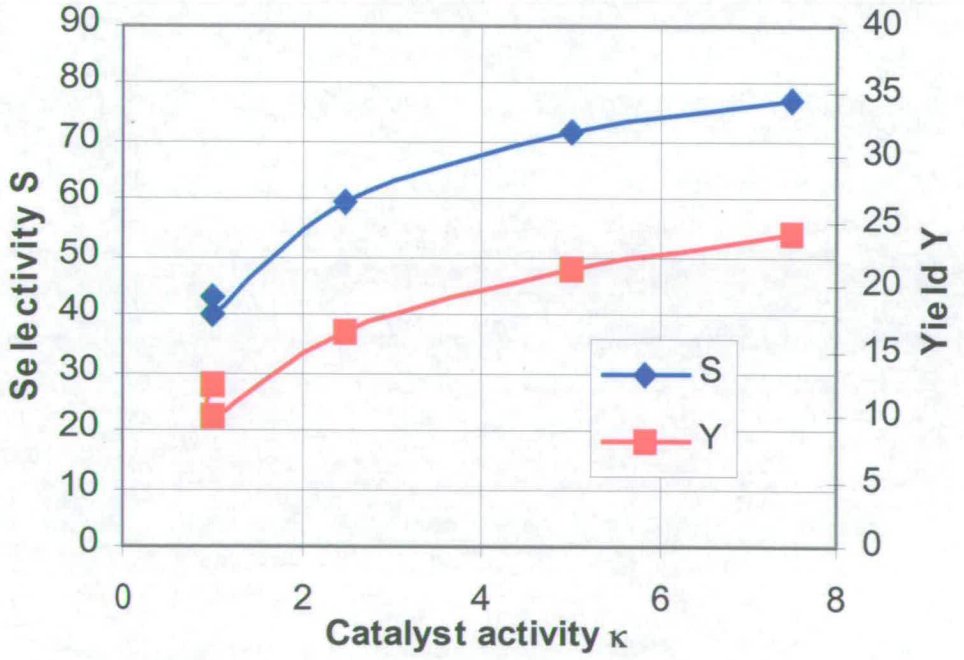

Figure 6-10. Yield *Y* and selectivity *S* obtained with membrane reactor as function of the catalyst activity κ compared to uncatalysed process in the falling film reactor; *mh*=0.025mm

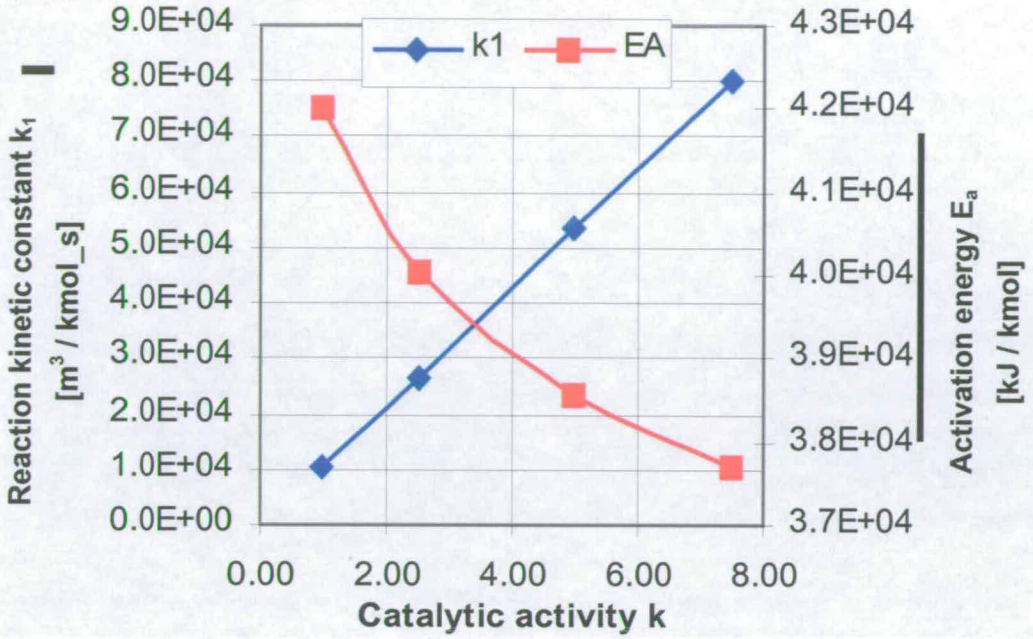

Figure 6-11. Reaction kinetic constant k_1 and activation energy $E_{A,1}$ versus the catalytic activity κ

6.3.3 Results: High conversion of toluene

High conversion of toluene would be desirable to reduce downstream separation effort. To achieve this goal the CMMR ($\kappa = 5$) is operated under standard conditions (Table 5-3) but the residence time is expanded and fluorine is fed in over-proportional quantity ($\theta = 2$) compared to standard operating conditions. Figure 6-12 shows the trajectories of conversion X, selectivity S and yield Y as a function of coordinate x^+. The conversion of toluene increases and the selectivity decreases steadily along the reactor. If we considered the yield Y as the most important parameter here, then its maximum value would mark the optimum residence time. This maximum value is achieved at a conversion X=80%, which is a good value. However, high conversion X is achievable only at high contacting times between the reactants and this gives rise to series reaction of the desired product to higher fluorinated compounds. Thus, at maximum yield Y the selectivity is down to S=47 % which is not much higher than what was achieved experimentally with the falling film reactor by Jähnisch (2000).

6.3.4 Results: Multiphase contacting

Fluorine is soluble in toluene and acetonitrile only in small amounts and reacts immediately when it gets in contact with the liquid resulting in very low penetration depth into the liquid phase, see Figure 6-13. The radical reaction system dominates when it comes to homogeneous phase reactions (see Figure 6-10). Therefore the contacting of gas, liquid, and solid phase has strong influence on the process.

In this work the catalyst is implemented in form of a solid catalytic layer situated between the gas and the liquid channels. There is a possibility that liquid breaks through the membrane into the gas channel driven by capillary forces. Here, the influence of a liquid layer between the catalyst and the gas phase is investigated. The operating conditions and the membrane specifications are given in Table 5-3.

In Figure 6-14 the selectivity S and the yield Y are plotted versus the layer of liquid on the catalytic layer, between the catalyst and the gas phase. A liquid layer of only 0.005mm reduces the selectivity from nearly $S = 65$ % to $S = 37$ %. Once the liquid layer is thicker than the reaction zone the catalyst serves no function anymore and the selectivity levels off to the value achievable without catalyst.

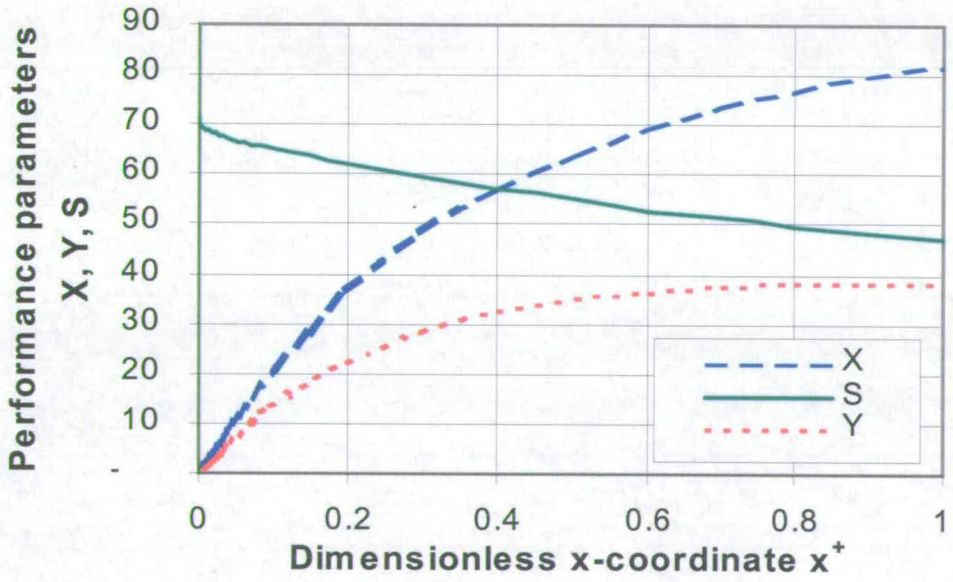

Figure 6-12. Performance parameters X, Y, S vs normalised x-coordinate; ε=0.7, τ=4; catalyst activity κ=5

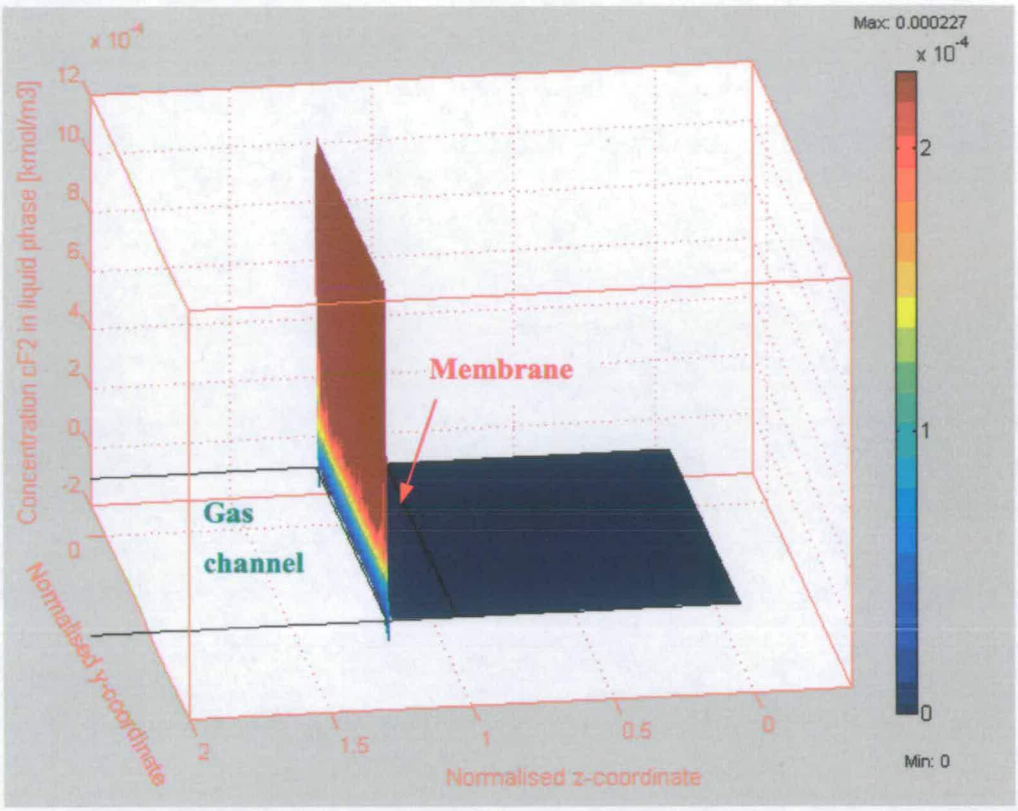

Figure 6-13. Concentration profile c_{F2} in the liquid phase in a cross-section of the membrane reactor. Black lines indicate the reactor shape.

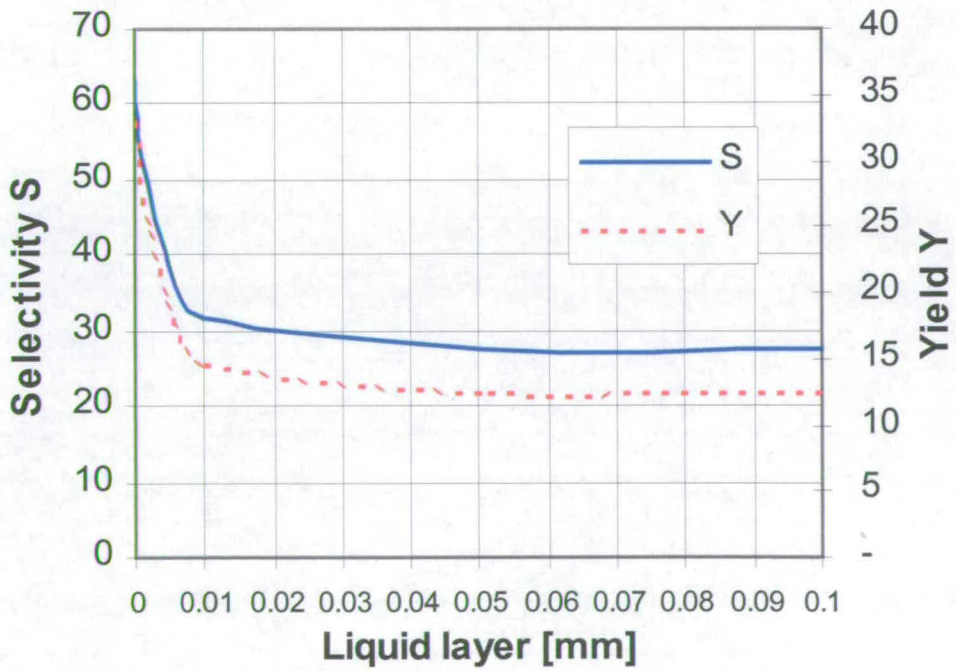

Figure 6-14. Selectivity S and yield Y vs liquid layer between solid and gas-phase; ε=0.7, τ=4; catalyst activity κ=5

6.4 Summary

The fluorination of toluene in the FFMR shows particularly strong sensitivity to the temperature in the reaction plane. The feed concentration of the reactants has significant influence on the performance, too. These operational parameters show opposite influence on the selectivity S and the conversion X. Thus, the setting of these parameters depends on the objective, the downstream separation effort, raw material costs, etc. For high yield Y the temperature should be approximately $T_l = 252$ K, the initial concentrations of fluorine and toluene should be relatively low, e.g. $x_{F2,F} = 0.075$ and $c_{Tol,F} = 2.5$ kmol/m^3. However, even at the best parameter setting the selectivity does not exceed $S = 45$ % at a reasonable conversion of toluene ($X = 38$ %) due to the strength of series reaction at high concentrations of intermediate products.

In principle, the findings obtained with the FFMR also apply to the CMMR, too. Additional parameters occur with the implementation of a membrane between the gas and the liquid phase. In general, a membrane imposes mass transfer limitations on the liquid phase reactants and products, which are detrimental to the conversion and the selectivity. Therefore a thin and porous membrane is desirable. Furthermore, the absorption of fluorine is reduced, which facilitates higher selectivity S but also results in lower conversion X. Only a membrane with catalytic function has the potential to significantly increase both, the selectivity S and conversion X (S=70% and X=31% at κ=5).

Considering downstream separation effort a high conversion of toluene would be desirable. Even with the CMMR this goal is not easily achieved because the selectivity S decreases drastically at high conversion X (S=47% and X=80% at κ=7.5). High X and S could only be achieved with an extremely high catalytic function κ of the membrane. Finally, the investigation of multiphase contacting of fluorine, toluene and a solid catalyst showed, that fluorine should absorb into the liquid phase in close proximity to the solid catalyst to positively influence the reaction system. Thus, the CMMR design with the catalyst between the gaseous and the liquid feed has great potential with this multiphase reaction. However, a liquid layer on top of the membrane has to be avoided to ensure optimum functioning of the catalyst. Here, a slightly elevated pressure in the gas phase would ensure that the liquid component does not break through the membrane by capillary forces and the contact surface lies inside the membrane (Cini and Harold, 1991).

Chapter 7

Non-adiabatic reactor analysis

7.1 Introduction

Direct fluorination reactions are often associated with uncontrollable explosion reactions. Indeed, during direct fluorination of aromatics a large amount of heat is generated (hydrogen substitution: $\Delta Hr_{(298)}$ = -473 KJ/mol). In solvent phase this reaction does not exhibit radical chain branching but the reaction is very exothermic and thermal run-away might occur if heat management is not sufficient (Bigelow, 1947).

To get an insight into the energy management with this process conducted in microchannels, the heat generated by the chemical reaction and the heat removal rate through conduction and convection are analysed. First, heat generation and heat removal are calculated separately to evaluate details about heat management with micro-channels. Thereafter, non-adiabatic simulations with the CMMR and FFMR models are accomplished to determine the actual local thermal conditions inside the reactor. The characteristics of the membrane and the reactor size are the most important variables under consideration. Results with the FFMR are used as a benchmark for the evaluation of the use of the membrane for heat management.

7.2 Heat generation and heat removal

7.2.1 Model and procedure

Approach

The energy conservation equation Eq. (3-3) can be transformed for illustration purposes and divided into the heat-generation term (1) and the heat-removal term (2):

$$\overline{v} \cdot \overline{c}_{p,l} \cdot \overline{\rho}_l \frac{\partial T_l}{\partial x} = \underset{(1)}{U\left(T_c - T_l\right)} + \underset{(2)}{\sum_i \left[\nu_i \cdot \left(\Delta H_{r,i}\right)\left(-r_i\right)\right]} \qquad (7\text{-}1)$$

where U is the heat transfer coefficient between the liquid phase and the coolant. Both terms plotted in a single graph can be used to characterise a non-isothermal reactor with respect to the operating temperature. Commonly, this type of plot is used with CSTRs where it indicates possible states of operation and the existence of multiple steady states. Here, the heat generation and heat removal curves of the micro-channels used with the FFMR and CMMR are investigated to determine the maximum steady state temperatures.

The heat removal term (1) represents the heat removal rate depending on the temperature difference between the reaction mixture and the coolant. The heat generation term (2) is used to calculate the heat of reaction as a function of the temperature. Because the individual reaction rates r_i are functions of the concentration of the involved species, heat generation term (2) has to be solved simultaneously with the mass conservation equations for each component.

Modelling domain

For the individual investigation of the heat removal and the heat generation terms the mathematical model for the FFMR and CMMR introduced in Chapter 3 is modified. Two individually simplified models are used to calculate the heat generation and heat removal term. In this manner the reaction rate does not have to be calculated as a function of the temperature, which is the most intensive detail of the model in terms of computational effort.

To obtain the heat removal lines the reaction rates of all reactions are set to zero, an external heat source is introduced at the boundary between liquid and gas phase and the heat transferred across the reactor bottom boundary is recorded as a function of the temperature in the reactor. The heat generation lines are obtained from an isothermal model of the reactor where the temperature is preset and the corresponding local heat of reaction in the reactor is recorded.

The heat and mass conservation equations are solved in a 2D finite element grid plus a stepper routine in x-direction along the reactor (see Chapter 3). The fluid flow is modelled as plug flow. The cooling channel is not implemented in the model; instead the reactor bottom represents a constant temperature heat sink.

Procedure

The determination of the heat generation curves is not as straight forward with plug flow type reactors as with CSTRs because the conversion (and thus the concentration profile) is a function not only of the temperature but it also varies spatially. Therefore the reactor is divided into n sections along the x-coordinate, see Figure 7-1, within which all parameters are assumed to be constant.

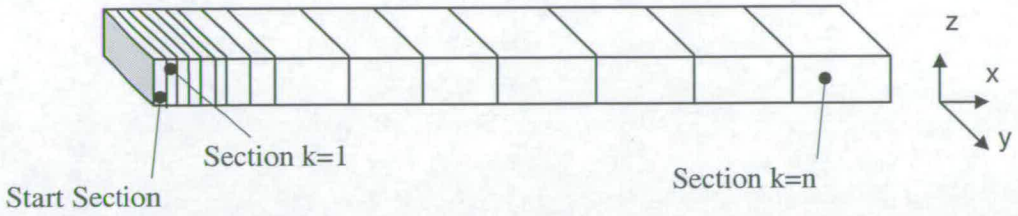

Figure 7-1: Division of the entire reactor length into n sections

The average heat generated in each reactor Section k is recorded as a function of the temperature to create the heat generation line, while the heat removal term does not change along the reactor assuming that the change in composition of the fluid does not have significant influence on the thermal conductivity. Equation (7-1) is adopted to these conditions and takes the following form:

$$\overline{v} \cdot \overline{c}_{p,l} \cdot \left(\frac{\Delta T_l}{\Delta x} \right)_{(k)} = \underset{(1)}{U \left(T_c - T_l \right)} + \underset{(2)}{\sum_i \left[\left(\Delta H_{r,i} \right) \left(-r_i \right) \right]_{(k)}} \tag{7-2}$$

In simulation practice the heat generation curves are recorded for the entire reactor at one constant temperature. Thus, considering the heat generation of Section 3 at T=260 K automatically implies that Section 1 and 2 were operated at 260 K, too. This is not exactly what happens in realistic reactor simulations where the temperature varies spatially. Therefore the results obtained here can only be an approximation of the real process.

With CSTRs the steady states of the reactor are indicated by the intersections of the heat generation and the heat removal curves. This is not the case with PFRs where the steady state in a reactor section lies between the intersection of these two lines and the previous steady state, due to the heat accumulation term on the left hand side of Eq. (7-2). Thus, we obtain a solution space with defined limits rather than an exact value.

The influence of the following parameters on the heat management is investigated: coolant temperature, reactant feed conditions, reactor geometry, and membrane design (membrane height mh, porosity ε and thermal conductivity). The influence of the porosity and the thermal conductivity on the heat removal are investigated separately (see following paragraph), while the other parameters are part of a sensitivity study where we distinguish three cases, see Table 7-1.

Table 7-1. Cases for sensitivity studies

Case	Constant	Variable
1	$x_{F2,F}$ = 0.1 aspect ratio a = 0.3 ch_g=5 mm θ=0.4 $\overline{v}_l = 0.00284$ m/s	0.0001< ch_l <0.0004m T=230 - 293 K mh=0 (no membrane)
2	$x_{F2,F}$ = 0.1 T=257 K a = 0.3 ch_g=5 mm θ=0.4 $\overline{v}_l = 0.00284$ m/s	0.0001< ch_l <0.0004 0<mh<0.05mm
3	T=257K a = 0.3 ch_g=2.5-5 mm $c_{Tol,F}$ = 0.998 kmol/m^3 $\overline{v} = 0.00284$ m/s	0.1< ch_l <0.4mm $x_{F2,F}$= 0.1-0.25 0<mh<0.05mm θ=0.4-1.0

7.2.2 Results

Thermal conductivity of the membrane

The thermal conductivity of the membrane, as it is modelled in this work (see Chapter 3) is calculated from the thermal conductivity of the solid membrane $\overline{k}_s$ material and the fluid in the membrane $\overline{k}_l$ using Eq. (3-5). The porosity of the membrane determines the individual weight of each of these two parameters. Thus, the parameters defining the thermal conductivity of the membrane are the conductivity ratio $\lambda=k_l/k_s$ and the porosity ε. The range of both parameters is shown in Table 7-2.

Table 7-2. Range of the conductivity ratio λ and porosity

	Variable	Lower limit	Upper limit
1	λ	Very highly conductive material => λ =0.0005	$k_s=k_l$ => λ=1
2	ε	Dense solid block => ε = 0	No membrane => ε = 1

In Figure 7-2 and Figure 7-3 the thermal conductivity of the membrane $\overline{k}_{mem}$ is shown as a function of λ and ε. Considering Figure 7-2 we find that the thermal conductivity of the membrane increases with decreasing λ at constant porosity. In a range of λ=0.1-1, though, the

thermal conductivity of the membrane increases only little and would not improve the heat management of the reactor significantly. In general, for a given fluid the solid material should be chosen so that $\lambda<0.01$. This is especially true for membranes with high porosity $\varepsilon>0.7$ where strong improvements, i.e. $\overline{k}_{mem}/\overline{k}_{l}>10$ can be achieved with highly conductive materials ($\lambda<0.003$), only.

Figure 7-3 shows the thermal conductivity as a function of the porosity with three different membrane materials: stainless steel ($\lambda=0.00427$), Silicon oxide SiO_2 ($\lambda=0.2245$) and Silicon Si ($\lambda=0.00129$). These samples are common membrane materials, and should be considered as representatives of material groups. In general the conductivity of the membrane increases with decreasing porosity ε. Considering marco-porous membranes made of stainless steel with porosity $\varepsilon=0.6$ - 0.8 the improvement in conductivity is 10-fold at best whereas micro-porous membranes would conduct up to 70 times better than the fluid in the pores. We find confirmed that a setting with ($\lambda>=0.1$) does not result in a pronounced improvement. In this work, the standard porosity of the membrane is $\varepsilon=0.7$ which results in a conductivity ratio of approximately $k_{mem}/k_{l}=7$ with a membrane made of stainless steel.

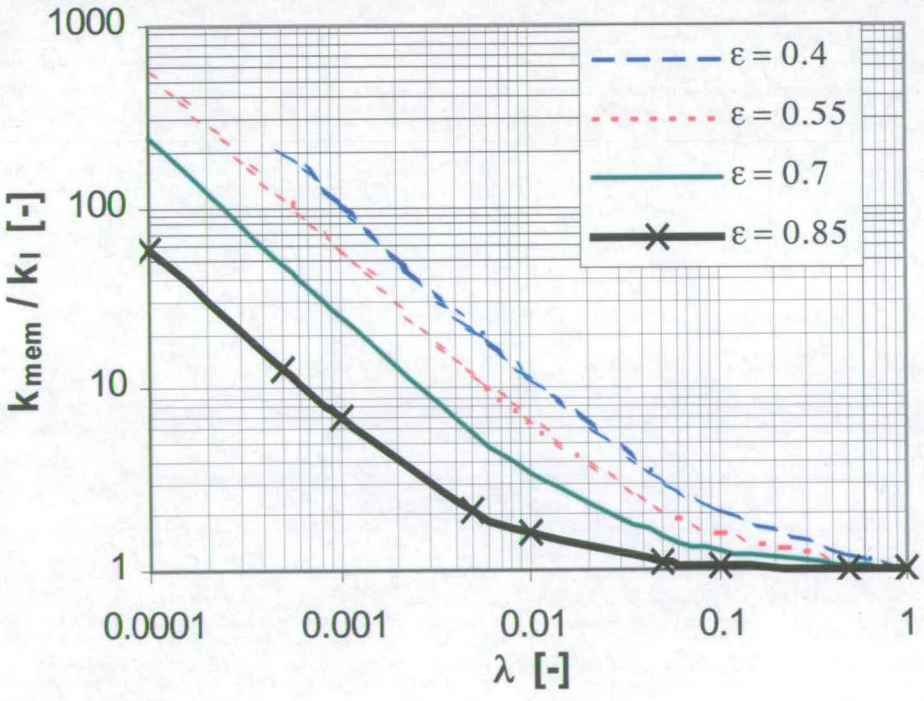

Figure 7-2.Thermal conductivity enhancement over pure liquid through solid membrane material

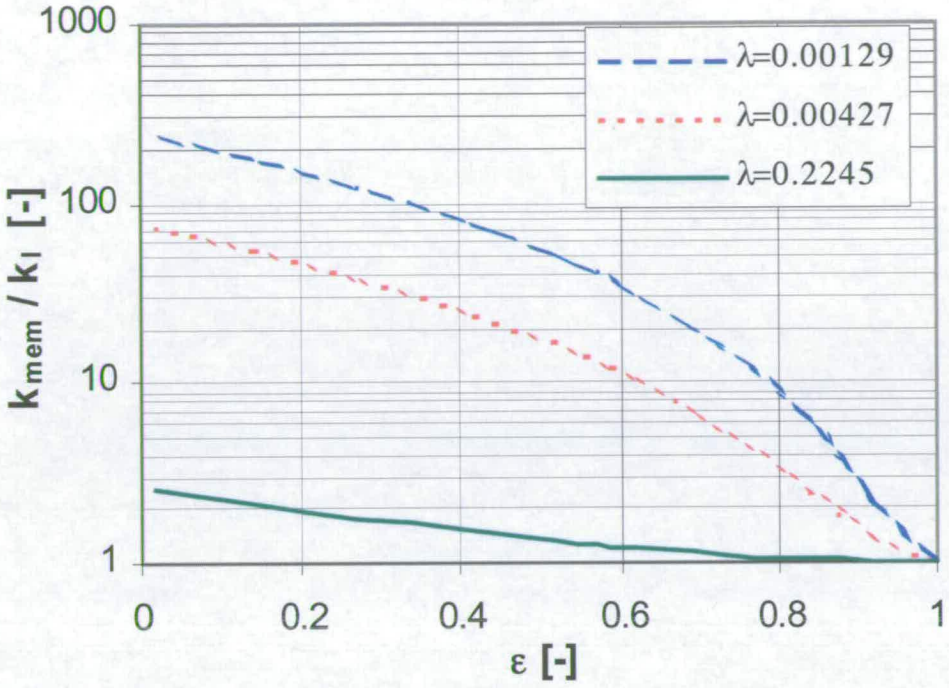

Figure 7-3. Thermal conductivity enhancement over pure liquid as a function of the porosity ε ; λ=0.0043 (refers to kAcN / kSt)

Results: Case 1

Simulation experiments were conducted to analyse the heat management with micro-channels without a membrane. Figure 7-4 to Figure 7-6 illustrate heat generation and heat removal lines at several coolant temperatures and reactor sizes. In the following it is explained how to interpret the plots used in this section:

- At the reactor entrance the state of the fluid is defined by temperature $T_{l,F}$ (equal to the coolant temperature T_c) where the heat production is larger than the heat removal term.
- Within Section 1 the chemical reaction exerts heat and the local steady state has a higher temperature then the feed. The intersections between the heat generation and heat removal lines represent the steady state at the mean local maximum reactor temperature T_{max} in each reactor section (from 1 to n).
- The exact position of the local steady states on the heat generation and the heat removal lines is not defined by the intersections between these two lines and thus cannot be specified accurately without knowledge about the fluid velocity, specific heat and the temperature gradient, see Eq (5-16). The heat accumulating fluid volume flow is very small und thus the local steady states can be expected to lie close to the intersections (at small temperature gradients).

- With increasing distance from the reactor mouth the actual temperature approaches the local maximum temperature T_{max}. This is due to the fact that heat generation in a reactor section decreases with increasing distance from the reactor mouth (seeFigure 7-4) and the heat generation and heat removal lines cross at decreasing temperatures.
- The heat removal lines in Figure 7-4 have a steep slope representing a high heat transfer coefficient. The highest possible temperature in the reactor can be determined through a worst case scenario: The intersection at the highest temperature of any intersections between a heat generation curve and the heat removal line is also the *maximum possible temperature* $T_{max,p}$ in the entire reactor.

Considering Figure 7-4 the maximum possible temperature can be identified with the standard reactor geometry and at several coolant temperatures. At low coolant and initial fluid temperature ($T_c = 230$ K) the maximum possible temperature is little elevated from the coolant temperature. Increasing the coolant temperature to $T_c = 273$ K we permit the process to pass the steep section of the S-shaped heat generation curve and $T_{max,p}$ increases to approximately 7 K above the coolant temperature.

The influence of an increasing reactor size on the heat management is illustrated in Figure 7-5 and Figure 7-6. With 2-fold increased reactor height and constant aspect ratio a, the heat production per meter length doubles and the heat removal performance is weaker. Nevertheless, $T_{max,,p}$ can be controlled tightly until a coolant temperature of approximately $T_c = 265$K. Exceeding this threshold $T_{max,p}$ is significantly higher than the coolant temperature, up to 50K at $T_c = 293$ K. Figure 7-6 illustrates results with a 4 fold bigger reactor and here, the width of the reaction plane and thus the generated heat is 4 times bigger per meter length. The heat removal deteriorated, yet again, which shows in the lower slope of the heat removal lines compared to the smaller reactors. Here, the reactor temperature is controllable up to $T_c = 250$ K. At higher coolant temperatures the generated heat near the reactor mouth increases sharply and we get a thermal run-away beyond the boiling point of the liquid components at about 360 K.

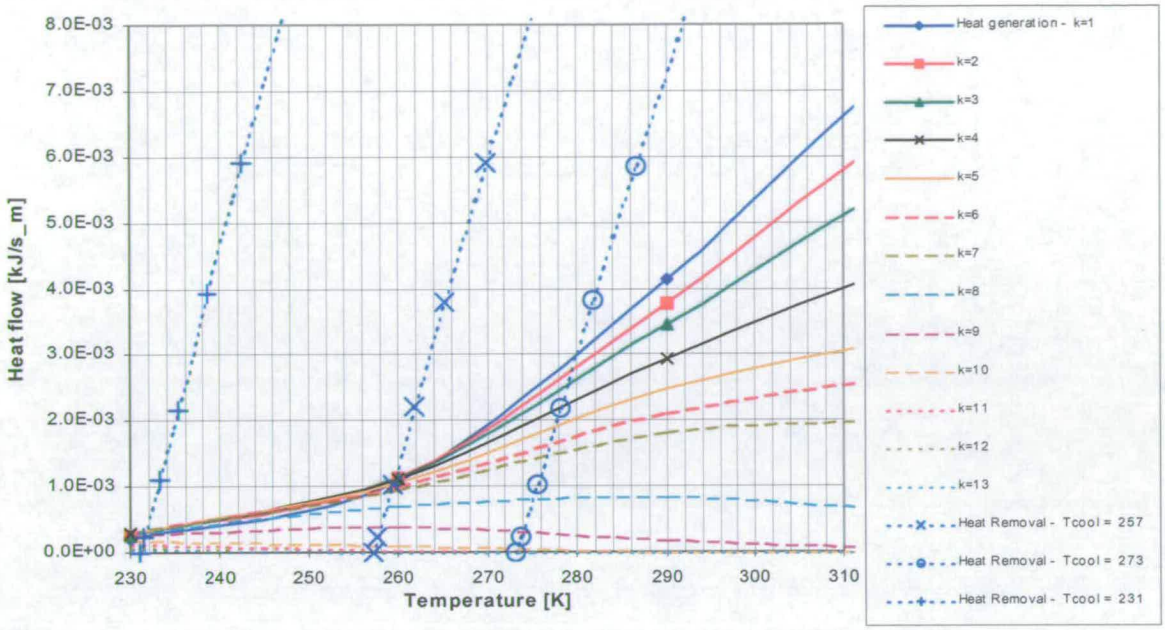

Figure 7-4. Heat generation lines for n reactor sections and heat removal lines at different coolant temperatures with the standard reactor geometry (height ch_l=0.0001m, width cw=0.0003m)

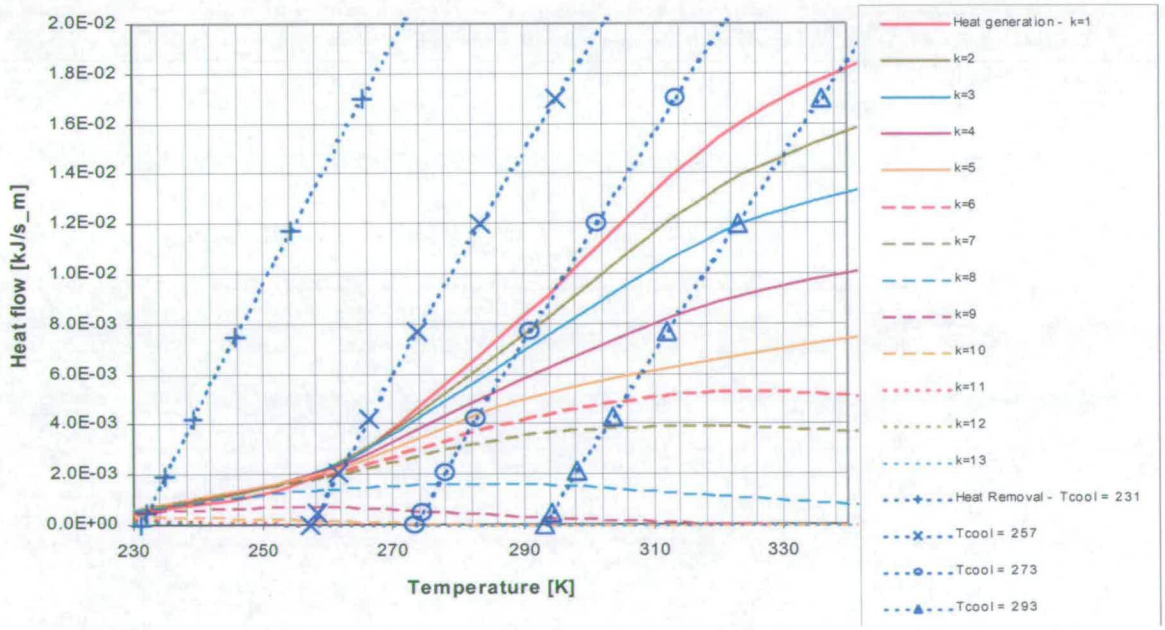

Figure 7-5. Heat generation lines for n reactor sections and heat removal lines at different coolant temperatures with reactor geometry: height ch_l=0.0002m, width cw=0.0006m.

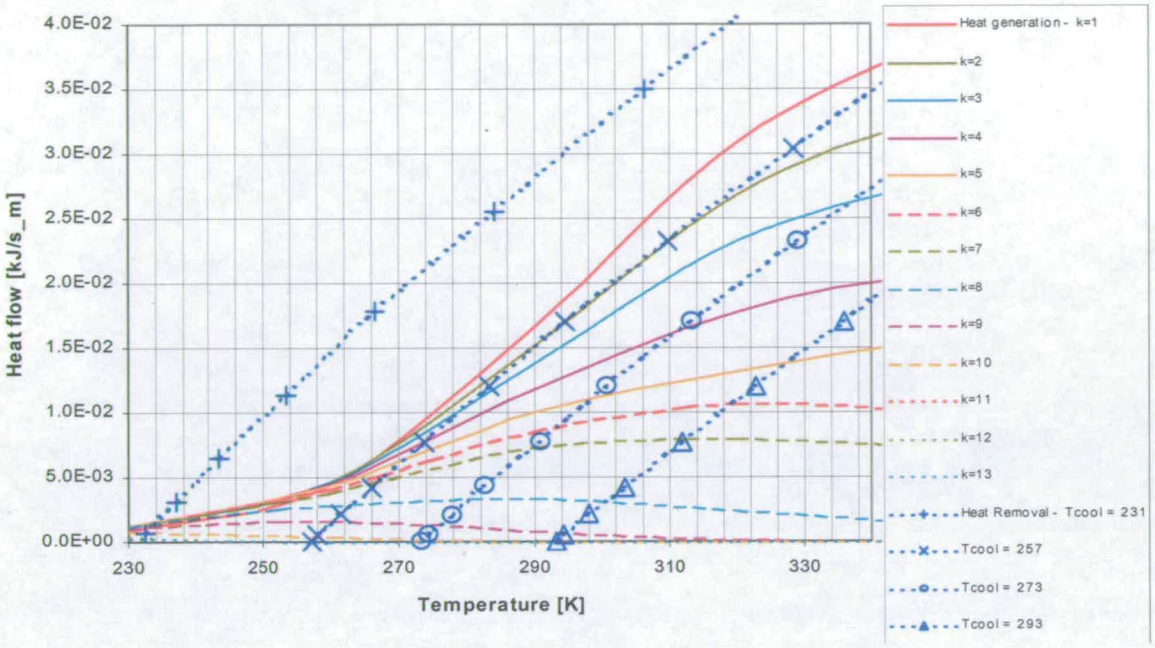

Figure 7-6. Heat generation lines for n reactor sections and heat removal lines at different coolant temperatures with reactor geometry: height ch_l=0.0004m, width cw=0.0012m

In Figure 7-4 the heat generation lines for sections near the reactor mouth have an S-shaped trajectory. Between 230K and 270K the heat of reaction increases whereas temperature increase above 270K results in decreasing heat generation. The physical phenomenon underlying this behaviour is fluorine mass transport to the reaction plane that involves gas and liquid phase transport.

Figure 7-7 shows the mass transfer coefficient of the gas and liquid phase. The liquid phase mass transfer coefficient increases by three orders of magnitude within the temperatures range of $T_c = 230\ \mathrm{K}$ to $380\ \mathrm{K}$ because of increasing rate of reaction. This effect is explicitly expressed with liquid phase absorption enhancement factor E that indicates the enhancing effect of the chemical reaction on the liquid phase mass transfer coefficient k_l (see Section E.3 in the Appendix). This factor increases strongly with rising temperature, see Figure 7-8.

Within the same temperature range the gas phase mass transfer coefficient k_g rises only little. The modified Thiele Modulus Φ_{mod} (defined in Section 3.3.4) is a useful number to show whether a process is reaction or gas phase mass transfer limited. Figure 7-8 shows that Φ_{mod} increases by two orders of magnitude in the temperature range under consideration, which indicates rising influence of gas phase mass transfer limitations on the process with increasing temperature. Thus the S-shaped trajectory of the heat generation lines is due to alternating fluorine mass transport limitations with increasing temperature shifting from liquid phase to gas phase limitation.

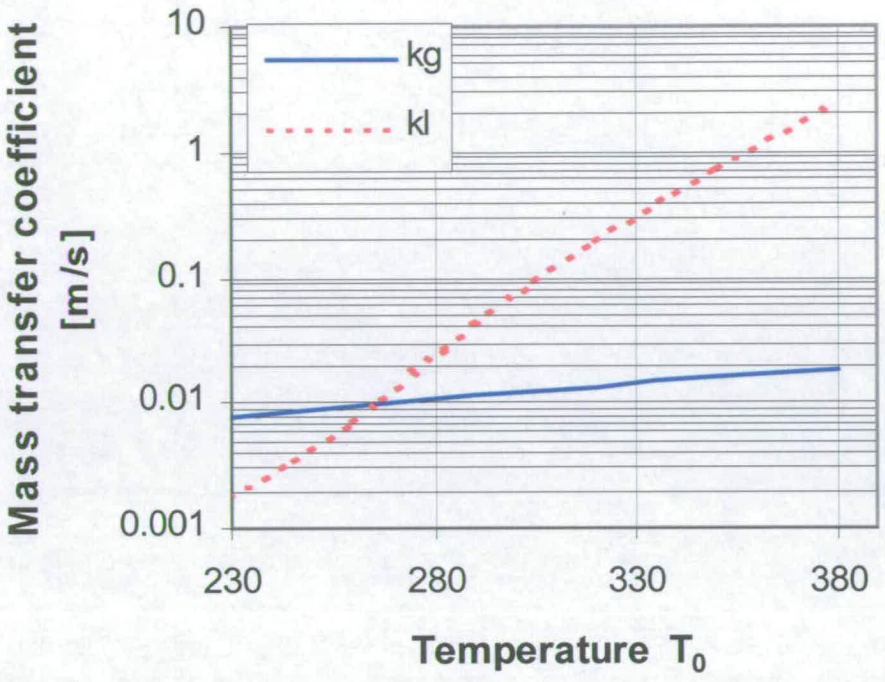

Figure 7-7. Mass transfer coefficients k_g and k_l in reactor Section 1 versus temperature

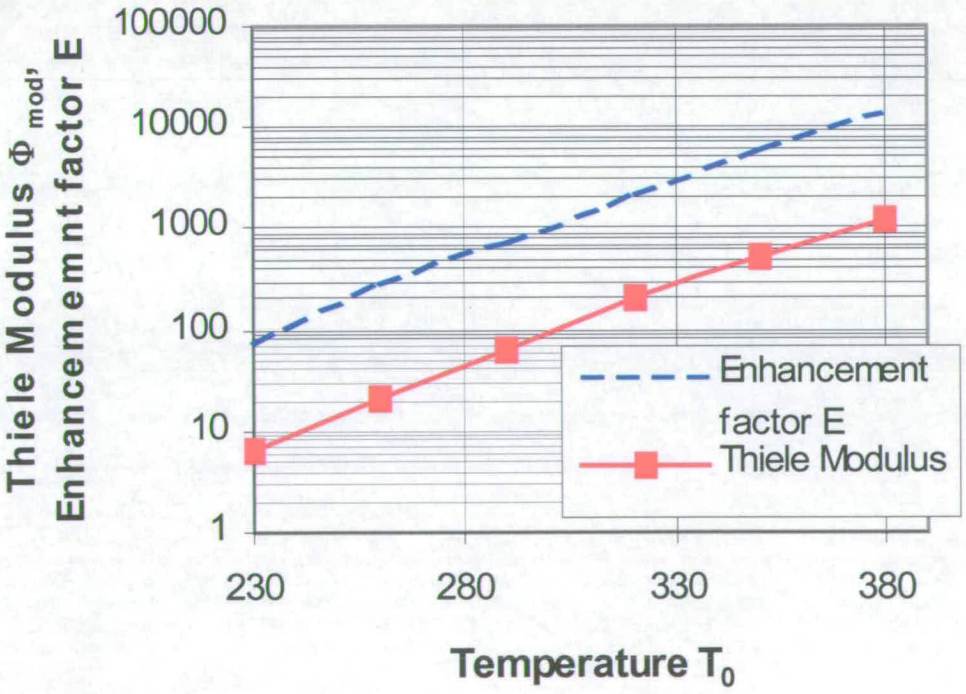

Figure 7-8. Absorption enhancement factor E and modified Thiele Modulus Φ_{mod} in reactor Section 1 versus temperature

Results: Case 2

In the section about the thermal conductivity of the membrane we found that a highly conductive membrane made of stainless steel implemented into the reaction plane improved the thermal conductivity at the reaction plane and should support the removal of heat towards the reactor walls. Here, membranes of varying thickness are investigated concerning their influence on the heat management with reactors of varying size and constant coolant temperature. It is assumed that the implementation of the membrane has no influence on the heat generation (this topic is investigated in Section 7.3) to be able to compare the heat removal characteristics between the FFMR and CMMR. Only the heat removal lines of the first three reactor sections are considered because it is near the reactor mouth where heat generation is highest.

In Figure 7-9 the heat removal lines for 3 different membranes are shown, including a membrane with zero thickness that is effectively a falling film reactor, at a coolant temperature of $T_c = 257$ K and the standard reactor geometry. With all three membranes the maximum possible temperature $T_{max,,p}$ is under tight control and the largest membrane performs best.

In Figure 7-10 the same kind of plot is displayed showing results achieved with the double-size reactor. The situation is similar compared to the smaller reactor but the maximum possible temperature $T_{max,,p}$ is allowed to rise up to 263 K with mh=0 (FFMR) and T_c=257 K. Increasing the reactor size to 4-fold the standard reactor size the slope of the heat removal lines decreases drastically, see Figure 7-11. With the largest membrane the maximum possible temperature $T_{max,p}$ is under reasonable control at 265K whereas with no membrane, i.e. mh=0, $T_{max,p}$ increases beyond the boiling point of the liquid at about 360K.

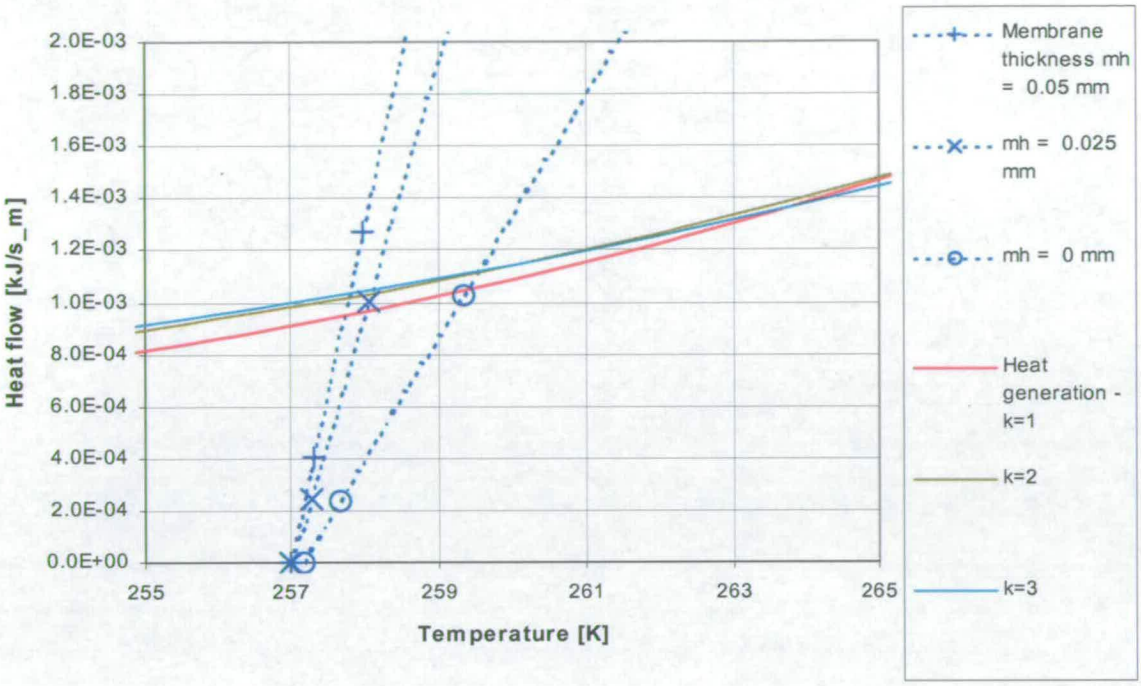

Figure 7-9. Heat generation lines for reactor Sections 1-3 and heat removal lines with varying membrane thickness at constant coolant temperature and standard reactor geometry (height ch_f=0.0001m, width cw=0.0003m)

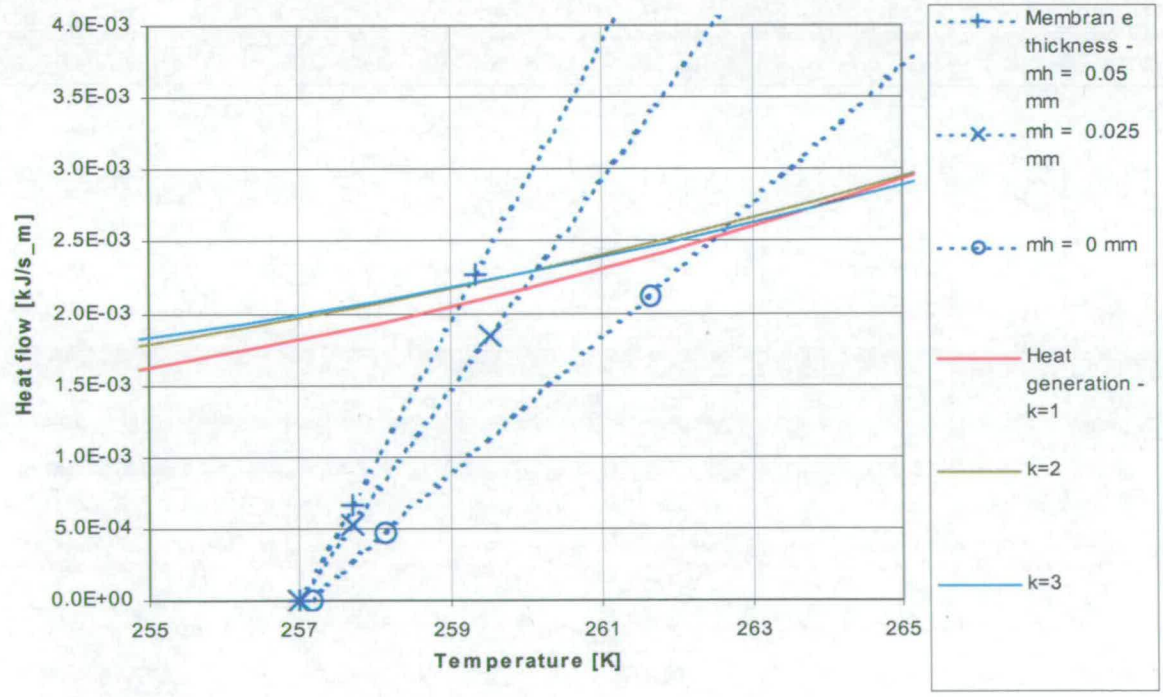

Figure 7-10. Heat generation lines for reactor Sections 1-3 and heat removal lines with varying membrane thickness at constant coolant temperature and double standard reactor size (height ch_f=0.0002m, width cw=0.0006m)

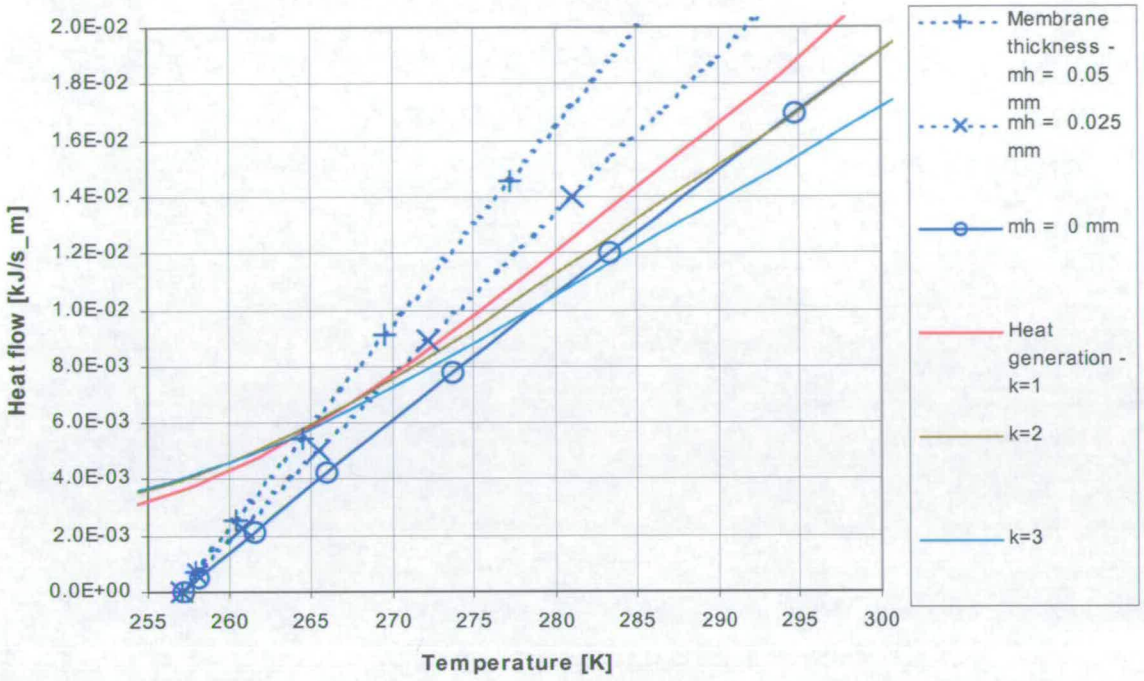

Figure 7-11. Heat generation lines for reactor Sections 1-3 and heat removal lines with varying membrane thickness at constant coolant temperature and 4-fold standard reactor size (height ch_l=0.0004m, width cw=0.0012m)

Results: Case 3

Here the influence of increased absorption of fluorine into the liquid phase is investigated. The rate of absorption is quantified using the dimensionless contacting time at constant liquid feed flow rate and sufficiently low liquid phase mass transfer resistance:

$$\Lambda = \frac{\text{intial rate of absorption}}{\text{liquid feed flow rate}} = \frac{k_g \cdot H_c \cdot p \cdot x_{F_2,0} \cdot cl}{\overline{v}_l \cdot c_{Tol,0} \cdot ch_l} \tag{3-6}$$

Thus, in practice the absorption rate can be increased at a given temperature, primarily through increasing the concentration of fluorine in the gas phase or increasing the overall mass transfer coefficient k_{total}, (see Section 5.2.2), which is calculated from k_g and k_l.. Table 7-3 describes three cases which are distinguished by the setting of k_g and $x_{F2,g,F}$ and thus the absorption of fluorine.

Table 7-3. Absorption parameter setting sensitivity studies

Case	$x_{F2,g,F}$	k_g at 260 K	Λ	Result
High F_2 absorption	0.25	9.40E-03 (ch_g=5mm)	6.7	High heat generation
Medium F_2 absorption	0.1	1.55E-02 (ch_g=2.5mm)	4.4	Medium heat generation
Low F_2 absorption	0.1	9.40E-03 (ch_g=5mm)	2.7	Low heat generation

The heat removal potential of the reactor is the same as in case 1 but the rate of heat generation rises with increasing Λ as we see in Figure 7-12. Here, heat generation lines at three different Λ are displayed along with heat removal lines at T_c=257 K and varying membrane thickness *mh*. We find that the highest Λ can be handled well, i.e. with little $T_{max,p.}$ elevation, employing the two thickest membranes whereas a thermal runaway, in terms of $T_{max,p.}$ may occur with thin membranes. Thin membranes would be perfectly suitable for heat removal with medium or low heat generation, allowing only a very small increase of temperature.

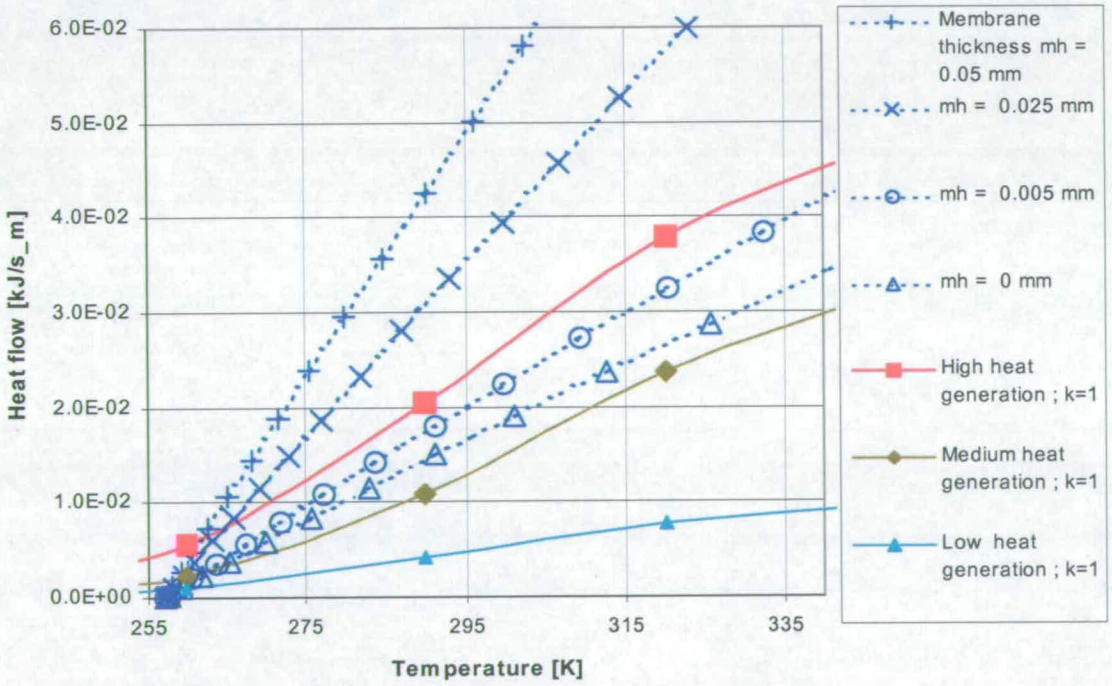

Figure 7-12. Heat generation at varying Λ and heat removal with varying *mh*; for sectionised tubular standard reactor (height ch_f=0.0001m, width *cw*=0.0003m)

7.2.3 Discussion

In this section heat generation and heat removal terms with the direct fluorination process in micro-channels are considered separately. In this manner meaningful comparison is possible concerning the heat management performance of different microreactor configurations under varying conditions. For the calculation of the heat generation and heat removal lines simplified mathematical process descriptions can be used, which facilitate easy numerical solutions with less demand on the solver routine. On the downside, it is not possible to determine the actual states of operation from this type of plot, due to some simplifications and the abandonment of the heat accumulation term in Eq. (7-2).

In general, heat removal with the standard size micro-channels is very efficient, which is reflected in the steep gradient of the heat removal curves. However, the direct fluorination process is very exothermic and isothermal operation is not achievable. Instead, depending on the temperature of the coolant, a temperature peak occurs near the reactor mouth.

Increasing the reactor size weakens the heat removal, which shows through the decreasing slope of the heat removal curves. This effect can lead to pronounced peak-temperatures or thermal run-away. Introducing a porous membrane made of a highly conductive material (i.e. stainless steel) into the reaction plane, the heat removal can be strengthened. Again, this shows through an increased slope of the heat removal lines. A CMMR could be designed two-times larger than a FFMR allowing the same maximum temperature at otherwise constant conditions. The size of the reactor is important with regard to up-scaling the reactor for industrial use.

The heat generation lines reflect the rate of reaction and the surface area available for contacting of the reactants. A measure of the overall rate of reaction is the dimensionless contact time Λ. At constant liquid phase conditions increasing absorption of fluorine results in rising values of Λ and thus higher rate of reaction. With standard operational conditions the generated heat of reaction can be removed effectively with a standard size FFMR or CMMR. Increasing the heat generation can result in thermal run-away unless a highly conductive membrane is incorporated into the reaction plane.

7.3 Non-isothermal process simulations

7.3.1 Model and procedure

In this section the focus is on the influence of reactor design (size of the reaction channel and thickness of the membrane) on the reactor performance measured in terms of selectivity S,

yield Y and conversion X. The mathematical model introduced in Chapter 3 is used to analyse heat generation and temperature distribution as they occur with the direct fluorination in the FFMR and the CMMR. The heat and mass conservation equations are solved in a 2D finite element grid plus a stepper routine in x-direction (see Chapter 3). The fluid flow is modelled as plug flow. The important reactor design parameters and operating conditions are displayed in Table 7-4, which are based on the standard conditions displayed in Table 5-3.

Table 7-4. Range of operational parameters

Variable	Value	Unit
$\overline{v}_l$	0.00284	m/s
T_c	257.15 K	K
$x_{Tol,F}$	0.0524	
$x_{F2,F}$	0.1	
θ	1	
ch,	0.0001 – 0.0004	m
cw	0.0003 – 0.0012	m
a	ch/cw=0.333	
cl	0.065 – 0.26	m
mh	0.0000625-0.05	m

First, the profile of the heat of reaction and the temperature inside the microreactors are recorded. Then, the influence of the thickness of the membrane on heat removal is analysed using a constant heat source rather than the actual heat generated by the fluorination reaction, to ensure comparable conditions. Next, the influence of the size of the reactor on the temperature within the reaction plane is investigated with heat generated by the reaction. When the reactor size is changed the dimensionless contact time Λ is held constant to obtain comparable results, which essentially results in an elongation of the reactor with increasing channel cross-section size. Here, the aspect ratio of the reaction channel is a constant value and is not considered a variable design parameter.

7.3.2 Results

Results : Heat of reaction and temperature profile

With microreactors considered in this work the heat of reaction is removed by conduction through the membrane (if existent), the liquid phase and the reaction channel body to the cooling channel, which is held at constant temperature. In Figure 7-13 and Figure 7-14 the heat generation profile and the resulting temperature along the standard FFMR and the corresponding CMMR are illustrated. It can be seen that we get the highest heat generation and a temperature hot spot near the beginning of the reactor with both reactor types.

The reactor without membrane (FFMR) stands out with significantly higher heat of reaction while the different membrane reactors show similar trajectories, see Figure 7-13. This effect is due to the diffusion limitation imposed by the membrane on the diffusion and thus the absorption of fluorine (see also Section 6.6.2). In this connection the membrane thickness does not have much influence because the reaction takes place in a narrow band thinner than the thinnest membrane investigated. The membrane thickness does influence the diffusion of intermediates and toluene, though, which has strong influence on the selectivity and the conversion of toluene (see also Section 6.6.2) but not on the heat generation.

The temperature distribution in the reaction plane with membranes of varying thickness is displayed Figure 7-14. The hot spot temperature with the FFMR is higher compared to the CMMRs because of higher heat generation near the reactor mouth. However, the hot spot temperature is only about 3K elevated from the base temperature of 257K. This result is in line with the result obtained in Section 7.2 (Case 1) where the heat generation and heat removal are considered separately, see Figure 7-4. With the standard size reaction channel the cooling works very effectively and brings back the temperature towards its initial value once the reaction rate gets slowed down towards the reactor end. The membrane reactors accomplish higher heat conduction from the reaction plane through the highly conductive membrane, which is further investigated in the next section.

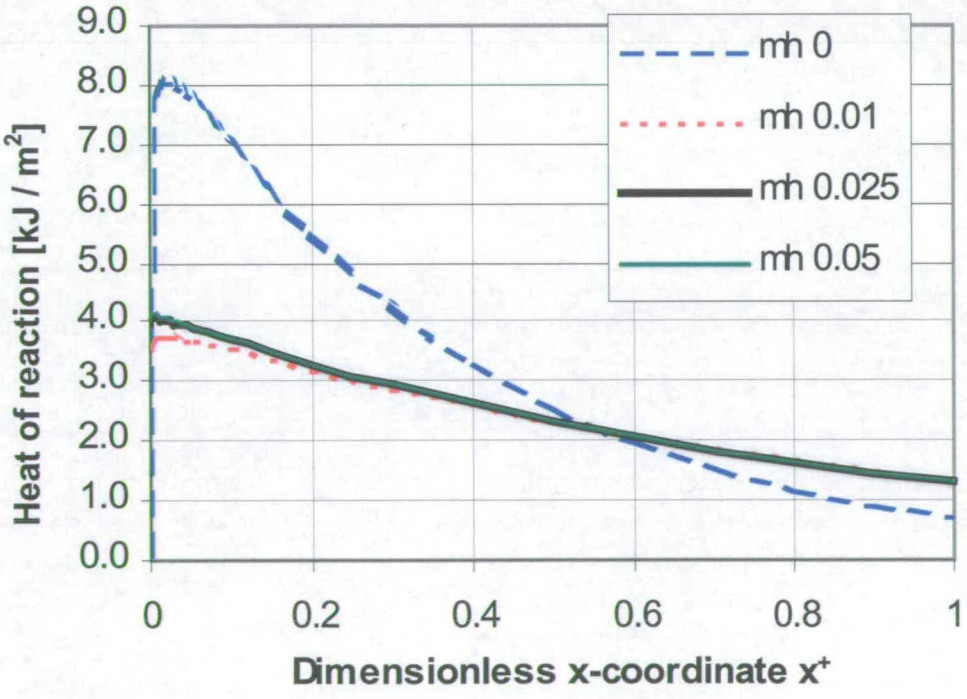

Figure 7-13. Heat generation with standard reactor geometry and varying membrane thickness *mh*; ch_f=0.0001m, *cl*=0.065m

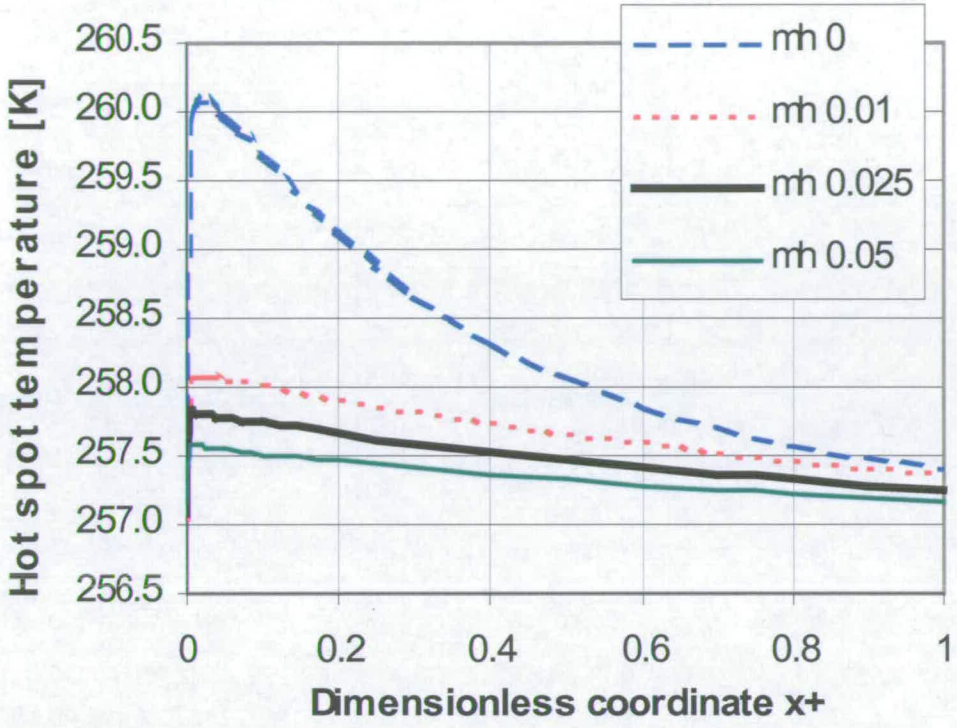

Figure 7-14. Temperature with standard reactor geometry and varying membrane thickness *mh*; ch_l=0.0001m, *cl*=0.065m

Results : Varying reactor size and constant external heating

In the following the influence of the reactor size on the reactor performance is investigated. To show the dependency between temperature in the reaction plane and the reactor size at constant aspect ratio the heat of reaction is modelled as a constant heat flux boundary condition (q=8 kJ/m^2), symbolising the maximum heat flux with reference to the real heat of reaction profile (see Figure 7-13). With the membrane reactor the membrane height increases proportionally with the reactor size. Figure 7-15 shows that the maximum reactor temperature increases significantly with rising size of the micro-channel. With the FFMR enlarging the channel from ch_l=0.0001m to 0.0005m results in a temperature increase from 260K to 274K. Considering the same range of ch_l with the CMMR the temperature increases from 258K to 262.5K, thus control of the hot spot is much improved. With increasing size of the reaction channels the benefit gained from the implementation of a membrane increases (see Figure 7-15). Furthermore, the thicker the membrane in relation to the channel height the stronger is the difference between the FFMR and the CMMR.

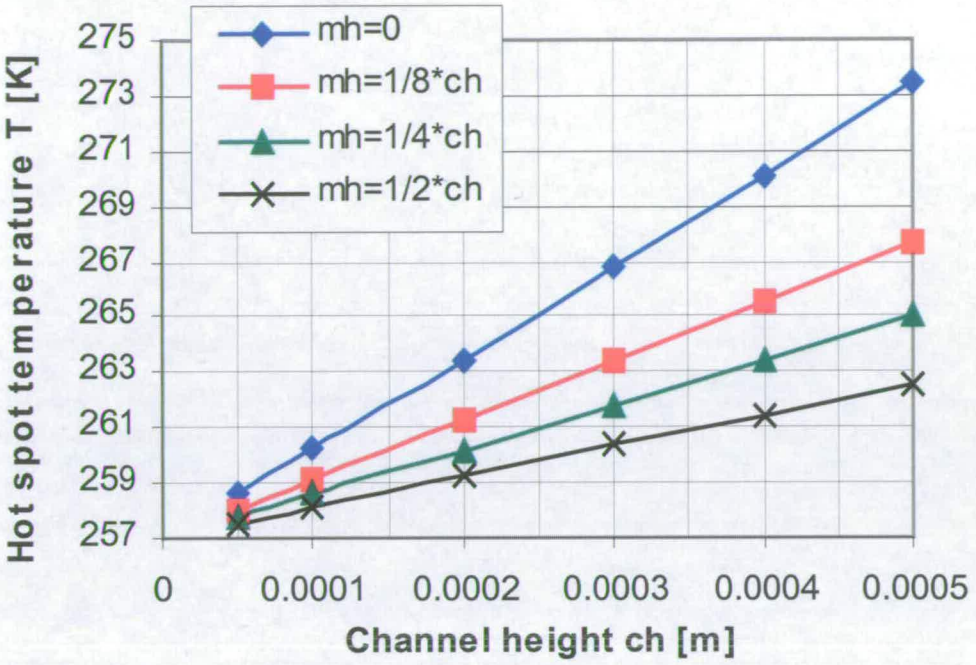

Figure 7-15. Hot spot temperature as a function of the channel height. Comparison between the FFMR and the CMMR with varying membrane thickness; constant heat flux boundary condition q = 8.0 kJ/m^2

Results : Varying reactor size and heat of reaction implemented

In this section the heat management performance of the CMMR and FFMR is investigated with varying reactor size and heat generated by the chemical reaction. Fluorine absorption is reduced by the membrane, which results in lower heat generation in a cross-section and lower temperature in the reactor. With the CMMR the membrane thickness increases proportionally with the channel height (ch_l = 0.1mm corresponds to mh=0.0125mm).

Figure 7-16 compares the maximum temperature occurring inside the CMMR and the FFMR as a function of the channel height ch_l. The temperature in the reactor rises with increasing channel size because thermal conduction paths elongate. This effect is particularly strong near the reactor mouth, where heat generation is strongest. To some extent this effect is compensated through a shifting of the hot spot towards downstream and lower concentrations of the reactants, which occurs with increasing cross-sectional area, and thus flow rate. The plot of the temperature in the FFMR rises with a significantly higher slope with increasing channel height compared to the CMMR. The temperature in the CMMR is more controlled, which is partly due to the fact that the heat of reaction near the reactor mouth is lower compared to the FFMR. This is also the reason why the temperatures recorded with the

CMMR cannot be compared to the predictions from Section 7.2 since those were calculated assuming the same heat load for the FFMR and the CMMR to allow a meaningful comparison. The results found with the FFMR (illustrated in Figure 7-16) correspond well with the maximum possible temperature predicted in Section 7.2, see Figure 7-9, Figure 7-10 and Figure 7-11. Interpreting Figure 7-11 (channel height of ch_l = 0.4mm) the maximum possible temperature $T_{max,p}$ predicted for reactor Section 1 is not realistic and the prediction for Section 2 ($T_{max,p}$ = 295K) is considered, which matches result of the process simulation exactly (T = 295K, see Figure 7-16).

Figure 7-17 shows the simulation results obtained with the FFMR and the CMMR with inert membrane (κ=1) near the reactor entrance. We find that the CMMR at standard size (ch_l = 0.0001) and a thin membrane (mh = 25 µm; porosity ε=0.7; tortuosity τ=4) has a lower selectivity S compared to the FFMR due to the diffusion limitations imposed on the liquid phase components. However, thanks to high heat transfer from the reaction plane with the CMMR the temperature in the reaction plane is stabilised and so is the selectivity, while with the FFMR the selectivity decreases drastically with increasing reactor size. The local conversion is higher with the FFMR because of a higher absorption of fluorine. The low conversion X with the CMMR near the reactor mouth is compensated through a higher conversion towards the reactor end (more pronounced gas feed distribution).

Figure 7-18 is equivalent to Figure 7-17 but the CMMR features a catalytic membrane (κ=5). Here, the selectivity and the product output at the reactor exit with the CMMR are roughly twice as high compared to the FFMR. The conversion X is approximately the same with both reactor types. The catalytic function of the membrane contributes most to the high selectivity achieved with the CMMR. The membrane thickness increases proportionally with the channel size, which has detrimental influence on the selectivity, which drops with similar slope as with the FFMR. In this manner, diffusion limitations compensate in a negative sense for improved heat removal with the membrane reactor.

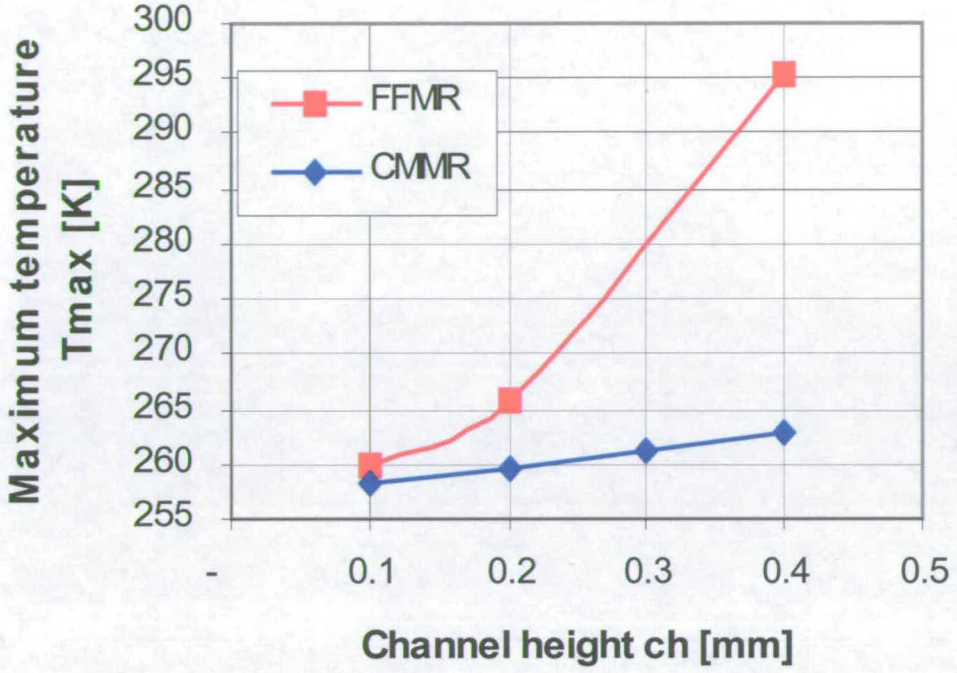

Figure 7-16. Maximum temperature as a function of the channel height. Comparison between the FFMR and the CMMR with membrane thickness proportional to ch_i; heat load created locally by chemical reaction

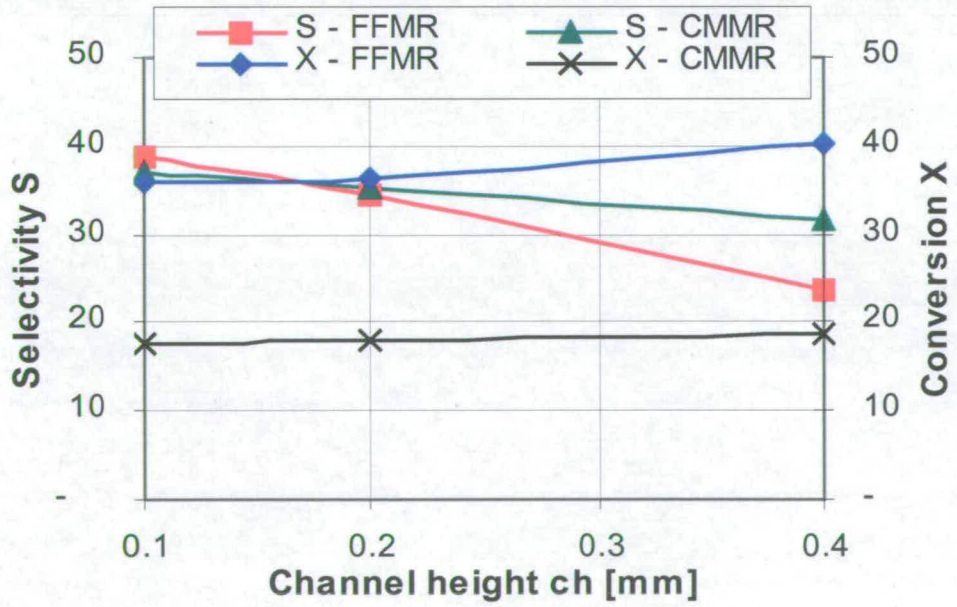

Figure 7-17. Comparison of X and S (near the reactor mouth) with the FFMR and the CMMR as function of the reactor size. Membrane thickness $mh = 0.025$; $\kappa=0$

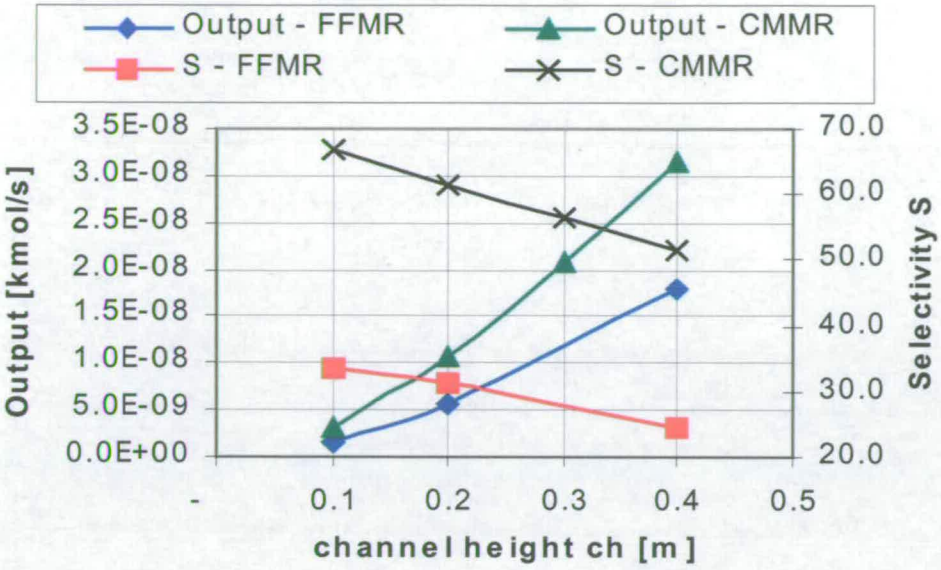

Figure 7-18. Comparison of the product output and *S* with the FFMR and the CMMR as function of reactor size. Membrane thickness *mh* increases proportional to the channel height ch_l; catalytic activity κ=5

7.3.3 Discussion

Heat generation and temperature distribution were analysed as they occur with the direct fluorination in a microreactor. Reactor design, i.e. the size of the reaction channel and the thickness of the membrane have great influence on the performance. With increasing reactor size the temperature in the reaction channel increases. Charged with equal heat load the membrane inside the CMMR strongly supports heat removal from the reaction plane. A standard size FFMR shows strong heat removal, but with increasing reactor size significant differences between the FFMR and CMMR occur. Due to stronger heat removal the selectivity obtained with the CMMR (constant membrane thickness) decreases with a lower gradient than with the FFMR when the reaction channel is increased.

The heat generated near the reactor entrance with a membrane reactor is lower compared to the FFMR with equal conditions because of lower absorption of fluorine. This fact also helps to control the temperature with a chemical reaction taking place inside the reactor. Coupled with high heat removal facilitated by the membrane and catalytic activity the membrane reactor performs significantly better than the FFMR especially with relatively large channels (ch_l = 0.0004mm).

The last paragraph of the previous section illustrates that mass transfer limitations and improved heat conduction with the CMMR cancel out and no strong effect is obtained through the implementation of an inert membrane with respect to the selectivity *S*. Great improvement of the selectivity can be achieved through the catalytic function of the membrane.

7.4 Entrance effects

7.4.1 Model and procedure

Approach

Near the reactor mouth there is an entrance zone where the velocity and temperature profiles change in direction of the x-coordinate. In this flow developing zone elevated heat transport between the liquid channel and the reactor housing can be expected. With the upcoming simulation study we investigate the occurrence of a thermal entrance zone in the FFMR and CMMR configurations. The heat transfer coefficient for the liquid channel is calculated using a procedure analogous to the one illustrated in Appendix E for the determination of mass transfer coefficients.

Model domain

The mathematical model for the FFMR and CMMR introduced in Chapter 3 is used for the investigation of the hydrodynamics and heat transport in the liquid phase. The numerical solver is based on a 3D finite element discretisation, which allows the calculation of second order spatial derivatives of the velocity vector comprised in the Navier-Stokes equations, and three-dimensional fluid flow can be simulated. The mass conservation equations are excluded from the model. The heat of reaction is introduced as a boundary condition at the top membrane wall with $q = 8\ kJ/m^3$ corresponding to the maximum heat of reaction obtained with standard operating conditions (see above).

Procedure

In microreactors the flow often is in the laminar regime due to the small dimensions and lower velocities at similar residence times compared to large-scale equipment. Here, the laminar boundary layer continues to grow until it occupies the whole channel cross-section. Laminar flow in a two-dimensional stationary duct is designated thermally fully developed when the dimensionless fluid temperature distribution, as expressed in brackets, at a cross-section is invariant, i.e. independent of x:

$$\frac{\partial}{\partial x}\left[\frac{T_l^* - T_l}{T_l^* - \overline{T}_l}\right] = 0 \qquad (7\text{-}3)$$

where: $T_l = f(x,y,z)$, unlike $\vec{v}_l$, which is a function of y and z only and is independent of x for fully developed flow. The thermal entrance length for standard cases is equal to the hydrodynamic entrance multiplied by the Prantl number, which for our process is bigger then

unity. Here, we are dealing with a conjugated heat transfer problem. According to Shah and London (1978) for a conjugated problem the flow is always thermally developing. However, the dimensionless fluid temperature varies much more near the reactor mouth compared to downstream where it approaches a constant value. With constant heat flux and the opposite wall at constant temperature an order of magnitude estimation is possible using the classic equation for the of the entrance length with constant wall temperature (Bejan, 246):

$$\frac{X_T}{D_h} \cong 0.05\,\mathrm{Re}_{Dh}\,\mathrm{Pr} \tag{7-4}$$

In microreactors developing flow may be the dominating flow regime. This is especially true for microreactors with a relatively large hydraulic diameter in the range $d_h = 0.15$ - 1mm and high Reynolds numbers larger than 100, see Figure 7-19. With the process considered in this work at a maximum velocity of u=0.00284m/s we find that the flow is fully developed after only a few millimetres.

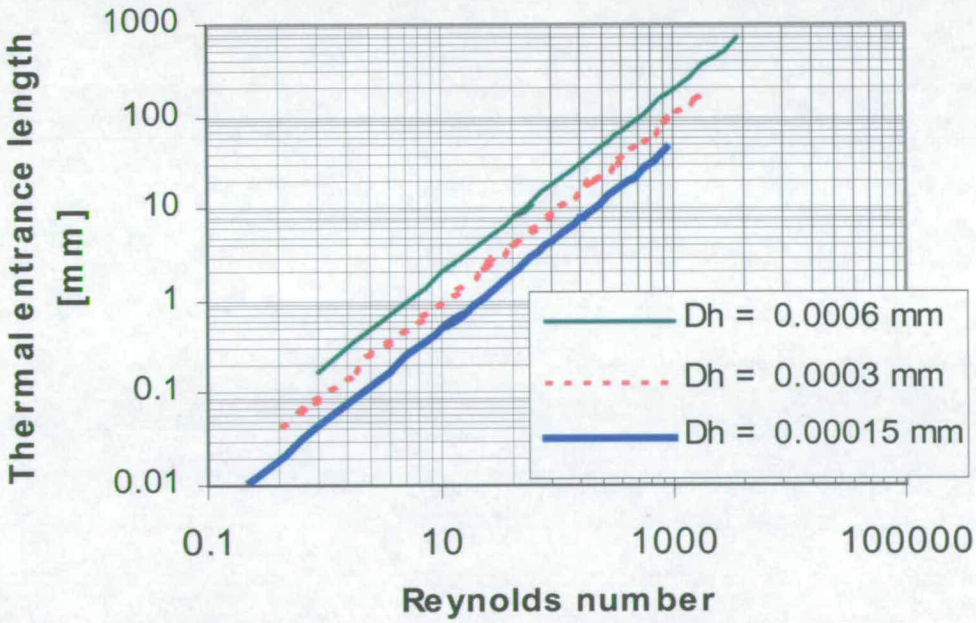

Figure 7-19. Thermal entrance length as a function of *Re* and d_h; *Pr*=6.4

7.4.2 Results

In Figure 7-20 the heat transfer coefficient between the liquid channel wall and the reactor housing is shown versus the x-coordinate. The maximum value on the dimensionless x-axis $x^+ = 1$ corresponds to $x = 6.5$ mm. Clearly, entrance effects cease to exist after about $x = 1$ mm into the reactor. Within this developing zone we find much increased heat transfer coefficients but the actual heat transported away from the liquid channel is small, see Figure 7-21. This is due to the fact that the liquid is cold near the reactor entrance and most of the heat is absorbed into the liquid phase before conduction towards the reactor housing occurs. Thus, the high transfer coefficient in the developing zone is not exploited in terms of high heat fluxes.

In Figure 7-21 the heat conduction through the membrane is compared to heat removal through the liquid channel. Near the reactor mouth heat conduction through the membrane works far more effectively than transport through the channel wall or bottom due to the proximity of the membrane to the reaction plane and high thermal conductivity. Heat transport through the channel bottom is particularly low see, Figure 7-21. Thus, in cases where the developing zones dominates most of the reactor, i.e. at Reynolds numbers Re>100 and d_h>0.3mm, most of the heat would be transported through the catalyst and the reactor walls. Here, a high aspect ratio, i.e. square cross-section, would be desirable because such reactors would not rely on heat conduction through the bottom but the membrane or the reactor wall.

Heat transport through the membrane (mh=0.05mm) continuous to be important throughout the reactor, also with developed flow. Transport through the reactor bottom becomes more important than through the walls keeping in mind the aspect ratio (a=0.33) of the reaction channel used in this work. Here, a low aspect ratio would be beneficial to increase heat conduction through the reactor bottom. However, the pressure drop of the liquid channel increases with decreasing aspect ratio and there also is a physical limit to the reduction of the liquid flow thickness.

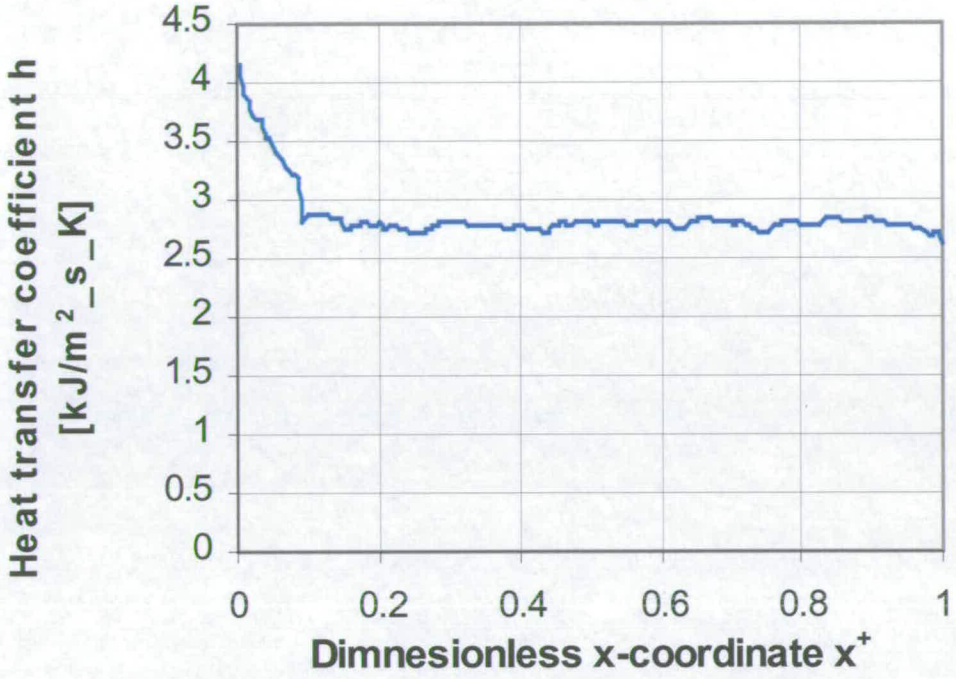

Figure 7-20. Heat transfer coefficient *h* between liquid channel and reactor wall

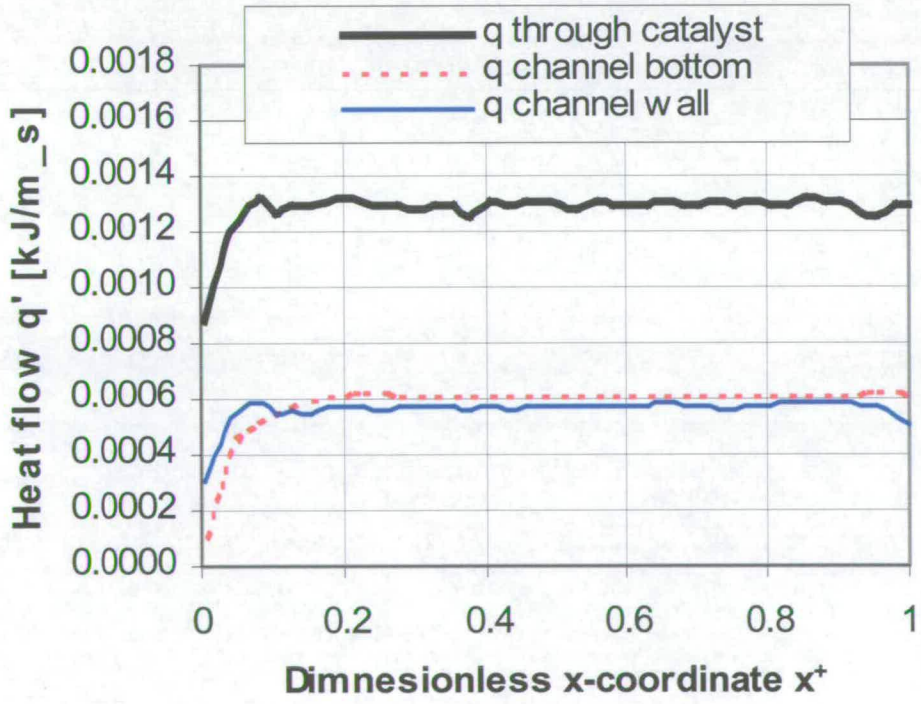

Figure 7-21. Heat flux *q* through the membrane, across the side wall and across the channel bottom; *ch*=0.2mm, *mh*=0.05mm

7.5 Summary

Heat generation and temperature distribution are analysed as they occur with the direct fluorination in a microreactor. In general, heat removal with the standard size microchannels is very efficient. However, the direct fluorination process is very exothermic and isothermal operation is not achievable. Instead, depending on the temperature of the coolant, a temperature peak occurs near the reactor mouth. Reactor design, i.e. the size of the reaction channel and the thickness of the membrane have great influence on the performance. Increasing the reactor size weakens the heat removal, which shows through the decreasing slope of the heat removal curves. This effect can lead to pronounced peak-temperatures or thermal run-away. Introducing a porous membrane made of a highly conductive material (i.e. stainless steel) into the reaction plane, the heat removal can be strengthened. Again, this shows through an increased slope of the heat removal lines. A CMMR could be designed two-times larger than a FFMR allowing the same maximum temperature at otherwise constant conditions.

The membrane inside the CMMR alters the concentration distribution and local occurrence of reactions, and also strongly supports heat removal from the reaction plane. This fact is significant especially with increasing channel size considering the safety of the process. However, the inert membrane has to be very thin, otherwise the selectivity benefits only little from the membrane because mass transfer limitations counteract the advantages achieved through improved heat removal. A catalytic membrane shows great potential to strongly improve the selectivity and the output of desired product. The zone of developing flow is very short and thus entrance effects do not have significant influence on the reactor performance.

In this section cooling was provided at constant temperature throughout the reactor. This type of cooling is feasible with two-phase cooling or single phase cooling with very high flow rates. In the next chapter the design of the heat sink and operational parameters are analysed to maximise control of the temperature in the reaction plane.

Chapter 8

Heat sink design

8.1 Introduction

So far all simulations assumed a constant temperature heat sink at the bottom reactor housing wall. In this chapter single phase cooling is considered by means of a coolant flowing in separate cooling channels. There are three different possibilities in which the coolant flow can be arranged relative to the reacting fluid: 1) co-current, 2) counter current, and 3) cross-flow. First, these coolant arrangements are employed to discharge the heat of reaction emerging from a single channel reactor. Thereafter, the same study is accomplished with parallel arrays of reaction channels where special focus is on the performance of cross-flow cooling.

8.2 Single channel CMMR configuration

8.2.1 Model domain

In this section the original CMMR model, introduced in Chapter 3 (see Figure 3-5 and Figure 3-6) is used including the cooling channel. Here, 3D finite element discretisation is necessary to be able to analyse heat conduction in all three dimensions of the Cartesian coordinate system. Due to high complexity of the model the amount of dependent variables has to be reduced and the mass conservation equations are excluded. Therewith, the gas channel does not have to be part of the model domain.

As consequence to the exclusion of the mass conservation equation the chemical reactions and thus the heat of reaction is not implemented in the model. Instead, the heat of reaction profile determined with 2D simulations in Section 7.5.2 is adopted and transformed into a heat load boundary condition for the heat conservation problem. This heat load profile is a function of the spatial x-coordinate, only and does not vary with the temperature. Thus, a feed-back situation of increasing temperature levels and increasing heat generation cannot

occur. The boundary conditions that apply uniquely to the reactor model used in this section are illustrated in Table 8-1. The thermodynamic properties of the coolant are shown in Table 8-2 which are essentially the properties of water. Pure water would freeze at the operating conditions used in this work and thus an additive would be necessary.

8.2.2 Procedure

In this section the cooling of a single channel is investigated. Two different heat load profiles are used representing the lower and upper limit of the range considered in this work :

1) A very uneven profile with high heat load near the reactor entrance (red line shown in Figure 8-1), as it occurs in the CMMR under the standard operating conditions (Table 5-3) but enlarged liquid channel ($ch_l = 0.2$ mm), elevated concentration of fluorine in the gas phase ($x_{F2,F}$=0.25) and catalytic activity κ=5.
2) A perfectly even heat load, representing the mean value of the uneven heat load (blue line in Figure 8-1).

In Table 8-3 the operating conditions and the applied heat load profiles are specified. The objective is to achieve a constant temperature in the reaction plane of the reactor. The performance of the cooling system is evaluated with regard to this objective.

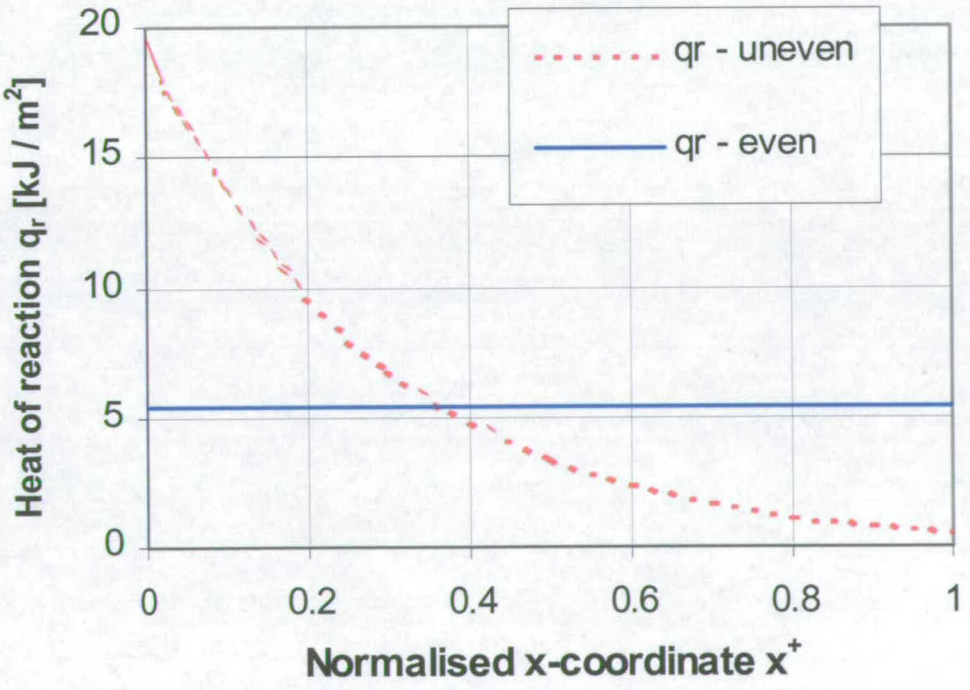

Figure 8-1. Uneven and even heat load boundary condition

Boundary	Conservation equation	Membrane Reactor - Boundary condition
membrane top wall	Energy	$-\overline{k}_{mem} \cdot \left(\frac{\partial T_{mem}}{\partial z} \right) = q_r$ where q_r is a heat load representing the heat of reaction
Cooling channel top wall	Energy	Stiff spring boundary approximating a Dirichlet boundary condition insuring continuity in flux. $-\overline{k}_c \cdot \left(\frac{\partial T_c}{\partial z} \right) = M(T_h - T_c)$ where M is a large enough number to let the temperature difference in the brackets approach zero.
Cooling channel bottom wall	Energy	$-\overline{k}_c \cdot \left(\frac{\partial T_c}{\partial z} \right) = 0$

Table 8-1. Boundary conditions with the CMM

Table 8-2. Property data of the liquid coolant (water) at T=273 K

Description	Parameter	Value	unit
Average local heat capacity	$\overline{c}_{p,c}$	4.22	$kJ \cdot kg^{-1} \cdot K^{-1}$
Average local thermal conductivity	$\overline{k}_c$	0.0006	$kJ \cdot s^{-1} \cdot m^{-1} \cdot K^{-1}$
average local density	$\overline{\rho}_{\Omega}$	1000	kg/m^3
Liquid flow rate (standard value)	V_c	$6.8 \cdot 10^{-09}$	m^3/s

Table 8-3. Operating conditions

	Parameter	Value	Unit
Mean liquid phase velocity	$\overline{v}_l$	0.00284	m/s
Height, liquif channel	ch_l	0.2	mm
Channel width	cw	0.6	mm
Channel height	hh	0.2-2	mm
Colling channel height	ch_c	0.2-2	mm
Uneven heat profile	q_r	$19.252 \cdot \exp(-3.488 \cdot x^+)$ where: $0<x^+<1$	kJ/m^2
Even heat profile	q_r	5.35	kJ/m^2

8.2.3 Result

Uneven heat load

In this section the performance of several coolant flow arrangements, including co-current, counter-current and constant temperature heat exchangers, is tested with a very uneven heat load. In Table 8-4 the results obtained with co-current coolant flow are illustrated. The standard deviation and the mean and maximum value of the temperature in the reaction plane are calculated for both spatial coordinates of the reaction plane. The temperature profile at the top of the membrane is illustrated in Figure 8-2 for the most interesting cases.

The base case is illustrated in the first row of Table 8-4 and Figure 8-2a. The flow rate of the coolant V_c is adjusted so that the temperature distribution in the reaction plane is relatively uniform (low standard deviation $s_{\bar{T}_l}[T_r\ (x)]$). However, the mean reactor temperature $\bar{T}_r$ =266 K is much higher than the desired temperature $T_{r,opt}$ = 257 K, which results in a high standard deviation with regard to the desired temperature of $s_{T_{opt}}[T_r\ (x)] = 7$ K. In the following, results of simulation experiments are investigated, which are obtained at operating conditions in the cooling channel that alternate from the base-case.

First, the thickness of the reactor housing *hh* is changed to investigate longitudinal heat conduction (in direction of x-coordinate) within the reactor housing. The temperature profile in the reactor with a thick reactor housing (*hh*=2) is shown in Figure 8-3 (different scaling factors are used for the cooling channel and the remainder of the reactor configuration) and conduction within the reactor housing is visualised by black arrows. This heat flux vector has a component parallel to the x-coordinate pointing towards the reactor mouth. In this manner the standard deviation $s_{\bar{T}_r}[T_r\ (x)]$ decreases with increasing *hh*. However, this heat flow causes a slight increase in the hot spot temperature near the reactor mouth and more pronounced transversal temperature deviation $s_{\bar{T}_r}[T_r\ (y)]$ (compare Figure 8-2a and Figure 8-2b). Altogether, the thickness of the reactor housing has only little influence under the conditions of this investigation.

A strong influence on the temperature profile in the reactor can be attributed to the height of the cooling channel ch_c. So far a very flat channel was considered where heat conduction in transversal direction did not play an important role. If the cooling channel is enlarged (with constant coolant flow rate V_c) a hot spot T_r = 271 K develops within the cooling channel sub-

domain at $x = 1/3 \cdot cl$ due to limitations in transversal heat conduction. This temperature increase at the top wall of the cooling channel results in higher temperature non-uniformity and higher mean and maximum temperatures in the reaction plane, see Figure 8-2c.

Another important parameter is the coolant flow rate V_c, as can be seen in Figure 8-2e. At reduced coolant flow the standard deviation of the temperature increases, signalising a non-uniform profile and a pronounced peak establishes near the end of the reactor ($x = cl$). Very good results can be achieved by reducing the coolant inlet temperature T_c by 7 K. In this manner we get a nearly isothermal temperature distribution (low $s_{\bar{T}_r}[T_r(x)]$) in the reaction plane and a mean temperature very close to the desired temperature (Figure 8-2d).

Considering a counter-current coolant flow arrangement we find a non-uniform temperature profile at the top of the membrane with a pronounced peak near the beginning of the reactor ($x = 0$), see Table 8-5 and Figure 8-2g. Lowering the coolant temperature does result in a mean temperature which is closer to the desired one but the standard deviation and the maximum temperature are not improved significantly.

At equal coolant inlet temperature the heat sink at constant temperature performs better than co-current coolant flow with regard to the highest temperature in the reaction plane (see Table 8-5). However, the standard deviation with respect to the mean temperature is higher and a heat sink at constant temperature is more difficult to establish.

Constant heat load

In this paragraph we assume a spatially constant heat load working on the reaction plane to test various cooling channel arrangements. The heat load does not vary along the reactor length and therefore the co-current and the counter-current coolant arrangements show similar performance. With co-current coolant arrangement a relatively high standard temperature deviation $s_{T_{r,opt}}[T_r(x)] = 6\,K$ with regard to the desired temperature and a high maximum temperature $T_{max} > 266$ K occur (Figure 8-4a). Reducing the coolant temperature does not improve the high standard deviation of the temperature $s_{\bar{T}_r}[T_r(x)] = 2\,K$ but the mean temperature is close to $T_{r,opt}$ and the maximum temperature is lower $T_{max} < 262$ K (Figure 8-4b). However, the best results can be achieved with a heat sink at constant temperature, see (Figure 8-4c).

Table 8-4. Temperature distribution at the top of the membrane at uneven heat distribution and co-current flow

hh	ch_c	V_c	T_c, T_0	$\overline{T}_r$	$s_{\overline{T}_r}[T_r(x)]$	$s_{T_{r,opt}}[T_r(x)]$	$s_{\overline{T}_r}[T_r(y)]$	$s_{T_{r,opt}}[T_r(y)]$	T_{max}
mm	mm	m^3/s	K	K	K	K	K	K	K
0.2	0.2	6.8E-09	257.15	264.28	0.24	7.15	0.51	7.22	266.14
0.5	0.2	6.8E-09	257.15	264.51	0.24	7.38	0.51	7.45	266.19
1	0.2	6.8E-09	257.15	264.51	0.22	7.38	0.52	7.45	266.40
2	0.2	6.8E-09	257.15	264.64	0.17	7.51	0.52	7.58	266.68
0.2	**0.2**	6.8E-09	257.15	264.27	0.27	7.14	0.51	7.21	266.12
0.5	**0.5**	6.8E-09	257.15	264.79	0.39	7.67	0.51	7.73	267.31
1	**1**	6.8E-09	257.15	265.76	0.91	8.68	0.52	8.71	269.02
2	**2**	6.8E-09	257.15	267.73	1.66	10.74	0.52	10.70	271.76
0.2	0.2	6.8E-09	**257.15**	264.28	0.24	7.15	0.51	7.22	266.14
0.2	0.2	6.8E-09	**252.15**	259.26	0.25	2.13	0.50	2.19	261.04
0.2	0.2	6.8E-09	**250.15**	257.25	0.26	0.28	0.50	0.51	258.99
0.2	0.2	3.4E-09	257.15	269.42	1.97	12.46	0.52	12.41	271.31
0.5	0.2	3.4E-09	257.15	269.81	1.95	12.84	0.52	12.80	271.66
1	0.2	3.4E-09	257.15	269.81	1.88	12.83	0.52	12.80	271.58

Table 8-5. Temperature distribution at the top of the membrane at uneven heat distribution with counter-current flow and constant temperature heat sink

hh	ch_c	V_c	T_c, T_0	$\overline{T}_r$	$s_{\overline{T}_l}[T_r(x)]$	$s_{T_{opt}}[T_r(x)]$	$s_{\overline{T}_l}[T_r(y)]$	$s_{T_{opt}}[T_r(y)]$	T_{max}
mm	mm	m^3/s	K	K	K	K	K	K	K
Counter-current flow									
0.2	0.2	**3.4E-09**	257.15	262.94	5.75	8.17	0.52	5.87	277.88
0.2	0.2	**6.8E-09**	**257.15**	260.96	3.69	5.32	0.51	3.89	270.82
0.2	0.2	6.8E-09	**255.15**	**258.96**	**3.69**	**4.11**	**0.51**	**1.89**	**268.78**
Constant temperature heat sink T=const.)									
0.2	0.2	/	257.15	258.757	1.46	2.18	0.51	1.70	263.99

Table 8-6. Temperature distribution at the top of the membrane at constant heat load; ch_c=0.2mm

Set-up	hh	V_c	T_c, T_0	$\overline{T}_r$	$s_{\overline{T}_l}[T_r(x)]$	$s_{T_{opt}}[T_r(x)]$	$s_{\overline{T}_l}[T_r(y)]$	$s_{T_{opt}}[T_r(y)]$	T_{max}
	mm	m^3/s	K	K	K	K	K	K	K
Co-current	**0.2**	6.8E-09	257.15	262.69	2.11	5.94	0.52	5.62	266.82
Co-current	**0.0**	6.8E-09	257.15	262.80	2.12	6.05	0.47	5.73	266.87
Co-current	0.2	6.8E-09	**253.15**	257.67	2.11	2.17	0.51	0.73	261.78
T=const	0.2	/	257.15	258.78	0.05	1.63	0.52	1.72	259.46

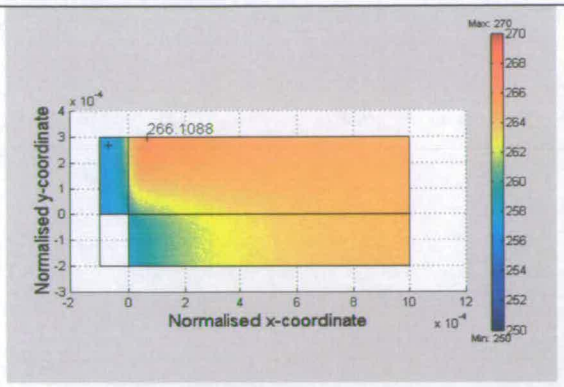

a) Co-current flow
hh=0.2mm, ch_c=0.2mm,
V_c=6.8E-9 m^3/s, T_c=257K

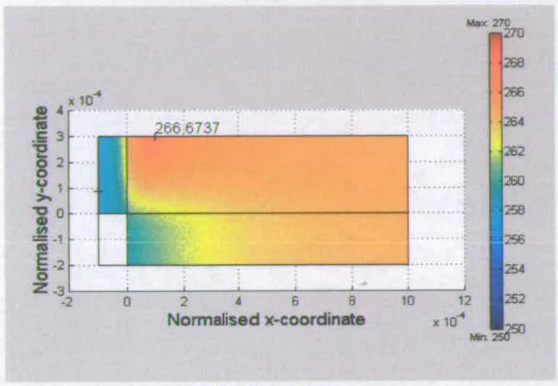

b) hh= 2mm

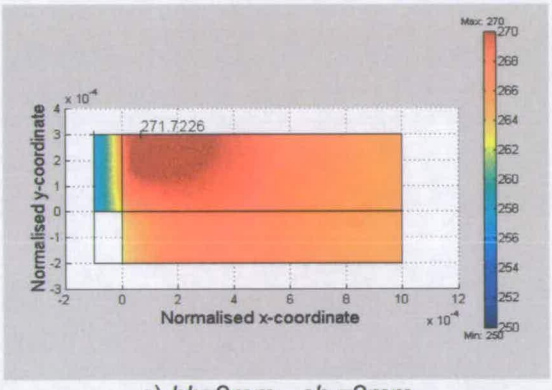

c) hh=2mm , ch_c=2mm

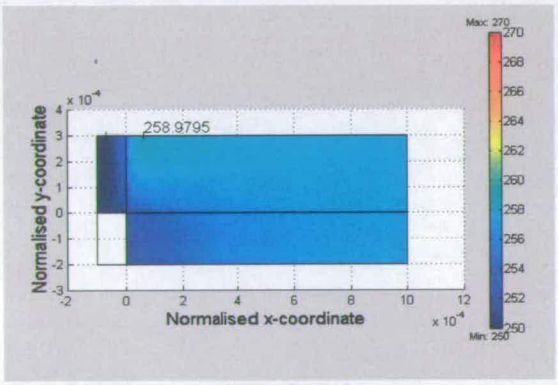

d) T_c=250K

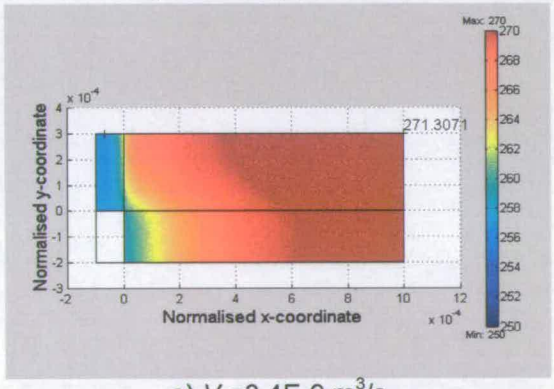

e) V_c=3.4E-9 m^3/s

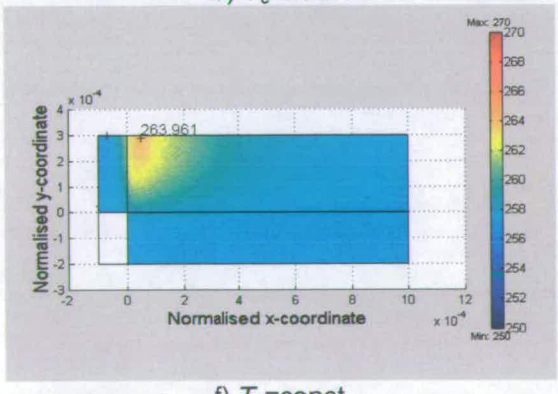

f) T_c=const.

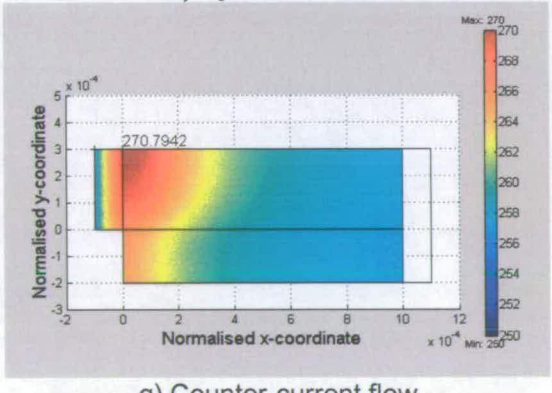

g) Counter-current flow

Figure 8-2. Temperature distribution T_r / K at the top of the membrane at uneven heat distribution under varying conditions

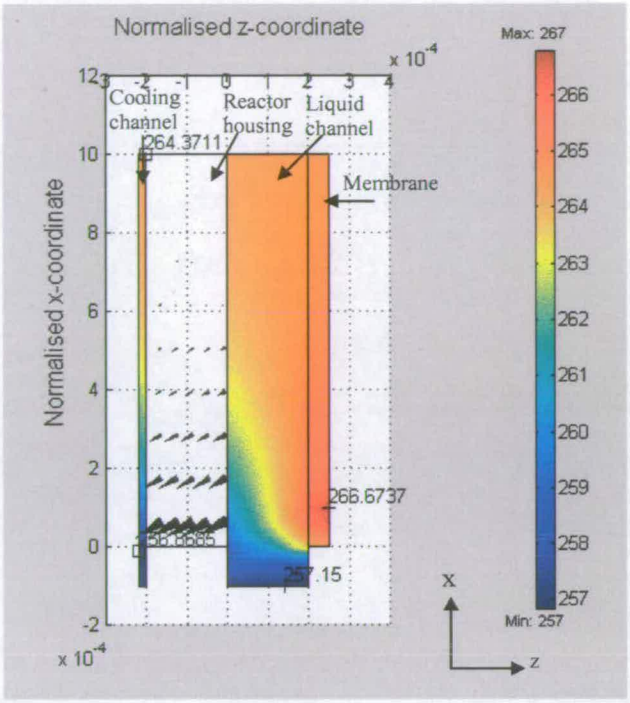

Figure 8-3. Temperature profile T_r / K in the cooling channel (co-flow arrangement), the liquid channel and the membrane domain; hh=2 mm, ch_c=0.2 mm, V_c=6.8·10^{-9} m^3/s

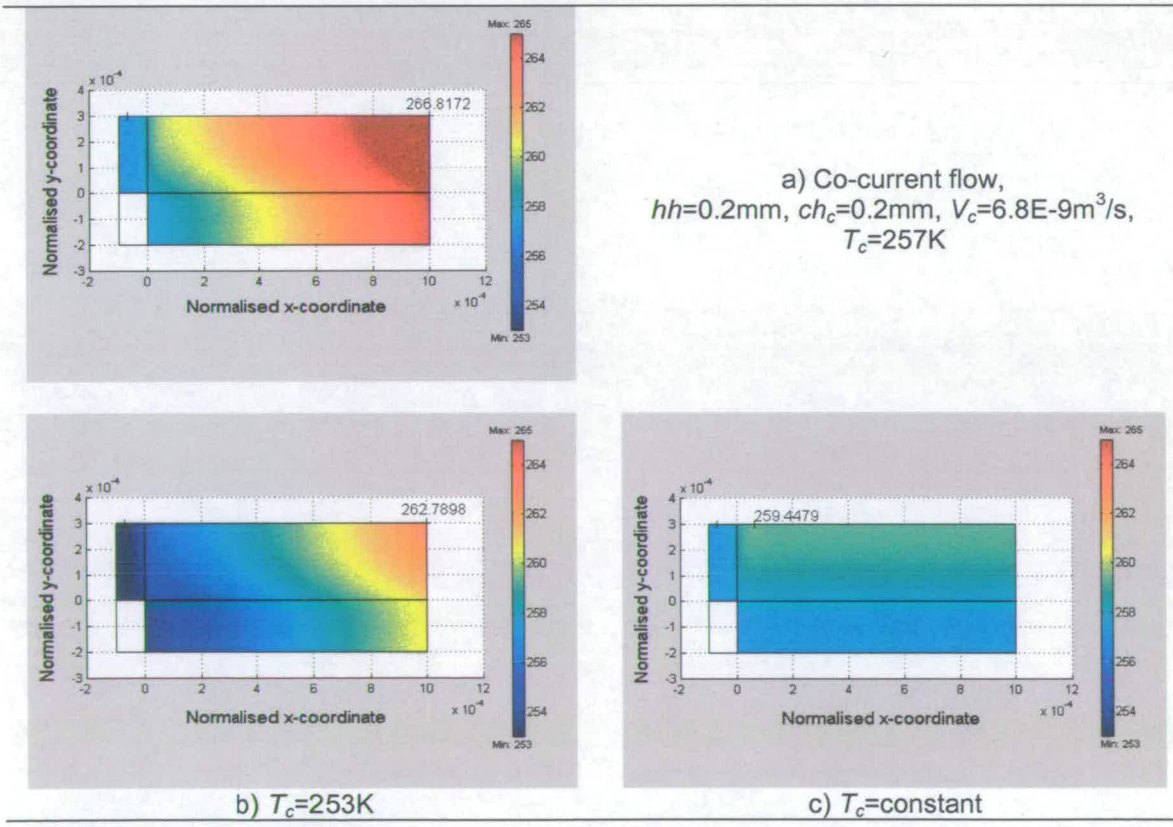

Figure 8-4. Temperature distribution T_r / K at the top of the membrane at even heat distribution under varying conditions (corresponding to Table 8-6)

Discussion and summary

With the CMMR under consideration and highly non-uniform heat profile, the co-current coolant flow arrangement shows the biggest potential to obtain an isothermal reaction plane temperature, compared to constant temperature heat sink and counter-current flow. The best results are achieved with a coolant flow set on a temperature $T_{c,0}$ that is cooler than the reactant inlet temperature $T_{l,0}$. Transversal heat transfer limitations can occur in relatively high cooling channels. In this manner hot spots in the cooling channel occur, leading to locally elevated temperatures in the reaction plane.

With a constant heat load co- and counter current heat exchangers feature similar performances and relatively high standard deviations have to be accepted at the considered coolant flow rate. Here, a heat sink at constant temperature performs best.

Rebrov et al. (2003) have investigated cross flow cooling with microreactor arrays and report satisfying performance with respect to the reduction of spatial temperature gradients. This coolant arrangement has great potential to perform well with uneven and even heat load profile considered in this chapter. The advantage is that the inlet flow rate to each coolant channel can be adjusted individually with respect to the local heat load. On the downside a complex flow distribution scheme has to be developed. In the following section cross-flow cooling is tested with parallel arrays of reaction channels.

8.3 Multiple channel reactor configuration

8.3.1 Model and procedure

In this section cooling of parallel arrays of reaction channels is investigated. The reactor consists of up to 64 channels. The model domain used in this section is based on the original model, introduced in Chapter 3 (see Figure 3-5). However, a detailed representation of all 64 parallel channels within the modelling domain is too complex and beyond the scope of this work. Therefore a simplified model is used which consists of the reactor housing and the cooling channel, only. In this reactor representation the mass conservation equations are unemployable. This means, that the chemical reactions and thus the heat of reaction are not implemented in the model. Instead, the heat of reaction profile determined with 2D simulations in Chapter 7 is adopted and transformed into a heat load boundary condition to the top of the reactor housing top wall, see Figure 8-5. The heat load profile is only a function of the spatial x-coordinate. Here, 3D finite element discretisation is used to be able to analyse heat conduction in all three dimension of the Cartesian coordinate system. The important boundary conditions and operational parameters are illustrated in Table 8-7 and Table 8-8, respectively.

The objective is to find a coolant arrangement that facilitates constant temperature at the top wall of the reactor housing. (Note that this is not equivalent with the goal of achieving a constant temperature in the reaction plane.) Special focus is on the performance of the cross flow heat exchanger and attention is paid to the transversal temperature profile (y-direction). The inlet temperature to all coolant channels is at $T_{l,0} = 257.15$ K and the individual flow rates are proportional to the heat load in each cross-section. The width of the reactor domain is variable representing between 1 and 64 reaction channels in parallel.

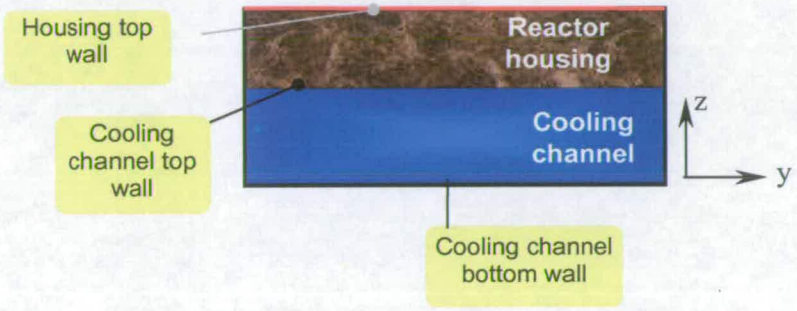

Figure 8-5. Scaled geometry of the two dimensional domain including boundary and sub-domain labels.

Table 8-7. Boundary conditions with the reactor domain

Boundary	Conservation equation	Membrane Reactor - Boundary condition
Cooling channel top wall	Energy	Stiff spring boundary approximating a Dirichlet boundary condition insuring continuity in flux. $-\bar{k}_c \cdot \left(\frac{\partial T_c}{\partial z}\right) = M(T_h - T_c)$
Cooling channel bottom wall	Energy	$-\bar{k}_c \cdot \left(\frac{\partial T_c}{\partial z}\right) = 0$
Housing top wall	Energy	$-k_h \cdot \left(\frac{\partial T_h}{\partial z}\right) = q_r$ where q_r is a heat load representing the heat of reaction

Table 8-8. Operating conditions

Parameter	Value	Unit
hh	0.2-2	mm
ch_c	0.2-2	mm
uneven profile	q_r=19.252·exp(-3.488·x^+) where: 0<x^+<1	kJ/m^2
even profile	q_r= 5.35	kJ/m^2
No. of channels in parallel	1-64	

8.3.2 Results

Uneven heat load

The performance of a reactor-integrated heat exchanger is investigated being confronted with a very uneven heat load. Special focus is on the maximum temperature and the temperature distribution in the reaction plane.

First, cross-flow cooling is considered. From Table 8-9 we find that very tight temperature control of a single channel reactor is possible with a cross flow reactor (see Figure 8-6a). Values obtained for the standard deviation $s_{\bar{T}_r}[\mathrm{T_r}(y)]$=0.005 K are low and the mean temperature $\bar{T}_r = 257.28$ K is close to the desired value $T_{r,opt} = 257.15$ K. Considering an array off 64 reaction channels in parallel we find that the maximum temperature in the reactor is elevated significantly from the desired temperature (>5K). Also, the standard deviation increases a lot in transversal ($s_{\bar{T}_r}[T_r(y)]$=1.17 K) and longitudinal ($s_{\bar{T}_r}[T_r(x)]$=0.71 K) direction. In general we can say that an increasing amount of parallel channels amplifies the non-uniformity and elevation of the maximum temperature (Figure 8-6b) with cross-flow cooling.

Next, the influence of the thickness of the reactor housing on the temperature in the reaction plane is investigated. Increasing the thickness of the reactor housing results in a slight decrease of the maximum temperature at the top of the reactor housing ((Figure 8-6c). This effect is due to the transversal heat conduction in the reactor housing. In Figure 8-7 the temperature profile in the reactor housing and the cooling channels is displayed and heat conduction within the housing is visualised by black arrows. Heat flows towards the inlet of the coolant and away from the temperature hot spot. Therewith the standard deviation in transversal direction decreases. However, heat dispersion in longitudinal counteracts the effectiveness of the cross-flow arrangement, which shows through elevated standard deviation in longitudinal direction $s_{\bar{T}_r}[T_r(x)]$.

Finally, the performance of the cross-flow reactor is compared to the co-current reactor with a highly non-uniform heat profile. We find that with a 64 channel array co-current flow is superior to cross-flow with respect to the highest temperature in the reactor, (see Figure 8-6b and (Figure 8-6d). However, the temperature profile non-uniformity at the top of the reactor housing is more pronounced with co-current flow, which can be seen from the values of the standard deviation in x- and y-direction ($s_{\bar{T}_r}[\mathrm{T_r(x)}]$ and $s_{\bar{T}_r}[\mathrm{T_r(y)}]$). Reducing the feed temperature from $T_{l,0}$ = 257 K to 252 K with the co-current flow setting further improves the performance of this cooler type where $s_{\bar{T}_r}[\mathrm{T_r(x)}]$ is still higher but $s_{\bar{T}_r}[\mathrm{T_r(y)}]$ is lower compared to the cross-flow cooler. Similarly, with the cross-flow arrangement we can expect

improvement through adjusting the inlet temperatures of the individual coolant channels with the cross-flow arrangement. Compared to the co-current setting the cross-flow reactor would require a more complicated adjustment of the various coolant inlet streams is required.

Constant heat load

In this paragraph we assume a constant heat load on the modelling domain to test various cooling channel arrangements. Here the domain width is chosen to represent 64 reaction channels including channel walls. The cross-flow arrangement with hh = 2.0 mm results in a maximum temperature T_{max} = 264.5 K which lies 7 K above the desired temperature and a relatively low standard deviation $s_{\overline{T}_r}[T_r(x)]$ = 0.94 K. Reducing the housing thickness to hh = 0.2 mm results in a increased hot spot temperature T_{max} = 270 K. This is due to the fact that at the reactor end there is a section without cooling channel, which is twice as big as the gap between cooling channels. Thus the conduction ways are long which results in elevated temperatures.

The heat load does not vary along the reactor length and therefore the co-current and the counter-current coolant arrangements show similar performance. With the co-current arrangement a relatively high standard temperature deviation $s_{\overline{T}_r}[T_r(x)]$ = 2.1 K and a moderate maximum temperature occur (T_{max} = 264.7 K, Table 8-10 bottom row) similar to the maximum temperature achieved with the best cross-flow arrangement. The maximum temperature in the reaction plane can be lowered by reducing the coolant inlet temperature to T_c = 255.15 K and this performance is superior to what can be achieved with the cross-flow reactor.

Table 8-9. Temperature distribution at the top of the membrane at uneven heat distribution; ch_c=0.2mm

No.	cw	hh	V_c	T_c, T_0	$\overline{T}_r$	$s_{\overline{T}_r}[T_r(x)]$	$s_{T_{r,opt}}[T_r(x)]$	$s_{\overline{T}_r}[T_r(y)]$	$s_{T_{r,opt}}[T_r(y)]$	T_{max}
	mm	mm	m^3/s	K	K	K	K	K	K	K
Cross-flow cooling										
64	29	0.2	4.35E-07	257.15	259.70	0.71	2.65	1.17	2.83	**266.22**
32	14.5	0.2	2.18E-07	257.15	258.64	0.59	1.60	0.62	1.63	**263.61**
10	4.53	0.2	6.80E-08	257.15	257.77	0.38	0.73	0.18	0.65	**260.60**
1	0.453	0.2	6.80E-09	257.15	257.29	0.17	0.22	0.01	0.14	**258.74**
64	29	2.0	4.35E-07	257.15	259.62	0.90	2.63	0.87	2.64	**263.75**
1	0.453	2.0	6.80E-09	257.15	257.35	0.19	0.28	0.05	0.20	**258.04**
Co-current cooling										
64	29	0.2	4.35E-07	257.15	262.67	1.61	5.76	0.02	5.57	264.19
64	29	2.0	4.35E-07	**257.15**	262.67	**1.41**	**5.72**	**0.003**	**5.58**	**263.98**
64	29	0.2	4.35E-07	252.00	257.67	1.61	1.69	0.02	0.52	259.19

Table 8-10. Temperature distribution at the top of the membrane at even heat load distribution; ch_c=0.2mm, channel-no.= 64, cw=29 mm

Set-up	hh	V_c	T_c, T_0	$\overline{T}_r$	$s_{\overline{T}_r}[T_r(x)]$	$s_{T_{r,opt}}[T_r(x)]$	$s_{\overline{T}_r}[T_r(y)]$	$s_{T_{r,opt}}[T_r(y)]$	T_{max}
	mm	m^3/s	K	K	K	K	K	K	K
Cross-flow	**0.2**	4.35E-07	257.15	261.63	0.94	4.59	2.15	5.01	270.24
Cross-flow	**2.0**	4.35E-07	257.15	261.34	0.33	4.21	1.57	4.52	264.50
Co-current	0.2	4.35E-07	257.15	261.13	2.12	4.52	0.01	4.02	264.74
Co-current	0.2	4.35E-07	**255.15**	259.13	2.12	2.90	0.01	2.00	262.74

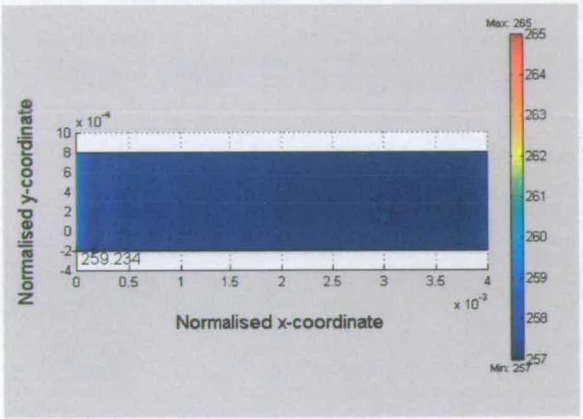

a) Cross-flow arrangement; 1 reaction channel, hh= 0.2mm, ch_c=0.2mm, V_c=6.8E-9m^3/s, T_c=257K

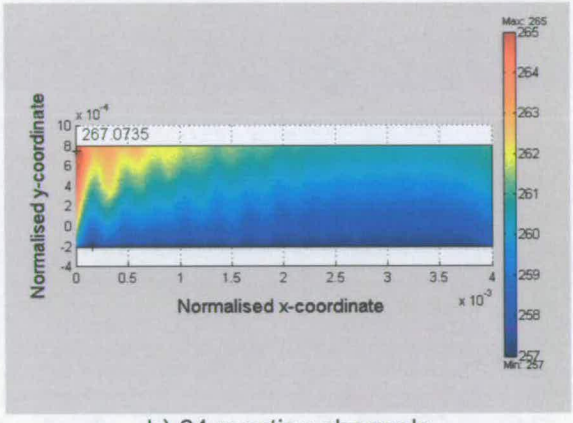

b) 64 reaction channels

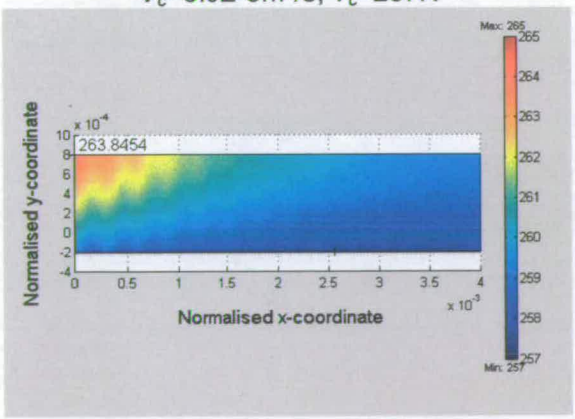

c) 64 reaction channel , hh=2mm

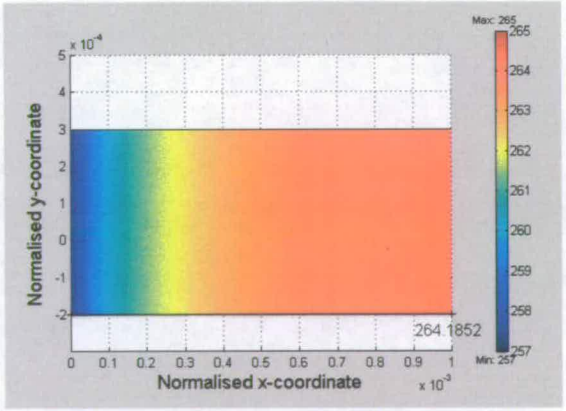

d) Co-current flow; 64 reaction channels

Figure 8-6. Temperature distribution T_r / K at the top of the membrane at uneven heat distribution under varying conditions (corresponding to Table 8-9)

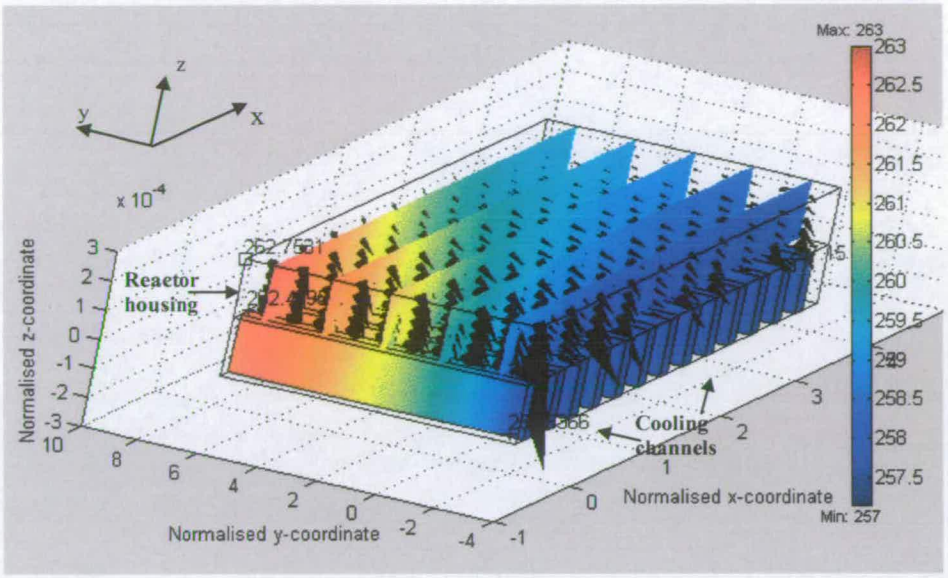

Figure 8-7. Temperature profile T_r / K in the cooling channel (cross-flow arrangement), the liquid channel and the membrane domain; hh=2 mm, ch_c=0.2 mm, V_c=4.35·10^{-7} m^3/s

8.3.3 Discussion

Considering a single channel reactor domain and highly non-uniform heat profile, the cross-flow coolant arrangement shows great potential to obtain an isothermal reaction plane temperature. This result is in line with findings by Rebrov et al. (2003) who reported results with cross flow cooling of ammonia oxidation in microreactor arrays (only few reaction channels in parallel) and found satisfying performance with respect to the reduction of spatial temperature gradients. Increasing the array of parallel reaction channels results in transversal temperature gradients. With 64 channels the cross-flow arrangement results in a pronounced hot spot near the reactor entrance.

Increasing the thickness of the reactor housing results in a slight decrease of the maximum temperature at the top of the reactor housing with cross flow cooling. This effect counteracts the effectiveness of the cross-flow arrangement, which can be seen from the elevated standard deviation in longitudinal direction, because heat is spread from the hot spot towards the end of the reactor where the coolant flow is relatively low. Rebrov et al. (2003) report similar results concerning the influence of the thickness of the reactor housing.

The temperature in large arrays of reaction channels is better handled with co-current coolant heat flow with regard to the maximum temperature. However, the standard deviation in x-direction is much higher with co-current flow. We have to keep in mind that there is potential for optimisation with the cross-flow reactor through the adjustment of the individual

coolant feed temperature. Hot spots may occur where the distance to cooling channels is too long and the reactor housing thickness *hh* is too low to allow longitudinal relaxation.

8.4 Summary

From the results obtained in this chapter we can deduce that with the process under consideration co-current cooling should be used for highly uneven heat generation profile along the reactor and large parallel arrays of reaction channels. For relatively even heat generation profile a heat sink at constant temperature, i.e. a boiling fluid, would be most efficient. Cross-flow cooling is interesting where only few micro-channels are arranges in parallel.

We cannot give a concrete result for the best cooling arrangement because the reactor conditions and thus the heat load profile in the reactor are not definite. However, in Chapter 6 a setting for the feed concentration of fluorine $x_{F2,F}$=0.075 was suggested to achieve high yield Y which results in a heat load which is closer to the even one than to the very uneven one with referring to Figure 8-1. Considering the results obtained with even heat load, a constant temperature heat load would be most efficient coolant arrangement but might not be wanted for reasons of complexity. Cross-flow cooling would work best if the parallel array of channels is not very big, again this arrangement is relatively complex. Furthermore, the gap between the individual cooling channels must not be too large which necessitates many cooling channels in parallel. Co-current coolant flow is not ideal but easy to implement and imposes no constraints on the size of the parallel array. Here, the coolant flow rate should be adjusted carefully and must not be too low, to avoid temperature hot spots near the reactor end.

Counter current coolant flow should be avoided. The intrinsic properties of counter-current flow lead a relatively poor performance with the process under consideration. If it was used the operation point of the reactor should feature low gradient of the heat generation line and large gradient of the heat removal line (see Chapter 7) as well as a high heat capacity and volume flow rate to avoid thermal runaway (see Appendix C).

Chapter 9

Conclusions

9.1 Outline

The goals for the work described in this thesis were:

- Identification of the range of application and the technological benefits gained by the use of microreactors designed for the production of chemicals.
- Design of a microreactor configuration for the chemical manufacture of fluorinated toluene and development of a process model.
- Acquisition of an understanding of the chemical process under consideration and testing of the reactor performance in a simulation study.

The former goal is concerned with the status quo of micro-reaction engineering. A lot of research has been done and many articles have been published but the industrial application of these devices did not proceed. To show the capabilities of microreactors we investigated processes that were conducted successfully in microreactors and had caused problems or could not be conducted in large-scale devices. In this manner we identified the special characteristics of microreactors and suitable concepts for microreactor design.

The direct fluorination of toluene benefits from micro-reaction technology because it is a simple process that is difficult to control and commercially interesting compounds can be produced. A novel catalytic membrane microreactor configuration (CMMR) was designed intended for the manufacture of mono-fluorinated toluene. A rigorous mathematical model was developed for this process. The usability of this microreactor was tested in a simulation study based on this model. We considered the influence of operating conditions, heterogeneous catalysis of the desired reaction, and heat management on the process performance. Heat management is particularly important with regard to process safety and process scale-up.

9.2 Applications of microreactor systems

Over the last decade a lot of reactions were accomplished with laboratory microreactors. Processes that made intense use of the unique characteristics of miniaturised channels were conducted successfully and show great potential for scale-up. Novel reaction routes and processes became feasible, because economical or technological limitations were overcome through miniaturisation. The efficiency of the individual chemical reaction processes was increased in terms of improved or unique product quality, higher selectivity, reduced equipment cost and process conditions unachievable in conventional equipment (i.e. spatial and temporal gradients of temperature and concentration).

The intrinsic first principle properties of microreactors include high gradients for temperature, concentration, density, or pressure, as well as high surface to volume ratios. Results from a literature review show that these unique characteristics of microreactors support process intensification and encourage the synthesis of unit operations. Micro-scale reactors are capable of process intensification through multifunctionality on various levels, i.e. on the catalyst level (e.g. through thin film catalysts with low diffusion barrier) and intra-reactor level (reproducible mixing of multi-phase fluidic systems). Inter-reactor multifunctionality, i.e. the synthesis of plant items in one unit, strongly benefits from the intrinsically steep gradients of temperature and concentration in microreactors.

In this thesis, the information illustrated above was used to design a catalytic membrane microreactor configuration (CMMR) that was proposed for the fluorination of toluene using elemental fluorine. Reactor multi functionality and process synthesis were the key design paradigms underlying the CMMR configuration. The most important feature of this reactor is a multifunctional catalytic membrane (with no permselectivity).

9.3 Development of microreactor models

Unlike traditional plant simulators that focus on flow sheets and unit operations, micro-chemical plant design emphasises detailed understanding of individual components. Therefore, a rigorous mathematical description of the direct fluorination of toluene process was created using heat, mass and momentum conservation equations. In this manner a detailed process model was obtained containing few and well-defined assumptions.

The differential equations in the mathematical model description were strongly coupled and thus, the governing equations had to be solved simultaneously with appropriate boundary conditions. Furthermore, the shape of the reaction channels led to an ill-conditioned modelling domain. A commercial finite element solver was found suitable to handle these problems. Scaling of the geometry and combining the finite element and finite difference schemes facilitated efficient numerical solution of the model equations.

Most of the physical property data involved was found in the literature or approximation techniques were available. Model parameters that could not be found in the literature were determined by matching the model to experimental results (Jähnisch et al. 2000). This procedure was applied with the absorption of fluorine and the reaction mechanism. The reaction mechanism of the direct fluorination of toluene was very complex and thus a simplified scheme was developed. The validation of the model with experimental data (Jähnisch et al. 2000) prove the applicability of the model within the range of parameters it has been created with, but limitations apply, see Section 9.5.

9.4 Simulation study

Model representations were developed for two different reactor configurations, i.e. the CMMR and a falling film mircoreactor (FFMR). The latter device was constructed by Jähnisch et al. (2000) for experimental work, and in this work served as benchmark process. With the CMMR configuration a membrane model was used based on equations describing heat and mass transfer as well as chemical reactions in a generalised membrane configuration, which is characterised through certain parameters. Values for these parameters give guidance for the design of the membrane.

9.4.1 Multiphase flow

The micro-fluidic systems under consideration can be considered to be a continuum and the Navier-Stokes equations apply. Thus, the fluid flow developed a laminar flow profile obeying the no-slip boundary condition on the channel wall. The structures of the CMMR and FFMR differ with regard to the interface of the reactants. The first reactor featured closed channels and with the latter the gas and liquid channel were open towards each other. Thus, a parabolic profile formed in the closed channels of the CMMR whereas a semi-parabolic profile developed in the open liquid channel of the FFMR.

The momentum of the gas and liquid flow was coupled with the FFMR. Thus, the relative velocities between the gas and liquid phase influence the constitution of the gas-liquid interface and therewith the gas phase mass transport of fluorine. As a result fluorine absorption was different with the CMMR and FFMR but these differences can be compensated through an individually adapted design of the gas channel. Furthermore, with the FFMR surface instabilities at the phase boundary may occur, which may alternate fluorine absorption significantly. These phenomena are difficult to predict and therewith the applicability of mathematical modelling may be impaired. This is in contrast to the CMMR where the gas/liquid interface is stabilised by the membrane.

The laminar flow profile in the liquid phase caused a residence time distribution and influenced transversal diffusion of the reactants and intermediates. Both phenomena did not alternate the performance of the reactor in a significant fashion compared to idealised plug flow.

The hydrodynamic entrance effects were insignificant because the developing flow regime in the gas and liquid phase was very short under the considered operating conditions. Also, the pressure drop of the fluid flow was very small and not a crucial variable concerning the design of the fluid channels.

9.4.2 Isothermal reactor analysis

The sensitivity of the fluorination process with regard to the most influential operating conditions was investigated. Here, the individual reactant feed conditions and the operating temperature were analysed separately assuming isothermal reactor operation. The temperature strongly influenced the individual reaction rates and there was on optimum temperature with regard to the performance of the reactor. Thus, tight temperature control was desirable, which is investigated in the next section. The feed conditions of the reactants had opposite influence on the selectivity of the desired product and the conversion of toluene. For this reason high conversion was achieved at low selectivity, only, and vice versa.

The CMMR features a membrane between the gas and the liquid phase. This membrane imposed mass transfer limitations on the liquid phase reactants and products, which had uniquely detrimental effect on the conversion and the selectivity. Therefore, it is important to fabricate the membrane as thin and porous as possible and practical. The catalytic membrane implemented at the gas/liquid phase boundary showed great potential to significantly increase both, the selectivity towards desired product and conversion of toluene.

9.4.3 Non-isothermal reactor simulation

The direct fluorination of organic compounds has a very high heat of reaction. Heat removal and temperature distribution within the reactor were very important because of high sensitivity of the process towards temperature, and safety considerations. The microreactor configurations feature small channels diameters and were able to dissipate the generated heat and control the temperature in the reaction plane. Increasing the channel size towards one millimetre diameter led to hot spots within the reaction plane or even thermal runaway and unsafe operating conditions. With the CMMR heat transfer was greatly improved by the membrane compared to the FFMR. This was true even with very porous membranes if a highly conductive membrane material was chosen (e.g. steel). As a result we were able to use larger reaction channels without compromising on the heat management.

Next, the influence of heat management and the reaction temperature on the selectivity of desired product was considered. The membrane inside the CMMR strongly supported heat removal from the reaction plane but also altered the concentration distribution and local occurrence of reactions. With an inert membrane the advantage of reinforced heat removal was balanced by mass transfer limitations, which reduce the selectivity. The latter effect is a function of the membrane characteristics and reduces with decreasing membrane thickness. With a catalytic membrane the positive effects predominated and significantly higher output was obtained per channel compared to the FFMR. This is desirable in connection with scaling-up for industrial use.

Finally, the design of the heat sink and its operational parameters were analysed for maximum control of the temperature in the reactor. Four different heat sink arrangements were investigated, i.e. cross flow, co-current flow, counter-current flow, and constant temperature coolant. It was found that the cross-flow coolant arrangement performed best with parallel arrays composed of less than ten channels. Here, complex adjustment of the flow rate in the individual cooling channels was necessary. Co-current cooling is simple to implement and performed reasonably well even with large parallel arrays of micro-channels. With all coolant flow appropriate arrangement operational parameters was important to avoid hot spots in the coolant channel due to transversal heat conduction limitations.

9.5 Limitations

The model contains detailed information about heat, mass and momentum conservation but some simplifying assumptions had to be taken:

- The reaction mechanism is based on information from the literature. This information does not describe the entire mechanism and therefore some assumptions had to taken to develop a detailed mechanism.
- The full reaction mechanism is to complex to be implemented in the process model and simplifications had to be introduced
- The heat of reaction for the individual reactions is derived from literature data, but not all information is available and assumptions had to be taken
- Power law reaction chemistry is assumed to describe heterogeneous catalysis occurring at the catalytic membrane
- The Henry constant for the material combination considered in this work is not available in the literature. An estimation based on an equation by Hildebrand is accomplished and verified using experimental data but some uncertainty remains.
- Surface instabilities occurring at the gas/liquid and to some extent also at the liquid/solid interfaces are not included in the process model. It is shown with the FFMR, that the driving forces for hydrodynamic instabilities exist and convective motion and oscillations may occur in the liquid phase due to the Marangoni-Bernard effect.

The validation of the simplified model for the FFMR with experimental data showed that the model for the FFMR works accurately (relative error approximately up to 8%) within the considered range of operational parameters. However, one data point at high initial reactant concentrations was not reproducible. Thus, the application of the process model is limited to the range of parameters it has been

successfully validated with due to the assumptions illustrated above. Extrapolation cannot be recommended, as the validation at elevated initial concentrations shows.

The membrane does not physically exist and models and parameters describing heat and mass transfer within the membrane correspond to a virtual device. Especially the reaction mechanism on the surface of the heterogeneous catalyst can only be known with an existing membrane. Thus, the results achieved with the membrane reactor correspond to a model membrane and are intended to give guidance for the construction of a membrane.

9.6 Summary

The membrane microreactor configuration developed in this work shows great potential for the conduction of the fluorination of toluene process. The two most important features are the integrated heat exchanger and the multifunctional membrane. The previous provides the basis for temperature control within the reactor. The latter facilitates control of the fluid flow and the chemical reaction, heat removal from the reaction plane and catalysis of the desired reaction in a complex mechanism. The catalytic function of the membrane has the potential to greatly improve the selectivity of the process and also the conversion without complicating downstream separation, because of its solid state.

These results were obtained with a detailed process model. Some assumptions had to be taken especially with regard to the reaction mechanism. Therefore limitations apply and the results should be reproduced experimentally.

9.7 Future work

In Section 9.5 the limitations of the process model are shown. The model could be improved by replacing some assumptions with data derived from experiments. The Henry constant should be determined from experiments that are uniquely accomplished to serve this purpose. In this connection the temperature

dependence of the Henry constant should be determined. Further experiments with the FFMR should be accomplished to generate a larger basis for the validation of the model and especially the reaction mechanism. Fluorination reactions are very exothermic and thermal runaway may occur if heat management fails. A dynamic model could used to investigate the process during start-up and shut down as well failure of coolant supply.

A membrane reactor should be built for the conduction of experiments to verify the results obtained in this simulation study and to proof the operation of the membrane reactor with experiments. Details about the membrane can only be determined with a physical existent membrane. The absorption of fluorine is proportional to the interfacial surface area. The current model assumes equal absorption surface with the FFMR and the CMMR. With a real membrane the absorption surface may be very high due to internal surface area, which would strongly improve the contacting, and thus the conversion per reactor volume.

The catalytic effectiveness of a solid Lewis catalyst and the choice of materials should be explored experimentally with the direct fluorination of toluene reaction. Some experiences about the use of solid acid catalysts were gained with similar reactions: Popular materials featuring Lewis acid sites are zeolites and fluorinated alumina or silica. Sams et al. (1976) conducted the direction fluorination of fluorobenzene on the surface of a molecular sieve. This process successfully suppressed any radical reactions towards polymerised product but hydrofluoric acid quickly corroded the silicate material. The corrosive environment inside the reactor due to the production of HF necessitates certain resistance with the catalytic material. Recently, catalyst materials with macro-porous structure have been developed which should slow down deactivation due to clogging, since these materials do not facilitate any shape selectivity the catalytic effect would have to derive from strong acidity. Aluminium fluoride for example is stable in HF environment and has strong acidic sites. In this connection, experiments should be conducted to investigate the possibility that the use of solid catalyst supports the absorption of the gaseous reactant therefore a co-solvent at industrial scale may be avoided (Wu et al., 2000).

Appendix A :

Fluorination of organic compounds

A.1 Fluorine bonding with hydrogen and carbon

The products obtained from reactions between fluorine and organic compounds show great difference to organic compounds containing other halogen molecules. The peculiarities of the fluorine compounds are mainly due to the exceptionally large energies of formation of the links of fluorine to hydrogen and carbon. In organic compounds substitution of hydrogen by a halogen leads to thermodynamically more stable compounds in case of fluorine, only, see Table A-1.

Table A-1. Bond dissociation energies in kJ/mole

C-H	C-O	C-C	C-N	**C-F**	C-Cl	C-Br	C-I
413	358	346	301	**485**	339	285	213

The strong links between fluorine and carbon and the strong electronegativity of fluorine have significant influence on the molecular activity of a compound. Fluorine can have a stabilising as well as a destabilising effect on a molecule even at a low level of fluorination. "C-F bonds have resulted in highly significant advances in many areas including electronics, medicine, agriculture, health care, and materials, and selective fluorinations have an important current and future role in all of those areas" (Clark and Bastock, 1996)

Owing to the large heats of reaction of elemental fluorine with organic compounds, and its tendency to remove hydrogen as HF, direct fluorination is very difficult, and was long thought to be impossible. Organic compounds react violently on contact with fluorine and tend to form mixtures of black tars with hydrogen fluoride. The aromatic pi-electron system can be distorted by adding fluorine to the ring. The fluorine replaces hydrogen and chlorine, adds on to double bonds and can also cause breakdown or building up of carbon chains (Clark and Bastock, 1996 and Lagow, 1991).

A.2 Methods of fluorination

The preparation of highly fluorinated compounds generally involves the use of one of three fluorinating agents based on:

- Elemental fluorine (including the use of F_2 diluted in inert gas)
- High oxidation state metal fluorides (e.g. CoF_3)
- Electrochemical fluorination (typically using HF containing an ionic fluoride)

The preparation of low-fluorinated compounds involves a much broader range of fluorinating methods, classified in:

- nucleophilic fluorine transfer (metal fluorides, HF)
- electrophilic fluorine transfer
- radical fluorine transfer

Metal fluorides are widely used for the substitution of halogens directly bonded to the ring. Substitution of halogens (commonly using a metal-fluoride) and NH_2 (Balz-Schiemann) represent two of the most important industrial routes to selectively fluorinated aromatics.

Halogen exchange (Halex) processes involve the preparation of fluoroaliphatic compounds from their chlorinated analogues using metal fluorides, e.g. the strong Lewis acidic antimony fluoride, as nucleophilic fluorinating agents.

The Balz-Schiemann reaction follows a two-step route to fluoroaromatics starting from aniline. The first step involves the diazotisation of an aniline. The second stage yields the fluoroaromatic after thermal decomposition of the aryldiazium fluoride. The industrial production is made complex by the need for two separate reactions. This process is widely used in industry for the preparation of nonactivated fluoroaromatics, such as fluorobenzene and fluorotoluenes in a continuous process.

The Halex and Balz-Schiemann reactions are the most common routes to create fluoroaromatics. However, both methods require complex precursors and functional groups present on the ring can cause side reactions. Direct fluorination would therefore offer advantages over either of the two processes (Clark and Bastock, 1996).

The direct fluorination of organic compounds has long been considered an uncontrollable reaction. It was shown in the early 20th century that the direct fluorination of organic compounds can be controlled (Bigelow, 1947). Dilution of fluorine and aromatic compounds by nitrogen and inert solvents, e.g. Acetonitrile, respectively result in a safe set-up.

Despite the apparent simplicity of the direct fluorination process it was not considered in industry until very recent, due to safety issue and low product selectivities. At low conversions at low temperatures (-35C) fluorine is considered an unselective reagent and at higher fluorine ratios give complex tar-like products, composed primarily of highly fluorinated polycyclohexanes (Clark and Bastock, 1996).

Appendix B

Reaction Chemistry – Direct Fluorination of Toluene

B.1 Literature review

The reaction mechanism of the direct fluorination of toluene is not available in the literature. Here, a mechanism is developed based on the findings of various researchers who did research with direct fluorination of organic compounds.

Organic fluorination reactions with elemental fluorine exhibit the general characteristics of free radical processes (Miller, 1956), which expresses through the explosive nature of the reactions and the complex mixture of reaction products obtained. Under non-polar conditions initiation may occur by thermal or catalytic dissociation of fluorine into atoms since the bond dissociation of fluorine is very low. But fluorine is not appreciably dissociated at room temperature. Thus, under such conditions Miller suggests free radical initiation by reactions between fluorine molecules and organic systems:

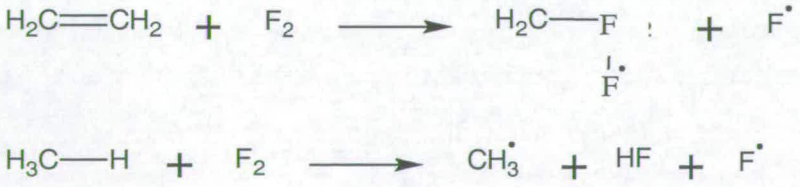

(B-1)

Fukurara and Bigelow (1941) investigated the vapour phase fluorination of benzene. They found that the product mixture of a direct fluorine benzene gas-phase reaction did not contain any aromatic compounds but C_6, C_{12} and compounds with shorter carbon chains. These results indicate that the reaction proceeds by an atomic mechanism involving, first addition, then substitution, and dimerisation or polymerisation. In the gas-phase fragmentation of the carbon

chain occurs, too. They suggest the following propagation mechanism referring to atomic fluorine addition:

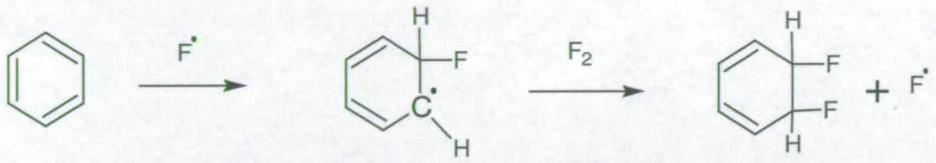

(B-2)

Theoretical consideration by Bockemueller (1936) on the energy change occurring in organic fluorination reactions explain the difference between fluorination and other halogenation reactions. The energy created by adding fluorine on a double bond or by substituting hydrogen by fluorine is large enough to break disrupt adjacent C-C bonds if the surroundings provide poor heat transfer. Heat management is improved in solvent phase, but here too, the fluorine attacks aromatic nuclei by a different mechanism from chlorine, often yielding polymerised products. The primary attack on the nucleus consists not of substitution but of addition, which agrees to the finding of Fukurara (1941), and is essentially the same as the atomic mechanism, in which a fluorine atom is attacking a double bond:

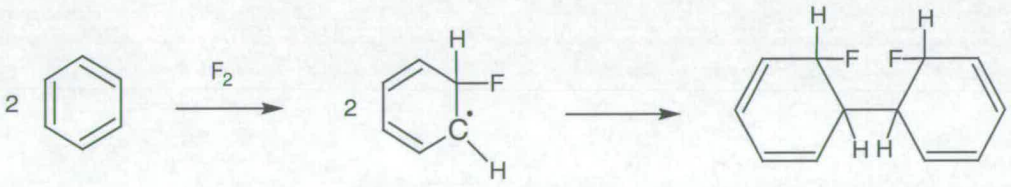

(B-3)

Similar results were found in liquid phase direct fluorination of toluene (Cacace and Wolf, 1977) where the product range contained complex chain propagation system exists consisting of polymerisation, addition, and side chain attack.

Fluorine can also act as an electrophile when encouraged by the surrounding solvent or catalyst. The electrophilic reaction of a halogen with an aromatic compound is initiated by the formation of an electrophile. When the halogen approaches the aromatic ring, the delocalised electrons in the ring repel electrons in the fluorine-fluorine bond. It is the slightly positive end of the fluorine molecule that acts as the electrophile. The presence of a strong Lewis Acids helps this polarisation (Chambers, 1996):

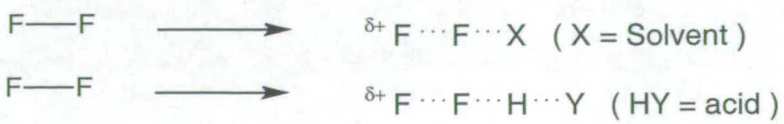

(B-4)

The electrophile aromatic substitution is a standard reaction in organic chemistry. The mechanism consists of two steps: 1) the formation of the electrophile and addition of a positive fluorine ion and 2) the removal of hydrogen from the aromatic ring:

(B-5)

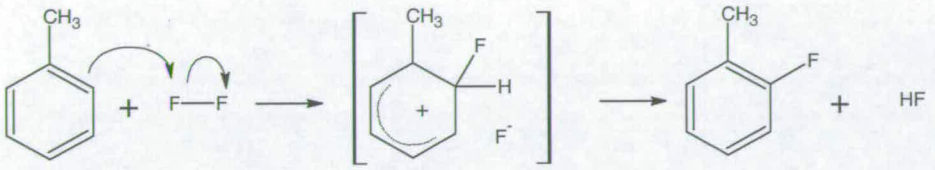

A detailed theoretical study of the mechanism of selective fluorination of saturated hydrocarbons in the liquid phase was accomplished by Fukaya and Morokuma (2003). This work is not concerned with aromatic compounds but the interaction of a polar solvent with fluorine and the organic compound is interesting. Polar solvents acts as radical scavenger, ionise the fluorine molecule and acts as an acceptor for the fluorine anion. Yet, this theoretical study cannot rule out the occurrence of radical fluorine and hydrocarbon compounds. The polar solvent $CHCl_3$ stabilises all species involved in the multi-step reactions. With Isopropanol lower energy barriers for transition states with the electrophilic reaction lower the competitiveness of the radical reaction.

B.2 Reaction mechanism

The direct fluorination of aromatics is a very complex reaction. Especially the radicals formed during the course of the reaction may react with any species available and also collisions with the reactor wall all other solids influence the termination of the chain reaction mechanism. Therefore, it seems impossible to write down a comprehensive mechanism for this reaction, which would be applicable in different conditions and reactor devices. However it is attempted here, to present a reasonably realistic reaction scheme, based on the information found in the literature (see Section B.1). Some by-products are symbolised by the word 'products'; radicals compounds are marked with a dot. The gaseous feed to the reactor consists of fluorine (F_2) diluted in nitrogen (N_2) and in the liquid phase toluene (Tol) is dissolved in acetonitrile (AcN). The letter 'X' symbolises an unspecified reaction partner, e.g. reactor walls.

$$F_2 + C_7H_8 \xrightarrow[\text{electrophilic reaction}]{k_r} C_7H_7F + HF$$

Initiation

$$F_2 + C_7H_8 \xrightarrow[\text{radical addition}]{k_{i1}} F^\bullet + C_7H_8F^\bullet$$

$$F_2 + C_7H_7F \xrightarrow[\text{radical addition}]{k_{i2}} F^\bullet + C_7H_7F_2^\bullet$$

radical chain propagation:

$$F^\bullet + C_7H_8 \xrightarrow[\text{radical addition}]{k_{q1}} C_7H_8F^\bullet \qquad F_2 + C_7H_8F^\bullet \xrightarrow[\text{radical addition}]{k_{p1}} F^\bullet + C_7H_8F_2$$

$$F^\bullet + C_7H_7F \xrightarrow[\text{radical addition}]{k_{q2}} C_7H_7F_2^\bullet \qquad F_2 + C_7H_7F_2^\bullet \xrightarrow[\text{radical addition}]{k_{p2}} F^\bullet + C_7H_7F_3$$

$$F^\bullet + C_7H_8F_2 \xrightarrow[\text{radical addition}]{k_{q3}} C_7H_8F_3^\bullet \qquad F_2 + C_7H_8F_3^\bullet \xrightarrow[\text{radical addition}]{k_{p3}} F^\bullet + C_7H_8F_4$$

$$F^\bullet + C_7H_7F_3 \xrightarrow[\text{radical addition}]{k_{q4}} C_7H_7F_4^\bullet \qquad F_2 + C_7H_7F_4^\bullet \xrightarrow[\text{radical addition}]{k_{p4}} F^\bullet + C_7H_7F_5$$

$$F^\bullet + C_7H_8F_4 \xrightarrow[\text{radical addition}]{k_{q5}} C_7H_8F_5^\bullet \qquad F_2 + C_7H_8F_5^\bullet \xrightarrow[\text{radical addition}]{k_{p5}} F^\bullet + C_7H_8F_6$$

$$F^\bullet + C_7H_8F_6 \xrightarrow[\text{radical substitution}]{k_{q7}} C_7H_7F_6^\bullet + HF \qquad F_2 + C_7H_7F_6^\bullet \xrightarrow[\text{radical addition}]{k_{p6}} F^\bullet + C_7H_7F_7$$

$$F^\bullet + C_7H_7F_7 \xrightarrow[\text{radical substitution}]{k_{q8}} C_7H_6F_7^\bullet + HF \qquad F_2 + C_7H_6F_7^\bullet \xrightarrow[\text{radical addition}]{k_{p7}} F^\bullet + C_7H_6F_8$$

$$F^\bullet + C_7H_6F_8 \xrightarrow[\text{radical substitution}]{k_{q9}} C_7H_5F_8 + HF \qquad F_2 + C_7H_5F_8^\bullet \xrightarrow[\text{radical addition}]{k_{p8}} F^\bullet + C_7H_5F_9$$

$$F^\bullet + C_7H_5F_9 \xrightarrow[\text{radical substitution}]{k_{q10}} C_7H_4F_9^\bullet + HF \qquad 2C_7H_4F_9^\bullet \xrightarrow[\text{radical addition}]{k_x} C_{14}H_8F_{18}$$

$$\phi^\bullet + \phi \xrightarrow[\text{radical polymerisation}]{k_{r1}} product \qquad etc.$$

termination

$$2 \cdot \phi^\bullet + X \xrightarrow[\text{radical polymerisation}]{k_{t1}} product$$

$$2 \cdot F^\bullet + X \xrightarrow[\text{recombination}]{k_{t2}} F_2$$

$$F^\bullet + \phi^\bullet \xrightarrow[\text{recombination}]{k_{t3}} product$$

where φ can be any hydrocarbon (C_7H_7F to $C_7H_6F_8$)

X symbolises unspecified reaction partners, i.e. reactor walls

Scheme 4-1: Reaction mechanism for the direct fluorination of toluene

With this simplified mechanism (see Scheme 4-1) the fluorination of the hydrocarbon is the dominant reaction in the microreactor whereas polymerisation and chain rupture do not occur in big extent, however the previous cannot be neglected which is suggested by the experimental results obtained in the solvent phase by (Biegelow 1947; Jaehnisch et al. 2000). At this stage three termination reaction steps are suggested, which are most obvious, while other reaction, e.g. the fluorination of acetonitrile, are not considered.

The reaction kinetics for this fluorination reaction, where toluene is diluted in Acetoniltrile, are not available in the literature and only few suitable experimental results were published. Thus, it is not possible to determine values for all the reaction kinetic constants involved, especially since the aromatic compounds change their nature during the course of the

reaction. Toluene is considered to be an activated aromatic while fluorine added to the ring yields passivates the ring. Furthermore the stable pi-electron system is disrupted which probably leads to a higher activated state.

The termination reactions are particularly difficult to model, because the presence of reactor walls or other collision partners (e.g. for energy withdrawal) may have strong impact and render data from the literature, measured at different conditions, obsolete. With the chain reaction mechanism under consideration the termination reactions play an important role, because it is them who determine the reaction order of the entire radical reaction system. The experimental results with the FF-microreactor (Jaehnisch, 2000) suggest, that the reaction system has 1^{st} order with respect to the limiting fluorine at a temperature of 257K. The reaction order may change with the temperature, however, there is too few experimental data to confirm such behaviour.

Following from these consideration further simplifications are introduced to reduce the number of parameters, most prominently: the abandonment of the second initiation reaction $r_{i,2}$, the reduction of the termination (only $k_{t,2}$ remains) and the polymerisation reactions.

The concentration of the hydrocarbon radicals is expected to be very low because of their high reactivity. Among these compounds the monofluorinated radical $C_7H_8F\bullet$ has the highest concentration and its reaction with toluene is the most likely polymerisation step to occur. For simplicity this is the only reaction of this kind remaining in the mechanism. Similarly $C_{14}H_{16}F\bullet$ has the second highest concentration, does not get involved in polymerisation but might react with a fluorine radical presenting the strongest termination reaction, see Scheme 4-2.

$$F_2 + C_7H_8 \xrightarrow[\text{electrophilic reaction}]{k_e} C_7H_7F + HF$$

Initiation

$$F_2 + C_7H_8 \xrightarrow[\text{radical addition}]{k_i} F^\bullet + C_7H_8F^\bullet$$

polymerisation

$$C_7H_8F^\bullet + C_7H_8 \xrightarrow[\text{radical polymerisation}]{k_{r1}} C_{14}H_{16}F^\bullet$$

radical chain propagation :

$$F^\bullet + C_7H_8 \xrightarrow[\text{radical addition}]{k_{q1}} C_7H_8F^\bullet \qquad F_2 + C_{14}H_{16}F^\bullet \xrightarrow[\text{radical addition}]{k_{p1}} F^\bullet + C_{14}H_{16}F_2$$

$$F^\bullet + C_7H_7F \xrightarrow[\text{radical addition}]{k_{q2}} C_7H_7F_2^\bullet \qquad F_2 + C_7H_7F_2^\bullet \xrightarrow[\text{radical addition}]{k_{p2}} F^\bullet + C_7H_7F_3$$

$$F^\bullet + C_{14}H_{16}F_2 \xrightarrow[\text{radical addition}]{k_{q3}} C_{14}H_{16}F_3^\bullet \qquad F_2 + C_{14}H_{16}F_3^\bullet \xrightarrow[\text{radical addition}]{k_{p3}} F^\bullet + C_{14}H_{16}F_4$$

$$F^\bullet + C_7H_7F_3 \xrightarrow[\text{radical addition}]{k_{q4}} C_7H_7F_4^\bullet \qquad F_2 + C_7H_7F_4^\bullet \xrightarrow[\text{radical addition}]{k_{p2}} F^\bullet + C_7H_7F_5$$

$$F^\bullet + C_{14}H_{16}F_4 \xrightarrow[\text{radical addition}]{k_{q5}} C_{14}H_{16}F_5^\bullet \qquad F_2 + C_{14}H_{16}F_5^\bullet \xrightarrow[\text{radical addition}]{k_{p5}} F^\bullet + C_{14}H_{16}F_6$$

$$F^\bullet + C_{14}H_{16}F_6 \xrightarrow[\text{radical addition}]{k_{q7}} C_{14}H_{16}F_7^\bullet \qquad F_2 + C_{14}H_{16}F_7^\bullet \xrightarrow[\text{radical addition}]{k_{p7}} F^\bullet + C_{14}H_{16}F_8$$

$$F^\bullet + C_{14}H_{16}F_8 \xrightarrow[\text{radical addition}]{k_{q9}} C_{14}H_{16}F_9^\bullet \qquad F_2 + C_{14}H_{16}F_9^\bullet \xrightarrow[\text{radical addition}]{k_{p9}} F^\bullet + C_{14}H_{16}F_{10}$$

termination

$$F^\bullet + C_{14}H_{16}F^\bullet \xrightarrow[\text{radical addition}]{k_t} C_{14}H_{16}F_2$$

Scheme 4-2: Reaction mechanism for the direct fluorination of toluene

This reaction mechanism is still too complicated and further simplification is achieved by rearranging the reaction equations in a mathematical way and applying the steady state approximation method. Here, it is assumed that the concentration of the radicals and all intermediates involved in chain propagation reactions are very small and therefore the rate of change of their concentrations is small, too. In this manner reaction steps can be combined to lumped reactions and Scheme 4-3 was derived. Here, the symbols for the compounds used in Scheme 4-2 were retained, but the lumped reactions leading to the compounds are assigned new labels.

$$F_2 + C_7H_8 \xrightarrow[\text{electrophilic reaction}]{k_1} C_7H_7F + HF$$

$$F_2 + 2Tol \xrightarrow[\text{radical addition}]{k_2} C_{14}H_{16}F_2$$

$$4 \cdot F_2 + C_{14}H_{16}F_2 \xrightarrow[\text{radical addition}]{k_3} C_{14}H_{16}F_{10}$$

$$2 \cdot F_2 + C_7H_7F \xrightarrow[\text{radical addition}]{k_4} C_7H_7F_5$$

Scheme 4-3: Simplified reaction mechanism for the direct fluorination of toluene

B.3 Reaction kinetics

The reaction kinetic constants for the reactions in Scheme 4-3 are derived from the elementary reaction in Scheme 4-2 based on the pseudo steady state approximation method, see Scheme B-4. Here it is assumed that intermediate compounds have a low concentration and this concentration is changing little during the reaction.

Considering Scheme B-4 we find that the electrophilic reaction is the same in all the reaction schemes discussed above. The radical initiation has been combined with the polymerisation and a chain propagation step, where the kinetics are determined by a combination of the initiation, the chain propagation and the termination steps. The two series reactions are a combination of chain propagation and termination steps and the reaction kinetics depend on the initiation, the chain propagation and the termination steps.

Unfortunately, not even for the elementary reactions in Scheme 4-2 values are explicitly given in the literature. Some kinetic data is available for the elemental reactions involved in the gas-phase fluorination of methane and ethane as well as solvent phase chlorination of some organic compounds, which are reported in the literature and summarised on an internet-based database hosted by the NIST, USA (2003a, 2003b) (see Appendix). Based on this data an attempt for an order of magnitude estimation is undertaken here, see Table B-1.

One of the major assumptions here implies that the kinetics for the elementary fluorination steps under consideration are similar in liquid and gas-phase. This assumption can be justified considering statements by Masel (2001): Generally solvents have much greater impact on ionic reactions than on radical reactions. Thus, concerning the liquid phase radical reactions only little error goes along with deriving data from gas phase reactions. Considering some chlorination and fluorination reactions for which the reaction kinetics in the gas and liquid phase is available, illustrated in the Appendix, we find that the differences are within an order of magnitude.

The electrophilic fluorination of toluene is an ionic reaction. Masel (2001) reports about ionic reactions in solvents phase: a) ionic species are stabilized by the presence of the solution and b) the solution changes the intrinsic barrier to ionic reactions, which, in general, does not affect the mechanism of a reaction. One sees the same elementary reactions in solution that one sees in the gas phase. However, ionic reactions show much higher overall rates in polar solvents than in the gas phase. Polar aprotic solvents favour reactions of ions while non-polar solvents (like toluene) favour radical reactions. No kinetic data is available for the electrophilic fluorination reaction but it can be deduced, that polar acetonitrile solvent supports this ionic reaction over the radical reaction.

$$k_1$$

$$k_2 = \left[k_i + \sqrt{\frac{k_{p,1} k_{q,1} k_i}{k_t}} \right]$$

$$k_3 = k_{q,9} \cdot \sqrt{\frac{k_i k_{p,1}}{k_t k_{q,1}}}$$

$$k_4 = k_{q,4} \cdot \sqrt{\frac{k_i k_{p,1}}{k_t k_{q,1}}}$$

Scheme B-4: Derivation of the kinetic constants for the reactions in Scheme 4-3 from elementary reactions in Scheme 4-2

Table B-1. Estimation of the kinetic data of the elementary reaction steps of Scheme 4-2 and the lumped reactions in Scheme 4-3 at a temperature of T = ~257 K

Reaction	Kinetic constant / / $l \cdot mol^{-1} \cdot s^{-1}$	Excitation from
k_i	>10 ; < 5000 (e.g. 200)	Gas phase fluorination of ethane and methane Ref: 1,2
k_{q1}	Approx. $1 \cdot 10^{10}$	Gas phase fluorination of toluene and methane Ref: 3,11
k_{p1}	Approx. $1 \cdot 10^{9}$	Gas phase fluorination of methane Ref: 14
k_{q4}	Approx. $5 \cdot 10^{10}$	Gas phase fluorination of toluene and methane, Ref: 3,11 (higher then kq1 because stabilising aromatic ring is broken)
k_{q9}	Approx. $5 \cdot 10^{10}$	Gas phase fluorination of toluene and methane, Ref: 3,11
k_t	>> $1 \cdot 10^{10}$ (e.g. $1 \cdot 10^{13}$)	Fluorination of methane Ref 14; we expect much bigger value due to micro-channel design
k_2	$1.4 \cdot 10^{4}$ +/-100%	calculation
k_3	$7.0 \cdot 10^{4}$ +/-100%	calculation
k_4	$7.0 \cdot 10^{4}$ +/-100%	calculation

B.4 Heat of reaction

The reaction mechanism proposed in this work, Scheme 4-3, involves four exothermic lumped reactions. The heat exerted by any of these lumped reactions is calculated from the heats of formation of the individual compounds involved and the bond strength of to atoms at standard temperature 298 K, e.g. fluorine and carbon, in a certain compound.

Reaction r_1

This reaction can be considered a one-step reaction where one hydrogen atom on the aromatic ring is substituted by a fluorine atom and hydrofluoric acid is formed. The heat of reaction is calculated from the heat of formation of the individual compounds:

No	$\Delta_f h$ / kJ mol^{-1}					$\Delta_r h$ / kJ mol^{-1}
1	F2	C_7H_8	→	F-C_7H_7	HF	
	0[1)]	50.5[1)]		-147.4[1)]	-279.5[1)]	-478

Reaction r_2

This reaction is a lumped reaction consisting of several reaction steps. Unfortunately, the heat of formation was not available for all compounds involved and thus some additional calculations had to be done and assumptions were taken. Fist the heat of formation of F-Toluene (F-C_7H_7) was determined (steps 2a-2c):

No	ΔH_f / kJ mol^{-1}					ΔH_r / kJ mol^{-1}	Remark
2a	C_7H_8		→	H•	C_7H_7•		
	50.5			211[1)]	312.6	D°(H-C_7H_7) =473.1[1)] (endothermic)	Assumption: D°(H-C_7H_7) = D°(H-C_6H_5)= 473.1
2b	F•	C_7H_7•	→	F-C_7H_7			
	79.39[1)]	ΔH_f(C_7H_7•) =312.6		-147.4[1)]		-539.39 (exothermic)	$\Delta_r h$ = |D°(F-C_7H_7)|
2c	F_2	C_7H_8	→	F•-C_7H_8	F•		
	0	50.5[1)]		-409.5	79.39[1)]	-D°(F-C_7H_7) + D°(F-F) [1)] = -380.61	ΔH_r calculated from D°(F•-C_7H_8), which is formed and D°(F-F)=158.78, which is broken; Assumption: D°(F•-C_7H_8)= D°(F-C_7H_7)

[1] **From CRC-Handbook of Chemistry and Physics**

With this knowledge we can now calculate the heat of formation of F•-$(C_7H_8)_2$ and F_2-$(C_7H_8)_2$ (steps 2d-2e):

	ΔH_f / kJ mol^{-1}				ΔH_r / kJ mol^{-1}	Remark
2d	F•-C_7H_8	C_7H_8	→	F•-$(C_7H_8)_2$		
	ΔH_f(F•-C_7H_8)= -409.5	50.5[1)]		-735.05	D°(CH_3-CH_3) = -376[1)]	Assuming that D°(CH_3-CH_3) = D°(C_7H_8- C_7H_8) =-376
2e	F•-$(C_7H_8)_2$	F•		F_2-$(C_7H_8)_2$		
	ΔH_f (F•-$(C_7H_8)_2$) = -735.05	79.39[1)]	→	-1195.05	-D°(F-C_7H_7)= -539.39	Assuming that D°(F-FC_7H_7) = D°(F-C_7H_7)

Finally, the overall heat generated by reaction r_2 can be calculated (step 2):

	ΔH_f / kJ mol^{-1}				ΔH_r / kJ mol^{-1}
2	F_2	2· C_7H_8	→	F_2-$(C_7H_8)_2$	
	0	2·50.5		-1195.05	**-1296.05**

Reaction r_3

This lumped reaction consists of 8 radical addition reaction steps where fluorine atoms are added on to the aromatic ring. The heat created with the addition of one F_2 molecule is illustrated in the following table:

	ΔH_f / kJ mol^{-1}					ΔH_r / kJ mol^{-1}	Remark
3a	F_2-$(C_7H_8)_2$	F•	→	F_3•-$(C_7H_8)_2$			
	ΔH_f (F_2-$(C_7H_8)_2$) =-1195.05	79.39[1)]		-1655.4		-D°(F-Tol)= -539.39	Assuming that D°(F•-F_2(C_7H_8)$_2$) = D°(F-C_7H_7)
3b	F_3•-$(C_7H_8)_2$	F_2	→	F_4-$(C_7H_8)_2$	F•		
	ΔH_f (F_3•-$(C_7H_8)_2$) = -1655.4	0[1)]		-2115.4	79.39[1)]	-D°(F-C_7H_7) + D°(F-F) =-380.61	Assumption: D°(F- F_3(C_7H_8)$_2$)= D°(F-C_7H_7)

The overall heat of reaction of the addition of one molecule F_2 is:

	ΔH_f / kJ mol^{-1}					ΔH_r / kJ mol^{-1}	
3c	F_2-$(C_7H_8)_2$	F_2	→	F_4-$(C_7H_8)_2$			
	-1195.05	0		-2115.4		-920	

This reaction occurs four times, thus the overall heat generated by reaction r_3 can be calculated (step 3):

	ΔH_f / kJ mol^{-1}				ΔH_r / kJ mol^{-1}
3	F_2-$(C_7H_8)_2$	4·F_2	→	F_{10}-$(C_7H_8)_2$	
	-1195.05	0		-4875.05	**ΔH_r(3c)·4 = -3680**

Reaction r_4

Reaction r_4 is a lumped reaction consisting of 4 radical addition steps where fluorine atoms are added to the toluene ring. These addition steps are similar to ones with reaction 3 and thus the heat of reaction can be calculated from reaction step 3c:

	ΔH_f / kJ mol^{-1}				ΔH_r / kJ mol^{-1}
4	$F\text{-}C_7H_7$	$2\cdot F_2$	$\rightarrow$	$F_5\text{-}C_7H_7$	
	-147.4[1)]	0		-1987.4	**ΔH_r(3c)·4 = -1840**

B.5 Reaction kinetic data collection

The exact reaction kinetic constants needed for the modelling of the direct fluorination of toluene are not available in the literature. The following list summarises the reaction kinetic data which was considered relevant for this process. The unit for reaction kinetic constants is [k]= l·mol^{-1}·s^{-1} and activation energy [E_A]= kJ/kmol.

Reaction conditions	Gas-phase	Liquid-phase	Gas-phase	Liquid-phase
	Fluorination (Radical X· = F· ; Molecule X_2=F_2)		Chlorination (Radical X· = Cl· ; Molecule X_2=Cl_2)	
Initiation Reaction involving k_i referring to scheme B.2				
Methane+ X_2	F_2+RH → CH_3·+HF+F· (T=300 – 400 K) k(298)=11.63 k(257)=0.56; err=200% E_A =-46977 k_0=2.0·10^9 (Ref. 1)			
Ethene+ X_2	F_2+C_2H_4 → CH_2CH_2F+·F (T=300 – 430 K) k(298)=20721 k(257)=6016.3 ; err=30% E_A=-19206 k_0=4.82 10^7 (Ref. 2)			

Propagation 1 (Reactions involving k_{qx} referring to scheme B.2 ; x∈[1,9])				
Methane+X·	CH_4+F· → R·+HF (T=180 – 410 K) k(298)=3.805·10^{10} k(257)=3.39·10^{10} ; err=50% E_A=-1788 k_0=7.83 10^{10} (Ref. 3)	F· + CH_4 → HF + ·CH_3 k=7.0 10^9 No T indicated, T influence expected to be low (Ref. 4)	·Cl + CH_4 → HCl + ·CH_3 (T=200 – 300 K) k(298)=6.18·10^7 k(257)=3.18·10^7 ; err=50% E_A=-10310 k_0=3.97 10^9 (Ref. 1)	Cl· + CH_4 → HCl + ·CH_3 (T=150 – 298 K) k(257)=2.429·10^5 ; err=no data E_A=-14000 k_0=7.83 10^{10} (Ref. 5)
Propane, 2,2-dimethyl+X·	·F + neo-C_5H_{12} → HF + $(CH_3)_3CCH_2$ k(298)= 4.0·10^{10} ; err=15% (Ref. 6)	F· + *n*-C_5H_{12} → Products Solvent: CCl_2FCClF_2 k= 5.7·10^{10} (Ref. 4)		
Cyclo-hexane +X·	·F+Cyclohexane → HF + Cyclohexyl k(298)= 7.91·10^{10} ; err=10% (Ref. 6)	F· + *c*-C_6H_{12} → Products Solvent: CCl_2FCClF_2 k= 7.3·10^{10} (Ref. 4)	·Cl+Cyclohexane→ HCl + Cyclohexyl k(296)= 1.85·10^{11} ; err=5% (Ref. 10)	Cl· + *c*-C_6H_{12} → HCl + *c*-C_6H_{11} Solvent: *c*-C_6H_{12} k= 5.6·10^9 (Ref. 9)
Ethene +X·	·F + C_2H_4 → PRODUCTS (T=296 K) k(298)= 1.63·10^{11}; err=25% (Ref. 7)		·Cl + C_2H_4 → CH_2CH_2Cl (T=200 – 300 K) k(298)=1.87·10^{11} k(257)=2.16·10^{11} k=1.87x10^{11} · (T/298 K)$^{-1.00}$; err=80% (Ref. 8)	Cl· + H_2C=CH_2 → HCl + ·CH_2CH_2Cl (T=150 – 293 K) k(293)=2·10^8 k(257)=1.467·10^8 E_A=-5400 k_0=1.83 10^9 (Ref. 5)
C_2F_4 +X·	·F + C_2F_4 → PRODUCTS (T=180 – 410 K) k(298)= 2.89·10^{10}; err=18% (Ref. 20)			
Toluene +X·	·F + Toluene → PRODUCTS k(296)=4·10^{10}; err=20% (Ref 11)		·Cl + Toluene → HCl + Benzyl k(298)=3.4x10^{10} (Ref 12)	Cl· + $C_6H_5CH_3$; addition Solvent: $ClCH_2CH_2Cl$ K(148) = 1.5 x 10^7 (Ref 13)

Propagation 2 (Reactions involving k_{px} referring to scheme B.2 ; x∈[1,9])				
Methane +X_2	$F_2 + \cdot CH_3 \rightarrow \cdot F + CH_3F$ (T=139 – 294 K) $k(294)=7.83\cdot10^8$ $k(257)=6.15\cdot10^8$ $E_A=-4099$ $k_0= 4.19\ 10^9$ (Ref. 14)		Not significant	
Ethene +X_2			Not significant	
Termination (Reaction involving k_t referring to scheme B.2)				
Acetonitrile +X·	$\cdot F + CH_3CN \rightarrow HF + CH_2CN$ $k(300)=7.5x10^9$ (Ref 15)	F· + CH_3CN Solvent: CCl_2FCClF_2 $k = 2.7 \times 10^{10}$ (Ref. 16)	Not significant	
	$\cdot F + \cdot CH_3 \rightarrow$ PRODUCTS $k(300)=6.81x10^{10}$ (Ref. 17)			
	$\cdot CH_3 + \cdot CH_3 \rightarrow C_2H_6$ (T=296 – 1800) $k=9.73x10^{10} \cdot (T/298)^{-1.20}\ e^{-2453/RT}$ $k(296)= 3.62x10^{10}$ (Ref 18)			
	Phenyl + Phenyl → Biphenyl $k=1.39x10^{10}\ e^{-466/RT}$ $k(300)=1.15\cdot10^{10}$ (Ref. 19)			

1)
Author(s): Seeger, C.; Rotzoll, G.; Lubbert, A.; Schugerl, K.
Title: A study of the reactions of fluorine with hydrogen and methane in the initiation phase using a miniature tubular reactor
Journal: Int. J. Chem. Kinet.
Volume: 13
Page(s): 39.00 - 58.00
Year: 1981

2)
Author(s): Kapralova, g.A.; Chaikin, A.M.; Shilov, A.E.
Title: The kinetics of the reaction of fluorine with ethylene under diffusion flame conditions
Journal: Kinet. Catal.
Volume: 8
Page(s): 421 - 427
Year: 1967

3)
Author(s): Atkinson, R.; Baulch, D.L., Cox, R.A.; Crowley, J.N.; Hampson, R.F, Jr.; Kerr, J.A.; Rossi, M.J.; Troe, J.
Title: Summary of Evaluated Kinetic and Photochemical Data for Atmospheric Chemistry
Page(s): 1.00 - 56.00
Year: 2001
Squib: 2001ATK/BAU1-56

4)
Author(s): Bucher, G.; Scaiano, J.C
Journal: J. Am. Chem. Soc.
Volume: 116
Page(s): 10076-10079
Year: 1994

5)
Author(s): Sergeev, G.B.; Smirnov, V.V.; Porodenko, E.V.; Pukhovsky, A.V.
Journal: Int. J. Chem. Kinet.
Page(s): 1321-1331
Year: 1985

6)
Author(s): Pearson, R.K.; Cowles, J.O.; Hermann, G.L.; Gregg, D.W.; Creighton, J.R.
Title: Relative performance of a variety of NF_3 + hydrogen-donor transverse-discharge HF chemical-laser systems
Journal: IEEE J. Quantum Electron.
Volume: 9
Page(s): 879
Year: 1973

7)
Author(s): Nesbitt, F.L.; Monks, P.S.; Scanlon, M.; Stief, L.J.
Title: Absolute rate constants for the reactions of $F(^2P)$ with C_2H_2 and C_2H_4 at T = 298 K
Journal: J. Phys. Chem.
Volume: 98
Page(s): 4307 - 4311
Year: 1994

8)
Author(s): DeMore, W.B.; Sander, S.P.; Golden, D.M.; Hampson, R.F.; Kurylo, M.J.; Howard, C.J.; Ravishankara, A.R.; Kolb, C.E.; Molina, M.J.
Title: Chemical kinetics and photochemical data for use in stratospheric modeling. Evaluation number 12
Journal: JPL Publication 97-4
Page(s): 1.00 - 266
Year: 1997

9)
Author(s): Raftery, D.; Iannone, M.; Phillips, C.M.; Hochstrasser, R.M.
Journal: Chem. Phys. Lett.
Volume: 201
Page(s): 513-520
Year: 1993

10)
Author(s): Aschmann, S.M.; Atkinson, R.
Title: Rate constants for the gas-phase reactions of alkanes with Cl atoms at 296 ? 2 K
Journal: Int. J. Chem. Kinet.
Volume: 27
Page(s): 613 - 622
Year: 1995

11)
Author(s): Ebrecht, J.; Hack, W.; Wagner, H.Gg.
Title: Elementary reactions of fluorine atoms with benzene, toluene, p-xylene and ethylbenzene
Journal: Ber. Bunsenges. Phys. Chem.
Volume: 93
Page(s): 619
Year: 1989

12)
Author(s): Markert, F.; Pagsberg, P.
Title: UV spectra and kinetics of radicals produced in the gas phase reactions of Cl, F and OH with toluene
Journal: Chem. Phys. Lett.
Volume: 209
Page(s): 445 - 454
Year: 1993

13)
Author(s): Sergeev, G.B.; Smirnov, V.V.; Pukhovskii, A.V.; Porodenko, E.V.
Journal: Vestn. Mosk. Univ., Ser. 2, Khim.
Volume: 26
Page(s): 291-295
Year: 1985

14)
Author(s): Moore, C.M.; Smith, I.W.M.; Stewart, D.W.A.
Title: Rates of processes initiated by pulsed laser production of F atoms in the presence of HCl, CH_4, and CF_3H
Journal: Int. J. Chem. Kinet.
Volume: 26
Page(s): 813 - 825
Year: 1994

15)
Author(s): Hoyermann, K.; Seeba, J.
Title: Mechanism and rate of the reaction of cyanomethyl radicals with oxygen atoms in the gas phase
Journal: Z. Phys. Chem. (Munich)
Volume: 188
Page(s): 215 - 226
Year: 1995

16)
Author(s): Bucher, G.; Scaiano, J.C.
Journal: J. Am. Chem. Soc.
Volume: 116
Page(s): 10076-10079
Year: 1994

17)
Author(s): Beiderhase, Th.; Hack, W.; Hoyermann, K.
Title: Elementary reactions in the C-H-F system
Journal: Z. Phys. Chem. (Munich)
Volume: 188
Page(s): 227 - 241
Year: 1995

18)
Author(s): Du, H.; Hessler, J.P.; Ogren, P.J.
Title: Recombination of methyl radicals. 1. New data between 1175 and 1750 K in the falloff region
Journal: J. Phys. Chem.
Volume: 100
Page(s): 974 - 983
Year: 1996

19)
Author(s): Park, J.; Lin, M.C.
Title: Kinetics for the recombination of phenyl radicals
Journal: J. Phys. Chem. A:
Volume: 101
Page(s): 14.00 - 18.00
Year: 1997

20)
Author(s): Butkovskaya, N.I.; Larichev, M.N.; Leipunskii, I.O.; Morozov, I.I.; Talroze, V.L.
Title: Mass-spectrometric study of the recombination of atomic fluorine with CF_3 radicals and CF_2 biradicals
Journal: Kinet. Catal.
Volume: 21
Page(s): 263 - 267
Year: 1980

Appendix C

Physical property data

C.1 Parameter values

The backbone of the reactor model developed in this work, which describes a real process, are the parameters that are associated with the components, i.e. physical property values, mass and heat transfer parameters and reaction kinetic values. The physical property data and most of the transport parameters are either available from literature or estimation strategies are reported. A summary of the physical property data found in the literature is illustrated in Table C-1. More detailed information about the origin of the data is given in Table C-2.

Table C-1: Summary of the physical property data found in the literature at T=257K

Description	Variable	Value, 257K	Unit
Acetonitrile			
density	ρ	820.37	kg/m^3
Viscosity (dynamic)	η	0.00052347	$kg \cdot m^{-1} s^{-1}$
Molecular weight	u_m	41.05	kg/kmol
Heat capacity	cp	1.8337	$kJ \cdot kg^{-1} K^{-1}$
Thermal conductivity	k	0.00021467	$kJ \cdot m^{-1} s^{-1} K^{-1}$
Nitrogen			
density	ρ	1.3097	kg/m^3
viscosity	η	2.06e-5	kg/m_s
Molecular weight	u_m	28	kmol/kg
Fluorine, gaseous			
density	ρ	1.7774	kg/m^3
viscosity	η	1.6158e-5	$kg \cdot m^{-1} s^{-1}$
Molecular weight	u_m	38	kg/kmol
Diffusivity in solvent nitrogen	$D_{F2,g}$	1.5536e-5	m^2/s
Critical pressure	p_c	5.17	bar
Critical temperature	T_c	144	K
Fugacity of the pure component	f_{pure}	25.003	MPa

Toluene			
density	ρ	900.02	kg/m^3
Molecular weight	u_m	92.13	$kg \cdot m^{-1} s^{-1}$
Viscosity (dynamic)	η	0.001006	$kg \cdot m^{-1} s^{-1}$
Diffusivity in solvent Acetonitrile	$D_{Tol,I}$	$1.9558 \cdot 10^{-9}$	m^2/s
Heat capacity	c_p	1.6108	$kJ \cdot kg^{-1} K^{-1}$
Thermal conductivity	k	0.000016171	$kJ \cdot m^{-1} s^{-1} K^{-1}$
Fluorine, dissolved			
Molar volume	v_m	25.3 (at normal boiling point 85K)	cm^3/mol
Molecular weight	u_m	38	kg/kmol
Diffusivity in solvent Acetonitrile	$D_{F2,I}$	4.6228e-9	m^2/s
Reaction Products			
density	$\rho_{F\text{-}Tol}$ $\rho_{F2\text{-}R}$ $\rho_{F10\text{-}R}$ $\rho_{F5\text{-}R}$	see Toluene 1040 kg/m^3 (value for di-benzene) see $\rho_{F2\text{-}R}$ see $\rho_{F\text{-}Tol}$	kg/m^3
Molecular weight	$u_{m,F\text{-}Tol}$ $u_{m,F2\text{-}R}$ $u_{m,F10\text{-}R}$ $u_{m,F5\text{-}R}$	110.13 222.27 374.26 186.12	kg/kmol
Diffusivity in solvent Acetonitrile	$D_{F\text{-}Tol,I}$ $D_{F2\text{-}R,I}$ $D_{F10\text{-}R}$ $D_{F5\text{-}R}$	$=D_{Tol,I}$ $1.1889 \cdot 10^{-9}$ $1.1891 \cdot 10^{-9}$ $=D_{Tol,I}$	m^2/s
Heat capacity	$c_{p,\varphi}$	$=c_{p,Tol}$	$kJ \cdot kg^{-1} K^{-1}$
Thermal conductivity	k_φ	$=k_{Tol}$	$kJ \cdot m^{-1} s^{-1} K^{-1}$

C.2 Parameter calculations

In this Section the equations are illustrated which are used in the process model for the calculation of various physical properties of a compound.

Table C-2. Detailed illustration of the origin of physical property data

Description	Var.	Approximation equation (incl. Temperature dependency)	Unit	Ref.
Fugacity of the pure component	f_L	The fugacities of pure gases are plotted versus the temperature reduced by the critical temperature in Hildebrand (1964). The values of a whole range of gases can be described with reasonable accuracy by a single line. The fugacity can be correlated as function of the reduced temperature in two steps by means of a 4th order polynomial and an exponential function: $f_{L_inter} = -0.4702 \cdot Tr^4 + 4.9203 \cdot Tr^3 - 19.6969 \cdot Tr^2 + 35.7774 \cdot Tr - 17.1481$ $f_L / p_{c,\varphi} = 0.101119 \cdot \exp(0.539593 \cdot f_{L_inter})$ where $T_r = T/T_c$ is the reduced temperature and $p_{c,\varphi}$ is the critical pressure of gas φ	bar	1)
Liquid phase Diffusion coefficients of solute 1 in solvent 2 at very low solute concen-tration	$D_{\varphi,l}$	The numerical empirical correlation by Wilke and Chang was used to calculate the Diffusion coefficient as a function of the temperature T_l: $D_{\varphi,l} = 7.4 \cdot 10^{-8} \left[(\Phi \cdot M_2)^{1/2} T_l / \eta_2 V_1^{0.6} \right]$ where M_2=molecular weight of solvent [kg/kmol] T_l=temperature [K] μ_2=viscosity of solution (solvent) [cP] ϕ=1.9 "associated parameters" of solvent, recommended value for methanol V_1=molal volume of the solute at its normal boiling point [cm^3/mol]: where: V_{F2}=25.3 cm^3/mol V_{Tol}=106 cm^3/mol $V_{F10\text{-}R}$=242.99 cm^3/mol	m^2/s	2)
Acetonitrile				
density	ρ	$\rho_{(T_l)} = [\rho_{(0°C)} + 10^{-3}\alpha \cdot T_l + 10^{-6}\beta \cdot T_l + 10^{-9}\gamma \cdot T_l]$ (T_l = 228.15 K – 338.15 K) where $\rho_{(0C)}$ =0.8035, α= -1.055, β= -0.138, γ= -6	kg/l	3)
viscosity	η	$\eta = A \cdot T_l^B$ (T_l = 273.15K-298.15K) where A=3.851·10^{-6}, B=-2.849 [T_l] = C	cP	4)
Heat capacity	c_p	Published data (NIST-Chemistry-Webbook) describing the heat capacity has a relatively large inaccuracy of about err=15%. A correlation by Mirzaliev, Shakhuradov, et al. (1987, from NIST-Chemistry-Webbook online) has been	kJ·$kg^{-1}K^{-1}$	5), 7)

		chosen to calculate values for the specific heat as a function of the temperature (T_l =253K-353K). Compared to data from other sources these values seemed systematically too low and thus the correlation was augmented to match experimental data better. Of course, there remains the uncertainty of the measurements. $c_p = 1.37 + 0.0004369 \cdot T_l + 5.3125 \cdot 10^{-6} \cdot T_l^2$ where $[T_l]$ = K		
Thermal conductivity	k	Estimation method by Robbins and Kingrea: $k = \{[88.0 - 4.94 \cdot H)(10^{-3})]\Delta S^*\}(0.55/T_r)^N c_p \cdot \rho^{4/3}$ where T_r=reduced temperature, T/T_c c_p=molal heat capacity of the liquid, cal·mol^{-1}K^{-1} ρ=molal liquid density [mol/l] ΔS^*=19.573 cal/K modified Everett entropy of vaporization, T_b= 354.75 K, normal boiling point T_c= 548.15 K, critical temperature ΔH_{vb}= 7127.96 cal/mol, molal heat of vaporisation at the normal boiling point The parameters H and N are obtained from a table; H depends on molecular structure and N on the liquid density at 20C. Here N=1 and H=0. The calculated thermal conductivities were compared to data from the CRC databook where an error of only err=3% was detected. With this data a simple temperature correlation was set-up: $k = 2.67 \cdot 10^{-9} T_l^2 - 2.22 \cdot 10^{-6} T_l + 6.09 \cdot 10^{-4}$	cal·cm^{-1}· s^{-1} ·K^{-1}	2)
Toluene				
density	ρ	$\rho_{(T_l)} = [\rho_{(0°C)} + 10^{-3}\alpha \cdot T_l + 10^{-6}\beta \cdot T_l + 10^{-9}\gamma \cdot T_l]$ (T_l = 273.15 K – 372.15 K) where $\rho_{(0C)}$=0.88412, α= -0.92248, β= 0.0152, γ= -4.223 $[T_l]$ = C	kg/l	6)
viscosity	η	$\eta = \exp(A + B/T_l + C \cdot T_l + D \cdot T_l^2)$ (T_l = 233.15K - 588.15 K) where A=-5.878, B=1287, C=0.004575, D=-4.499·10^{-6} $[T_l]$ = C	cP	3
Heat capacity	c_p	The specific heat of toluene is calculated by means of a correlation given by CHERIC (T_l = 178K - 583K): $c_p = -56.32368 + 1.767199 \cdot T_l - 5.189027 \cdot 10^{-3} \cdot T_l^2 + +5.493583 \cdot 10^{-6} \cdot T_l^3$ where T_l [K] the correlated values were compared to NIST online values which are based on research articles. The error among the published data is as high as the error between the literature values and the correlation above (err<2.5%)	kJ·kmol^{-1}K^{-1}	4), 7)

Thermal conductivity	k	The thermal conductivity of toluene is calculated by means of a correlation given by CHERIC (T_l = 178K - 581K): $k=0.2031-0.0002254 \cdot T_l - 2.47 \cdot 10^{-8} \cdot T_l^2$ where $[T_l]=K$ This correlation was compared to an estimation method by Robbins and Kingrea (in "Properties of liquids and gases", Reid, Sherwood). The maximum deviation between the two approaches is err=20%.	$W \cdot m^{-1} \cdot K^{-1}$	4), 2)
Fluorine				
		Nitrogen and Fluorine are considered ideal gases and thus the density can be calculated form the ideal gas law. This assumption is backed up by data from the NIST "Chemistry Webbook" (2003). The detected error was not more than 0.2%		7
	η	The viscosity of N_2 and F_2 is reported in the NIST online Database as a function of pressure and temperature. This data can be correlated as a function of the temperature by means of a third order polynomial (between condensation and critical point): $\eta = 4 \cdot 10^{-8} \cdot T_l^3 - 1 \cdot 10^{-4} \cdot T_l^2 + 0.1078 \cdot T_l - 1.1841$ where $[T_l]=K$	μPa·s	7
Nitrogen				
		Nitrogen and Fluorine are considered ideal gases and thus the density can be calculated form the ideal gas law. This assumption is backed up by data from the NIST "Chemistry Webbook" (2003). The detected error was not more than 0.2%		7
	η	The viscosity of N_2 and F_2 is reported in the NIST online Database as a function of pressure and temperature. This data can be correlated as a function of the temperature by means of a third order polynomial (between condensation and critical point): $\eta_{N_2} = 7 \cdot 10^{-8} \cdot T_l^3 - 9 \cdot 10^{-5} \cdot T_l^2 + 0.0832 \cdot T_l - 0.4776$ where $[T_l]=K$	μPa·s	7

C.3 References

1) Hildebrand, J.H., "The solubility of nonelectrolytes", 3rd edition, Reinhold (1950)

2) Reid R.C., Prausnitz J.M., Poling B.E., "The properties of gases and liquids". 4th edition, McGraw-Hill (1987)

3) National Research Council (U.S.), "International critical tables of numerical data, physics, chemistry and technology"., vol III, page 27, McGraw-Hill Book Company (1933)

4) Department of Chemical Engineering, Korea University, Thermodynamics and Properties LAB., Seoul 136-701, Korea, www.cheric.org (2003)

5) Mirzaliev, A.A.; Shakhuradov, Sh.G.; Guseinov, S.O., "Investigation of the isobaric heat capacity of nitriles at different temperatures" Izv. Vyssh. Ucheb. Zaved., Neft i Gaz, Vol. 30, No. 4, 55-58 (1987)

6) National Research Council (U.S.), "International critical tables of numerical data, physics, chemistry and technology"., vol VII, page 218, McGraw-Hill Book Company (1933)

7) NIST-Chemistry-Webbook online, http://webbook.nist.gov

Appendix D

Reactor stability and heat back-mixing

D.1 Problem statement

Heat back-mixing may occur in microreators with integrated heat exchanger through heat transport inside the reactor walls (e.g. with co-current coolant flow) and through the coolant flow (e.g. with counter-current coolant flow) in upstream direction with regard to the flow direction of the reactant. With microreactors the reactor housing takes up a considerable share of the overall reactor volume allowing longitudinal and transversal heat conduction. Counter currant flow is prone to heat back mixing because the convective coolant flow absorbs the heat of reaction and transports this heat to the feed of the reactant. In such cases the temperature inside the coolant and in the reaction plane near the mouth can increase significantly and thermal run-away may occur. Particularly strong temperature increase can be expected if the coolant temperature rises above the reaction fluid temperature, and thus the fluid is heated by the coolant.

D.2 Procedure

Here we want to show the mechanisms that could lead to thermal run-away and estimate the likelihood of occurrence. We look at three states of a case where thermal runaway occurs under operating conditions as shown in Table D-1. Here, we employ the same type of plot we in Chapter 7 to evaluate the effect of heat back-mixing on the reactor operability. In prior considerations the coolant flow temperature was constant and steady. In this section, the temperature of the coolant in a reactor Section (see Figure D-1) may change with time. Thus, the 2D plots in the next Section feature a built-in a time dimension. The temperature increase of the coolant between time instants is estimated because a detailed time-variant model would have required setting-up dynamic simulations of the entire reactor and coolant channel. As a

prerequisite for reasonable heat exchange it is required that the coolant can absorb more heat per degree temperature change than the reactor fluid:

$$\left[\overline{v}\cdot\overline{c}_p\cdot A\right]_l=\left[\overline{v}\cdot\overline{c}_p\cdot A\right]_c \qquad \text{(D-1)}$$

Table D-1. Operating conditions

Parameter	Value	Unit
ch_l	0.2	mm
cw_l	0.6	mm
hh	0.2-2	mm
$x_{F2,0}$	0.1	
$x_{Tol,0}$	0.0504	
M (260K)	9.40E-03	m/s
H_c (260K)	1.25E-02	kmol m^{-3} bar^{-1}

D.3 Results

In Figure D-1 the heat generation curve in reactor-section 1 and heat removal curves at different coolant temperatures are displayed. The maximum possible temperature in a reactor section at a given point of time t is determined by the intersection between the heat generation and removal lines. As a necessary condition to obtain an intersection the slope of the heat generation curve has to be flatter then the one of the heat removal line with the feed state of the reactant t_0 shown as a yellow line on the far left of the plot. Orange circles indicate operational states at different points of time t_1, t_2 and t_3 (within reactor Section 1).

- At time instant t_0 the reactant and the coolant are on the same initial temperature $T_{1,0}=T_{c,0}=267$ K. At this temperature heat is generated (see intersection of yellow line and red heat generation line) and the temperature in the reaction plane increases. The slope of the heat generation line at T=267K is lower than the one of the heat removal line and an intersection can be expected at moderate maximum possible temperature $T_{max,p}$ (state 1' in Figure D-1) at time instant t_1. The actual temperature in the reaction plane (state 1) establishes between $T_{max,p}$ (state 1') and $T_{c,0}$. We assume that the coolant temperature T_c did not change between t_0 and t_1 and $T_{c,1}=T_{c,0}$.
- The heat created in the entire reactor at time instant t_1 is conducted to the coolant and transported by the coolant flow to reactor-section 1 and the reactor feed. Thus in the next time instant t_2 the temperature of the coolant T_c has to be higher than before.

The extend of the increase depends on the heat capacity of the coolant and the rate of heat being transported upstream to where it was produced.

- In this example at the second point of time t_2 the temperature of the coolant increased to $T_{c,2}$=277 K while the reactant feed temperature $T_{1,0}$ remained constant at 267 K. Thus at the reactor mouth the reactant is heated by the coolant and additionally heat is created by the chemical reaction. The temperature in the reaction plane establishes between state (2') and $T_{c,1}$ at a value T_1=292K. Here, the slope of the heat generation for reactor section 1 is steeper than at t_1 while the slope of the heat removal line remained constant. Thus $T_{max,p}$ (state 2') is much higher than 1' and we can speak of thermal runaway. Considering the slopes of the heat generation and removal line at time t_2 a strong increase of the temperature in the next time step can be expected with further increase of the coolant temperature T_c.
- At time instant three the temperature in the reaction plane increased to T_1 315K while the coolant is at $T_{c,3}$=282K. This thermal run-away can only occur if the heat generation is not limited by depletion of the reactants throughout the reactor.

With co-current coolant arrangement thermal runway is less likely to occur. In contrast to counter-current flow heat backmixing does not occur due to the flow of the coolant. However, with co-current coolant flow in microreactors heat may be conducted within the reactor housing in longitudinal direction, see Figure 8-3. Under the conditions considered in this work the temperature increase near the reactor mouth due to longitudinal convection is very low, which is illustrated in Table 8-5. Thus, thermal runaway driven by heat back mixing is weak with co-current coolant flow. The same can be said for cases where a constant temperature heat sink or cross flow cooling is used. In this case longitudinal heat transport is extremely small due to a relatively even temperature level throughout the reactor.

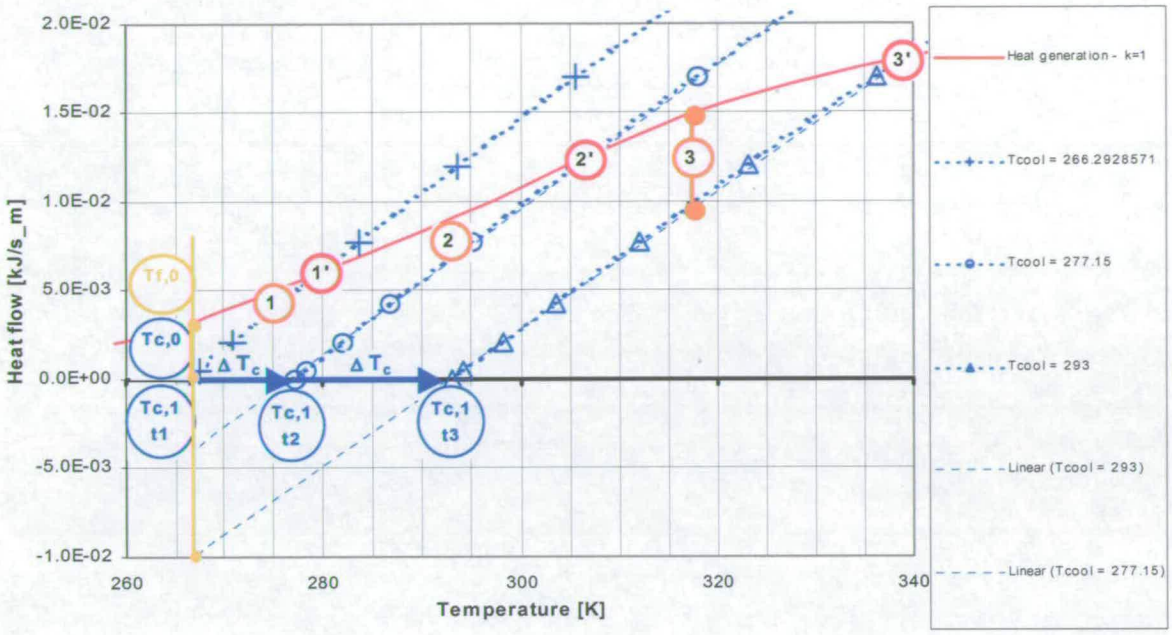

Figure D-1. Temperature profile in the cooling channel (cross-flow arrangement), the liquid channel and the membrane domain; hh=2 mm, ch_c=0.2 mm, V_c=4.35·10^{-7} m^3/s

Appendix E

Gas-phase mass transfer coefficient

E.1 Introduction

Problem statement

The absorption of a gas into a liquid can be divided into three steps:

- the transport from the bulk gas flow to the interface
- the phase change at the interface itself where there is no resistance so that Henry's law is satisfied:

$$c^*_{F2,l} = H_c \cdot p^*_{F2,g} \tag{E-1}$$

where H_c has the dimension $kmol \cdot m^{-3} bar^{-1}$ and $p_{F2,g}^*$ and $c_{F2,l}^*$ are the partial pressures and the concentration of fluorine at the gas/liquid interface

This assumption is justified even though in real applications there is a resistance at the interface otherwise the initial absorption mass flow would be infinite. The mass flow can only be as high as the impingement of the gas on the liquid surface, which is not the limiting process, here.

- the transport from the interface to the bulk liquid flow.

Absorption regimes

For the absorption from a gas phase into a falling liquid film the inherent instability of falling films has to be taken into account even at very low Reyolds numbers. Waves form on the film surface even in the absence of any disturbances due to the motion of the vapour. In a review by Killon and Garimella (2001) four different flow regimes are distinguished:

- $Re < 20$ smooth laminar film
- $20 < Re < 200$ laminar film with capillary waves
- $200 < Re < 4000$ film with roll waves
- $4000 < Re$ smooth turbulent film

The formation of waves leads to an increase in the mass transfer coefficient through induced fluid motion in the gas phase rather than higher surface area. Commenge et al (2003) determined the gas phase mass transfer coefficient for the falling film microreactor introduced above. They found the following correlation in terms of non-dimensional numbers:

$$Sh = 0.330 \cdot \mathrm{Re}^{0.816}\, Sc^{0.33} \qquad 30 < \mathrm{Re} < 110 \tag{E-2}$$

where the Sherwood Sh number increases with both the Schmid Sc and most importantly with the Re number. Comparing the range of the Reynolds number to the flow characterisation shown above, we find that this correlation was done for laminar film with capillary waves.

E.2 Smooth film absorption

In the smooth laminar film regime, in absence of any waves or turbulences, the concentration distribution can be calculated through solving the convection-diffusion equations and the momentum conservation equation.

$$-\nabla\left(D_{F_2,g} \cdot \nabla c_{F_2,g}\right) = -\overline{v}_g \cdot \nabla c_{F_2,g} \tag{3-1}$$

$$\vec{v}_g \cdot \nabla\left(\overline{\rho}_g \vec{v}_g\right) = -\nabla p + \nabla \cdot \left(\overline{\mu}_g \nabla \vec{v}_g\right) \tag{3-2}$$

These equations are not implemented in the reactor model introduced in Chapter 3, where the gas-phase was modelled as plug flow with lumped variables in transversal direction. Therefore a mass transfer coefficient k_g had to be determined to describe the limitations on the absorption rate imposed by the gas phase. This mass transfer coefficient can be calculated using the same procedure that is used to obtain the heat transfer coefficient (Welty et al., 2000; Deen, 1998):

$$\overline{c}^{*}_{F_2,g}(x) = \frac{\int_0^{cw} c^{*}_{F_2,g} \cdot dy}{\int_0^{cw} dy} \tag{E-3}$$

$$\overline{c}_{F_2,g}(x) = \frac{\int_A \vec{v} \cdot c_{F_2,g} \cdot dzdy}{\int_A \vec{v} \cdot dzdy} \tag{E-4}$$

$$\overline{N}_{F_2}^{\,*}(x) = \frac{\int_0^{cw} -\frac{1}{1-x_{F_2,g}} D_{F_2,g} \left(\frac{\partial c_{F_2,g}}{\partial z} \right)^* \cdot dy}{\int_0^{cw} dy} \tag{E-5}$$

$$k_g(x) = \overline{N}_{F_2}^{\,*} / (c^*_{F_2,g} - \overline{c}_{F_2,g}) \tag{E-6}$$

The biggest influence on the mass transfer coefficient originates form the channel size and the diffusion coefficient. The relative velocity between the gas and the liquid flow influences the development of the laminar boundary layer and thus the mass transfer across the interface. Also, entrance effects occur, noticeable through increased mass transfer in the developing flow. The modelling approach and results are illustrated in the result Section 5-2.

E.3 Liquid-phase and over-all mass transfer coefficients

In the liquid phase the concentration profile of the absorbed component is depending on the transversal diffusion and chemical reaction:

$$-\nabla \left(D_{F2,l} \cdot \nabla c_{F2,l} \right) = -\overline{v}_l \cdot \nabla c_{F2,l} - r_{F2} \tag{E-7}$$

This equation is describing the reactive flow and is fully implemented in the process model. Thus, the determination of an explicit mass transfer coefficient is not needed for process simulations. However, for the characterisation of the process it can be interesting to compare the gas and the liquid phase mass transfer coefficient to determine the extent of the individual contributions to the overall mass transfer limitation. Here the liquid phase mass transfer coefficient is calculated from the mass conservation equation (Eq. D-7). For fast first order reactions Astarita (1967) derived the following equation to calculate the rate of absorption with respect to the limiting component:

$$\overline{N}_{F_2}{}^{*} = -D_{F_2,l}\left(\frac{dc_{F_2}}{dx}\right)^{*} = \sqrt{k_{F_2} \cdot D_{F_2,l}} \cdot c_{F_2}{}^{*} \tag{E-8}$$

where

$$k_l = \sqrt{k_{F_2} \cdot D_{F_2,l}} \tag{E-9}$$

is the liquid phase mass transfer coefficient. The absorption flow is obviously a function of the rate of reaction in the liquid phase and Danckwerts (1970) introduced an enhancement factor E to quantify the influence of the reaction. This factor is calculated as the ratio of the mass transfer coefficient as it is introduced above and the mass transfer coefficient for physical absorption.

$$E = \frac{k_l}{k_{l,p}} \tag{E-10}$$

For simplicity the physical absorption is calculated by means of the film model:

$$k_{l,p} = D_{F_2,l} / \delta \tag{E-11}$$

where δ is the film thickness near the surface, which is the height of the entire microchannel. Danckwerts (1970) describes the film model as "not very realistic" because it assumes stagnant film. This assumption is correct for pure developed laminar flow where no velocity components exist transversal to the direction of flow (see also Section 5.2.4). The absorption flow rate can then be calculated according to the following equation:

$$\overline{N}_{F_2}{}^{*} = \frac{1}{\frac{1}{k_g} H_c \frac{\overline{u}_{m,g}}{\overline{\rho}_g} + \frac{1}{k_l}} \left(\overline{x}_{F_2,g} H_c - \overline{c}_{F_2,l}\right) \tag{E-12}$$

where the denominator marks the total resistance to the flow across the gas/liquid interface. If one of the mass transfer coefficients is much larger than the other one, the previous can be cancelled from this equation. With irreversible fast reactions the bulk liquid phase concentration of the absorbed component $c_{F2,l}$ is equal to zero.

E.4 Sherwood number with smooth and wavy film

At approximately Re=20 the transition from a flat liquid surface to wavy flow occurs which results in a vortex-mixing effect within the gas-phase. The calculation of a mass transfer coefficient for the previous is described above and a Sherwood number correlation for Re>30 is reported by Commenge (2003). In the capillary wave regime the mass transfer coefficient rises drastically with increasing Reynolds number, see Figure E-1.

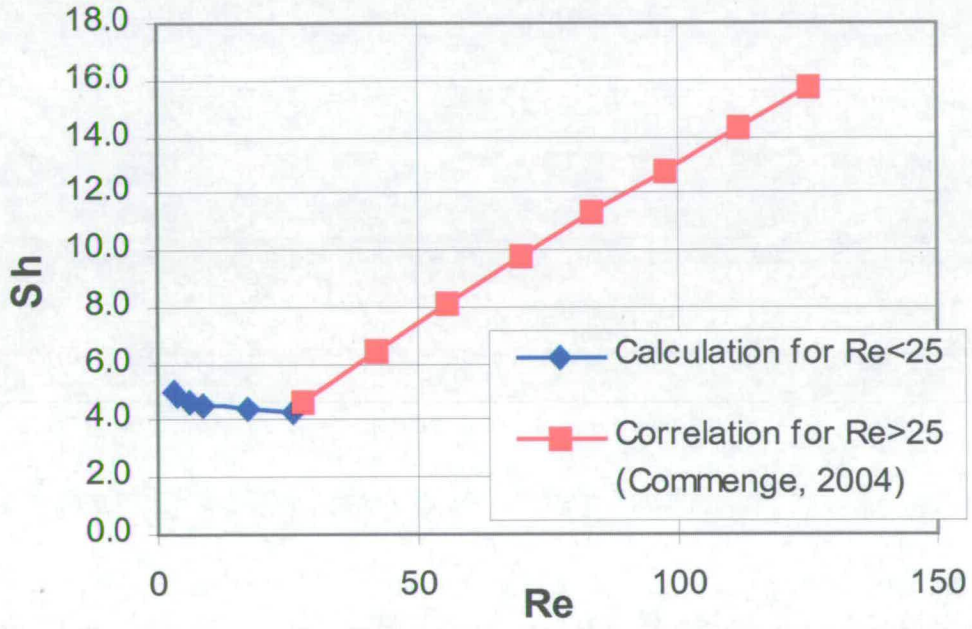

Figure E-1. Sh vs Re for smooth lamiar film Re<25 and wavy laminar flow Re>25

Appendix F

Finite Difference Method

F.1 Model implementation

The finite difference CMMR model was layed-out as a short-cut model, which was intended for more complex plant synthesis modelling. Here, efficiency of the numerical solver routine is the biggest concern. In this connection the process model as it is introduced in this chapter is simplified and the following assumptions were taken:

- The model domain consists of the 2D plane described by the x and z coordinates referring to Figure 3-3 and Figure 3-5.
- The reactor is operated isothermally. As a consequence only the fluid channels and the membrane are taken into account and Eq. (3-2) is redundent.
- In the liquid channel, instead of a solving the momentum equation a laminar flow profile is introduced to the mass conservartion equation.
- Fluid flow in the gas channel is modelled as convective plug flow.

With all these assumptions implemented into the model only the mass conservation equation remains (Eq. 3-2):

$$-\nabla\left(D_{\varphi,\Omega}\cdot\nabla c_{\varphi,\Omega}\right)+\vec{v}_{\Omega}\cdot\nabla c_{\varphi,\Omega}=-\sum\nu_{\varphi,i}\cdot r_i \tag{3-2}$$

For the case under consideration, where second order differentials with respect to x (i.e. diffusion in x-direction) are neglected, simplified rendering can be used:

$$\underbrace{-D_{\varphi,\Omega}\cdot\frac{\partial^2 c_{\varphi,\Omega}}{\partial z^2}}_{term1}+\underbrace{u_l(z)\cdot\frac{\partial c_{\varphi,\Omega}}{\partial x}}_{term2}=\underbrace{-\sum\nu_{\varphi,i}\cdot r_i}_{term3} \tag{3-2b}$$

The finite difference approximation is based on replacing the derivatives by difference quotients on a discrete numerical grid. Each sub-domain, i.e. gas-, liquid channel and membrane, has its individual implemetation of the finite difference technique. The mass transfer equation for each domain and the finite difference implementation is illustrated in Table F-1.

Table F-1. Mass transfer equation for each domain and finite difference implementation with reference to Eq. (3-2b) and inividual finite difference solution scheme

Domain	Finite difference formulation	Remark
Gas channel	1st order ordinary differential equation, in difference form $\underbrace{\overline{v}_g \cdot \frac{\Delta c_{F_2,g}}{\Delta x} ch_g}_{term\,2} = \underbrace{k_g \cdot (H_c \cdot \overline{x}_{F_2,g} \cdot p - c_{F_2,S}^{*})}_{term\,1}$ the finite differece term is replaced by the boundary condition at the gas/liquid interface	Lumped in *z*-direction and 1st order forward difference scheme in *x*-direction. Initial value problem, solved with the shooting method;
Membrane	2nd order ordinary differential equation $f_1 = \underbrace{\frac{\Delta v_\varphi}{\Delta z}}_{\substack{term\,1 \\ \text{with substitution,} \\ \text{see } f_2 \text{ below}}} = \underbrace{\sum \nu_{\varphi,i} \cdot r_i / D_{\varphi,eff}}_{term\,3}$ $f_2 = \frac{\Delta c_\varphi}{\Delta z} = v_\varphi$ where v_φ is a substitute for the partial derivative of the concentration of component φ	2nd order differential replaced by two 1st order forward differences. Boundary value problem, solved with iterative shooting method using explicit Euler solver algorithm
Liquid channel	2nd order partial differential equation $\underbrace{u_l(z) \cdot \frac{\partial c_{\varphi,l}}{\partial x}}_{term\,2} = \underbrace{D_{\varphi,l} \frac{\partial^2 c_{\varphi,l}}{\partial z^2}}_{term\,1} - \underbrace{\sum \nu_{\varphi,i} \cdot r_i}_{term\,3}$ replace 2nd order differentials and no chemical reaction: $f_{i,j} = \left(\frac{\partial c_{\varphi,l}}{\partial x}\right)_{i,j} = \alpha \frac{\left(c_{\varphi,i,j+1} - 2 \cdot c_{\varphi,i,j} + c_{\varphi,i,j-1}\right)_l}{\Delta z^2}$ where $\alpha = \frac{D_{\varphi,l}}{u_l(z)}$	Method of lines: replace 2nd order differentials by finite differences and handle 1st order differentials by means of a solver algorithm, see Eq. (3-9)

The gas channel is modelled as a lumped stream neglecting diffusion in axial direction and is not computationally intensive. Considering the numerical solution of the mathematical equations the liquid channel and the membrane are the crucial sub-domains. Within the membrane the chemical reaction necessitates a very fine grid resolution due to its fast kinetics. Additionally, the iterative shooting method routine makes the membrane the computationally most intensive sub-domain. The membrane has to be solved for each step in

x-direction, thus, a large step size in x-direction increases the overall efficiency of the code. This step size is determined by the numerical solution scheme used for the liquid phase. Therefore, it is important to implement an efficient solver for the partial differential equation in the liquid phase, which is further considered in the next section.

F.2 Liquid channel PDE-solver

The method of lines is used to solve the partial differential equation describing mass transfer in the liquid phase. The basic idea is that a partial differential equation problem is reduced to a more simple ordinary differential equation problem by discretising all but one of the independent variables. In this manner we can take advantage of the powerful methods developed for ordinary differential equations for initial value problems (Madsen, 1975).
Stepping in direction of the x-coordinate may be explicit or implicit depending on whether the formula for solution at a certain time step involves past information or future information. Examples for popular explicit solvers are: Euler and Runge-Khutta methods. Any numerical solver algorithm has its own convergence and accuracy characteristic. The 'Crank-Nicolson' method is useful for the use with parabolic partial differential equations (Trefethen, 1996) and is chosen as stepping algorithm (subscript l, signalising reference to the liquid phase, is omitted to simplify rendering):

$$c_{\varphi,i+1,j} = c_{\varphi,i,j} + \frac{h}{2}\left(f(c_\varphi, x)_{i,j} + f(c_\varphi, x)_{i+1,j}\right) \qquad \text{(F-1)}$$

where : x=independent variable, $c_{\varphi,i}$ =dependent variable, i=index in x-coordinate, j=index in z-coordinate, $h=x_i-x_{i-1}$ step in x-direction. For improved efficiency Eq. (3-9) can be rearranged and combined with the partial differential equation illustrated in Table F-1 to give Eq. (3-10).

$$\mathrm{F_{i,j}} = \left((1-\alpha)\cdot \mathrm{c}_{\varphi,\mathrm{i,j}} + \frac{1}{2}\cdot\alpha\cdot\left(\mathrm{c}_{\varphi,\mathrm{i,j+1}} + c_{\varphi,\mathrm{i,j-1}}\right)\right)/(1+\alpha) \qquad \text{(F-2)}$$

$$\mathrm{c}_{\varphi,\mathrm{i+1,j}} = \mathrm{F_{i,j}} + \frac{\alpha}{2(1+\alpha)}\left(c_{\varphi,i+1,j+1} + c_{\varphi,i+1,j-1}\right)$$

where : $\alpha = \dfrac{h\cdot D_{\varphi,l}}{u_l(z)}$ is the 'modulus of the equation'

With the Crank-Nicolson method for the mass conservation equation in one spatial dimension this linear system is tridiagonal and thus both work and storage required are modest.
The accuracy of approximate solutions depends on step sizes in space and time. The Crank Nicolson method is the simplest implicit method for the mass conservation equation that is both unconditionally stable and second order accurate in time. The greater stability of this implicit finite difference method allows taking larger time steps than with explicit methods but they require more work per step since system of equations must be solved at each step. Using the Crank Nicolson method oscillation may occur. It is recommended for $\alpha<1$ accepting moderate oscillations (Jenson and Jeffreys, 1977). Detailed information about the Lax Equivalence Theorem that relates consistency and stability and convergence can be found in the literature, e.g. Fletcher (1988).

F.3 Results and discussion

In this section, the finite difference method is used to simulate a chemical reaction in the membrane reactor. The reaction kinetics are initially introduced at low values, which are increasing in the course of the study. At low reaction kinetics the shooting method within the membrane and the CN solver within the liquid channel work well. However, with increasingly fast kinetics, approaching the real kinetics of the fluorination of toluene, the shooting method algorithm for the membrane becomes inefficient because an extremely fine grid size has to be chosen. Furthermore, we intended to extent the scope of the model to accomplish non-isothermal modelling. This step, however, necessitated 3D modelling and efficient simultaneous solution of coupled differential equations. The finite element method is a more natural way of dealing with boundary value problems and therefore is considered in the next section.

Appendix G

Miscellaneous

G.1 Surface effects

G.1.1 Influence of gravity on the shape of the fluid

The wetting of a horizontal plate covered with a liquid film depends on the ratio of gravitational force and surface tension force. Low gravitational force can lead to depletion of the liquid layer. Here, we neglect the existence of a meniscus. A related issue is the deformability of a surface, where the dissipation and surface tension are the dominating properties the ratio of which is the crispation or capillary number:

$$C = \frac{\eta \cdot \alpha}{\sigma \cdot d_h} \tag{G-1}$$

Vanishing values of the capillary number correspond to infinite surface tension and undeformable liquid surfaces. The surface tension restores the equilibrium shape of a liquid surface. Typical values of C in standard thermocapillary convection are in the range $10^{-3} \cdot 10^{-7}$.

The fluid combination considered in this work results in an intermediate capillary number of $C=1.472 \cdot 10^{-5}$ with the FFMR where gas and liquid are in direct contact. Thus, capillary waves could occur if operated at a high relative velocity $\overline{v}_{g,rel}$. However, the relative velocities occurring in this work are too low to trigger capillary waves, see Appendix D. In this work a flat liquid surface is assumed where there is no curvature and no waves.

G.1.2 Fluid instabilities

Several effects can result in instabilities at the interface:

- Rayleigh-Benard Instability: This type of convection is buoyancy driven due to density differences, which is also known as natural convection. A liquid which is heated from below tends to develop this type of convection, however there are forces working against this movement: 1) viscous forces and 2) radiation and conductive relaxation.
- Steady state cellular Marangoni Benard convection: The surface tension of a two-component liquid at a gas/liquid interface varies with the composition and the temperature of the liquid. If the tensile forces in this surface are out of balance, and if the surface tension variation is large enough to overcome viscous drag and heat and mass diffusivities, Marangoni convection may occur. With this type of convection surface elements are driven into the surface region with higher surface tension. If thermal and solutal Marangoni numbers are competing at an undeformable interface occilatory Maragoni effects occur. To initiate a convective motion the surface tension gradient must be large enough to overcome dissipation effects of viscous drag and of heat and mass diffusion. The balance of these effects in the Benard-Marangoni system is expressed by the thermal and solutal Marangoni numbers.

Raleigh Bernard convection is strong in situation where a fluid layer is heated from the bottom and cooled from the top. In this work, the reactors are arranged so that cooling is applied from the bottom while the heat of the chemical reaction is exerted at the top of the liquid layer. This setting is the opposite of what is mentioned before and therefore stabilises the fluid.

With the FFMR the gas and the liquid phase are in direct contact and the evaluation of the Marangoni numbers is relatively straight forward. Inside the CMMR a membrane is implemented at the gas/liquid interface, which is suppressing convection in the liquid phase. The effect of a pronounced Marangoni convection on the chemical reaction in the FFMR may be: 1) toluene is transported towards the reaction plane from the bulk and intermediate products are transported away from the reaction zone,

2) the absorption of fluorine might be influenced due to surface renewal through the convective motion.

Phenomenon 1) results in a mixing effect balancing the concentration of intermediate products and toluene over the entire cross-section, thus reducing unfavourable concentration arrangements in the reaction plane. In this way series reactions towards highly fluorinated compounds may be lessened and selectivity S improved.

A measure for the rate of absorption (phenomenon 2) of fluorine into the liquid phase is the overall mass transfer coefficient:

$$k_{total} = \frac{1}{\frac{1}{k_g} H_c \frac{u_{m,g}}{\rho_{m,g}} + \frac{1}{k_l}} \tag{G-2}$$

where k_g and k_l are the mass transfer coefficients for the gas and the liquid phase respectively. If one of these resistances dominates it becomes mass transfer limiting. Figure 5-10 in Section 5.3.2 shows that the liquid phase resistance dominates at a temperature $T < 260\,\mathrm{K}$ and a standard gas channel geometry. Therefore, less liquid phase resistance through surface renewal due to Marangoni convection could have an impact. In the following the liquid phase resistance is investigated.

In Chapter 4 we assumed that the surface renewal rate is insignificant which leads to a simplified equation for k_l, see Eq. F-9. Here, this effect is taken into account and an equation derived by Astarita (1967) for a fast 1st order reaction based on Danckwerts' surface renewal model is used:

$$k_l = \sqrt{D_{F_2,l} \cdot \left(s + k_{F_2}\right)} \tag{G-3}$$

where s is the surface renewal rate, which is the reciprocal value of the convective time constant τ_{conv}.

In Table G-2 values for the reaction rate of fluorine and the surface renewal rate due to Marangoni convection are illustrated. The surface renewal rate is calculated for the dominating Maragoni effect ignoring other forces influencing the convective motion. Clearly, at temperatures $T \geq 257\,\mathrm{K}$ the reaction rate constant dominates, whereas at

lower temperatures and low concentrations of fluorine surface renewal may be significant.

Table G-1. Calculation of the thermal and solutal Marangoni numbers

Thermal Marangoni number			Solutal Marangoni number		
Parameter	Value	Unit	Parameter	Value	Unit
ΔT	3.2	K	Δc_B	0.02	kmol/m^3
$\Delta\bar{\sigma}_l = \frac{\partial\bar{\sigma}_l}{\partial T_l}\Delta T_l^*$	-0.4032	mN/m	$\Delta\bar{\sigma}_l = \frac{\partial\bar{\sigma}_l}{\partial c_{Tol}}\Delta c_{Tol}$	-0.020432	mN/m
Ma_{th}	809.67		Ma_{conc}	2955.41	
τ_{diff}	0.16	s	τ_{diff}	11.36	s
τ_{conv}	0.00020	s	τ_{conv}	0.0038	s

Table G-2. Surface renewal rate s due to Marangoni convection and rate of disappearance of fluorine assuming a pseudo 1st reaction with respect to fluorine.

Parameter	Unit	Case1	Case2	Case3
T_l	K	231	257	257
$x_{F2,0}$		0.1	0.1	0.25
ch	M	0.0001	0.0001	0.0001
k_{F2}	1/s	1200	20000	80000
s	1/s	3200, $Ma_{th.}$ dominates	260.2, $Ma_{conc.}$ dominates	2780, $Ma_{conc.}$ dominates

G.2 Residence time

In this study the fluid flow in microchannels is laminar and with the CMMR we obtain the characteristic parabolic flow profile and no-slip boundary condition on the reactor walls. The velocity profile of steady Poiseuille flow can be derived from the Navier-Stokes equations. With the parabolic velocity distribution the residence time distribution with a can be derived analytically and the result is:

$$E(t) = \begin{cases} 0 & t < \frac{\tau}{2} \\ \frac{\tau^2}{2 \cdot t^3} & t \geq \frac{\tau}{2} \end{cases} \qquad \text{(G-4)}$$

where τ is the mean residence time (or space time), $\tau/2$ is the minimum residence time and t is the time of passage. This equation gives the residence time distribution of a full parabolic profile and affects all liquid phase components. The FFMR has open liquid channels and therefore a nearly semi-parabolic profile develops. For series

reactions in a flow reactor the most important variable is the space time or contacting time (Fogler, 2001). Accurate adjustment of the residence time and thus a narrow residence time are desired.

G.3 FEM method: Derivation of element equations

The derivation of finite element equations starts with the construction of the weighted-residual or the weak form of the differential equations 3-1 to 3-3. The idea is to seek a polynomial approximation of the solution of the form

$$u \approx U^e(x,z) \equiv \sum_{j=1}^{n} u_j^e \psi_j^e(x,z) \qquad \text{(G-5)}$$

where u^e_j is the value of the approximate solution U^e at the jth node (x_j, y_j) of the finite element e and ψ^e_j are the approximation functions over the element; is the approximation of the dependent variable. The variable u denotes the dependent differential parameter, i.e. $\vec{v}_\Omega$ and p with Eq. (3-1), $c_{\varphi,\Omega}$ with Eq. (3-2), and T_Ω with Eq. (3-3). Employing Eq. (3-11) U^e is described by a finite number of unknown coefficients u^e_j, the so-called degrees of freedom (DOF) and the approximation functions ψ^e_j. The coefficients u^e_j are determined such that the original differential equations are satisfied in the weighted integral sense.

The reasons for choosing algebraic polynomial approximation functions are: a) the integrals of these functions can easily be evaluated numerically and b) interpolation theory of numerical analysis can be used to develop the approximation functions systematically. When described in terms of local coordinates, the basis functions ψ^e_j assume one of a few basic shapes. These are the shape functions and with linear elements in 1D, for example, any basis function on any mesh element is one of the following:

$$\psi_1^e(x) = x \qquad \psi_2^e(x) = 1 - x \qquad \text{(G-6)}$$

The functions ψ^e_j exhibit properties, which are known as interpolation properties, namely, ψ^e_j is the function which is linear on each of the mesh intervals e, is equal to 1 at the j^{th} node point, and is equal to 0 at the other node points. Interpolation functions derived using the dependent unknown (not its derivatives) at the nodes are called the Lagrange family interpolation functions. A Lagrange element with order k uses polynomials of order k to approximate u. The order of an element is an important parameter, similarly to the grid resolution, regarding accuracy and computational intensity of the numerical solver.

This approximation is then inserted into the weak form of the equation to determine the parameters u^e_j. Weight functions are introduced to obtain the necessary and sufficient number of n algebraic equations. If the weight functions are equal to the approximation function we obtain the Garlekin finite element model as FEMLAB is using.

The weak form over an element is equivalent to the differential equation and the natural boundary conditions of the element, which is the specification of the derivative of u at the element boundary. The approximation of u is required to satisfy the essential boundary conditions, i.e. values for the variable u.

The integrals occurring in the weak form are computed approximately using a quadrature formula. Such a formula computes the integral over a mesh element by taking a weighted sum of the integrand evaluated in a finite number of points in the mesh element. The order of a quadrature formula is the maximum number n such that it integrates all polynomials of degree k exactly. Thus, the accuracy of the quadrature increases with its order. On the other hand, with increasing order the number of evaluation points also increases. As a rule of thumb one can take the order of the quadrature to be twice the order of the finite element. In FEMLAB's data structures the order of the quadrature formula is denoted by 'gporder'. (gp stands for Gauss points). The order of pointwise constraints of the Lagrange element is denoted by 'cporder' and by default equals the order k of the highest polynomial in the element. The setting of these parameters can influence the accuracy of the numerical solution. Within the scope of this work particularly careful adjustment was required to solve the Navier-Stokes equation set.

More details about the solution of the weak-function can be taken from the Femlab reference manual (Femlab, 2003).

G.4 Pressure drop

The pressure drop of fluid flow in a duct is a function of the reactor geometry. In Figure G-1 the absolute level of pressure loss of the gas flow and its dependence on the channel height at constant aspect ratio a=0.33 is illustrated at standard operating conditions, see Table 5-2. Figure G-1 shows that the pressure drop with the gas channel is very low for the entire range of the channel size.

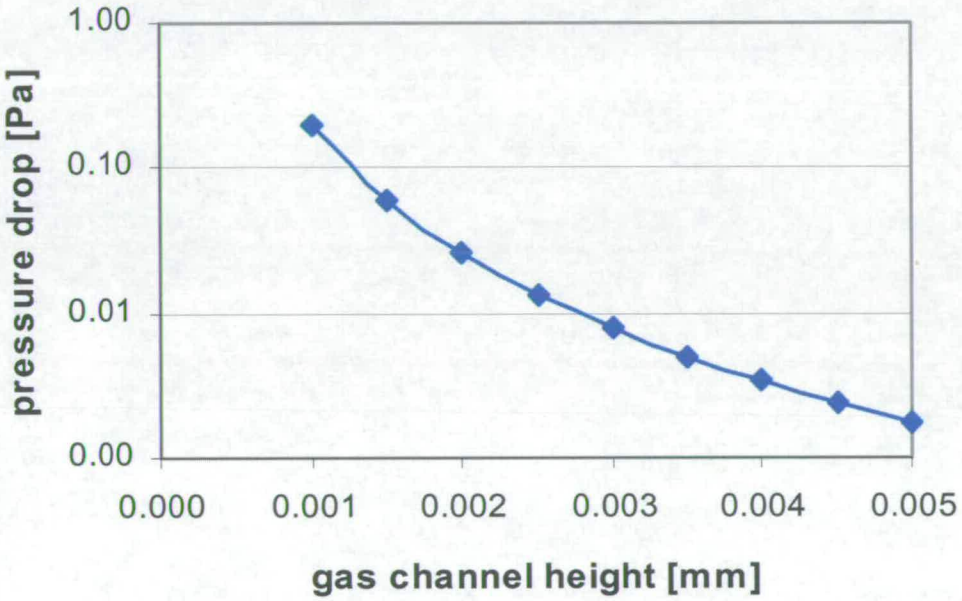

Figure G-1. Pressure drop vs gas channel height at constant volume flow and aspect ratio, $\overline{v}_l = 0.0032 - 0.016\ m/s$

G.5 Gas flow entrance length

When the gas flow enters the CMMR as plug flow we get hydrodynamically developing flow near the reactor mouth and parabolic flow further downstream. Analogical to heat transfer through pipe walls where a thermal developing zone exists, we get a compositional developing zone with mass transfer through the porous membrane wall. Laminar flow in a two-dimensional stationary duct is designated as

fully developed when, the dimensionless concentration distribution, as expressed in brackets, at a cross-section is invariant, i.e. independent of x:

$$\frac{\partial}{\partial x}\left[\frac{c_{F2,g}^{*}(x,y)-c_{F2,g}(x,y,z)}{c_{F2,g}^{*}(x,y)-\overline{c}_{F2,g}(x)}\right]=0 \qquad \text{(G-7)}$$

where: $c_{F2,g}$ is a function of x,y and z, unlike the velocity $\vec{v}_g$, which is a function of y and z only and is independent of x for fully developed flow.

The length of flow development is defined by the hydrodynamic development or compositional development depending on which effect is dominating. The compositional entrance length for standard cases is equal to the hydrodynamic entrance length multiplied by the *Sc* number. In this work *Sc* is smaller then unity, which means that the hydrodynamic entrance zone dominates. The standard formula for the prediction of the hydrodynamic entrance length is

$$L_g = 0.05 \cdot \mathrm{Re} \cdot d_h \qquad \text{(G-8)}$$

which is appropriate to estimate the length of flow development. Results with various hydraulic diameters d_h are plotted as a function of the Reynolds number *Re*, see Figure G-2. With *Re*=4 and d_h=0.0085m, which are standard values for the operation of the direct fluorination process we get an entrance length of L_g=2.5mm.

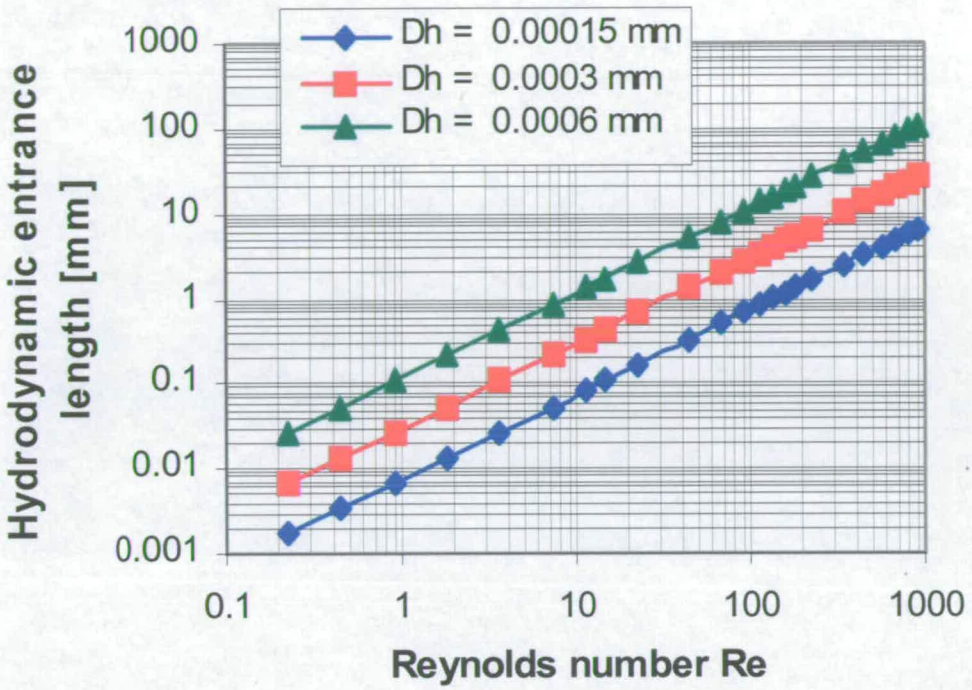

Figure G-2. Hydraulic entrance length in the gas channel

Nomenclature

$c_{\varphi,\Omega}$	Concentration of component φ
$c^{+}_{\varphi,\Omega}$	Dimensionless concentration of component φ
$c^{*}_{F2,S}$	Concentration of component F_2 in the liquid phase in equilibrium with the partial pressure of the same component in the gas phase $x^{*}_{F2,g} \cdot p$
$c^{*}_{F2,g}$	Concentration of component F_2 in the gas phase at the phase boundary
$\overline{c}_{\varphi,\Omega}$	Local average concentration in sub-domain Ω
$c_{p,\varphi}$	Heat capacity of component φ
$\overline{c}_{p,\Omega}$	Average local heat capacity
cl	Reactor length
ch_{Ω}	Liquid channel height
cw	Liquid channel width
d_h	Hydraulic diameter of the liquid channel
$D_{\varphi,l}$	Diffusion coefficient of component φ in solvent acetonitrile
$D_{eff,\varphi}$	Effective diffusion coefficient of component φ in solvent acetonitrile in the membrane
$D_{F2,g}$	Diffusion coefficient of fluorine in the diluent nitrogen
E	Absorption enhancement factor due to chemical reaction
E_A	Activation energy
f_L	Fugacity of pure gases
F_{φ}	Molar flow rate of component φ
hh	Height of the reactor housing
H_c	Henry's law coefficient of fluorine in the liquid mixture
$\Delta H_{r,i}$	Heat of reaction of reaction i
$\Delta H_{V,\varphi}$	Heat of reaction of vaporisation of component φ
$\overline{k}_{\Omega}$	Average local thermal conductivity in sub-domain Ω
k_{φ}	Thermal conductivity of component φ
k_{Ω}	Mass transfer coefficient in Domain Ω
$k_{l,p}$	Mass transfer coefficient – physical absorption in the liquid phase
k_{total}	Overall mass transfer coefficient from gas bulk into liquid
k_i	Reaction kinetic constant of reaction i
$k_{i,0}$	Pre-exponential factor of reaction i
L_{Ω}	Hydrodynamic entrance mength
F_{φ}	Molar flow rate of component φ
$\overline{N}^{*}_{F_2}$	Average local flux of fluorine across the gas/liquid interface
$p_{c,\varphi}$	Critical pressure of component φ
p_{φ}	Partial pressure of component φ
p^{*}_{φ}	Partial pressure of component φ in equilibrium with the concentration of component F_2 in the liquid phase $c^{*}_{F2,l}$
p	Absolute pressure

q_Ω	Heat flux in sub-domain Ω
Re	Reynolds number
r_i	Reaction rate of reaction I
$\Re$	Universal gas constant
$s_{\bar{T}_r}[T_r\ (x,y)]$	Standard deviation of the temperature in the reaction plane with respect to the mean temperature in the reaction plane in direction of the x or y coordinate
$s_{T_{r,opt}}[T_r\ (x,y)]$	Standard deviation of the temperature in the reaction plane with respect to the desired temperature in the reaction plane in direction of the x or y coordinate
S	Selectivity with respect to the desired product
T_{max}	Maximum temperature averaged over width of reaction plane
T_Ω	Temperature in domain Ω
$\bar{T}_\Omega$	Mean temperature in domain Ω
$T_{r,opt}$	Desired temperature in the reaction plane
T_r	Temperature in the reaction plane
u^e	Dependent variable in PDEs
$u_{m,\varphi}$	Molecular weight of component φ
$\bar{u}_{m,\Omega}$	Average molecular weight in domain Ω
U^e	Finite element approximation of dependent variable u
U	Heat transfer coefficient
$(u,v,w)_\Omega$	Local velocity components in 3D Cartesian coordinates
ww	Width of the channel walls
x, y, z	Cartesian coordinates
x_Ω, y_Ω, z_Ω	Length, width, height of the model geometry implemented in the FE-solver (may be different from cl, cw, ch of the actual reactor configuration)
$\vec{v}_\Omega$	Velocity vector in 3d Cartesian coordinates
$\bar{v}_\Omega$	Average velocity of the bulk flow in x direction in domain Ω
$\bar{v}_{g,rel}$	Relative velocity in the gas phase $\bar{v}_{g,rel} = \bar{v}_g - u_l^*$
v_l^*	Local velocity of the liquid phase at the boundary to the gas phase
$V_{m,l}$	Molal volume
V_Ω	Volume flow rate in domain Ω
X	Conversion of toluene
x_φ	Mole fraction of component φ
$x_{F2,g}^*$	Mole fraction of component F_2 in the gas phase at the boundary to the liquid phase
$\bar{x}_{F2,g}$	Average mole fraction of component F_2 in the gas phase
x_{fac}, y_{fac}, z_{fac}	Scaling parameters in 3D Cartesian coordinates
Y	Yield of desired product with respect to the reactant toluene

GREEK LETTERS

$\bar{\alpha}_\Omega$	Average local thermal diffusivity $\bar{k}_\Omega/(\bar{\rho}_\Omega \cdot \bar{c}_{p,\Omega})$
γ_a, γ_c	Geometric factors describing the membrane
δ	Characteristic length
δ_φ	Hildebrand solubility coefficient for compound φ
ε	Membrane porosity
κ	Dimensionless catalyst activity
λ	Ratio of thermal conductivities in the membrane (liquid/solid)
Λ	Dimensionless contact time
$\bar{\eta}_\Omega$	Average local dynamic viscosity

η_φ	Dynamic viscosity of compound φ
$\nu_{\varphi,i}$	Stoichiometric coefficient of compound φ with reaction i
$\overline{\rho}_\Omega$	Average local density
ρ_φ	Local density of compound φ
σ_φ	Surface tension of compound
$\overline{\sigma}_l$	Mean surface tension in liquid phase
τ	Membrane tortuosity; residence time
Φ	Thiele modulus
Φ_{mod}	Modified Thiele modulus
Ω	Modelling domain
ψ^e	Approximation function within element e
θ	Lnitial molar ratio of the reactants fluorine and toluene

SUBSCRIPTS

l	Liquid channel (sub-domain)
g	Gas channel (sub-domain)
c	Cooling channel (sub-domain)
h	Reactor housing (sub-domain)
i,j	Domain grid index in direction of x and z coordinate respectively
j	Node in 1D finite element formulation
mem	Membrane (sub-domain)
s	Solid membrane material
F	Reactor feed
S	Solute gas
Ω	Sub-domain: gas channel, liquid channel, membrane or solid reactor body
φ	Component: F_2, Tol, F-Tol, F_2-R, F_5-R and F_{10}-R
0	Initial value

SUPERSCRIPTS

+	Nondimensionalised parameter
*	Parameter at gas/liquid phase boundary

Acronym List

CMMR	Catalytic membrane microreactor
FFMR	Falling film microreactor
FEM	Finite element methode
2D	Two dimensional
3D	Three dimensional
err	Absolute error
err_{rel}	Relative error

References

Alonso C., Morato A., Medina F., Cesteros Y., Salagre P., Sueiras J.E., "Effect of the aluminium fluoride phase for the Cl/F exchange reactions in CCl2F2 (CFC-12) and CHClF2 (HCFC-22)", Appl. Catal. B-Environ., Vol. 40, 259–269 (2003)

Astarita G., "Mass transfer with chemical reaction.", Amsterdam (1967)

Balz G., Schiemann G., Ber. Dtsch. Chem. Ges., Vol. 60, 1186 (1927)

Bigelow L.A., "The action of elemental fluorine upon organic compounds", Chem. Revs., Vol. 40, 51 (1947)

Benson R.S., Ponton J.W., "Process miniaturisation – a route to total environmental acceptability?", Trans. IChemE, Vol. 71, 160-168 (1993)

Bockemueller W., "Organische Fluorverbindungen", Ferdinand Enke Verlag, Stuttgart (1936)

Burns J.R., Ramshaw C., Bull A.J., Harston P., "Development of a Microreactor for Chemical Production". In 1st conference on Microreaction Technology, Frankfurt/M. 23-25 February 1997, ed by Ehrfeld W., Springer-Verlag Berlin Heidelberg (1998)

Buchanan G.R. " Finite Element Analysis", Schaum's outline series, McGraw-Hill (1995)

Cacace F., Wolf A.P., "Substrate selective and orientation in aromatic substitution by molecular fluorine", J. Am. Chem. Soc, Vol. 100, No. 11, 3639-3641 (1978)

Chambers R.D., Skinner Ch.J., Hutchinson J., Thomson J., "Elemental fluorine part 1. Synthesis of fluoroaromatics", J. Chem. Soc., Perkin Trans. 1, Vol. 7, 605-609 (1996)

Chambers R.D., Spink R.C.H., "Microreactors for elemental fluorine", Chem. Commun., Vol. 10, 883-884 (1999)

Chang C.C., Lund C.R.F., "Selective chlorination of aromatic hydrocarbons", PhD Dissertation, Chem. Eng. Dept., University of Buffalo, NY, USA (2001)

Chau J.L.H., Yeung K.L., "Zeolite microtunnels and microchunnels", Chem. Commun., Vol. 9, 960-961 (2002)

Chiang A.S.T., Chao K.J., "Membranes and films of zeolite and zeolite-like materials", J. Phys. Chem. Sol., Vol. 62, 1899-1910 (2001)

Cini P., Harold M.P., "Experimental study of the tubular multiphase catalyst", AIChE Journal, Vol. 37, No. 7 (1991)

Clark J.H., Macquarrie D.J., "Heterogeneous catalysis in liquid phase transformation of importance in the industrial preparation of fine chemicals", Org. Process Res. Dev., Vol. 1, 149-162 (1997)

Clark J.H., Wails D., Bastock T.W., "Aromatic fluorination", CRC Press, London (1996)

Commenge J.-M., Framboisier X., Rode S., Schanen V., Pitiot P., Matlosz M., "Gas-phase mass-transfer measurements in a falling-fim microreactor", 7th international conference on Microreaction Technology, Lausanne (2003)

Constantinides A., Mostoufi N., "Numerical Methods for Chemical Engineers with Matlab Applications", Prentice Hall (1999)

Conte L., Gambaretto G.P., Napoli M., Fraccaro C., Legnaro E., "Liquid-phase fluorination of aromatic-compounds by elemental fluorine", J. Fluorine Chem., Vol. 70, 175-179 (1995)

Coronas J., Santamaria J., "Catalytic reactors based on porous ceramic membranes", Catal. Today, Vol. 51, 377-389 (1999)

Cussler E.L., "Non-Selective Membranes for fast separations", J. Chem. Technol. Biot., Vol. 78, Issue 2/3 (2003)

Danckwerts P.V., "Gas-liquid reactions", McGraw-Hill, (1970)

Dautzenberg F.M., Mukherjee M., "Process intensification using multifunctional reactors", Chem. Eng. Sci., Vol. 56, 293-303 (2001)

Deen W.M., "Analysis of Transport phenomena", Oxford University Press (1998)

DeMas N., Guenther A., Schmidt M.A., Jensen K.F., "Microfabricated multiphase reactors for the selective direct fluorination of aromatics", Ind. Eng. Chem. Res., Vol. 42, 698-710 (2003)

Ehrfeld W., Hessel V., Moebius H., Richter Th., Russow K., "Potentials and Realization of Microreactors". In Microsystems technology for Chemical and Biological Microreactors, ed by Ehrfeld W., Wiley-VCH (1996)

Ehrfeld W., Hessel V., Loewe H., "Microreactors: New technology for modern chemistry", Weinheim, Chichester, Wiley-VCH (2000)

Ehrfeld W., Hessel V., Kiesewalter S., Loewe H., Richter, Th., Schiewe J., "Implementation of Microreaction Technology in Process Engineering". In 3rd International Conference on Microreaction Technology: Industrial Prospects, ed by Ehrfeld W., Springer-Verlag Berlin Heidelberg (2000b)

Femlab, "Internet Knowledge Base", http://www.comsol.com/support/knowledgebase/ (2004)

Femlab, "Helpdesk", Manual distributed with the software package (2002)

Fletcher C., "Computational Techniques for Fluid Dynamics, I and II", Springer (1988)

Floyd T.M., Losey M.W., Firebaugh S.L., Jensen K.F., Schmidt M.A., "Novel Liquid Phase Microreactors for Safe Production of Hazardous Specialty Chemicals". In 3rd International Conference on Microreaction Technology: Industrial Prospects, ed by Ehrfeld W., Springer-Verlag Berlin Heidelberg, (2000)

Fogler S.H., "Elements off Chemical Reaction Engineering", 3rd Edition, Prentice Hall International Series (2001)

Franz A.J., Jensen K.F., Schmidt M.A., "Palladium membrane microreactors". In 3rd International Conference on Microreaction Technology: Industrial Prospects, ed by Ehrfeld W., Springer-Verlag Berlin Heidelberg, (2000)

Froment G.F., Bischoff, K.B., "Chemical reactor analysis and design", John Wiley & Sons (1990)

Fukaya H. and Morokuma K., "A Theoretical Study of the Mechanism of Selective Fluorination of Saturated Hydrocarbons by Molecular Fluorine. Participation of $CHCl_3$ Solvent Molecules in the Ionic Process", J. Org. Chem., Vol. 68, 8170-8178 (2003)

Fukuhara N., Bigelow L.A., "The action of elemental fluorine upon organic compounds. XI. The vapor phase fluorination of benzene", J. Am. Chem. Soc., Vol. 63, 2792 (1941)

Grakauskas V., "Direct liquid-phase fluorination of aromatic compounds", J. Organic Chemistry, Vol.35, No.3 (1970)

Golman B., Shinohara K., Kobayashi M., "Selectivity and yield of exothermic consecutive reactions in catalytically active porous membrane reactor", J. Chem. Eng. Jpn., Vol. 30., No. 3, 507-513, (1997)

Green A.J., Hearn S., Wood M., "Methodologies for Process Intensification". In 2nd int. Conference on Process Intensification in Practice Applications and Opportunities, ed by Semel J., MEP (1997)

Hansen C.M., "Hansen Solubility Parameters: A User's Handbook", CRC Press (1999)

Harold M.P., Zaspalis, V.T., Keizer K., Burggraaf A., "Intermediate production yield enhancement with a catalytic inorganic membrane - I. Analytical model for the case of isothermal and differential operation", Chem. Eng. Sci., Vol. 48, 2705-2725 (1993)

Hessel V., Ehrfeld W., Golbig G., Haverkamp H., Loewe H., Storz M., Wille Ch., Guber A.E., Jaehnisch K., Baerns M., "Gas/ liquid microreactors for direct fluorination of aromatic compounds using elemental fluorine". In 3rd International Conference on Microreaction Technology: Industrial Prospects, ed by Ehrfeld W., Springer-Verlag Berlin Heidelberg, (2000)

Hildebrand J.H., Scott R.L., "The solubility of non-electrolytes", New York, Dover (1964)

Hsu C.T., Cheng P., Wong K.W., "A lumped parameter model for stagnant thermal conductivity of spatially periodic porous media", J. Heat Transf., Vol. 117, 264-269 (1995)

Hsing I-M., Srinivasan R., Harold M.P., Jensen K.F., Schmidt M.A., "Simulation of micromachined chemical reactors for heterogeneous partial oxidation reactions", Chem. Eng. Science, Vol. 55, 3-13 (2000)

Ilinitch O., Cuperus F.P., Nosova L.V., Gribov E.N., "Catalytic membrane in reduction of aqueous nitrates: operational principles and catalytic performance", Catal. Today, Vol. 56, 137-145 (2000)

Isaacson E., Keller H.B., "Analysis of numerical methods", Wiley, New York (1966)

Jähnisch K., Baerns M., Hessel V., Ehrfeld W., Haverkamp V., Loewe H., Wille Ch., Guber A., "Direct fluorination of toluene using elemental fluorine in gas/liquid microreactors", J. Fluorine Chem., Vol. 105, 117-128 (2000)

Jenson V.G., Jeffreys G.V., "Mathematical Methods in Chemical Engineering", 2nd Edition, Academic Press (1977)

Jensen, K.F., "Microchemical Systems: Status, Challanges, Opportunities". AIChE J., Vol. 45, No. 10, (1999)

Julbe A., Farrusseng D., Guizard Ch., "Porous ceramic membranes for catalystic reactors - overview and new ideas", J. Membrane Sci., Vol. 181, 3-20 (2001)

Kaerger J., Ruthven D.M., "Diffusion in zeolites and other microporous solids", Wiley, New York (1992)

Kemnitz E., Menz D.H., "Fluorinated metal oxides and metal fluorides as heterogeneous catalysts", Prog. Solid St. Chem., Vol. 26, 97-153, (1998)

Killion J.D., Garimella S., "A critical review of models of coupled heat and mass transfer in falling-film absorption", Int. J. Refrig., Vol. 24, No. 8, 755-797 (2001)

Kolditz L., Nitzsche V., Heller G., Stoesser R., "On the effect of different oxidation-states of nickel and chromium in heterogeneous halogen exchange", Z. Anorg. Allg. Chem., Vol. 476, No. 5, 23-32 (1981)

Lagow R. J. "Direct Fluorination". In: Encyclopedia of chemical technology, ed by Kroschwitz J. I., Howe-Grant M., 4th ed., New York, Chichester, Wiley (1991)

Lerou J.J., Harold M.P., Ryley J., Ashmead J., O'Brien T.C., Johnson M., Perrotto J., Blaisdell C.T., Rensi T.A., Nyquist J., "Microfabricated Minichemical Systems: Technical Feasibility". In Microsystems Technology for Chemical and Biological Microreactors, ed by Ehrfeld W., VCH (1996)

Masel, R.I., " Chemical kinetics and catalysis ", Wiley-Interscience (2001)

Madsen, N.K., "The method of lines for the numerical solution of partial differential equations", In Proceedings of the SIGNUM meeting on Software for partial differential equations table of contents, Moffitt Field, California, United States, 5-7 (1975)

Miller W.T., Dittman A.L., "Mechanism of Fluorination. I. Fluorine Sensitised Oxidation of Trichloro- and Tetrachloroethylen, J. Am. Chem. Soc., Vol. 78, 2793 (1956)

Mitsutani A., "Future possibilities of recently commercialised acid/based chemical processes", Catal. Today, Vol. 73, 57-63 (2002)

Miyazaki M., Kaneno J., Kohama R., Uehara M., Kanno K.,. Fuji M., Shimizu H., Maeda H., "Preparation of Functionalised Nanostructures on Microchannel Surface and Their Usage for Enzyme Microreactors", 7th international conference on Microreaction Technology, Lausanne (2003)

Nagasawa H., Mae K., "Development of Multi-functional Microstructure Device for Inorganic Fine Particle Crystallization", 7th international conference on Microreaction Technology, Lausanne (2003)

Nishida N., Stephanopoulos G., Westerberg A.W., "A review of process synthesis", AIChE Journal, Vol. 72, No. 3, 321-351 (1981)

Nisisako T., Torii T., Higuchi T., "Novel Microreactors for Functional Polymer Beads", 7th international conference on Microreaction Technology, Lausanne (2003)

NIST, "Chemical Kinetics Database on the Web: A compilation of kinetics data on gas-phase reactions", http://kinetics.nist.gov/index.php (2003a)

NIST, "NDRL/NIST Solution Kinetics Database on the Web: A compilation of kinetics data on solution-phase reactions", HTTP://KINETICS.NIST.GOV/SOLUTION/INDEX.PHP (2003b)

Quiram D.J., Jensen K.F., Schmidt M.A., "Integrated Microchemical systems: Opportunities for Process design", in 5th international conference on: Foundations of computer-aided process design, ed by Malone M. F., Trainham J. A., Carnahan B., AIChE Symp. Series, vol. 96, (2000a)

Perkins J.D., "Process systems engineering to support the development of future process systems", in 2nd int. Conference on: Process Intensification in Practice Applications and Opportunities, ed by Semel J., MEP (1997)

Peureux J., Torres M., "Liquid-phase hydrogenation in a membrane reactor", Catal. Today, Vol. 25, No. 3-4, 409-415 (1995)

Rebrov E.V., Seijger G.B.F., Calis H.P.A., deCroon M.H.J.M., van den Bleek C.M., Schouten J.C., "The preparation of highly ordered single layer ZSM-5 coating on prefabricated stainless steel microchannels", Appl. Catal. A: General, Vol. 206, 125-143 (2001)

Rebrov E.V., de Croon M.H.J.M., Schouten J.C., "Optimisation of heat transfer characteristics, flow distribution, and reactor processing for a microstructured reactor/heat-exchanger optimal performance in platinum catalysed ammonia oxidation", Chem. Eng. J., Vol. 4139, 1-16 (2003)

Reddy J. N., "Introduction to the Finite Element Method", 2nd edition, McGraw-Hill (1993)

Reid R.C., Prausnitz J.M., Poling B.E., "The properties of gases and liquids", 4th edition, McGrawHill, (1987)

Rinard I., "Miniplant Design Methodology". In 2nd International Conference on Microreaction Technology, ed by Ehrfeld W., Renard I.H., Wegeng R.S., AIChE, New York (1998)

Rodriguez L.M., Alcaraz J., Hernandez M., Dufaux M., Taârit Y.B., Vrinat M., "Fluorinated alumina: characterization of acid sites and relationship between acidity and activity in benzene alkylation", Appl. Catal. A: General, Vol. 189, 53–61 (1999)

Sams L.C., Reames T.A., Durrance M.A., "Molecular Sieve Fluorination of Fluorobenzene Using Elemental Fluorine", J. Org. Chem., Vol.43, 2273-2275 (1978)

Saracco G., Neomagus H.W.J.P., Versteeg G.F., vonSwaaij W.P.M., "High-temperature membrane reactors: potential and problems", Chem. Eng. Sci., Vol. 54, 1997-2017 (1999)

Schuster A., Lakshmanan R., Ponton J., Sefiane K., "Modelling a novel miniaturised reactor / separator system", J. Chem. Technol. Biot., Vol. 78, 342-346 (2003)

Schwalbe T., Autze V., Wille, G., "Chemical synthesis in microreactors", Chimia, Vol. 56, 636-646 (2002)

Shah R.K., "Laminar flow forced convection in ducts: a source book for compact heat exchanger analytical data", Academic Press, New York (1978)

Sloot H.J., Versteeg G.F., Vanswaaij W.P.M., "A non-permselective membrane reactor for chemical processes normally requiring strict stoichiometric feed rates of reactants", Chem. Eng. Sci., Vol. 45, No. 8, 2415-2421 (1990)

Srinivasan R., Hsing I-M., Berger P.E., Jensen K.F., "Micromachined Reactors for Catalytic Partial Oxidation reactions", AIChE J., Vol.43, No.11, 3059 (1997)

Štěpánek F., Kubicek M., Marek M., Adler P.M., "Optimal design and operation of a separating microreactor", Chem. Eng. Sci., Vol. 54, 1493-1498 (1999)

Stankiewisz A., "Process intensification in in-line monolithic reactor", Chem. Eng. Sci., Vol. 56, 293-303 (2001)

Sykes P., "Reaktionsmechanismen der Organischen Chemie", 9th edition, Wiley/VCH (1988)

Tilgner I.C., Lange C., Schmidt H.W., Maier W.F., "Three-phase hydrogenation with microporous catalytic membranes", Chem. Eng. Techol., Vol. 21, No. 7, 565-570 (1998)

Trefethen L.N., "Finite Difference and Spectral Methods for Ordinary and Partial Differential Equations, x+315 pages. Graduate textbook, privately published at http://comlab.ox.ac.uk/work/nick.trefethen (1996)

Veser G., "Experimental and theoretical investigation of H-oxidation in a high-temperature catalytic microreactor", Chemical Engineering Science, Vol. 56, 1265-1273 (2001)

Vitulli G., Verrazzani A., Pitzalis E., "Pt/gamma-Al2O3 catalytic membranes vs. Pt on gamma-Al2O3 powders in the selective hydrogenation of p-chloronitrobenzene", Catal. Lett., Vol. 44, No. 3-4, 205-210 (1997)

Wang X., Jacobson A.J., "Synthesis of Large ZSM-5 Crystal under High Pressure", Mat. Res. Soc. Symp., Vol. 658 (2001)

Wan Y.S.S., Chau J.L.H., Gavriilidis A., Yeung K.L., "Design and fabrication of zeolite-based microreactors and membrane microseparators", Micropor. Mesopor. Mat., Vol. 42, 157-175 (2001)

Wegeng R.S., Drost M.K., Benchley D.L., "Process intensification through miniaturization of chemical and thermal systems in the 21st century". In 3rd International Conference on Microreaction Technology: Industrial Prospects, ed by Ehrfeld W., Springer-Verlag Berlin Heidelberg (2000)

Welty R.J., Wicks C.E., Wilson R.O., Rorrer G., "Fundamentals of Momentum, Heat and Mass Transfer", 4th edition, Wiley (2000)

Westerterp K.R., van Swaaij W.P.M., Beenackers A.A.C.M., "Chemical reactor Design and Operation", John Wiley&Sons (1987)

Wu S., Gallot J.E., Bousmina M., Bouchard Ch., Kaliaguine S., "Zeolite containing catalytic membranes as interphase contactors", Catal. Today, Vol. 56, 113-129 (2000)

Xu B., Ooi K.T., Wong T.N., Choi W.K., "Experimental investigation of flow friction in Micorchannels", Int. Commun. Heat Mass, Vol. 27, No. 8, 1165-1176 (2000)

Yu S., Ameel T.A., "Slip-flow heat transfer in rectangular microchannels", Int. J. Heat Mass Tran., Vol. 44, 4224-4234 (2001)

Zaspalis V.T., Vanpraag W., Keizer K., "Inorganic porous membranes as catalytic active materials – concept and experiments", Abstr. Pap. Am. Chem. S., Vol. 198, No. 37 (1989)